Thermo-Mechanical Behavior and Shakedown of Shape Memory Alloy Cable Structures

by

Daniel B. Biggs

A dissertation submitted in partial fulfillment
of the requirements for the degree of
Doctor of Philosophy
(Aerospace Engineering)
in The University of Michigan
2017

Doctoral Committee:

Professor John A. Shaw, Chair
Associate Professor Samantha H. Daly, University of California, Santa Barbara
Nilesh Mankame, General Motors Corporation
Associate Professor Veera Sundararaghavan
Professor Alan S. Wineman

Daniel Biggs

dbbiggs@umich.edu

ORCID iD: 0000-0002-2534-9861

ACKNOWLEDGEMENTS

This work would not have been made possible without the help of my many family members and friends, whom I am indebted to and sincerely thank. My laboratory colleagues Chris Churchill, Ben Reedlunn, Ryan Watkins, Kannan Dasharathi, Will LePage, and Corin Bowen provided invaluable support and guidance. Many thanks to the tech staff in the Aerospace Department: Terry Larrow, Tom Griffin, Dave McLean, and Aaron Borgman, who have helped me troubleshoot on more occasions than I can remember! I thank General Motors for providing funding and insight into applications for my research. I am very grateful to my advisor John Shaw for taking me under his wing early on as an undergrad and guiding me patiently through my doctorate. Finally, I am indebted to all my family members including my wife, parents, twin brother, sister, and in-laws for their ongoing emotional support.

TABLE OF CONTENTS

LIST OF FIGURES

Figure

LIST OF TABLES

Table

ABSTRACT

Shape memory alloys (SMAs) are a versatile class of smart materials that exhibit adaptive properties which have been applied to solve engineering problems in wide-ranging fields from aerospace to biomedical engineering. Yet there is a lack of understanding of the fundamental nature of SMAs in order to effectively apply them to challenging problems within these engineering fields. Stranding fine NiTi wires into a cable form satisfies the demands of many aerospace and civil engineering applications which require actuators to withstand large tensile loads. The impact of increased bending and twisting in stranded NiTi wire structures, as well as introducing contact mechanics to the unstable phase transformation is not well understood, and this work aims to fill that void.

To study the scalability of NiTi cables, thermo-mechanical characterization tests are conducted on cables much larger than those previously tested. These cables are found to have good superelastic properties and repeatable cyclic behavior with minimal induced plasticity. The behavior of additional cables, which have higher transition temperatures that can be used in a shape memory mode as thermo-responsive, high force actuator elements, are explored. These cables are found to scale up the performance of straight wire by maintaining an equivalent work output. Moreover, this work investigates the degradation of the thermal actuation of SMA wires through novel stress-temperature paths, discovering several path dependent behaviors of transformation-induced plasticity.

The local mechanics of NiTi cable structures are explored through experiments utilizing digital image correlation, revealing new periodic transformation instabilities. Finite element simulations are presented, which indicate that the instabilities are caused by friction and relative sliding between wires in a cable.

Finally, a study of the convective heat transfer of helical wire involving a suite of wind tunnel experiments, numerical analyses, and an empirical correlation is presented. This provides a method to better model the thermal behavior of helical SMA actuators and highlights the non-monotonic dependence of the convective heat transfer coefficient of helical wire with respect to the angle of the flow.

CHAPTER 1

Introduction

Shape memory alloys (SMAs) are a unique class of smart materials known for their ability to either: (1) recover large deformations through the addition of thermal energy (heating), or (2) accommodate large deformations when mechanically loaded. These adaptive properties are called *the shape memory effect* and *superelasticity*, and stand out compared to properties of other smart materials (piezoelectric materials, dielectric elastomers, shape memory polymers, etc.) due to the combination of relatively large actuation and high work output that they provide.

To exhibit the shape memory effect, the material is first mechanically deformed into a new temporary shape that appears to have a permanent plastic set. The deformation can then be recovered upon heating above a transition temperature, whereby the material reverses the mechanical deformation and returns to its original remembered shape. Under a bias load (such as a spring or dead load), this effect can be harnessed to exert mechanical work on the environment and allows the material to be used as a highly compact and thermally activated actuator.

To exhibit superelasticity, the material is held at an ambient temperature above the transition temperature and is mechanically loaded, undergoing large deformations through a stress-induced transformation. When the material is subsequently unloaded, it fully recovers to its original state by reversing the phase transformation. This effect is utilized to provide enhanced resilience of metallic structures, often to accommodate large bending deformations. The large amount of dissipated energy with each transformation cycle is also favorable for applications requiring good vibration damping properties.

SMAs have a vast theoretical and developmental foundation, including complex metallurgy and materials science. A complete review will not be attempted here, but there are many good references on the matter including several well-regarded books on topics ranging

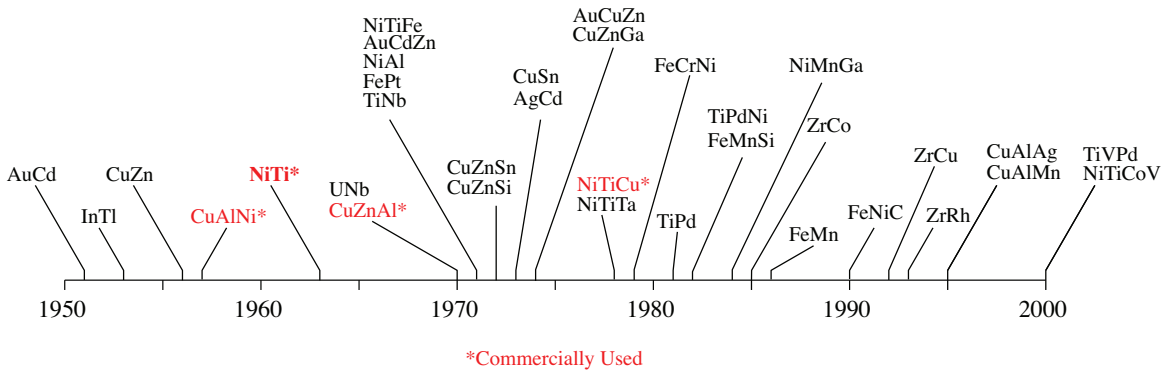

Figure 1.1: Notable shape memory alloys discovered since 1950. [83]

from general shape memory alloy behavior to the thermodynamics of solid phase transformations (see [2, 10, 33, 37, 41, 67]). For a general introduction to shape memory alloy properties, the reader is directed to Shaw et al. [83] for a concise overview. Selected topics will be covered here to guide the reader through a few of the relevant material properties of shape memory alloys.

1.1 Shape Memory Alloy Background

Shape memory alloys exhibit two unique adaptive properties: *the shape memory effect* and *superelasticity*. The most widely used shape memory alloy is nearly equiatomic nickel titanium[1] (NiTi) and was discovered in the early 1960's by the U.S. Naval Ordinance Laboratory [55]. Since then, there have been numerous discoveries of various alloys exhibiting shape memory and superelastic properties, a timeline of which can be seen in Figure 1.1. Interestingly, NiTi has remained at the forefront due to a combination of superior adaptive properties, moderate cost of manufacturing, biocompatibility, and corrosion resistance. There have been numerous applications to date that harness these unique properties.

The first major application for shape memory alloys came in the form of pipe couplers for hydraulic lines in the F-14 fighter jet [55]. To join the hydraulic lines, nitinol tubes were formed with an interference fit to the hydraulic lines, then mechanically expanded and stored at cryogenic temperatures. When the hydraulic lines were to be joined, the nitinol tube was slipped over the joint and allowed to warm to room temperature, creating an effective seal. Since then, many applications have utilized the shape memory mode for thermal actuation of SMA wires, typically through joule heating. Some examples include adaptive wings which

[1]NiTi is also commonly referred to as *nitinol* – a name created by the researchers who discovered the alloy and is a concatenation of **NiTi** and the initials of the **N**aval **O**rdinance **L**aboratory.

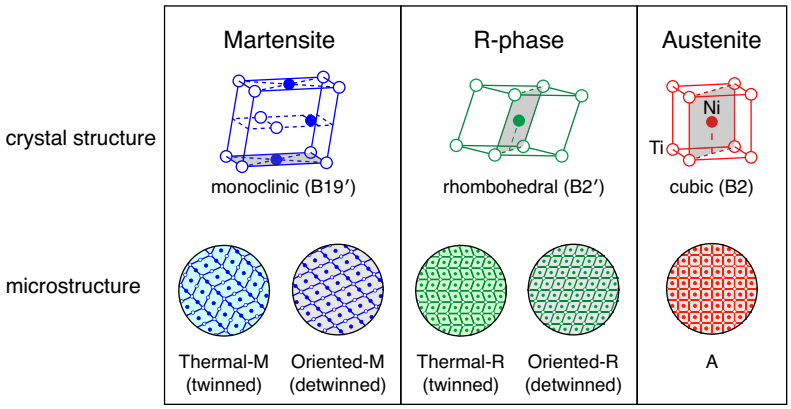

Figure 1.2: Crystal structures and microstructures of three solid phases of NiTi. [83]

feature morphing geometry [47], non-destructive release mechanisms and a heat engine [54], and more recently, advanced aerospace applications including variable geometry inlets and chevrons and torque tubes. [44]. Surprisingly, one of the major business sectors utilizing shape memory alloys is the medical sector. Here, the good biocompatibility and the increased resilience of NiTi structures in the superelastic mode (relative to stainless steel, for example) are used advantageously. The main applications in the medical sector include cardiovascular stent-grafts, dental wires and drills, and catheter guide wires to name a few [34, 11]. There has also been growing interest in the civil engineering field to utilize shape memory alloys for applications such as pre- or post-tensioning concrete structures to improve damage resilience [4] or damping of seismic vibrations [52]. Steel structural elements such as cables are typically kept in the elastic range when used in civil structures, but a superelastic NiTi cable could offer increased resilience, load limiting, and increased damping of seismic vibrations [72].

Both the shape memory effect and superelasticity are predicated on a solid to solid phase transformation, that is characterized by a shift in the crystal lattice structure. NiTi has two primary solid phases, shown in Figure 1.2, and a third intermediate phase. The high temperature phase is called *austenite* and has a highly ordered and symmetric B2 cubic crystal lattice. This phase is most suitable to use as the reference state of the material, because it has a well defined configuration and known microstructure. The low temperature phase, called *martensite*, is a monoclinic B19' crystal structure, which displays a loss of symmetry when transformed through shearing and elongation of the cubic crystal structure of austenite. To accommodate for the loss of symmetry when transforming from austenite to martensite, the material creates a highly twinned and self-accommodated microstructure called *thermal-martensite*. There are 12 symmetry-related lattice correspondent variants (LCVs) of martensite, or to put it more simply, 12 different ways in which one can deform an austenite lattice into a martensite one. These are found by applying the deformation

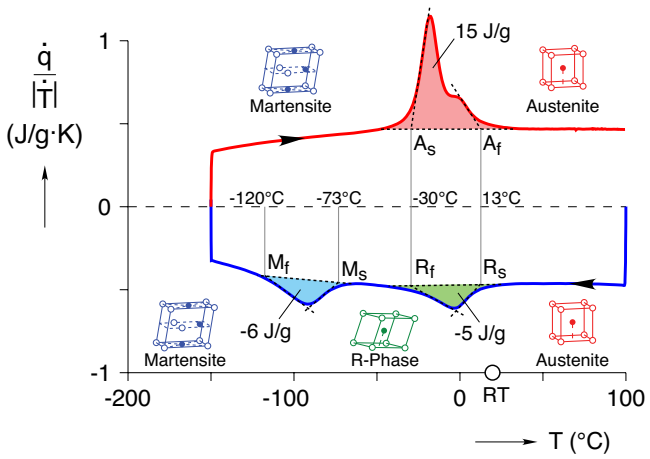

Figure 1.3: Differential scanning calorimetry of typical NiTi wire. [83]

(shear and elongation) along the various symmetric directions in the cubic structure, while also considering several possible rotations. When the material transforms from austenite to martensite, it must form a compatible interface (or *habit plane*), but therein lies a problem. No single variant of martensite is perfectly compatible with austenite. However, groups of variants of martensite can in fact be compatible on average. There are 192 groups of LCVs of martensite that satisfy this condition (most involving some form of a twinned structure), and are called *habit plane variants* [10]. The third and final phase is called *R-phase*, which has a rhombohedral B2' crystal structure. This is an intermediate phase that appears in most NiTi alloys, and, while often overlooked, it has a noticeable impact even on the macroscopic stress-strain behavior.

To characterize the transformation temperatures and latent heat properties, differential scanning calorimetry (DSC) is most commonly used. A typical DSC curve is shown in Figure 1.3. A DSC machine works by heating two sample pans, one with a specimen and one empty, and compares the energy required to change the temperature in small increments to calculate the heat flow into the specimen. The normalized heat flow can then be plotted to highlight phase transformations and their respective latent heat released or absorbed and to pick off transformation temperatures. The transformation temperatures are denoted by what phase the material is transforming into (R,M,A) and whether the temperature is picked off at the start or finish of the transformation (ex: A_s, A_f). There is typically a large temperature hysteresis between austenite and martensite, while austenite and R-phase tend to have a much smaller hysteresis. The DSC curve shown in Figure 1.3 is typical of a superelastic specimen, because the material is in the austenite phase at room temperature and within 20–40°C of A_f. Typical shape memory specimens are instead in the martensite phase at room

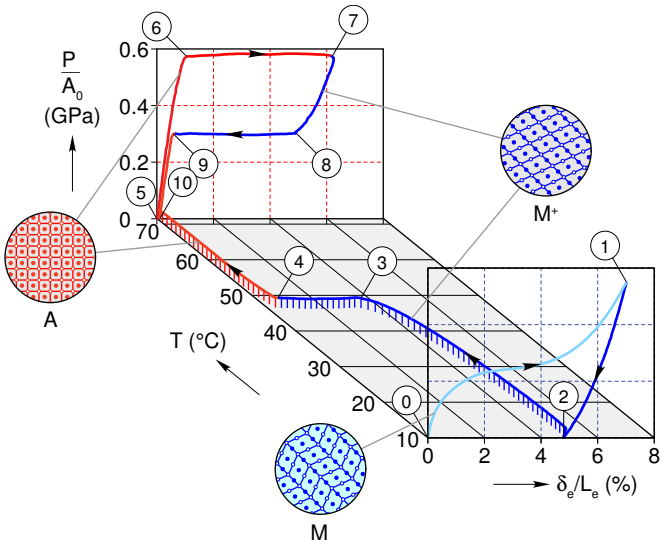

Figure 1.4: Experimental data showcasing the shape memory effect (⓪–⑤) and superelasticity (⑤–⑩) of a NiTi wire. [83]

temperature, because it is much easier to heat up a specimen (such as by joule heating) than to cool it to sub-ambient temperatures. It is reasonably easy to change the transformation temperatures by shifting the alloy composition by either adding more nickel or titanium, on the order of fractions of a percent, or by using different heat treatments. While it is easy to shift the transformation temperatures, controlling the exact transformation temperature of a finished SMA material remains a challenge and lot-to-lot variability is non-trivial (see [66] for a review of NiTi metallurgy). Furthermore, transformation temperatures will often shift with thermo-mechanical cycling of the material, but will often reach a steady state level.

Thermo-mechanical response data capturing the shape memory effect and superelasticity is shown in Figure 1.4. Here, a single wire specimen is subjected to a specified load and temperature history such that both the shape memory effect (steps ⓪–⑤) and superelasticity (steps ⑤–⑩) can be showcased. The sequence of events is as follows:

⓪–① Detwinning thermal martensite into oriented martensite, with a softening of the tangent modulus where the majority of the detwinning is occurring.

①–② Elastic unloading with slight re-twinning, indicated by additional recovery beyond what would be purely elastic.

②–⑤ Heating stress free to above the austenite finish temperature, with transformation to austenite occuring from ③–④, which recovers the deformation associated with the earlier detwinning process.

⑤–⑥ Elastic loading in austenite.

⑥–⑦ Nucleation of stress-induced martensite at ⑥, and propagation of the localized transformation front under constant stress to ⑦.

⑦–⑧ Elastic unloading, with slight curvature indicating some early transformation.

⑧–⑨ Nucleation of reverse transformation to austenite at ⑧, and reverse propagation of a localized transformation front, again under constant stress, to ⑨.

⑨–⑩ Elastic unloading, returning to the reference state of undeformed austenite.

For further review of shape memory alloy properties (e.g. rate sensitivity and localization phenomena) and useful experimental techniques (e.g. infrared thermography and digital image correlation), see the helpful series of papers titled, *Tips and tricks for characterizing shape memory alloy wire* [83, 20, 21, 22, 74].

It should be apparent now that, to fully understand the behavior of shape memory alloys in general and NiTi in particular, a single stress-strain curve at room temperature, which might suffice for many conventional materials, is inadequate. There is a rich third dimension of temperature that NiTi is highly sensitive to and a nuanced microstructure that has macroscopically noticeable impacts – both of which cannot be neglected. At this point, even though there are a plethora of uniaxial data on NiTi, examining properties under different modes of loading or with complex structures, such as cables, remain an active area of research.

1.2 Motivation

Shape memory alloys have been extensively researched for over 30 years, however due to the complexity of the material, the processing and fabrication of fine monofilament wires has only recently been well understood. Most applications to date make use of the optimized adaptive properties (the shape memory effect and superelasticity) in wires or similarly thin structures. The medical sector, for instance where smaller structures are more ideal, has made great use of NiTi stents and guide wires [34]. However, there is significant untapped potential for this material for use in large scale structures such as those found in the aerospace or civil engineering practices. A few examples include morphing wings that fully adapt to a variety of aeroelastic loading and control conditions, pushing the fuel economy of commercial airliners beyond their current plateau, or, perhaps buildings with fail-safe devices that withstand

seismic activity such as earthquakes and remain structurally sound while repairs can be administered. This has the immediate benefit of saving lives, but would also help preserve many historic and culturally significant buildings globally that are currently at risk. These applications require SMA forms that can withstand loads on the order of 10 to 100 kN or more, which would quite clearly require a scaled up version of the fine wires that are currently commercially available.

In fact, there has already been growing interest in the research community to develop advanced SMA structures for use in both the aerospace and civil engineering fields. In aerospace engineering, there have been several demonstrated devices, including SMA-controlled morphing airfoils, adaptive control surfaces of a wing using hingeless ailerons and torque tubes, bundles of SMA wires used to thermally actuate an F-15 jet's inlet cowl geometry, and SMA beams used to create variable geometry jet engine exhaust chevrons to promote noise reduction [47, 44]. On the civil engineering side, there is already a vast amount of literature proposing applications such as the damping of stayed cables in bridges [91], SMA isolation and pier re-centering devices [86], SMA restrainers for simply supported bridges [28], and the bending of NiTi bars as an alternative method of seismic restraining [15]. Other examples include SMA bolted joints, bracings and restrainers to prevent earthquake damage, and prestressing concrete with SMA cables as an alternative to rebar, to name a few. Recent reviews of civil engineering applications by Janke et al. [52] and Alam et al. [4] provide a good overview from a civil engineering standpoint.

Manufacturing large diameter SMA elements such as monolithic bars remains a challenge. Large diameter bars under cyclic loading were investigated by DesRoches et al. [29], showing reasonable properties although the largest diameter bar had increased residual strain. Ortega et al. [65] investigated casting NiTi bars to reduce cost, but showed slightly inferior properties. McCormick et al. [63] also showed the potential of hot rolled large diameter NiTi bars, offering cost savings relative to cold drawing. Further processing advances such as tailored heat treatments were recommended by Frick et al. [40] to improve adaptive properties. In spite of these recent advances, however, fine NiTi wires remain significantly cheaper to produce, and, more often than not, also have superior properties. One solution gaining popularity is to strand NiTi wires into a cable (or wire rope) to create a larger adaptive structure, which provides a cost effective solution that nicely circumvents the difficulties of manufacturing larger SMA bars (such as even quenching and cold working). Reedlunn et al. [75, 76], showcased the large potential for superelastic SMA cables and quoted a price that showed a cable stranded with small wires, to make up roughly the same outer diameter as a large bar, was 85% cheaper than the price of the large monolithic bar.

The purpose of this dissertation is to carry forward research on shape memory alloy cables by: (1) characterizing larger than previously tested superelastic cables to provide insight into their scalability, (2) exploring the previously uncharacterized shape memory effect through thermal actuation of shape memory cables, and (3) examining the local mechanics of the phase transformation in NiTi cables, as both increased bending and twisting and contact mechanics have been shown to cause complex transformation behavior. Studying these topics, the importance of degradation and path dependence of the shape memory effect in straight wires was observed and characterized and is presented as a complement to the topic of thermal actuation of NiTi cables. Finally, as a special consideration of helical SMA structures that are electrically heated and cooled through convective flows, the topic of convective heat transfer of SMA springs was also studied.

1.3 Organization

This dissertation, which covers the topics of large superelastic cables, thermal actuation of shape memory cables, path dependence and shakedown of shape memory wire, local transformation behavior in superelastic twists, and the convective heat transfer of helical springs, is organized as follows.

Chapter 2 presents an experimental campaign to characterize superelastic 7×7 cables much larger than those which were previously tested. The rate sensitivity and ambient temperature dependence are presented, along with cyclic behavior and ultimate failure. This work was part of a larger collaboration to test the feasibility of using large superelastic shape memory alloy cables for pre-stressing concrete beams in civil engineering applications.

Chapter 3 explores the thermal actuation behavior of shape memory alloy cables. An experimental setup developed for this study to precisely and rapidly control the temperature field is utilized to characterize 7×7 and 1×27 cables, as well as straight wire. The three specimens are then compared using specific metrics which provide a basis for evaluating their performance.

Chapter 4 presents a series of experiments and discussion that delve into the nuanced path dependent shakedown of straight NiTi wire. The generation of transformation-induced plasticity is decoupled between cooling and heating portions of the shape memory actuation cycle, and the role of cooling stress in altering the transformation behavior is examined. These results provide evidence for an explanation describing new dependencies of the microstructure of martensite on the applied load.

Chapter 5 examines the local stress-induced transformation phenomena of superelastic 1×3 twists. In the first half of this chapter, the twists' thermo-mechanical behavior is experimentally characterized through isothermal and fast-rate cycling experiments. The localization events captured using digital image correlation and thermography are also presented. In the second half, the twists' behavior are modeled using finite element analysis and compared with the experimentation. The role of contact mechanics in influencing the localization phenomena is also examined.

Chapter 6 explores the convective heat transfer of springs in a crossflow in three parts: (1) an experimental campaign to measure the convective heat transfer coefficient in a wind tunnel under a wide array of flow and stretch conditions, (2) simulations to validate the experimental data and provide additional insight into the local surface heat transfer effects, and (3) an empirical correlation that can be readily implemented into component models, such as for a SMA heat engine.

Chapter 7 reviews the conclusions found through this research endeavor, summarizes the impact of the work, and offers recommendations for future work.

CHAPTER 2

Characterization of Large Superelastic Cables

The purpose of this chapter is to present an experimental study that characterizes the thermo-mechanical behavior of large superelastic cables intended for reinforcing concrete beams. Through characterizing the material properties of a NiTi cable much larger than previously tested, the scalability of cable structures in general can be better understood. This work was part of a larger campaign that included bonding tests of NiTi cables in concrete and bending tests of NiTi cable reinforced concrete beams. As part of the thermo-mechanical testing completed here, the rate sensitivity, ambient temperature dependence (and Clausius-Clapeyron slope), core wire response, cyclic behavior, and ultimate failure were all quantified.

As mentioned, this study was part of a collaborative effort to better our understanding of NiTi reinforced concrete beams. Recently, there has been significant interest in the use of SMAs to solve long-standing problems in the civil engineering field. With regards to mitigating earthquake related damage, demonstrated ideas include SMA bolted joints, bracings and restrainers to retrofit deficient structures, SMA cables to prestress concrete as an alternative to steel rebar, and dampers and isolators [4, 15, 91, 86]. In particular, DesRoches et al. [28] found SMA restrainers for simply supported bridges to be very effective at reducing hinge displacements (relative to steel restrainers) due to improved elastic strain range and damping properties. Furthermore, the rehabilitation of concrete beams through post-tensioning of SMA cables with joule heating was investigated by Song et al. [87].

The improved damping characteristics of NiTi (over conventional steels) have generated a large amount of interest for seismic isolation applications [80]. For instance, the use of SMA damping for cable stayed bridges was recently investigated by Torra et al [91] showing useful damping characteristics. A review by Janke et al. [52] highlighted several civil engineering applications including an active SMA spring damper design, SMA devices to retrofit historic

buildings for earthquake damage mitigation, and iron based SMA fasteners which could repair cracked concrete beams by putting the cracked region in post-tension.

These seismic damping applications make use of the highly hysteretic behavior of superelastic NiTi, through which a large amount of energy is dissipated. The damping characteristics for superelastic wires have been shown to be well suited for practical applications such as bridge systems [32, 3]. Surprisingly, the NiTi material in the martensite phase also shows favorable damping characteristics [31, 92]. Work has also been done by Heller et al. [46] on how to address the strong thermo-mechanical coupling while retaining useful damping characteristics in civil applications.

For these civil applications involving quite large SMA members, a cabled structure stands out as a particularly useful form. Wire rope in general has ubiquitous use in many engineering fields, with many advantages over monolithic bars, including, large stiffness in tension while having good flexibility in bending and torsion and load carrying redundancy which provides a form of damage tolerance. For background and overview information to wire rope technology and engineering, the reader is directed to two particularly useful resources, one by Costello [27] and another by McKenna et al. [64]. Reedlunn et al. [75, 76, 72] provided the first and a quite thorough investigation into the thermo-mechanical behavior of two superelastic NiTi cables, of 7×7 and 1×27 constructions. These cables combine the adaptive properties of SMAs (shape memory effect and superelasticity) with the aforementioned useful properties of wire rope to great effect.

For civil applications, the 7×7 cable characterized by Reedlunn would be considered small, with an outer diameter of 2.48 mm. A larger superelastic 7×7 cable with an outer diameter 7.96 mm was characterized here in order to, (1) investigate if the good superelastic properties shown by Reedlunn are indeed scalable to a larger diameter cable, and (2) provide a thorough characterization of the thermo-mechanical properties of this cable as part of a larger experimental study of concrete beams reinforced with superelastic NiTi cables. The experimental study of these reinforced concrete beams included bonding tests completed by I. Vieito and F. Martínez-Abella at the University of A Coruña in Spain, and bending tests were conducted by B. Mas and A. Cladera at the University of Balearic Islands in Spain.

2.1 Thermo-Mechanical Experiments

The experiments performed for the thermo-mechanical characterization of the SMA cables explored various aspects of their mechanical behavior, including their strain rate sensitiv-

Subset	Experiment ID	Strain Rate (s^{-1})	Free Length L (mm)	Gage Length L_e (mm)	Ambient T_a (°C)
Rate Sensitivity					
	A1	2×10^{-5}	247.2	99.681	21.7
	A2	1×10^{-4}	244.5	99.741	21.8
	A3	1×10^{-3}	243.0	95.830	21.4
	A4	1×10^{-2}	244.0	96.005	21.6
Elevated Temperature					
	A1	2×10^{-5}	247.2	99.681	21.7
	B2	2×10^{-5}	89.5	49.380	30.4
	B3	2×10^{-5}	93.0	49.935	41.0
Core Wire					
	C1	2×10^{-5}	98.8	56.265	21.6
50 Cycle Fatigue					
	D1	1×10^{-3}	246.0	99.749	21.7
Failure					
	E1	1×10^{-3}	247.2	99.540	21.7

Table 2.1: Summary of uniaxial experiments for thermo-mechanical characterization.

ity, temperature dependence, core wire behavior, cyclic shakedown, and ultimate failure strength. A summary of the experimental parameters is provided in Table 2.1. The first group comprises four experiments (A1, A2, A3, A4), whose purpose was to quantify the sensitivity of SMA cables to loading rate. The second group includes three experiments at different ambient temperatures at or above room temperature (A1, B2, B3), which was used primarily to measure the thermo-mechanical coupling (Clausius-Clapeyron slope), but also helps one appreciate the three-dimensional temperature-stress-strain space that SMA cables occupy. The core wire experiment (C1) provides the underlying uniaxial tension behavior of monofilament wire (0.885 mm diameter) used in the 7×7 cable. The shakedown experiment (D1) shows the cyclic strain ratcheting behavior of the cable. Finally, the failure experiment (E1) quantifies the approximate load the cables can withstand before breakage.

2.1.1 Experimental Set-up for Uniaxial Mechanical Tests

The primary experimental setup used to characterize the cables is shown in Figure 2.1a. The experiments were performed in an Instron load frame, model 5585, with a 200kN capacity. Attached to the load frame were a 200kN Instron load cell and wedge grips. A laser extensometer (EIR, model LE-05) was used to measure the relative displacement of two laser tags attached by a flexible epoxy to the middle portion of the specimen. This

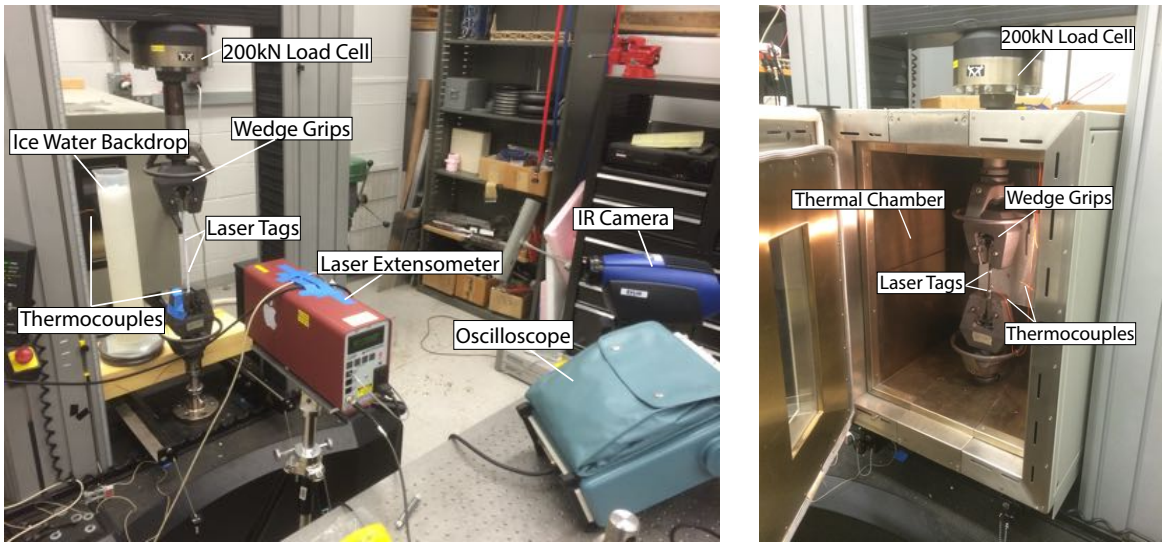

(a) (b)

Figure 2.1: Experimental setup. (a) Rate sensitivity setup. (b) Elevated temperature setup.

was used to measure the average strain in a gage section away from stress concentrations at the grips and to avoid measurement artifacts from a small, but noticeable, amount of grip slippage. An oscilloscope verified the laser extensometer's output to check for possible glare or alignment issues. Two thermocouples were used to record the ambient and specimen temperatures. The thermocouples were attached to Fluke thermocouple amplifiers that provided a 1 mV/°C output.

Certain modifications to the setup were necessary for parts of the thermo-mechanical characterization. For the elevated strain rate sensitivity experiments (faster than the near isothermal rate of 2×10^{-5} s^{-1}), a FLIR IR camera recorded the specimen's full-field temperature history. To improve the accuracy of the IR measurements, specimens were first airbrush painted with a thin coating of matt white to raise the emissivity to about 0.94. The elevated temperature experiments were performed in an Instron thermal chamber as seen in Figure 2.1b, without any IR measurement, relying solely on the thermocouple measurements.

Gripping the specimens was a challenge. In our initial attempts, the outer fibers of the cable specimen would break during loading, typically at the onset of phase transformation and again at saturation when local stress concentrations were the largest. The issue was identified to be caused by the sharp teeth in the v-groove of the grip platens. The solution was an extensive specimen preparation procedure that involved epoxying on tin-plated copper ferrules. To prepare a specimen, about 37 mm of the end of the cable's outer strands were

(a) (b)

Figure 2.2: Photographs of a 7×7 cable specimen end with epoxied tin-plated copper ferrules. (a) Before experiment. (b) After experiment.

first unwound from around the core strand, and the core strand was coated in epoxy. The outer strands were then rewound around the core strand, and more epoxy was spread over the outside of the cable. A ferrule (32 mm length, 8.3 mm inner diameter, 0.2 mm thick) was then slid over the cable and epoxy, while ensuring enough epoxy filled the gaps between the ferrule and cable. The specimen with epoxied ends was then cured in an oven at 100°C for 45 minutes. One end of a cable specimen with the epoxied ferrule is shown in Figure 2.2a before an experiment, and the same end is shown in Figure 2.2b after the experiment. One can see that during the experiment the grip plastically deformed the ferrule and left teeth marks, but this extra layer effectively distributed the wedge grip's stress concentrations on the cable wires while maintaining a strong hold on the specimen. With this arrangement, specimens could be taken well beyond the loads needed for stress-induced transformations, and the ultimate breaking strength of the cable could be estimated.

2.1.2 Strain Rate Sensitivity

The mechanical responses of superelastic SMAs are well known to exhibit a strong dependence on the loading rate, even at low strain rates that would normally be considered quasi-static for conventional materials. The cause of the SMA's sensitivity is not due to inertia effects or viscoelasticity, but is due to temperature excursions caused by latent heat of transformation released or absorbed during stress-induced forward and reverse transformations, respectively. If the ambient medium is unable to extract or supply heat to the specimen fast enough, the temperature of the specimen must change. Since the transformation stresses in SMAs are strongly dependent on temperature (as shown in the next section), even a small temperature change causes a significant change in stress within the specimen

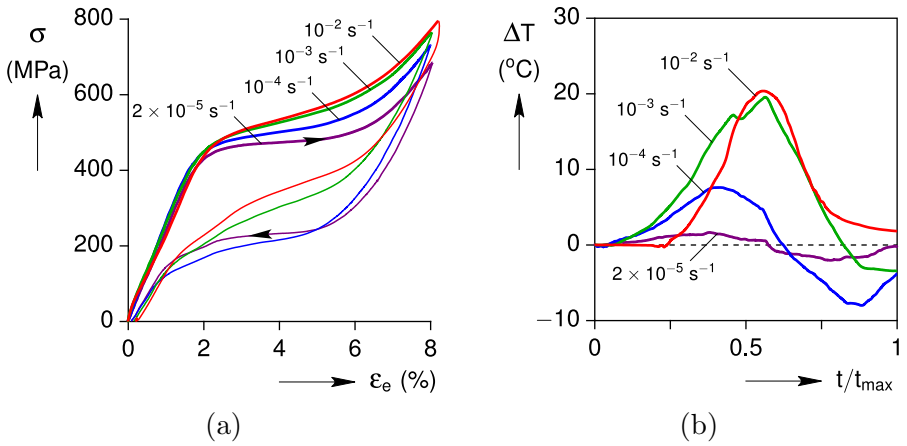

Figure 2.3: Rate sensitivity data. (a) Normalized force-displacement graph. (b) Temperature change.

during a constant displacement-rate superelastic test. During the forward transformation (A→M) while loading, latent heat is released, the specimen temperature rises above ambient temperature, thereby causing the stress to evolve upward. During the reverse transformation (M→A) while unloading, latent heat is absorbed, the specimen temperature drops, and the stress evolves downward. More details can be found in Shaw and Kyriakides [84]. While the strain rate sensitivity of NiTi wire and strips has been well studied (see [49, 14, 97]), the SMA cables here are significantly more massive and their sensitivity to strain rate was as yet unquantified.

All experiments shown below were performed on a new cable specimen to avoid any accumulated damage that otherwise might have occurred. One end of the specimen was held fixed, while the other end of the specimen (vertically oriented) was displaced (δ) upward by the testing machine's crosshead. All experiments were performed in displacement control at constant rate during loading and unloading, during which the axial load P (by the load cell) and gage strain ε_e (by the laser extensometer) were recorded. The results are reported below in terms of the stress measure $\sigma = P/A_0$, where A_0 is the cross-sectional area of 49 parallel wires (as defined in Reedlunn, et. al. [75]). It should be noted that due to the hierarchical and helical construction of the cable, the local stress within a wire involves combined extension-bending-twisting and varies with its location within the cable, so σ should be just considered the normalized axial load.

Figure 2.3 shows the responses of our SMA cables at four strain rates from 2×10^{-5} s^{-1} to 10^{-2} s^{-1} (based on the normalized grip displacement δ/L) in room temperature, stagnant air. Figure 2.3a provides the mechanical "stress-strain" responses, according to our stress measure σ and laser extensometer strain ε_e, showing higher stresses during loading at progressively

higher strain rates. The cause of the strain rate sensitivity is shown in Figure 2.3b which plots the temperature changes in the specimen as measured by the specimen thermocouple. At the slowest rate the temperature change in the specimen is small, with a slight increase during loading (between t/t_{max}=0 to 0.5) and a slight decrease during unloading (between t/t_{max}=0.5 to 1). Nevertheless, this experimental response can be considered to be the nearly isothermal, quasi-static response.

By contrast, the response at 10^{-4} s^{-1} shows an elevated stress during loading and a reduced stress during unloading (Figure 2.3a), and the specimen temperature changes are larger (about +/- 8°C relative to room temperature in Figure 2.3b). At 10^{-3} s^{-1}, the effect is larger yet, and the specimen temperature rises by about 20°C during loading. Since there was no pause between loading and unloading, the temperature of the specimen remained above room temperature for much of the unloading segment, resulting in an elevated stress even during reverse transformation (although latent cooling contributed to drive the temperature downward). The response at the fastest rate 10^{-2} $s^{-}1$ was similar to that at 10^{-3} s^{-1}, and the thermocouple recorded a similar rise in temperature by about 20°C during loading. The specimen temperature again remained above ambient during unloading and never reached it before the load reached zero. Full-field IR measurements were recorded (for all but the slowest experiment), and unlike typical single wire experiments, the temperature field showed no evidence of localized transformation but rather a uniform heating or cooling along the length of the cable. Since the thermocouple data adequately summarizes the temperature effects, the IR data are not shown. Overall, we conclude that the 10^{-3} s^{-1} response is close to the adiabatic response of the cable, and note that this is a slower strain rate than is necessary to reach the adiabatic limit of single SMA wire (typically near 10^{-2} s^{-1}). Thus, the rate sensitivity is dependent on the size of the specimen, in accordance with heat transfer scaling.

The progression of energy dissipated during a superelastic cycle (area within the stress-strain loop) is interestingly non-monotonic with increasing strain rate, starting at a nominal value in the lowest rate (isothermal) case, becoming larger at intermediate rates, but then decreasing to below the starting value as the rate increases further and approaches the adiabatic response. However, one should not conclude this is always the case, since it depends on how the experiment is run. If the experiment had been paused between loading and unloading to allow the specimen to reach ambient temperature, the area within the energy dissipated would have increased monotonically with strain rate (see, for example Chang, et. al. [14]). Thus, the rate dependence in SMAs is largely governed by transient heat transfer between the SMA and the ambient medium. It should also be emphasized that the

experiments shown here quantify the rate sensitivity in stagnant air, which is not a very conducive medium for heat transfer, relying largely on natural convection. The strain rate sensitivity within a solid body, like concrete, will probably not be as severe, since thermal conduction will likely improve heat transfer to/from the SMA cable.

2.1.3 Elevated Temperature

Experiments were performed at elevated temperatures to explore the temperature sensitivity of our SMA cable and to measure the thermo-mechanical coupling in terms of the Clausius-Clapeyron slope. These experiments were run at the slow (nearly isothermal) strain rate of 2×10^{-5} s^{-1} at ambient temperatures near 20°C, 30°C, and 40°C. The mechanical responses are shown in Figure 2.4a with the corresponding specimen and ambient temperature histories shown in Figure 2.4b. The initial linear elastic segments and A→M stress plateaus were fitted with tangent lines, and the intersection was selected as the onset stress. Using these onset stresses, the Clausius-Clapeyron slope for this cable was found to be 4.6 MPa/°C (see Figure 2.4c), which is lower than typical values for straight wire near 7 MPa/°C. Also, the effective elastic modulus for extension of the cable, based on the linear fit used above, was 23.9 GPa, 26.6 GPa, and 32.5 GPa for the respective 20°C, 30°C, and 40°C experiments, which is consistent with a progressively decreasing amount of initial R-phase.

2.1.4 Core Wire

The only straight wire within the 7×7 cable is the central wire in the core strand, which we term the core wire, and it is the only wire that experiences direct uniaxial tension when the cable is stretched. Although the other 48 wires in the cable are loaded in more complex deformation modes, the core wire's mechanical response provides a useful baseline for comparison to the full cable response. Figure 2.5a provides the uniaxial response of a core wire that had been excised from a 7×7 cable. The experiment was performed at room temperature and at a slow strain rate (2×10^{-5} s^{-1}), and Figure 2.5b confirmed that the specimen remained nearly isothermal (specimen changes within about +/- 0.4°C). Compared to the full cable, the core wire's response is stiffer, transformations occur at higher stress levels and transformation plateaus are more distinct and flat. The initial elastic modulus of the core wire was 33.6 GPa (compared to 23.9 GPa for the full cable), and the A→M plateau stress was 520 MPa (compared to 460 MPa for the full cable). While the modulus of the core wire was larger than the cable's effective modulus, it was unexpectedly lower than other superelastic

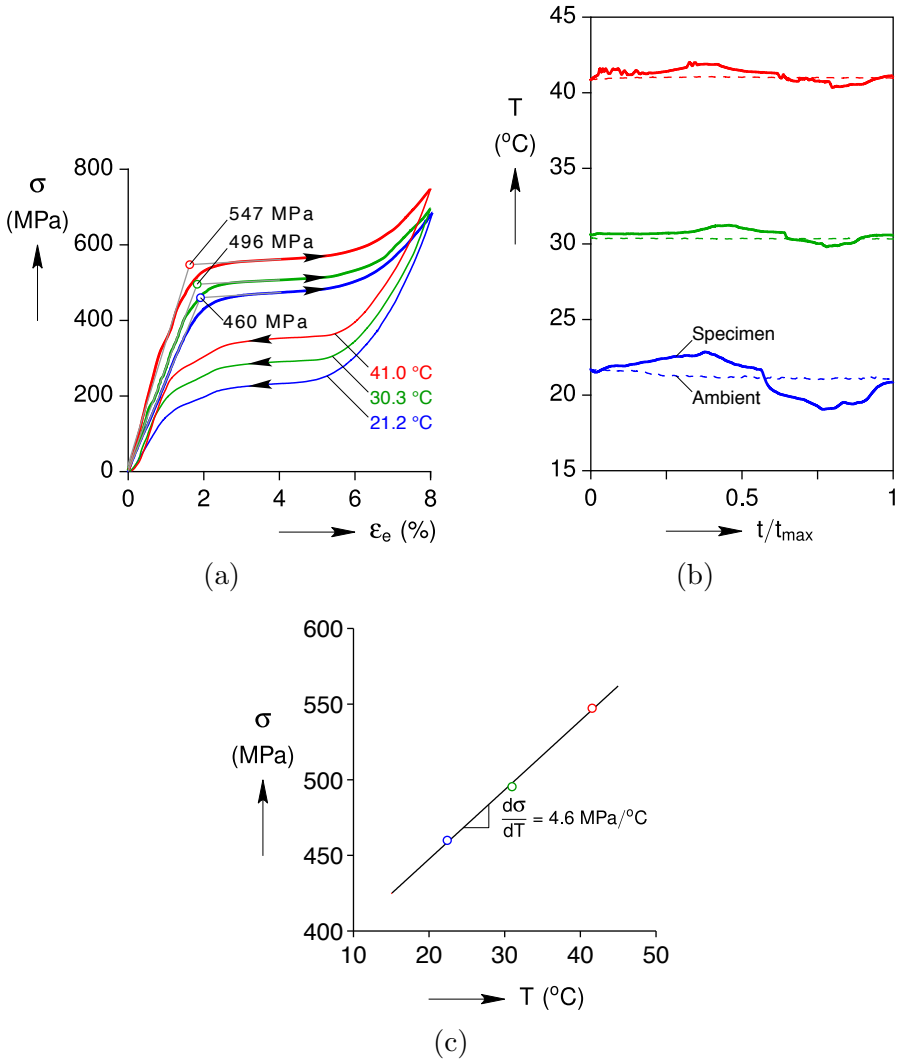

Figure 2.4: Elevated temperature data of 7x7 cable. (a) Mechanical responses and fits of A→M onset stresses. (b) Measured temperature histories. (c) Fitted Clausius-Clapeyron slope.

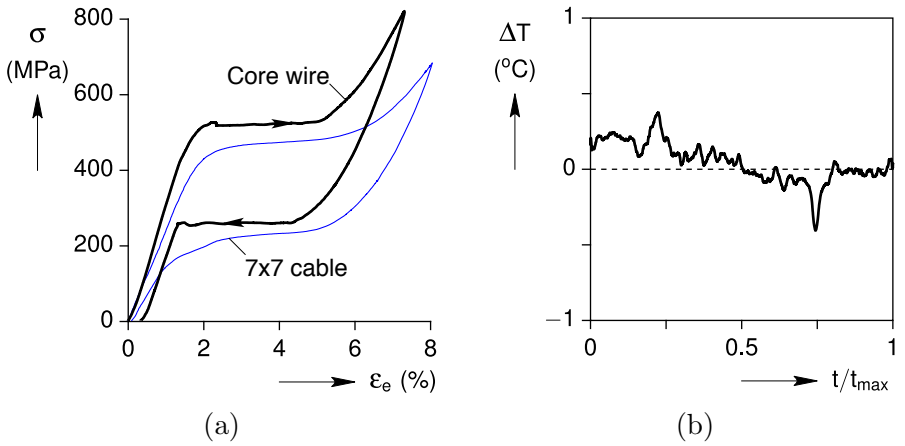

Figure 2.5: Core wire data at room temperature. (a) Mechanical response of core wire compared to the full cable. (b) History of measured temperature change in core wire.

NiTi wires we have tested elsewhere. To verify the low elastic modulus, a new core wire was tested at 60°C ambient temperature, and the elastic modulus was measured to be 66 GPa, which is indeed a typical value for NiTi austenite. This was further evidence that the material was not fully austenite (a mixture of R-phase and austenite) at room temperature, where R-phase detwinning contributed additional compliance in the wire's apparent elastic response. As discussed later, the low elastic modulus created difficulties for the use of SMA cable as reinforcement in concrete, but it should be possible to minimize the presence of the R-phase by optimizing the cable's heat treatment in the future.

The reason why the cable's response has more gradual and positive sloped plateaus is due to the heterogeneous stress distributions between and within individual wires in the cable. As previously mentioned, only the core wire experiences pure tension. The other 48 wires have helical configurations that create a combination of tension, torsion, and bending loading modes within a given wire. This leads to the following complications: (1) the relative amounts of tension-torsion-bending varies from wire to wire, depending on their helix angles and mean helix diameter; (2) twisting and bending creates strain gradients across a wire's cross-section; and (3) the local stress state within a wire's cross-section is multi-axial, since it involves both normal strains (extension and bending) and shear strains (twisting). Consequently, the load sharing is unequal between wires, and local transformation stresses are reached in different wires at different times during loading/unloading of the cable. Some wires transform early, while others transform late, resulting in a gradual evolution of the apparent tangent modulus in the macroscopic response of the cable. More details of the load sharing between cable subcomponents can be found in Reedlunn, et al. [76].

2.1.5 Cyclic Behavior and Failure

The cyclic behavior and ultimate failure strength of an SMA cable are important functional and durability considerations, so the final two experiments in this thermo-mechanical characterization address how the cable responds to repeated load-unload cycles and to extreme loading to its breaking strength. Figure 2.6a shows the mechanical response of a cable specimen subjected to 50 loading cycles to 8% maximum axial strain at a strain rate of 10^{-3} s^{-1} in room temperature air. This relatively fast strain rate was chosen in order to complete the experiment in a reasonable amount of time and to explore the cyclic behavior under severe conditions. We consider this experiment to be a rather brutal test, since the maximum axial stresses reached over 700 MPa at maximum strain. Nevertheless, the cable remained intact. Figure 2.6a does show, however, a dramatic evolution in the response to progressively lower transformation stresses during cycling, accompanied by a reduction in stress hysteresis and a small amount (less than 1%) residual strain ratcheting. The most severe changes occurred in the first few cycles, and each successively cycle exhibited a decreasing incremental change from its previous cycle, asymptotically approaching a limit cycle. This behavior is known as *shakedown* or *functional fatigue*, typically observed in superelastic wires when subjected to large cyclic stresses. Figure 2.6b plots the corresponding specimen temperature history, showing significant temperature excursions (as expected for this strain rate) that after an initial transient settled down to about (+13°C, -8.5°C) in late cycles. The evolutions of A→M (during loading) and M→A (during unloading) onset and saturation transformation stresses with cycling are plotted in Figure 2.6c, showing exponential-like decays in all cases approaching stable asymptotic values.

Lastly, a cable was loaded monotonically to failure at a strain rate of 10^{-3} s^{-1} as shown in Figure 2.7. The cable failed at a peak stress of 1150 MPa, which corresponds to an impressive 31.1 kN load. The gage strain at failure was about 20%, which demonstrated reasonably good ductility. Shown in Figure 2.8 are selected images of the cable breaking as captured by a high speed digital camera. The cable broke near the upper grip, indicating perhaps that we had not completely eliminated the stress concentration there. Thus, the measured failure stress should likely be considered a lower bound value. Nevertheless, it is concluded that the cable has a desirable ultimate load.

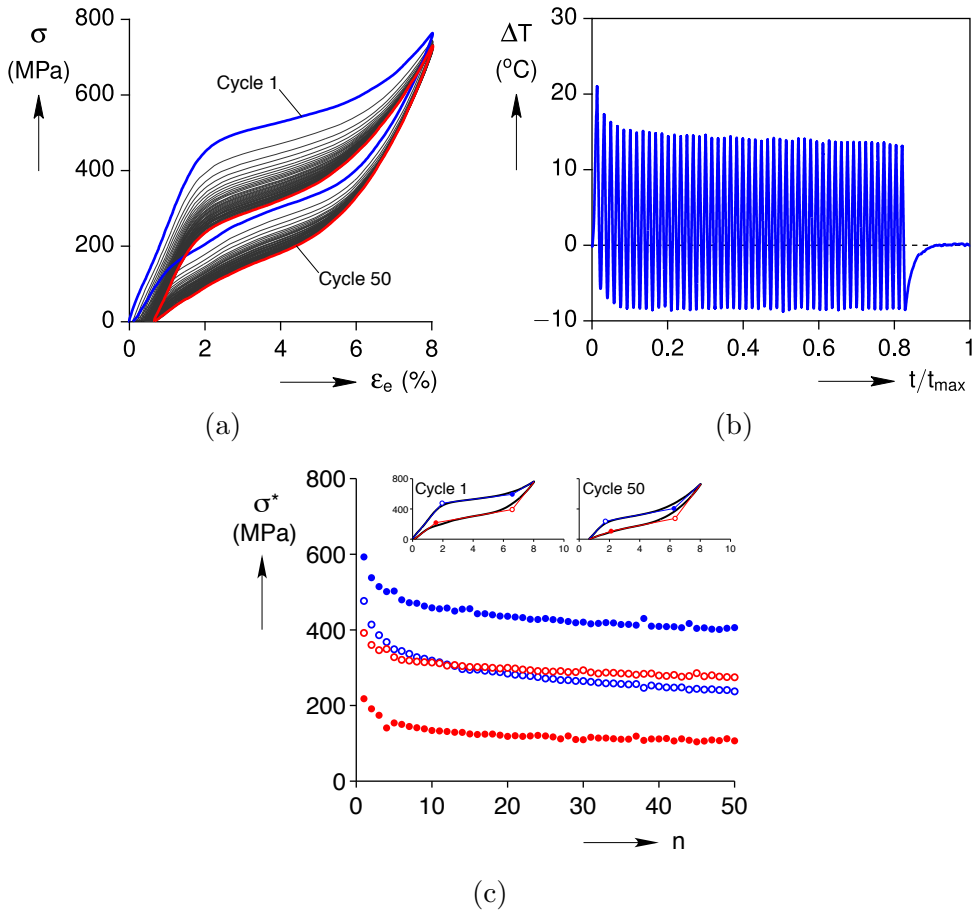

Figure 2.6: Cyclic test of 7x7 cable. (a) Mechanical response. (b) Specimen temperature change history. (c) Onset and saturation stresses, during loading and unloading, versus cycle number.

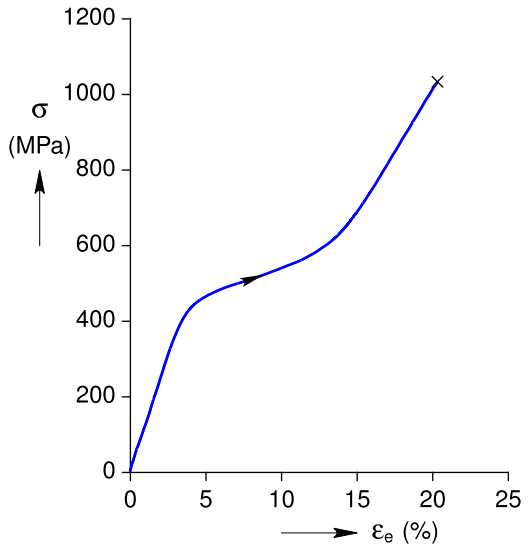

Figure 2.7: Normalized force-displacement graph for load to failure test.

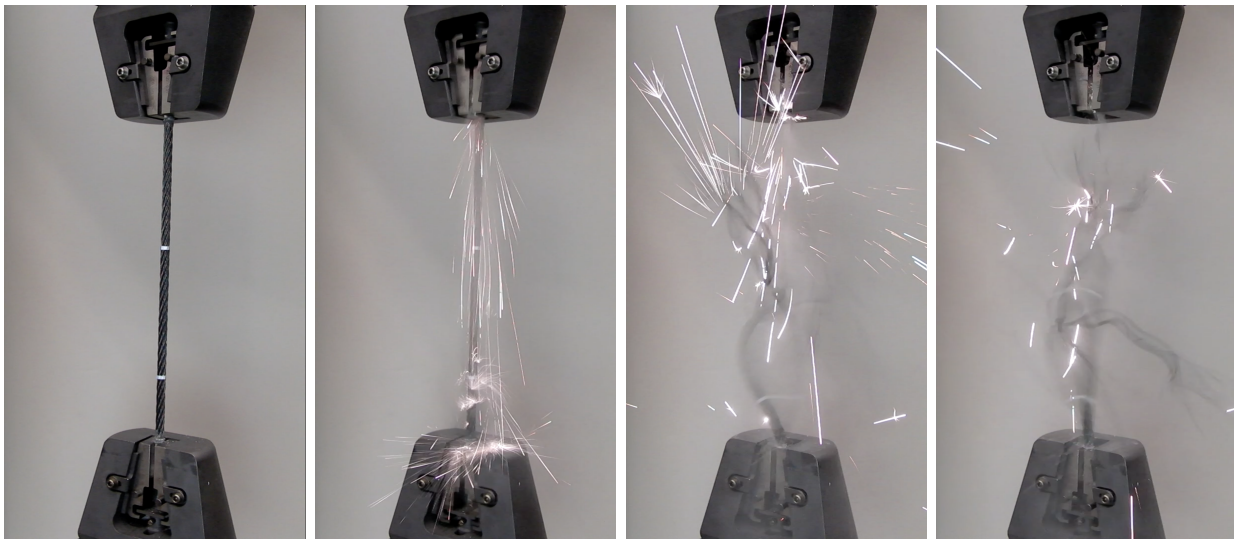

(a) t = 1/60 s (b) t = 2/60 s (c) t = 3/60 s (d) t = 4/60 s

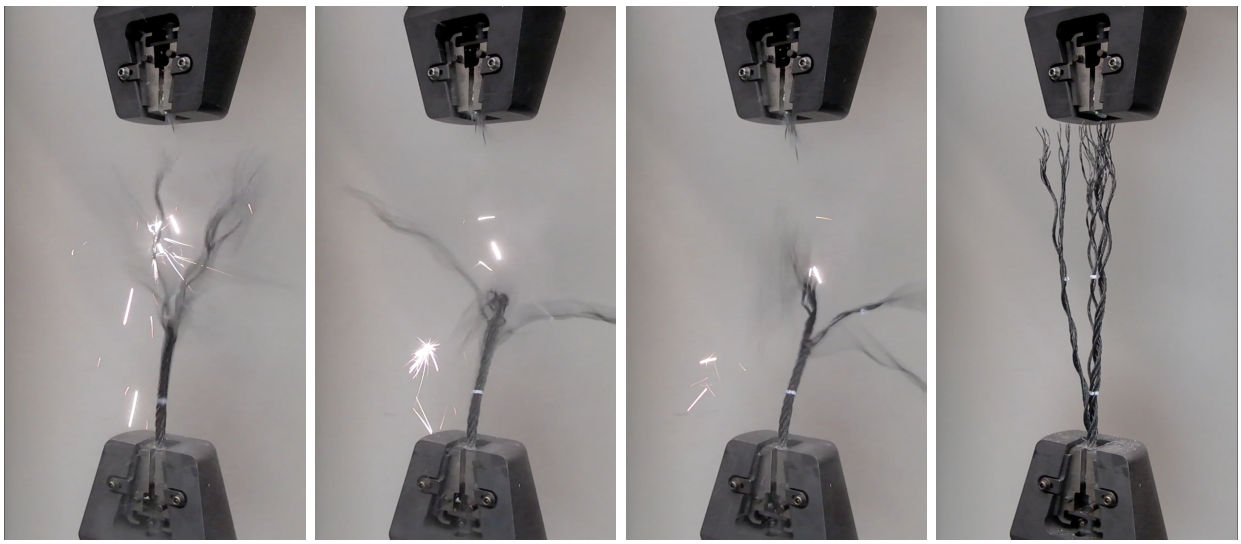

(e) t = 5/60 s (f) t = 6/60 s (g) t = 7/60 s (h) t = 1 s

Figure 2.8: Selected image sequence of a cable failure.

2.2 Conclusions

The thermo-mechanical properties of a 7×7 cable, much larger than previously tested (7.96 mm diameter), were characterized to reveal good superelastic properties. The isothermal mechanical response showed good superelasticity through a large transformation strain and relatively small plastic deformation after the first cycle. The rate sensitivity showed that the cable reached an adiabatic limit at a slower speed (1×10^{-3} s^{-1}) than typical of a single straight wire 1×10^{-2} s^{-1}, in accordance with the heat transfer scaling. The Clausius-Clapeyron slope was measured to be 4.6 MPa/°C, which is lower than typical of straight wire. A cyclic experiment highlighted the cable's resilience to repeated cycles (under a fairly tortuous loading scheme), and an ultimate failure was measured to be an impressive 31.1 kN (approx. 7000 lbs).

Initially, there was an issue with the initial elastic tangent modulus having a value lower than anticipated, which could prove detrimental for civil applications. However, through additional testing of the core wire at higher temperatures, the cause of the lower modulus of elasticity was found to be the presence of R-phase at room temperature. With a slightly modified heat treatment, this could be eliminated by shifting the R-phase to a lower sub-ambient temperature. The initial elastic tangent modulus would then have a larger value, closer to what was originally anticipated. This large 7×7 cable has thus been shown to have desirable properties, and with confidence is recommended for civil engineering applications.

CHAPTER 3

Characterization of Shape Memory Actuator Cables

This chapter expands the previous research scope of superelasticity in NiTi cables to now explore the shape memory effect. This is the first experimental study to characterize the thermal actuation response of shape memory alloy cables. Two NiTi cables (of 7×7 and 1×27 constructions) and straight wire were thermally cycled under varying dead loads to measure the strain response and reaction torque that accompany the phase transformation. The 7×7 cable was found to have a transformation response akin to that of the straight wire, with only marginal change in reaction torque with transformation. The 1×27 by contrast, was shown to have an increased transformation strain particularly at lower loads, and a large reaction torque during phase transformation. Overall, both cables were found to effectively scale up the thermal actuation behavior of straight wire, making them ideal for applications requiring large actuation forces. Furthermore, the ability to tailor the cable geometry to alter the transformation response without changing the underlying material composition or fabrication process offers a unique opportunity to further optimize a NiTi thermal actuator for any given application.

In the aerospace industry, there has been growing interest in advanced materials and actuators to push the flight envelope and boost fuel economy. This has a large impact not only on the end cost to passengers, but from an environmentally conscious standpoint, it can help reduce the total quantity of emissions. While current airfoils and control surfaces are fairly optimal under cruise conditions, during take-off and landing (or other less-than-ideal flight conditions) there are gains to be made in efficiency. A variable geometry airfoil, for instance, would allow the wing to be morphed into more ideal shapes to better fit any given flight condition. To date, there have been several demonstrated prototypes of SMA based morphing airfoils, or even variable geometry engine inlet and exhaust features to help improve fuel economy or reduce noise [47, 68, 44]. In one interesting application, a bundle of NiTi 1×19 strands were used as an actuator to create a variable area fan nozzle prototype,

providing an estimated 9% reduction in thrust specific fuel consumption [5, 79]. Even in the civil engineering field there have been some promising applications for NiTi cables used in thermal actuation. One group demonstrated the use of a SMA cable to post-tension a cracked concrete beam through joule heating, putting the beam into compression and effectively closing the crack [87].

These examples show that there is large potential for shape memory cables in aerospace and civil applications, particularly because the stranding of NiTi wires into cables allows the thermal actuator to be scaled up to produce much larger forces. These NiTi cables are very promising because they make use of the adaptive properties of NiTi tension elements in conjunction with the desirable properties of wire rope. However, to date there has been no thorough experimental characterization of such cables. This work aims to fill this gap in literature by providing thermal actuation data on NiTi cables of 7×7 and 1×27 constructions. Exploratory experiments were performed to study the actuation behavior of these cables and straight monofilament wire of the same material. The specimens were held under various dead loads ranging from 50 MPa to 400 MPa and thermally cycled 25 times from 140°C to 5°C at a rate of 12°C/min using a novel experimental setup that improved upon previous setups used in our research lab [48, 50, 18]. The thermo-mechanical actuation responses were characterized, and performance metrics of actuation stroke, residual strain, and work output were compared between specimens.

3.1 Specimens

This study was designed to build on previous work done on superelastic SMA cables by extending the focus on the shape memory effect and actuation. Two cable geometries, shown in Figure 3.1, and monofilament wire were ordered from Fort Wayne Metals using their NiTi #6 specification, with an active A_f of ≥ 50°C. To ensure similar material properties, the cables were initially made from a single material batch, and both cables and wire underwent identical drawing and heat treatment processes. The monofilament wire diameter was 0.508 mm and both cables were wound using this wire. However, due to the increased thermal mass of the cables, the heat treatment that worked for the monofilament wire was inadequate for the the cables. Comparable heat treatments were found for the cables by increasing the dwell time of the heat treatment to match the shape memory properties between the cables' core wires and the monofilament wire. After putting the cables through this additional heat treatment, the core wires' properties were nearly identical to the monofilament wire properties.

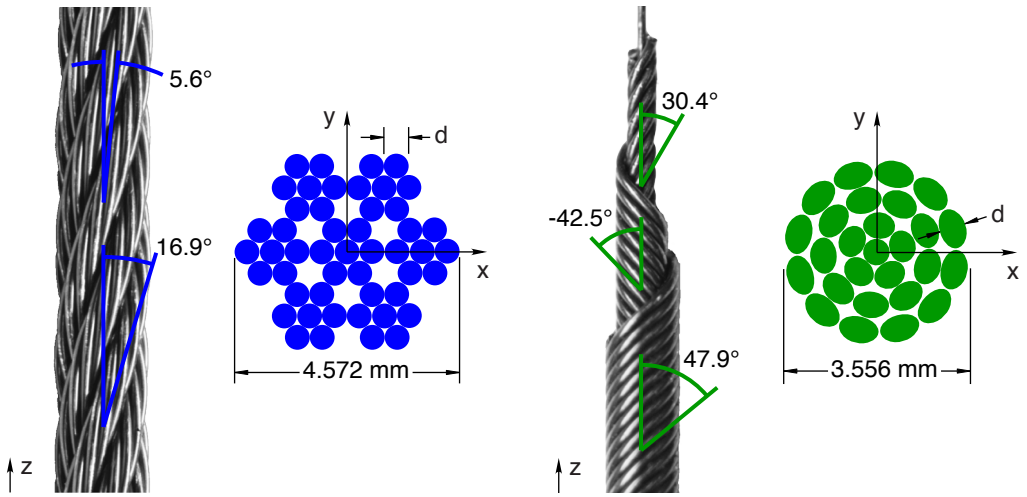

(a) (b)

Figure 3.1: Cable specimen geometries, (a) 7×7 cable, (b) 1×27 cable.

The first cable, in Figure 3.1a, is a conventional multi-stranded construction and labeled as the 7×7 cable. This cable is comprised of seven strands of seven wires each. The core strand has a central straight wire with six outer wires wrapped in a right handed layup. The outer six strands are similar to the central strand, but the wires are wrapped in a left handed layup around their central wire. The outer six strands are then wrapped in a right handed layup around the central strand to complete the cable. In each outer strand is composed of the outer wires wrapped at a helix angle of -11.3° about central wires, while the outer strands themselves are wrapped at a helix angle of 16.9°.

The second cable, in Figure 3.1b, is a less conventional construction and labeled as the 1×27 cable. This cable has multiple layers of wires wrapped around a central straight wire, with a first layer of five wires wound in a right handed layup. The second added layer has nine wires wrapped in a left handed layup, and the final layer has twelve wires wrapped in a right handed layup. This alternating layup construction is intended to reduce the reaction torque of the cable when in pulled tension. In this cable, the inner most layer has a helix angle of 30.4°C, the middle layer has a helix angle of -42.5°C, and the final outer layer has a helix angle of 47.9°C. Note, this is the opposite handedness of the 1x27 cable used in Reedlunn, et al. 2013.

3.2 Experimental Setup

The experimental setup designed to actively control the temperature and load on the cable and wire specimens is shown in Figure 3.2. The design objectives of the setup were: (1) ability to cool the specimen to sub-ambient temperatures, and (2) have an unobstructed view of the specimen to allow for later imaging the specimen for digital image correlation and IR thermography. The setup consisted of a MTS servohydraulic load frame, a 5kN MTS load cell and a 400 in-oz Futek torque cell, a MTS mechanical extensometer, thermocouples, and a temperature-controlled conductive aluminum block. The aluminum block was moved into contact with the cable specimen by a micrometer stage, and was designed to allow for controlled heating and cooling of the specimen (via embedded cartridge heaters and chilled oil piping) to accurately control the temperature of the specimen. Good thermal contact between the specimen and aluminum block was ensured by Omegatherm thermal paste, and the temperature was controlled by a proportional-integral-derivative (PID) algorithm run on an Arduino microcontroller with a thermocouple as the input source. The advantage of this setup is the ability to precisely specify a uniform temperature field at any instant in time, in contrast with joule heating which may cause a non-uniform temperature profile. The specimen was gripped in a clamped-clamped setup with ER collets, chosen for their radially symmetric clamping, which is preferable for cable specimens. For the straight wire specimen, the 5kN load cell was replaced with a 500N MTS load cell, and the mechanical extensometer was replaced by a laser extensometer to provide better load resolution and avoid bending the specimen, respectively.

The conductive aluminum block setup was designed and tested with infrared thermography to produce a uniform temperature field ($\leq \pm 1°C$) on the front surface of the specimen. The use of thermal paste, combined with gradual and controlled temperature changes, kept the gage section of the cable specimen within a reasonable temperature of the aluminum block ($\leq \pm 1°C$). The load measurement was accurate to less than 0.1% of the load cell's maximum (5kN for cables and 500N for monofilament wire), and similarly the mechanical extensometer (1.000in gage length) was accurate to 0.1% of its maximum elongation of 0.225in. The thermomechanical control and measurements were quite clean and allowed for fine features, such as R-phase transformation around 40°C, to be visible.

The data acquisition and control diagram is shown in Figure 3.3. The load cell, torque cell, and mechanical extensometer signals were read by the data acquisition (DAQ) hardware through an analog signal conditioning amplifier. The load cell signal was used to control the specimen in load control through the MTS computer software, with a constant load specified

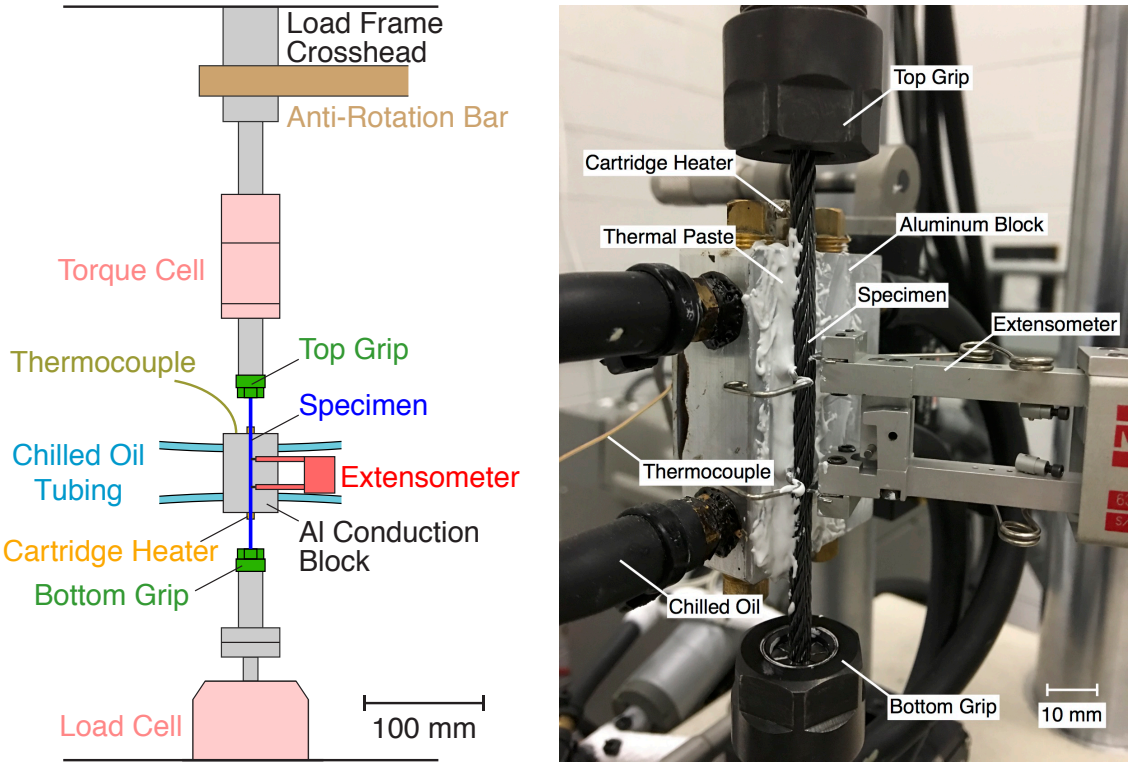

(a) (b)

Figure 3.2: Experimental setup. (a) Schematic, (b) Closeup photograph of specimen.

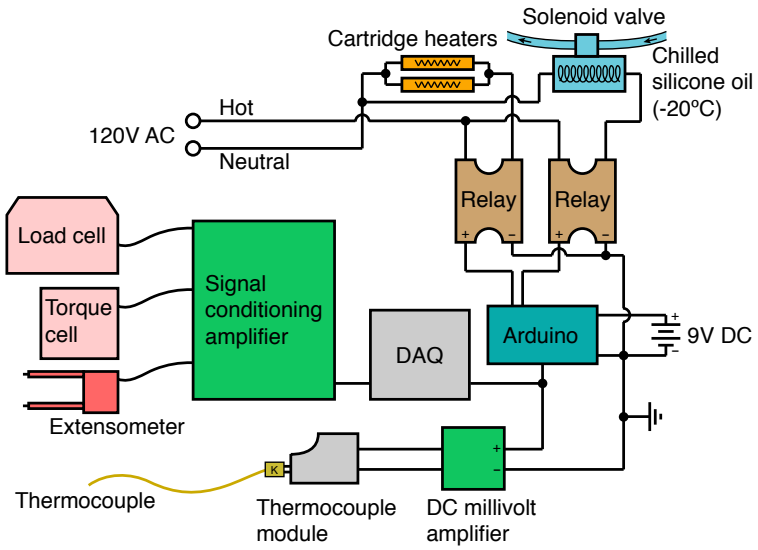

Figure 3.3: Data acquisition and control schematic.

for dead load experiments. The temperature of the aluminum block was measured with a K-type thermocouple. It was initially amplified to a 1mV/°C signal by a Fluke thermocouple module, then further amplified (25×) by a DC millivolt amplifier, which were both battery powered to minimize potential noise. The signal from the DC millivolt amplifier was sent to the DAQ for data logging and an Arduino controller for input into the temperature control algorithm. The Arduino controlled two solid state relays; one for heating the cartridge heaters embedded in the Al conduction block, and one for cooling by triggering a solenoid valve to start/stop the flow of chilled silicone oil. The heating was controlled by a PID controller, but the cooling was a hardcoded to a prescribed flow rate when cooling was desired. This control method effectively eliminated any PID instabilities from competing heating and cooling systems when attempting to reach a desired temperature. The DAQ recorded signal data at a frequency of 5 Hz, which equated to approximately 7500 data points per cycle.

The precision of the load and temperature control undergoing repetitive cycles are shown in Figure 3.4. The shakedown behavior and evolution of actuation response over 25 cycles can be seen in Figure 3.4a, and the time histories of average axial stress, axial strain, and temperature for the first cycle are shown in Figure 3.4b. Prior to the start of the experiment, the specimen was heated up stress free to 140°C (fully austenite), which was the reference configuration. The axial strain (δ_e/L_e), which was calculated by normalizing the extensometer displacement (δ_e) by the initial extensometer gage length (L_e), was zeroed at the reference temperature of 140°C at a very small load (just to keep the specimen taut).

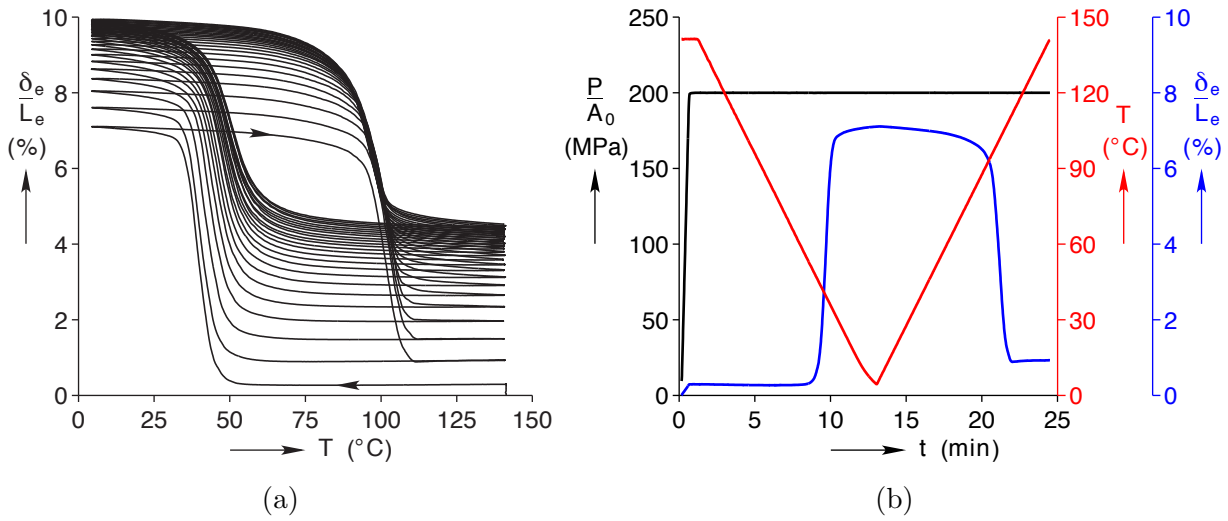

(a) (b)

Figure 3.4: Example cycling data for 7×7 cable under 200 MPa dead load, (a) Thermal actuation strain response over 25 cycles, (b) Cycle 1 time histories.

The experiment began with the initial loading of the specimen to a prescribed dead load, which was held under load control for the remainder of the experiment. The dead load value is reported as an average axial stress (P/A_0), which was calculated by normalizing the recorded load (P) by a reference area ($A_0 = n\pi d^2/4$) based on the number of wires (n) and the wire diameter (d). The temperature was ramped down to 5°C and back up to 140°C at a rate of 12°C/min, and then repeated for 25 thermal cycles.

3.3 Results

The experimental study consisted of four dead load temperature cycling experiments on each of the three specimens: the straight monofilament wire, 7×7 cable, and 1×27 cable. The experiments were exploratory in nature, and the data provided is intended as a first look at the thermal actuation response and general performance of SMA cables. A set of cycling experiments were performed, each on a new, as-received specimen under varying dead load magnitudes. The load levels were selected for each specimen type, based on their different sensitivities to functional fatigue (or shakedown). The 1×27 for example, had a relatively large amount of plasticity when cycled at 200 MPa dead load, while the monofilament wire experienced relatively little plasticity even at 400 MPa dead load. The normalized dead load values were 50, 100, 200, and 400 MPa for the single straight wire, 50, 100, 200 and 300 MPa for the 7×7 cable, and 50, 100, 150, and 200 MPa for the 1×27 cable. The straight wire response will be examined first in order to orient the reader to these types of experiments

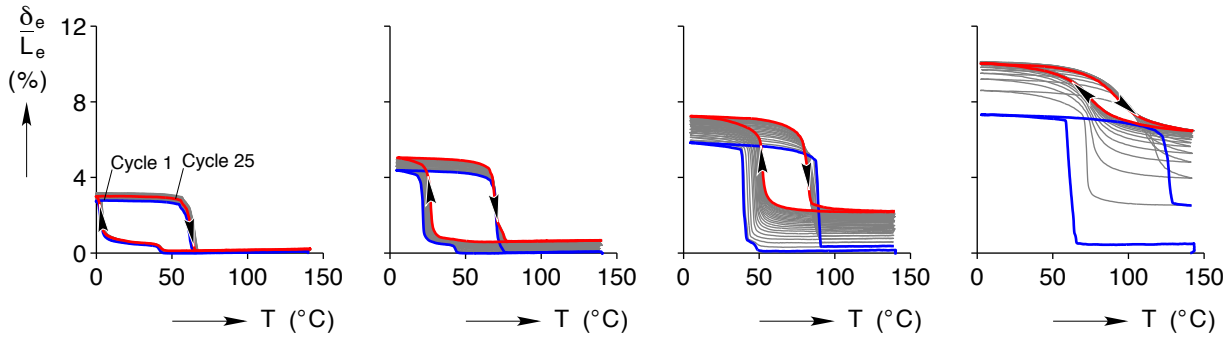

(a) 50 Mpa (b) 100 MPa (c) 200 MPa (d) 400 MPa

Figure 3.5: Thermal actuation of straight wire under varying dead load conditions.

and to characterize the uniaxial behavior of this specific NiTi alloy. The 7x7 cable will then be examined, followed by the 1x27 cable, and finally a comparison of all three specimens.

3.3.1 Wire Responses

The thermal actuation (strain-temperature) response of SMAs are known to have a strong dependence on the applied load. The wire specimens were not subjected to training prior to testing, and lack any two-way shape memory effect that would indicate repeated prior cycling. Thus the wires require a nominal load to have a noticeable strain increase with the forward transformation upon cooling. The amount the strain increases depends on the magnitude of the applied load as well as how the load is applied. While many SMA actuator applications use a bias spring or similar bias element that has a non-constant load, a dead load (constant applied load) was opted for here. Several magnitudes of load, specifically 50, 100, 200, and 400 MPa, were used to test straight wire specimens, as shown in Figure 3.5. Twenty five thermal cycles between 140°C and 5°C were conducted on each specimen and shown here. Note that the 50 MPa case was taken closer to 0°C in order to not cut off the transformation early as the A→M transformation temperature was very close to 5°C. In general, increasing the applied load increases the actuation strain, while also increasing the degradation and buildup of plasticity. Clearly, under a low 50 MPa load, there is very little plasticity and evolution in the actuation response, but by 400 MPa there is significant plasticity and evolution.

For better comparison between the dead load experiments on straight wire, the cycle 1 data and cycle 25 data for each load case are compared in Figure 3.6. On cycle 1 shown in Figure 3.6a, the strain on forward transformation was 2.8% for the 50 Mpa case, 4.4% for 100 MPa, 5.8% for 200 MPa, and 7.3% for the 400 MPa case. The transformation temperatures

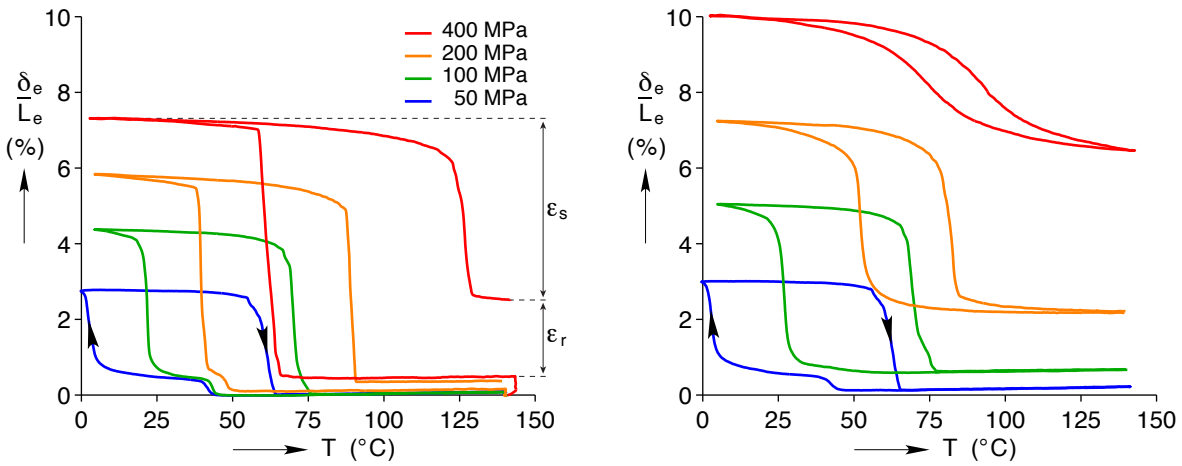

(a) Cycle 1 (b) Cycle 25

Figure 3.6: Comparison of straight wire thermal actuation data.

shift upwards with increasing load as would be expected from the Clausius-Clapeyron relation. There is also a clear R-phase transformation around 40-50°C and accompanying 0.4% strain increase in the 50, 100, and 200 MPa specimens, but not in the 400 MPa specimen. This is because the R-phase is stable at lower loads and suppressed under higher loads. Most of the specimens recovered the majority of the transformation strain, except for the 400 MPa specimen which had a strain of 2.5% after heating to 140°C (0.5% of which is elastic strain).

The cycle 25 data are shown in Figure 3.6b. The 50 MPa case has little change from cycle 1, but each higher load has increasingly more evolution in the actuation response. This is most apparent from the collapse of the hysteresis, and large residual strain. The 400 MPa case in particular has a transformation that is gradual over a wide temperature range, and a very large (6.5%) strain when mostly austenite at 140°C. The collapse of the hysteresis and widening of transformation temperatures is due to built-up plasticity and residual stresses that cause a shift the transformation temperatures. The R-phase is also no longer apparent in the 100 and 200 MPa cases, but is still apparent in the lowest 50 MPa case.

The transformation temperatures were picked off at the mean strain on each cycle (average of min/max strains of each heating or cooling segment). The mean strain point was close to the point of peak strain rate, but proved to be more stable to compute. The A→M (M_p) and M→A (A_p) transformation temperatures on cycle 1 and cycle 25 are shown in Figure 3.7. The temperature hysteresis was fairly independent of load on cycle 1, at Δ57°C under 50 MPa and Δ65°C on for the 400 MPa specimen. Thermal cycling under load had a large impact on the transformation temperatures, especially for the higher load cases. The temperature hysteresis for the 400 MPa case, for instance, decreased to Δ18°C on cycle 25.

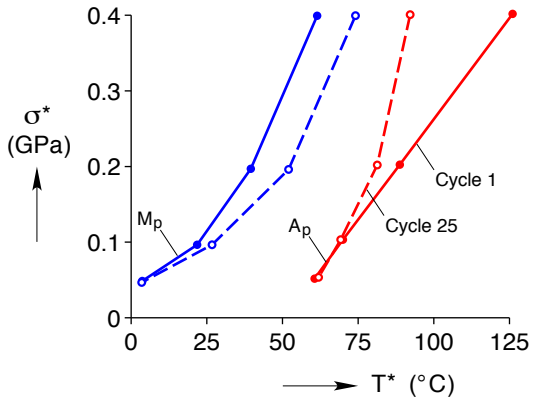

Figure 3.7: Transformation temperatures for straight wire showing cycle 1 and 25.

Most of this change was from a shift in A_p, which decreased by 34°C.

A comparison of stroke and residual strain data for each dead load case is shown in Figure 3.8. The stroke was measured by subtracting the final strain after the heating portion from the maximum strain at the minimum temperature of each experiment. The stroke for the 50 and 100 MPa experiments was fairly consistent throughout cycling, while the 200 MPa experiment has a slightly downward trend (starting at 5.5% and ending at 5.0%). The 400 MPa experiment had a more noticeable decrease in stroke, starting at 4.8% and decreasing to 3.6%. The stroke is also non-monotonic with load, and has an optimum at 200 MPa. The residual strain was quantified by taking the strain at the peak temperature of 140°C in each cycle and subtracting the elastic strain measured during loading prior to the first cycle, in an effort to quantify only the unrecovered portion of the axial strain. The result here is monotonic with load, as would be expected. The 400 MPa case has clearly the most degradation, having a residual strain totaling 6.2% on cycle 25, and appears to have reached an asymptotic limit in fewer cycles than the other cases.

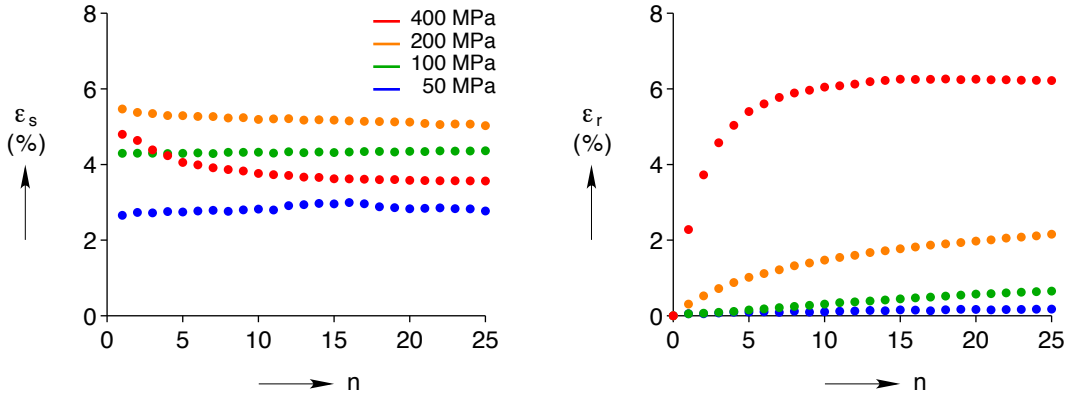

(a) Stroke (b) Residual Strain

Figure 3.8: Straight wire data showing evolution of stroke and residual strain with cycling.

3.3.2 7×7 Cable Responses

Of the two cables, the 7×7 cable has the more conventional design found in many typical applications. This cable has relatively small helix angles, making its response ideally more akin to that of a single, monolithic bar or straight wire. The 7×7 cable was tested under four different dead loads with nominal stress values of 50, 100, 200, and 300 MPa. Unlike a straight wire, however, there is now a reaction torque when the ends are constrained from rotating (as they were in this study). The thermal actuation responses, including both strain and reaction torque for all 25 cycles of these tests are shown in Figure 3.9. The strain response here has similar trends to those seen in straight wire. The thermal actuation is smaller at 50 MPa and there is little evolution with 25 cycles. By 300 MPa, there is a larger thermal actuation with significant evolution and plasticity developing with subsequent cycling. The R-phase is clearly visible in the 50 and 100 MPa cases, but it is no longer apparent in the 200 MPa case.

The reaction torque has a relatively small and constant value throughout the thermal cycles when the nominal load is 50 MPa. With increasing dead load, the magnitude of reaction torque increased as well as the change with temperature or dependence on thermal cycling. In general, the reaction torque had an inverse relationship with the strain response. When the strain was at its minimum (at 140°C), the torque was at its maximum, and similarly when the strain is at its maximum (at 5°C), the torque is at its minimum.

The thermal actuation data (both strain response and reaction torque) are summarized in Figure 3.10. On cycle 1 of the strain responses shown in Figure 3.10a, the strain in martensite after the forward transformation under the low 50 MPa load was a meager 3.1% strain, but

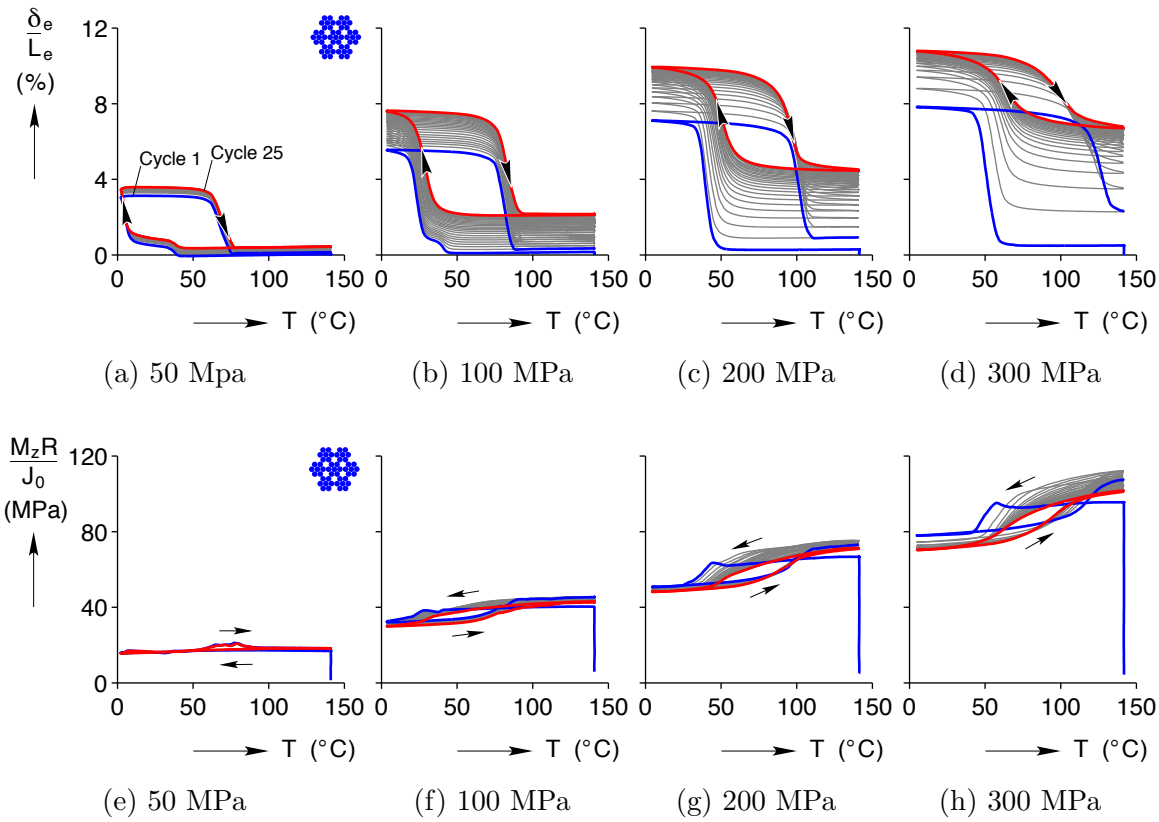

(a) 50 Mpa (b) 100 MPa (c) 200 MPa (d) 300 MPa

(e) 50 MPa (f) 100 MPa (g) 200 MPa (h) 300 MPa

Figure 3.9: Thermal actuation of 7×7 cable under varying dead load conditions.

increased to 5.5% for the 100 MPa case. Under 200 MPa nominal load the fully martensite strain appeared to saturate at 7.1% strain, and increasing the load to 300 MPa only yielded slightly higher strain of 7.8%. On reverse transformation, the 50 and 100 MPa cases had more or less complete recovery, and returned to 0.15% and 0.35% strain respectively. The 200 MPa case began to show noticeable plasticity and only recovered to 0.93% strain, and the 300 MPa case had a large degradation shown by a austenite strain of 2.32%.

The cycle 25 strain response data are summarized in Figure 3.10b. The main effects that are apparent from cycling are, (1) residual strain has accumulated in each experiment, causing the thermal actuation loops to walk up in strain by varying amounts, and (2) the hysteresis loop has collapsed for the cases with larger nominal load. The 50 and 100 MPa preserved the shape of their strain responses, but the 200 and 300 MPa cases show significant evolution and broadening of transformation regions. Further, the 50 and 100 MPa cases ended with minimum strains of only 0.4% and 2.2% strain, but the 200 and 300 MPa cases show increased degradation with minimum strains of 4.5% and 6.8%.

The reaction torque data is shown in Figures 3.10c-3.10d for comparison. On cycle 1, the cables end in noticeably higher torque after returning to 140°C than the torque they developed after the initial elastic loading. On cycle 25, the torque responses had become more monotonic and the open hysteretic loop had closed. As mentioned previously, the trend is that the higher nominal load experiments developed a higher torque in general, but also a higher difference in torque between high and low temperature regimes and is inversely related to the strain response.

The measured transformation temperatures for the 7×7 cable had a similar trend to that of the straight wire specimens, as shown in Figure 3.11. Cycle 1 had a slightly larger hysteresis between A_p and M_p, at Δ61.4°C for the lowest 50 MPa experiment and increased to Δ73.5°C for the 300 MPa experiment. The temperatures remained approximately constant for the 50 MPa experiment throughout cycling, but were drawn inwards for the 300 MPa experiment where the hysteresis decreased to only Δ18.1°C.

The actuation stroke again shows a non-monotonic dependence on load, as shown in Figure 3.12a. The stroke is again optimal under 200 MPa load and recovers a strain of 6.2% on cycle 1. On cycle 25, both the 100 and 200 MPa specimens recovered 5.4% strain on heating. The 300 MPa specimen had a large decrease in stroke with cycling, starting at 5.5% on cycle 1 and decreasing to 4.0% by cycle 25.

The residual strain for the 7×7 cable specimens, shown in Figure 3.12b, was monotonic with load as would be expected. The 300 MPa specimen had the largest final residual strain

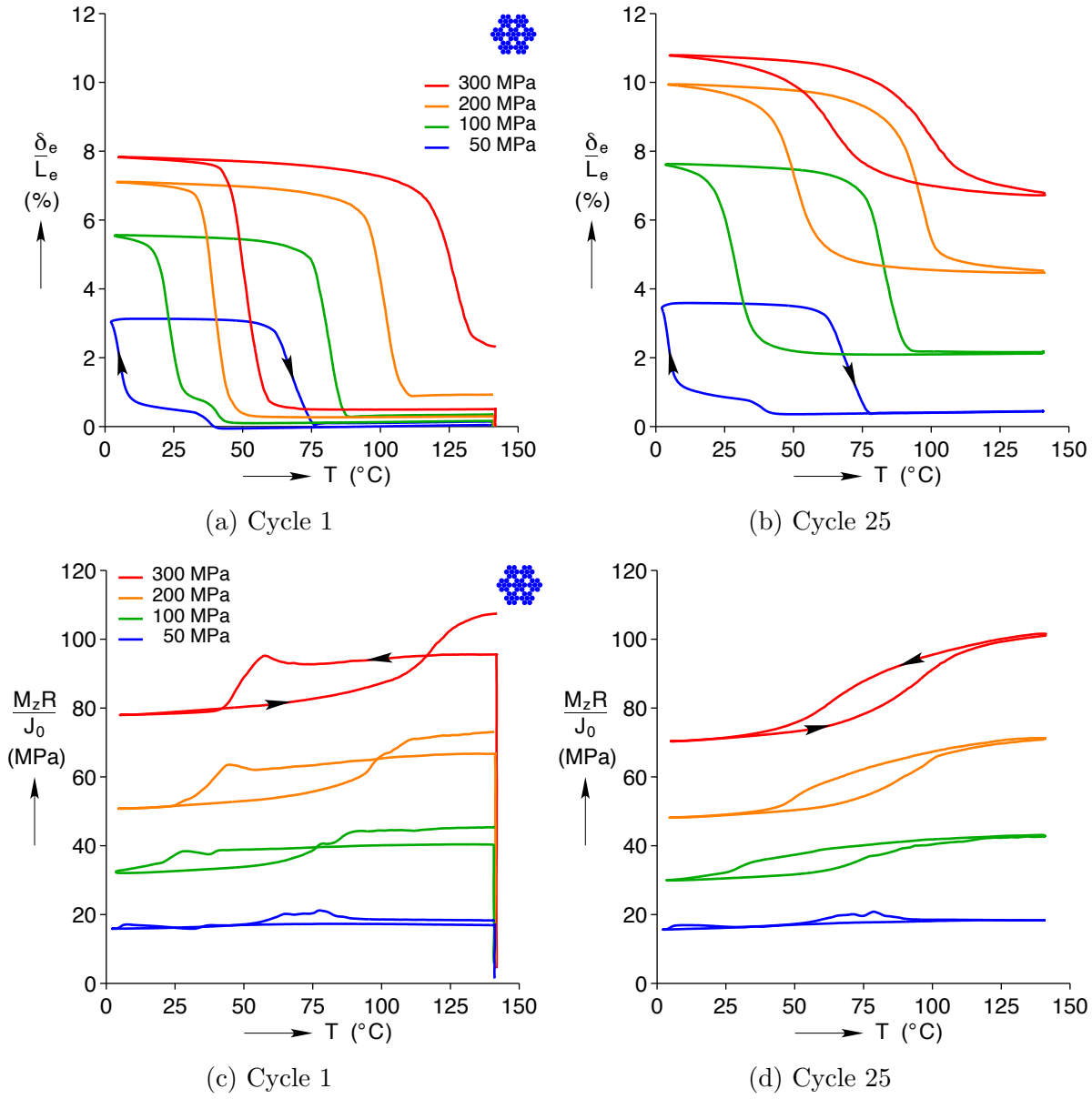

(a) Cycle 1

(b) Cycle 25

(c) Cycle 1

(d) Cycle 25

Figure 3.10: Comparison of 7×7 thermal actuation data.

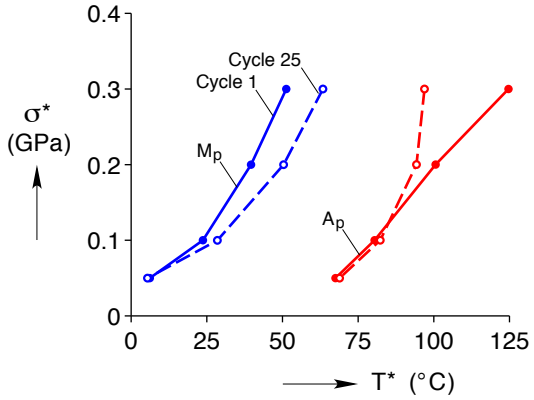

Figure 3.11: Transformation temperatures for the 7×7 cable showing cycle 1 and 25.

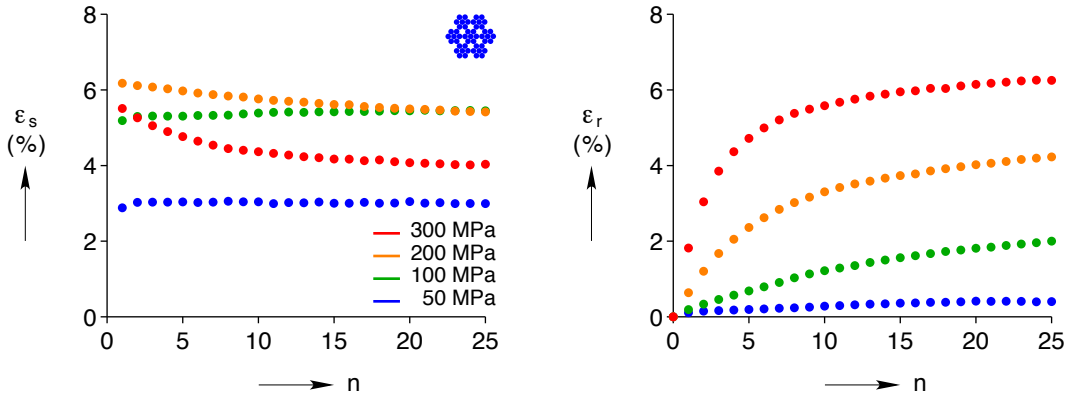

(a) Stroke (b) Residual Strain

Figure 3.12: 7×7 cable data showing evolution of stroke and residual strain with cycling.

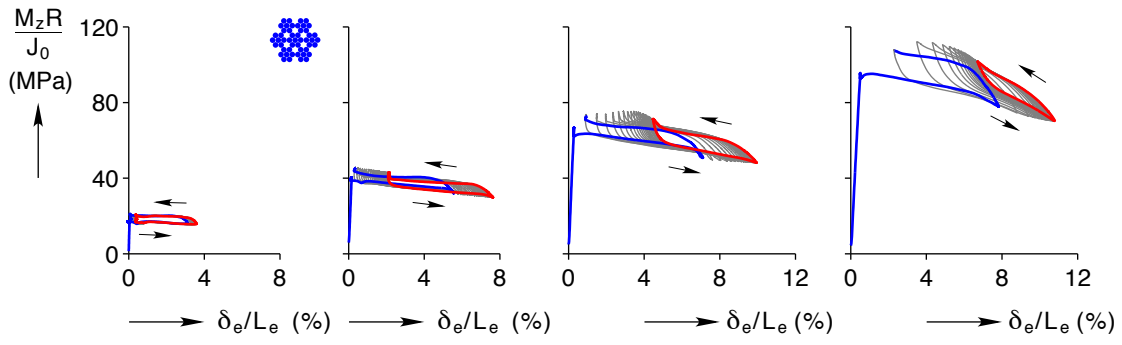

(a) 50 MPa (b) 100 MPa (c) 200 MPa (d) 300 MPa

Figure 3.13: Strain and torque relationship with cycling in the 7×7 cable under varying dead loads.

of 6.3% on cycle 25, the 200 and 100 MPa specimens had intermediate residual strains of 4.2% and 2.0%, and the 50 MPa specimen had the smallest final residual strain of 0.4%.

3.3.2.1 7×7 Cable Torque-Strain Relationship

For further comparison of the torque-strain responses with thermal actuation, the torque and strain cycling data are directly compared in Figure 3.13. In each dead load case here, there is an initial increase in torque from the elastic loading of the 7×7 cable at the start of the experiments. There is a noticeable hysteresis in the actuation loop even for the 50 MPa experiment, which was less noticeable when comparing the torque and temperature data. The hysteresis and actuation loop remain approximately the same size with cycling for all but the 300 MPa experiment which has the most plasticity and collapse of hysteresis loop. The reaction torque, aside from the hysteresis, was roughly constant with respect to the strain response for the 50 MPa experiment. With increasing dead load, there was an increasing dependence of reaction torque to the nominal strain, indicated by the steeper negative slope. This comparison is highlighted in Figure 3.14. Here the trend is clear, that particularly on cycle 25, the higher dead load experiments not only experience a larger average reaction torque, but also have a larger variance in torque between the high and low strain regimes. From a time history perspective, the torque and strain data are out of phase with each other, as shown in Figure 3.15. While the strain ratchets up with cycling and the reaction torque decreases, the out of phase nature remains strongly apparent even in later cycles. This is useful to note because there is a different trend in the 1×27 cable that changes from early cycles to later cycles.

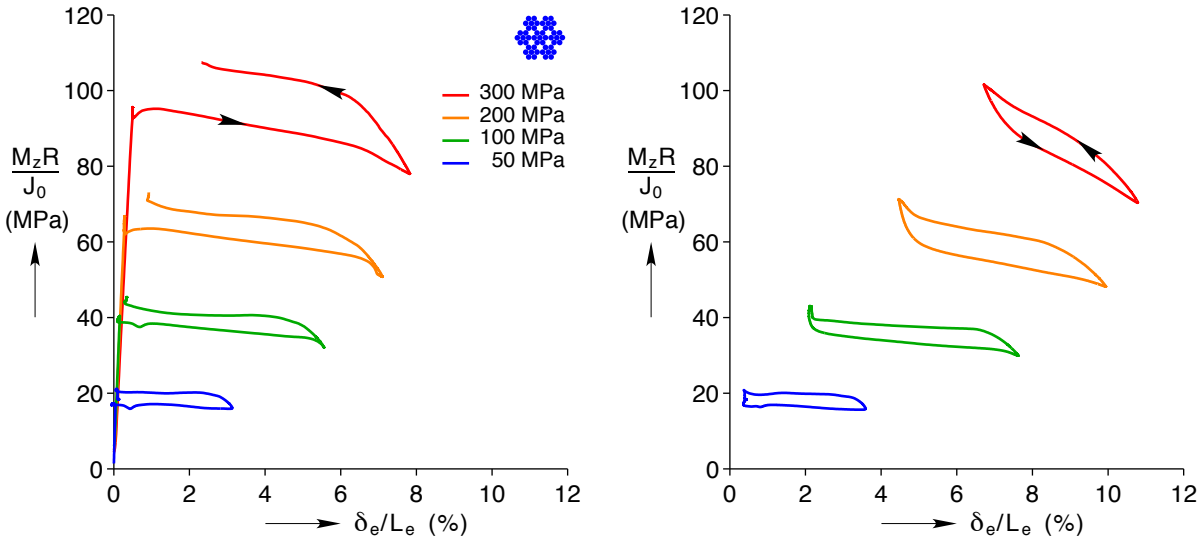

(a) Cycle 1 (b) Cycle 25

Figure 3.14: Comparison of strain and torque relationships in the 7×7 cable.

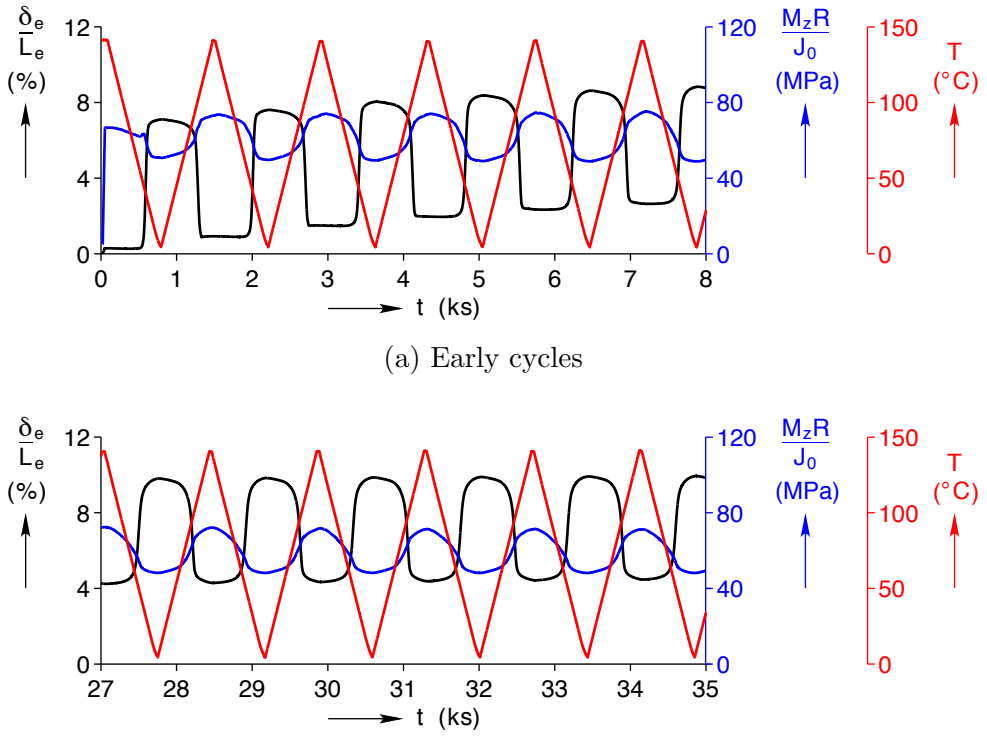

(a) Early cycles

(b) Later cycles

Figure 3.15: Time history of the 7×7 cable at 200 MPa.

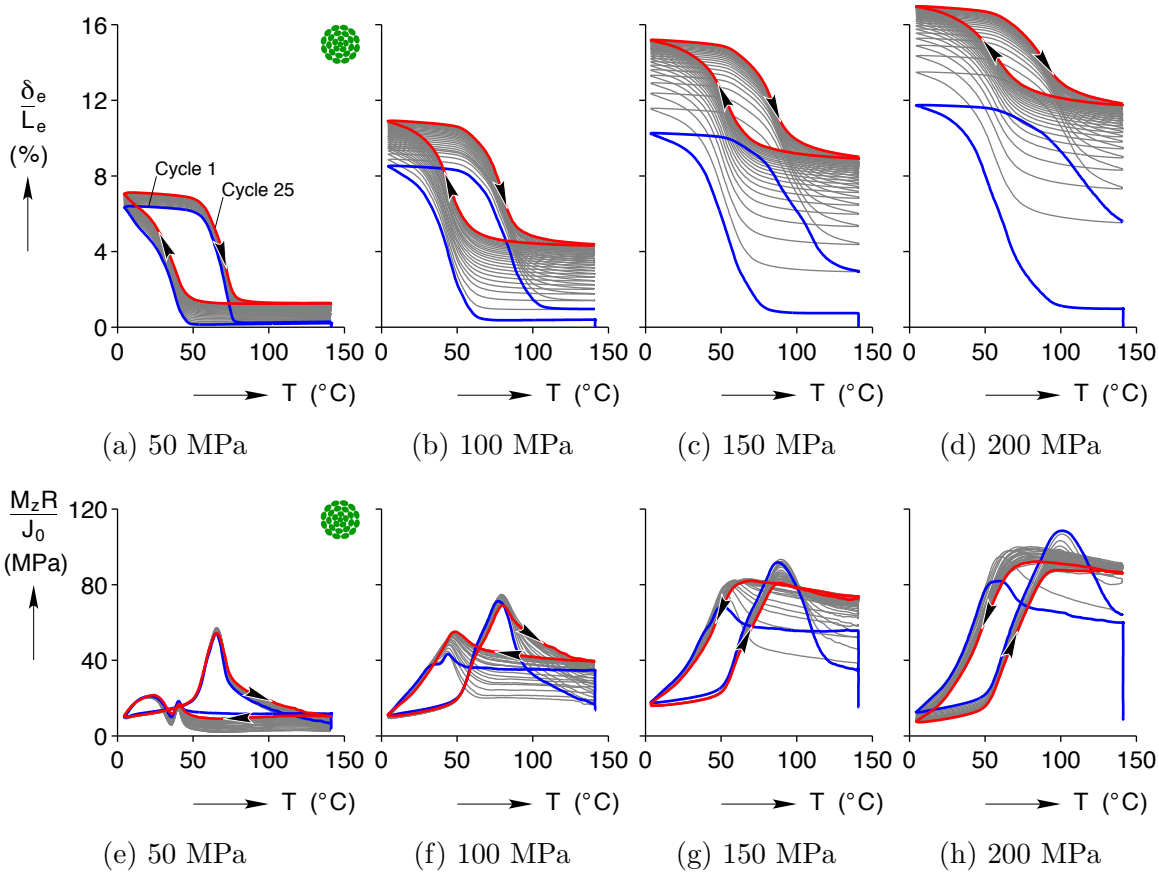

(a) 50 MPa (b) 100 MPa (c) 150 MPa (d) 200 MPa

(e) 50 MPa (f) 100 MPa (g) 150 MPa (h) 200 MPa

Figure 3.16: Thermal actuation of 1×27 cable under varying dead load conditions.

3.3.3 1×27 Cable Responses

The 1×27 cable is an interesting cable to draw contrast with the 7×7 cable because of its different hierarchical construction and much larger helix angles. The 1×27 has three layers with progressively more number of wires (5, 9, and 12) and alternating lay directions around a central straight core wire. In general, this produces a more flexible cable with a larger torque response. This cable was tested under dead loads with nominal stress values of 50, 100, 150, and 200 MPa. The strain response and reaction torque for these experiments are shown in Figure 3.16. The thermal actuation strain was noticeably larger in the 1×27 cable and had more evolution of the thermal actuation loop even at a relatively small load of 100 MPa. The 200 MPa nominal load appeared to be fairly tortuous for this cable (shown by the open loop strains on the first few cycles), and was chosen as the maximum dead load. The 50 MPa case appears to have two regions of transformation on cooling, indicated by a kink in the slope of the strain-temperature response around 30°C.

The reaction torque at first glance is highly complex, but offers some insight into the

inter-layer cable motion. The torque was highly non-monotonic throughout cycling for both the 50 and 100 MPa dead load cases, as shown in Figures 3.16e, 3.16f. There were mid-cycle spikes in the reaction torque that correspond to peak transformation temperatures on cooling and heating. Each layer of the 1×27 cable has an alternating direction, and as the cable transforms these layers must slide relative to each other to accommodate axial elongation or contraction. The sliding motion (which would primarily be in the hoop direction) cause the large mid-cycle increase in the reaction torque. For the higher dead load experiments of 150 and 200 MPa (Figures 3.16g, 3.16h), the mid-cycle spike in reaction torque was still apparent, but shook out by cycle 25 yielding a hysteretic loop closer resembling that of the 7×7 cable.

The strain and torque thermal actuation data for the set of dead load cases are summarized for comparison in Figure 3.17. The 1×27 cable is remarkably more flexible than either of the other two specimens. Under a low 50 MPa nominal stress the cable transforms to a large 6.3% strain on cycle 1, as shown in Figure 3.17a. The actuation strain increases monotonically with load, reaching a maximum of 11.7% for the 200 MPa case. The 50 MPa specimen was able to fully recover the deformation, but the other specimens showed fairly significant plasticity ending their first cycles at 0.96%, 2.94%, and 5.55% strain for the 100, 150, and 200 MPa cases, respectively. By cycle 25, the actuation loops ratcheted in strain and had a collapse of hysteresis loop in a monotonically increasing manner with dead load, as shown in Figure 3.17b.

The reaction torques of the 1×27 cable on cycle 1, shown in Figure 3.17c, all exhibit the mid-cycle spikes in torque. These spikes are monotonically increasing with dead load magnitude, and noticeably larger on heating during reverse transformation to austenite, than on cooling during forward transformation to martensite. By cycle 25, shown in Figure 3.17d, the 50 and 100 MPa dead load experiments still exhibited this mid-cycle reaction torque spike. The specimens with higher loads of 150 and 200 MPa had a shift in torque response towards one that is more monotonic. The 200 MPa case particularly resembles the 7×7 cable, where there was an inverse relationship between torque and strain, with high strain corresponding to low torque and low strain corresponding to high torque. This shift with cycling could be caused by either reduced inter-layer sliding in the 1×27 cable, or reduced resistance to sliding. Both scenarios would reduce the reaction torque that develops during transformation.

The measured peak transformation temperatures are shown in Figure 3.18. The transformation temperature hysteresis on cycle 1 was fairly small at Δ36.8°C and Δ49.0°C for the 50 MPa and 200 MPa experiments, respectively. The transition temperature hysteresis

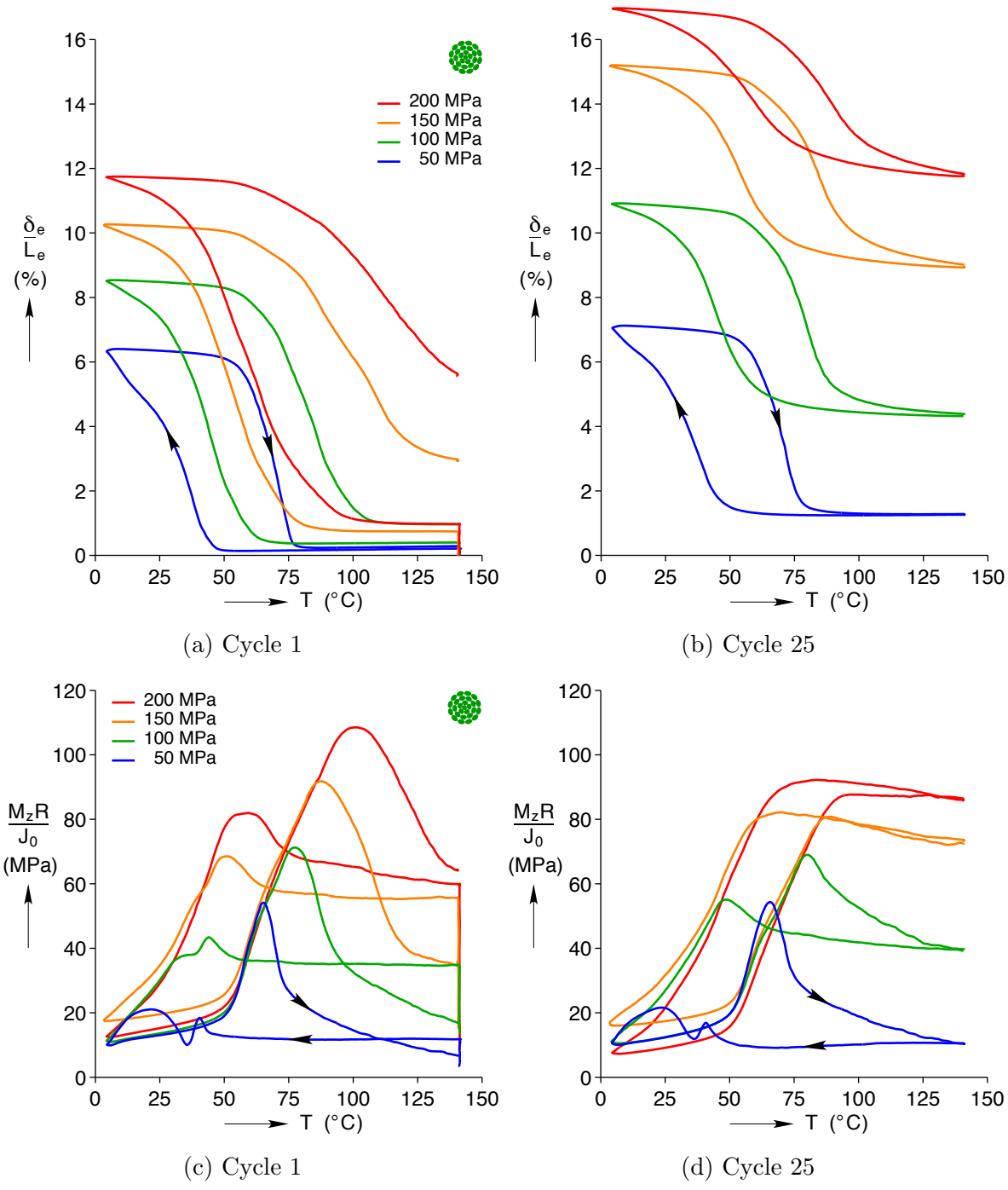

(a) Cycle 1

(b) Cycle 25

(c) Cycle 1

(d) Cycle 25

Figure 3.17: Comparison of 1×27 thermal actuation data.

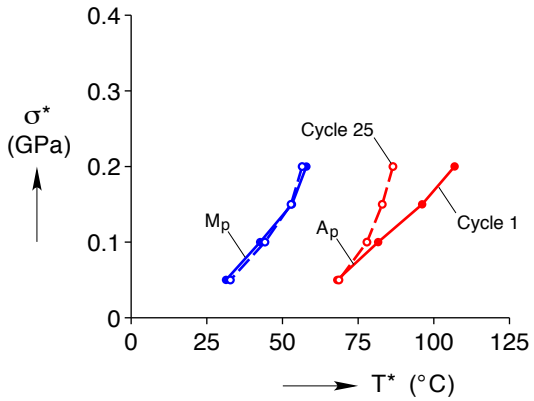

Figure 3.18: Transformation temperatures for the 1×27 cable showing cycle 1 and 25.

decreased with cycling as expected, dropping to $\Delta 30.0°C$ for the 200 MPa case. However, the shift was completely comprised of a decrease in A_p, with little change in M_p. In both the 7×7 cable and straight wire specimens, both forward and reverse transformation temperatures drew inwards.

The actuation stroke is fairly consistent between the different dead load magnitudes, as shown in Figure 3.19a. The 1×27 cable had an optimal stroke of 7.5% on cycle 1 and 6.5% on cycle 25 when under 100 MPa nominal stress. Both 50 and 200 MPa specimens had a stroke of approximately 6% on cycle 1, but the 200 MPa specimen degraded to 5.2% stroke on cycle 25 while the 50 MPa specimen maintained a higher 5.8% stroke. Overall, these strokes are larger than those measured on the 7×7 cable and straight wire specimens.

The residual strain cycling data of the 1×27 cable are shown in Figure 3.19b. Here, all of the dead load experiments had similar asymptotic behavior with cycling. The 200 MPa case had the largest final residual strain of 10.9% as expected. The residual strain decreased monotonically with decreasing load, totaling 8.3%, 4.0%, and 1.1% for the 150 MPa, 100 MPa, and 50 MPa experiments, respectively.

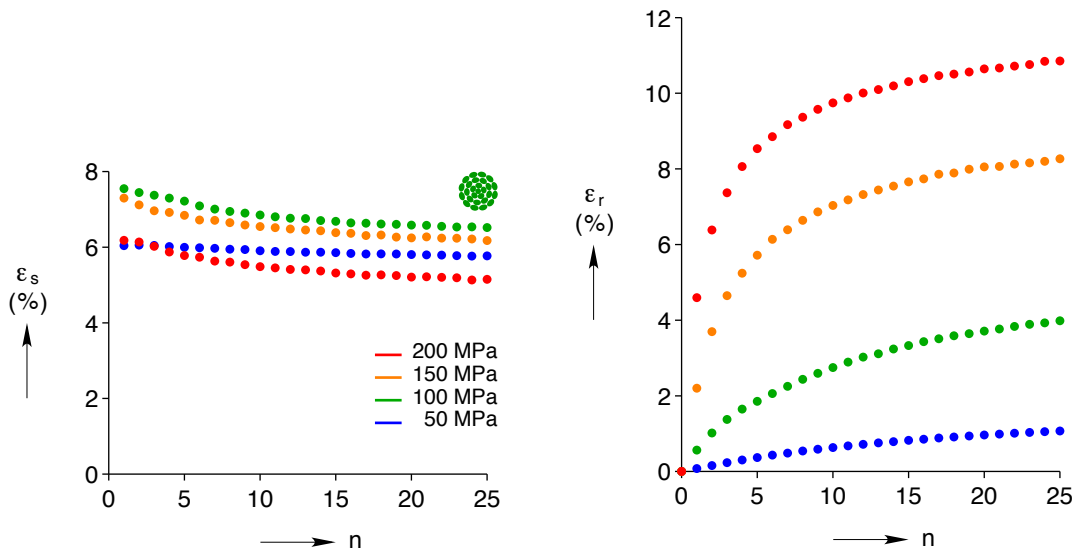

(a) (b)

Figure 3.19: 1×27 cable data with cycling. (a) Stroke, (b) Residual strain.

3.3.3.1 1×27 Cable Torque-Strain Relationship

To gain clarity in the torque-strain relationship in the 1×27 cable, it is useful to directly compare the data. To this end, the torque-strain responses with cycling are shown in Figure 3.20. The 50 MPa and 100 MPa experiments are strongly non-monotonic, and retained their mid-cycle torque increases throughout all 25 cycles. The 50 MPa case has two torque spikes on cooling (from two different layers transforming at different nominal strain levels), but one large torque spike on heating. The 150 and 200 MPa specimens begin with a similar non-monotonic relationship between torque and strain, but with cycling shift towards a more linear relationship, particularly in the 200 MPa case. These comparisons are more apparent in Figure 3.21, where all of the cycle 1 experiments and cycle 25 experiments are summarized. The time history data for early and later cycles are shown in Figure 3.22. These data corroborate the conclusion that the torque experiences a spike during transformation, when the strain rate is the highest. As mentioned previously, this is caused by inter-layer sliding. With cycling, the torque spikes appear to diminish, potentially due to decreased sliding or decreased resistance to sliding with the buildup of plasticity.

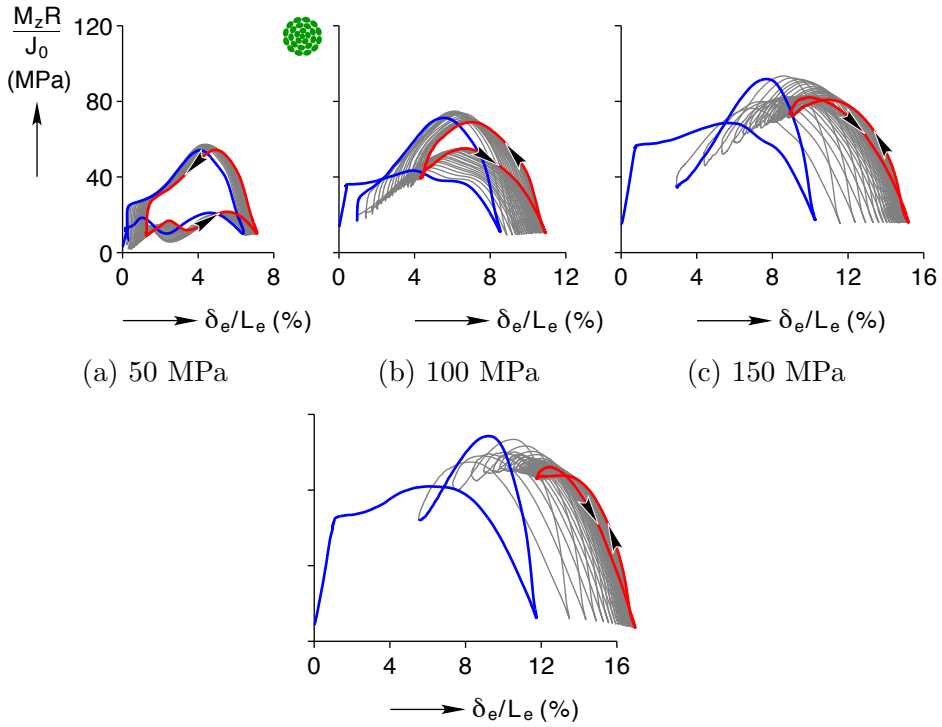

(a) 50 MPa (b) 100 MPa (c) 150 MPa

(d) 200 MPa

Figure 3.20: Strain and torque relationship with cycling in the 1×27 cable under varying dead loads.

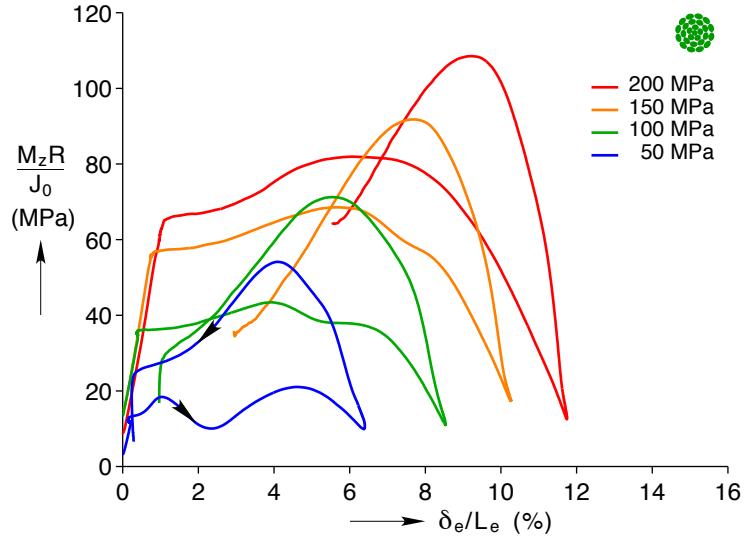

(a) Cycle 1

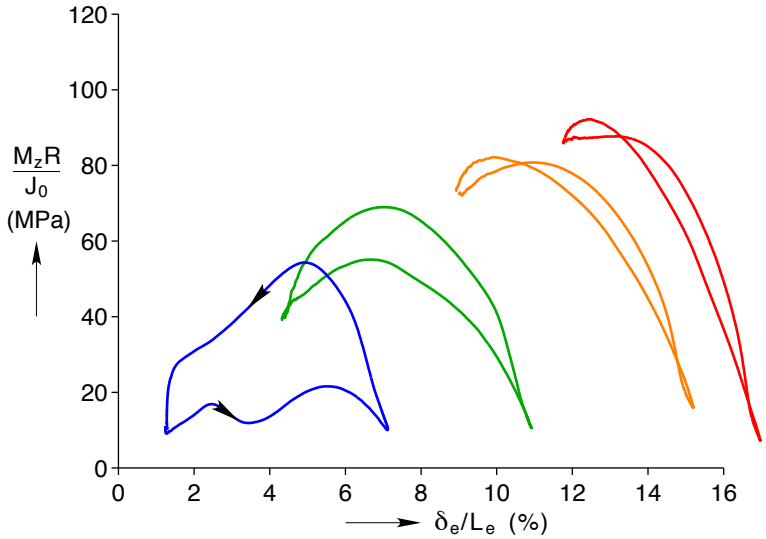

(b) Cycle 25

Figure 3.21: Comparison of strain and torque relationships in the 1×27 cable.

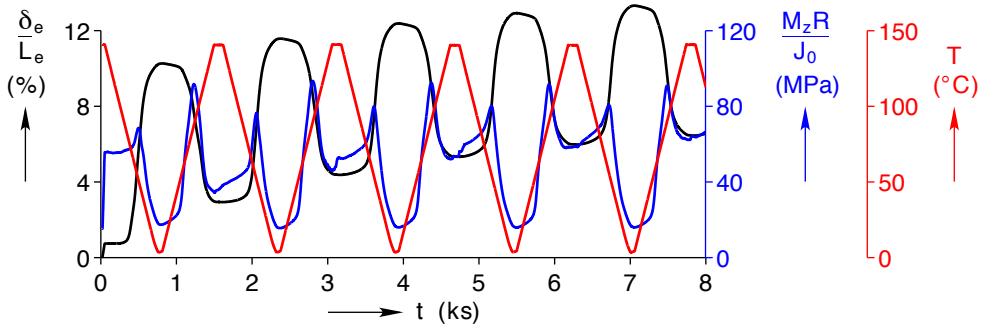

(a) Early cycles

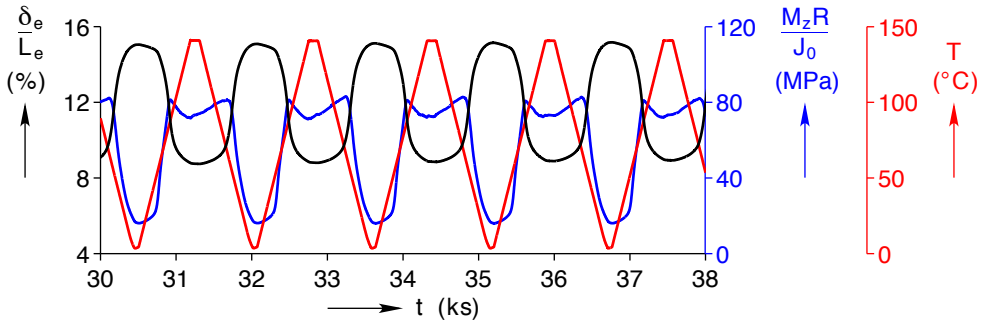

(b) Later cycles

Figure 3.22: Time history of the 1×27 cable at 150 MPa.

3.3.4 Comparison of Straight Wire and Cable Specimens

Having examined the thermal actuation behavior or each specimen individually, it is useful now to compare the relative behaviors of the 7×7 cable, 1×27 cable, and straight monofilament wire. The 100 MPa dead load experiments showed large actuation strains without inducing a large amount of plasticity in each specimen, and were chosen as a basis to first compare the strain responses and reaction torques. Next, performance metrics of actuation stroke, residual strain, and the specific work output, along with a summary of the thermal actuation responses is presented.

As a baseline comparison, the data for the 100 MPa dead load experiments on the three specimens are shown in Figure 3.23. Here, Figures 3.23a and 3.23b show the axial strain response and Figures 3.23c and 3.23d show the reaction torque of the 1st and 25th cycles respectively. There are several trends visible in the strain response data on cycle 1: (1) progressively increasing transformation strain between the straight wire, 7×7 cable, and 1×27 cable (δ_e/L_e = 4.4%, 5.5%, 8.5%), (2) a distinct R-phase around 40°C in the straight wire and 7×7 cable but not present in the 1×27 cable, (3) nearly vertical slope in the straight wire data, indicating all of the material was transforming at the same temperature, but an increasing slope in the 7×7 and more so in the 1×27 cable data, indicating material was transforming over a wide range of temperatures, and (4) increasing open loop strains from the straight wire through the 1×27 cable (ε_r = 0.01%, 0.19%, 0.57% respectively). On cycle 25, the straight wire, 7×7 cable, and 1×27 cable had progressively increasing residual strain (ε_r = 0.6%, 2.0%, 4.0%), and the distinct R-phase was no longer visible in the straight wire or 7×7 cable.

The 1×27 cable is clearly the most flexible with a much larger transformation strain, but the different strain rates (in temperature space) between the three specimens is particularly interesting. This is caused by a gradient in the stress states through the thickness of each cable. In the 1×27 cable, the inner most wires are experiencing primarily pure tension, but the outer fibers experience increasing levels of bending and twisting. This causes the outer fibers to be more compliant relative to the inner ones, and proportionally carry less load. Recalling the Clausius-Clapeyron relationship and the dependence on transformation temperature to the stress level, the stress gradient should cause the inner most wires (which experience the highest axial stress) to transform at the highest temperature, followed by the second layer and so forth, with the outermost layer transforming last at the lowest temperature.

The torque data, shown in Figures 3.23c,3.23d, highlight the increased reaction torque

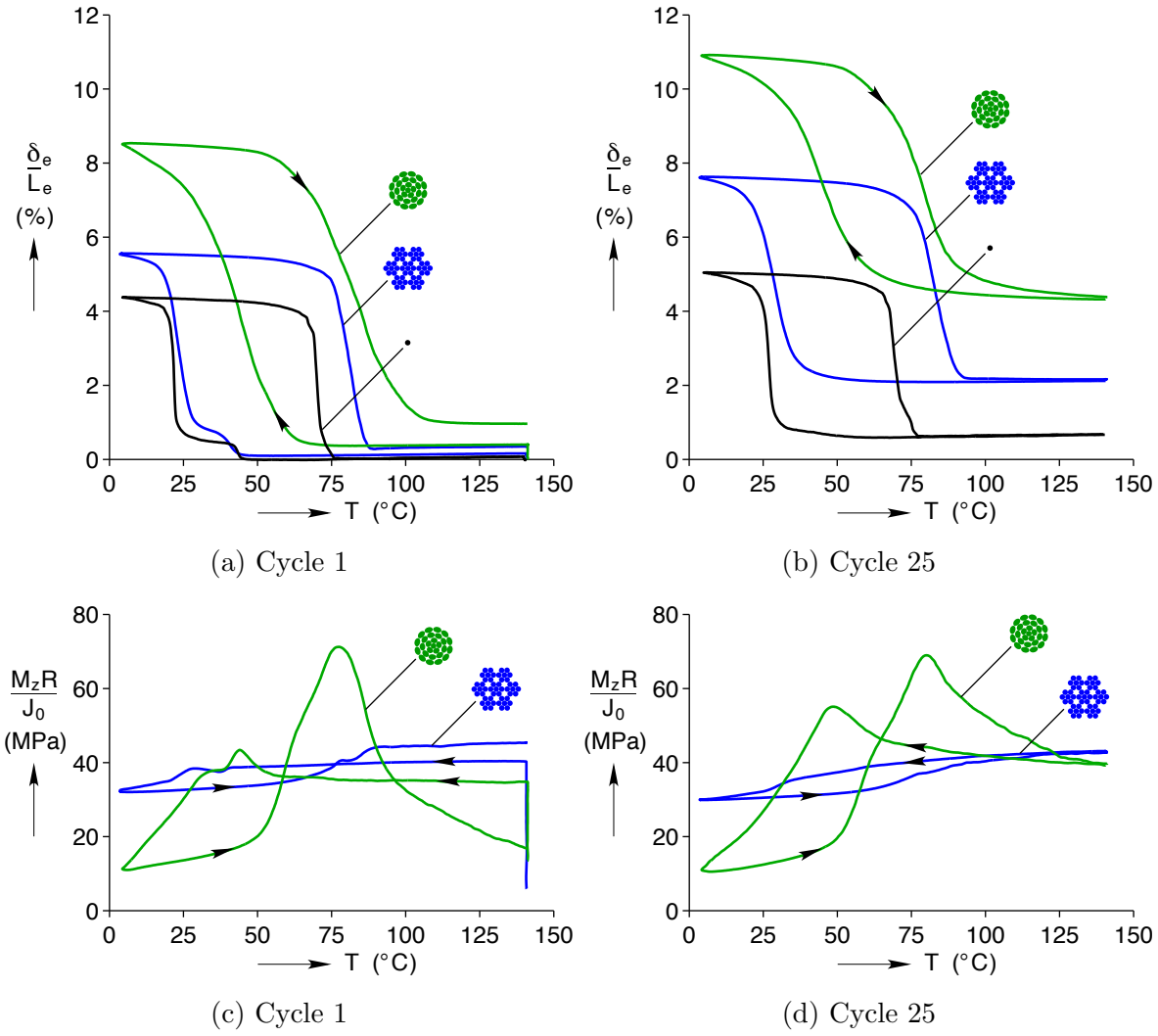

(a) Cycle 1

(b) Cycle 25

(c) Cycle 1

(d) Cycle 25

Figure 3.23: Selected dead load cycles at 100 MPa on the 7×7 cable, 1×27 cable, and monofilament wire.

developed in the 1×27 cable relative to the 7×7 cable. Both cables have the general trend of having higher torque when in the mostly austenite state at 140°C, and lower torque when in the mostly martensite state at 5°C. This is caused by a decrease in the elastic modulus when transforming from austenite and martensite (around 70 GPa in austenite to below 30 GPa in martensite for straight wire). The large helix angles in the outer two layers of the 1×27 cause a large reaction torque during transformation. This could be potentially from relative sliding between the layers, or due to different layers transforming at different temperatures.

3.3.4.1 Actuation Stroke and Residual Strain

The actuation stroke is an interesting metric to use for comparing the different specimens because it is an important design criterion for an actuator. One key advantage of an SMA over other smart materials, such as piezoelectrics, is its relatively large stroke. A comparison of the actuation stroke data for all 25 cycles for the three specimens at 100 MPa load are shown in Figure 3.24a. For this 100 MPa case, the stroke remained stable with cycling for the monofilament wire and the 7×7 cable. The monofilament wire recovered 4.3% strain and 4.4% strain, and the 7×7 cable recovered 5.2% and 5.4% strain, on the 1st and 25th cycles, respectively. The 1×27 cable had a larger stroke, recovering 7.5% strain and 6.5% strain, respectively. While the 1×27 cable's stroke degraded somewhat with cycling, even on the 25th cycle it is able to elongate 48% more than the monofilament wire.

Using the ε_s data for the 1st and 25th cycle, it is possible to construct a plot of ε_s versus dead load level (average axial stress, P/A_0), which is shown in Figure 3.24b. In this figure, the closed circles represent the 1st cycle data, and the open circles represent the 25th cycle data. This plot summarizes the influence that the dead load has on ε_s, as well as the extent that it degrades with cycling, while comparing the results of all three specimens. One immediately clear trend is that each specimen has a non-monotonic dependence of ε_s on the load, with an optimal dead load value which maximizes stroke. For the 1×27 cable, the maximum is at 100 MPa, and it is around 200 MPa for both the 7×7 cable and monofilament wire. This non-monotonic behavior could be explained in the following way. When the load is smaller, there is insufficient energy to overcome the barrier for transforming the poorly oriented grains. When the load is too large, the deformation from transforming from A to M is accompanied by larger amounts of plasticity, causing a loss in recoverable strain. Thus, by this line of reasoning, there should be an optimal load to maximize ε_s.

The maximum global ε_s seen here occurs with the 1×27 cable under 100MPa load, with values of 7.5% on the 1st cycle and 6.5% on the 25th. Under a smaller 50MPa load, both

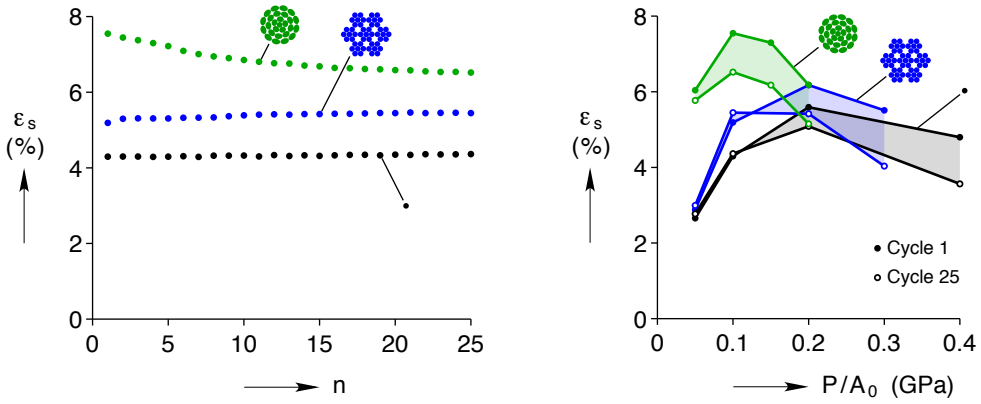

Figure 3.24: Actuation stroke. (a) Cycles 1-25 at 100 MPa, (b) Compiled cycle 1 (closed circles) and cycle 25 (open circles) data.

the 7×7 cable and monofilament wire had a ε_s of less than 3%, but the 1×27 cable had a surprisingly large ε_s of 6%. Interestingly, on the 1st cycle at 200 MPa load, both the 1×27 and 7×7 cables have a similar ε_s of 6.2%. However, after cycling 25 times, the 7×7 cable has a ε_s of 5.4%, exceeding that of the 1×27 cable which was only 5.2%. There is also an obvious trend that the amount of degradation of ε_s increases with increasing load (which is most clearly seen in the monofilament wire). Even under a relatively large 400 MPa load, the monofilament wire was able to sustain a ε_s of 3.6% after 25 cycles.

In contrast with the performance metric of the actuation stroke, the residual strain (ε_r) provides a useful comparison for how much damage and plasticity has built up in each specimen after cycling as well as how sensitive the different specimens are to the applied load. Figure 3.25a shows ε_r for each specimen as it accumulates with cycling, specifically under 100 MPa load. After 25 cycles, the 1×27 cable has the largest ε_r of 4.0%, the 7×7 cable has approximately half that at 2.0%, and the monofilament wire has the smallest ε_r of 0.6%. The damage has a single exponential like behavior, increasing the most on the first cycle, and the least on the last cycle. For example, on the 1×27 cable, ε_r increased by 0.56% after the first cycle, but only by 0.06% on the last cycle.

The total accumulated ε_r through 25 cycles for each specimen can be plotted against the applied load, as seen in Figure 3.25b. This provides a measure of the sensitivity of the specimen to the dead load. Each specimen had four dead load experiments, as indicated by the closed circles on the plot. Linear fits to the data are overlaid to help visualize the trends shown by the data. The monofilament wire is shown to have the lowest stress sensitivity, with a slope of 18.2 %/GPa. Next is the 7×7 cable, with slightly increased stress sensitivity of 24.8

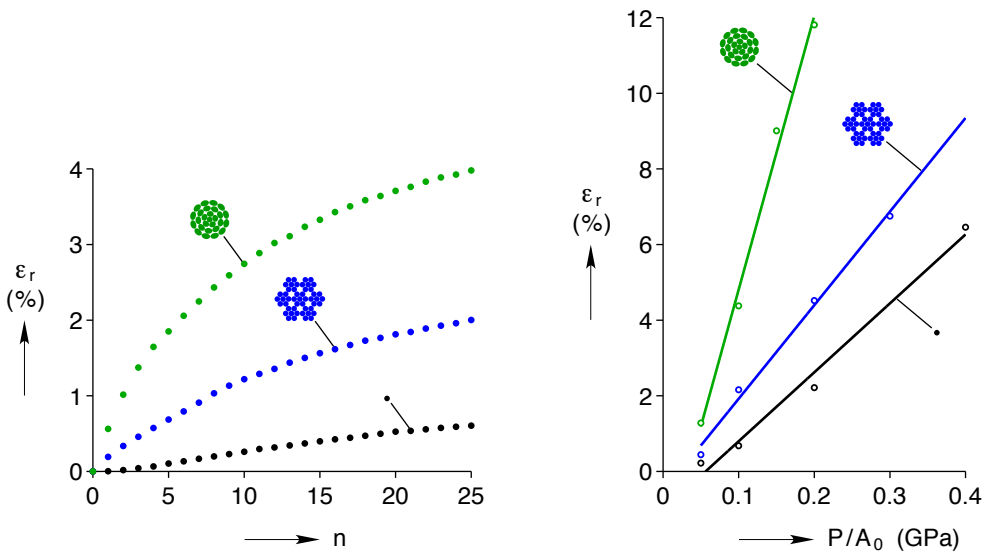

(a) (b)

Figure 3.25: Residual strain, (a) Cycles 1-25 at 100 MPa, (b) Accumulated ε_r through cycle 25.

%/GPa. The 1×27 cable's ε_r grows very rapidly, which is why this cable was only stressed to 200 MPa, and exhibited a stress sensitivity four times larger than the monofilament wire at 72.4 %/GPa. As an illustrative example based on this data, if one were to specify 6% as the maximum allowable ε_r, then the monofilament wire, 7×7 cable, and 1×27 cable could sustain loads below 400 MPa, 270 MPa, and 120 MPa, respectively.

3.3.4.2 Specific Work and Thermal Actuation Envelopes

The work output is an important factor when designing an actuator. Ideally when scaling up an SMA wire to an SMA cable, the work output should remain the same, indicating no loss of performance. The specific work (w), or work per unit mass, provides a fair comparison for the work output and is given by,

$$\mathrm{w} = \frac{1}{\rho}\left(\frac{P}{A_0}\right)\left(\frac{\Delta\delta_e}{L_e}\right)\frac{1}{c}\,. \tag{3.1}$$

The reader may recognize P/A_0 as the average axial stress and $\Delta\delta_e/L_e$ as the recovered axial strain measured by the extensometer. In the numerator, $P \cdot \Delta\delta_e$ is the work. In the denominator, ρ is the mass density of NiTi (6.5×10^6 g/m^3), and when multiplied by the volume ($A_0 \cdot L_e$) provides the total mass (assuming all of the wires are straight). To account for the additional length of helical wires in a cable, the volume is multiplied by a correction

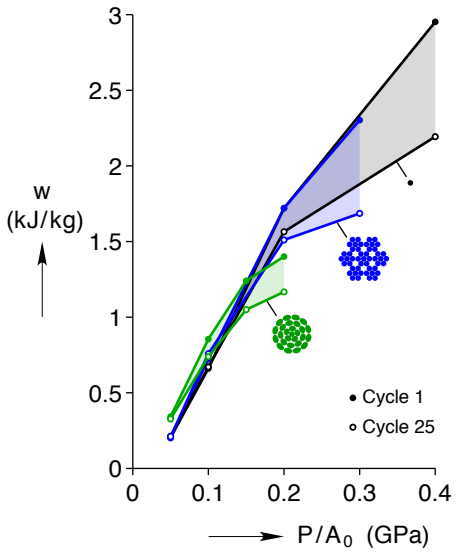

Figure 3.26: Specific work.

factor (c) that represents the increase in mass per length per wire, relative to the single straight wire. This factor was calculated by dividing the weight of a unit length of a cable by the number of wires and the weight of a unit length of a single straight wire. The values found for c are 1.1041 and 1.3578 for the 7×7 and 1×27 cables, respectively. This indicates that in a unit length, the 7×7 cable has 10.4% extra length of wire, and the 1×27 cable has 35.8% extra length of wire compared to a bundle of an equal number of straight wires to its respective cable.

The resulting specific work cross plotted against applied dead load, for cycle 1 and cycle 25 is shown in Figure 3.26. While previously it was shown that ε_s was non-monotonic with respect to the applied load, the general trend shown here is that there is a monotonic increase in specific work output when applying a larger dead load. This implies that even though there is a slight decrease in ε_s, it is less than the proportional increase in load, resulting in a net increase in specific work. This trend still holds even after considering the long-term shakedown behavior. At least up through 400 MPa, the material is able to output monotonically increasing work with increasing stress despite the additional plasticity in the material.

Interestingly, the 7×7 cable data line up very closely to the monofilament wire data, especially so for the cycle 1 data. There was a 10% decrease in the 7×7 cable's work output at 300 MPa on the cycle 25 relative to the interpolated work output of the monofilament wire. It is unclear as to what caused the additional shakedown. Two possibilities are: (1) the

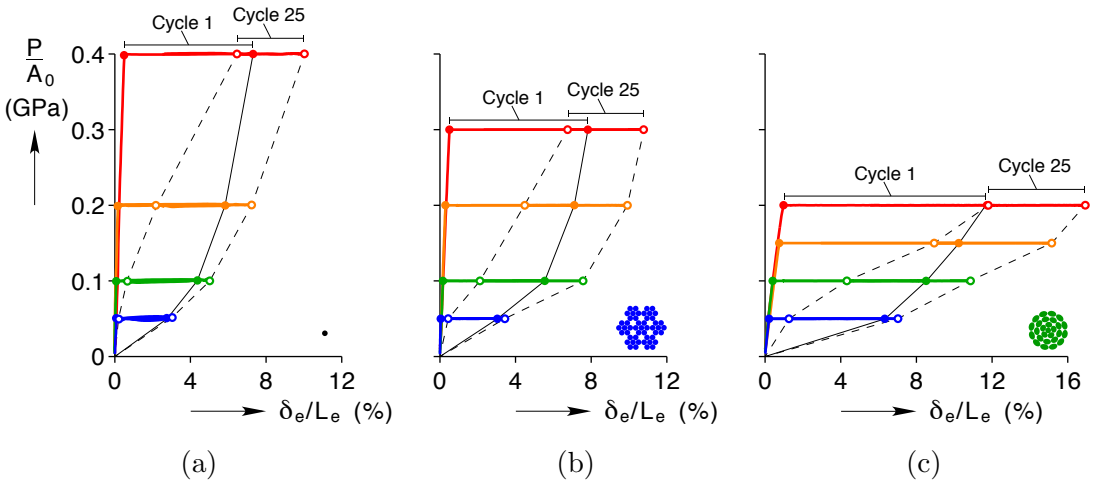

(a) (b) (c)

Figure 3.27: Normalized load-displacement during thermal actuation showing cycle 1 and 25 envelopes. (a) Straight wire, (b) 7×7 cable, (c) 1×27 cable.

center strand carries proportionally more load (because it is slightly stiffer than the outer strands) which should cause more shakedown of the center strand, (2) contact between the wires causes friction and stress concentrations that increase the shakedown. That being said, the additional shakedown is minor and negligible especially at 200 MPa and below. This leads the the conclusion that the 7×7 cable has effectively scaled up the monofilament wire's actuation response (to carry 49× the load) without a large negative impact to the work output of the actuator.

The 1×27 cable matches or slightly exceeds the monofilament wire up through 150MPa. At a low load of 50 MPa, the 1×27 cable is able to provide 60% more specific work than the monofilament wire or 7×7 cable. This is because the cable had double the ε_s at almost 6% strain compared to the monofilament wire or 7×7 cable, which both had less than 3% strain. Unsurprisingly, this cable's performance suffers at 200 MPa, dropping by 25% compared to the monofilament wire. This could have been anticipated based on the increased amount of shakedown seen at this load for the 1×27 cable. Clearly, it is advantageous to use this cable under smaller applied loads.

By plotting the stress-strain data on cycle 1 and 25 and tracing lines between the cycle start and end points, a summary of the thermal actuation envelopes can be made as shown in Figure 3.27. The dashed line encases the stress-strain space (an envelope) that each specimen resided in on cycle 25. This highlights the change in behavior in thermal actuation with increasing flexibility. The straight wire and 7×7 cable are more resilient to higher loads, while the 1×27 can output large transformation strains at nominal loads as low as 50 MPa.

3.4 Conclusions

The experimental study explored the actuation performance and behavior of straight monofilament wire, a 7×7 cable, and a 1×27 cable under dead load temperature cycling. Care was taken to match the straight wire and cables' material properties and allowed the subsequent study to focus on geometric differences between the specimen types. An experimental setup was presented that precisely controlled the load and temperature boundary conditions while measuring the axial strain response and reaction torque. Cycling the different specimens under dead load conditions revealed actuation performance and shakedown behavior.

The actuation behavior of the 7×7 cable was shown to closely match the straight monofilament wire. Similar to the straight wire, the 7×7 cable exhibited a distinct R-phase transformation, and an abrupt A to M transformation on cooling. This cable had a slightly larger transformation stroke and slightly more shakedown with cycling. It was concluded that the 7×7 cable effectively scaled up the performance of the monofilament wire because it was able to carry 49 times the load while maintaining an equivalent work output.

The 1×27 cable had different actuation behavior compared to the other two specimens. This cable had no visible R-phase transformation on cooling and exhibited a more gradual phase transformation spanning a large temperature range. The 1×27 cable had a larger actuation stroke, but also exhibited more shakedown and higher sensitivity to the applied load. The work performance was degraded at the higher loads, but at low loads was noticeably larger than the other two specimens.

Both cables offer a promising opportunity to scale up the thermal actuation of straight wire to much larger loads. This enables new compact and light weight actuators for use in aerospace or civil engineering disciplines where large forces are essential. Furthermore, they highlight the unique ability to tailor the response of the actuator to better optimize its performance to any given application, without having to modify the materials composition or processing.

CHAPTER 4

Path Dependent Shakedown of Shape Memory Wire

Understanding the long-term steady state behavior and degradation of NiTi as a thermal actuator plays a critical role in its end use for applications. In Chapter 3, the first cycle response along with the shakedown behavior of two cables and monofilament straight wire was measured to provide a complete characterization of these specimens. It has been well stated in literature (but cemented through this work) that the thermal actuation and even more so the degradation both strongly depend the applied load. However, it was newly discovered that the shakedown was much more nuanced than simply depending on the magnitude of the applied load. In fact, as it will be shown in this chapter, *how* and *when* the nominal load was applied has an even larger impact on the development of plasticity. The shakedown was found to be strongly path dependent, with the majority of plasticity occurring on heating (transforming from M→A). Furthermore, the amount of plasticity developing on heating is in turn dependent on the applied load on cooling. Both of these newly discovered material effects have considerable implication on both the end product use and the scientific understanding of transformation induced plasticity.

The understanding that the shape memory effect deteriorates with cycling has long been a concern and point of research in the SMA community [35]. However, most works have focused on the effect of bias stress during thermal cycling [9, 36, 45, 61]. The cause of this deterioration is known to be transformation induced plasticity with the formation and accumulation of dislocation loops [70]. There has been some effort with reasonable success to use cold working or heat treatments to stabilize the shape memory effect [57]. The main solution to provide long-term cyclic stability (which is utilized heavily in industry), however, is to strain limit the material [89]. This can extend the lifetime of an NiTi wire actuator to millions of cycles, but at a heavy cost of limiting the maximum strain to often under 2%.

Modeling and measuring the current degraded state has a large role in predicting the lifetime of any given wire. Measuring the resistivity, which can be correlated with the phase

fraction and residual locked in martensite, has been shown to have good potential in this regard [17, 18]. However, the majority of models are almost exclusively phenomenological (as is customary in general for plasticity), thus requiring additional experimental efforts to push forward our scientific understanding [38, 96, 60]. There have been a few insightful models that attempt to explain the cause of plasticity, one citing dislocation motion during transformation [71], and another referencing the austenite-martensite interface mismatch [69]. However, to date there has been no conclusive experimental evidence showing when and where the plasticity is developing.

Recent experimental work by Churchill showed an intriguing effect of running repeated *clockwise* versus *counter-clockwise* rectangular paths in stress-temperature space on NiTi wires [16]. Here it was shown that the clockwise cycles had worse degradation than the counter-clockwise counterpart. However, the results were inconclusive due to two issues: (1) each experiment had largely different maximum temperatures, and later experiments showed that the maximum temperature of each thermal cycle is also a dominant effect in promoting plasticity, and (2) the wire specimens were pre-conditioned (i.e. trained through numerous thermal cycles) and further cycling was also shown to potentially decrease the macroscopic strain if the wire was then cycled under a lower load than it was conditioned at. Both of these effects are large enough to explain the difference in shakedown experienced between the clockwise and counter-clockwise experiments.

As an interesting anecdote, while running a thermal cycling experiment on a 7×7 cable, a surprising discovery was made. During the first cycle after cooling to 5°C under 300 MPa dead load, the torque cell reading was found shorted with ground and had no measurable voltage. The experiment had to be scrapped, but just to see what would happen the cable was unloaded before heating back up to to 140°C. Remarkably, the cable fully recovered its deformation! On a typical dead load experiment where the load was instead maintained through heating, the cable would have had an unrecovered strain of over 2%. The experimental study that is presented in this chapter began with this experiment, with the new goal of explaining why all of the plasticity was prevented by unloading before heating. For simplicity, all of the following experiments were conducted on straight wire so that the complex mechanics of cables did not influence the nuanced plasticity results.

4.1 Materials and Experimental Setup

Two experimental setups were used in here in studying the shakedown of straight wire. The majority of experiments presented here were conducted by the author on the same experimental setup shown previously in Chapter 3, and using the same NiTi wire as the NiTi cables. Specifically, Fort Wayne Metals designated NiTi #6 with an austenite finish temperature above 50°C such that it is martensite at room temperature. The exception is the set of experiments studying the influence of maximum temperature (Section 4.3). These experiments were conducted by Chris Churchill on an experimental setup utilizing thermoelectric plates, and with a slightly higher temperature NiTi alloy wire (equiatomic NiTi with 90°C austenite finish temperature). These additional experiments measuring the influence of maximum cycle temperature were included because they are previously unpublished and complement the rest of the chapter nicely.

The primary experimental setup used in this study (as described previously, but reproduced here for clarity) is shown in Figure 4.1. The temperature control setup consisted of an aluminum block which had embedded cartridge heaters for active heating and embedded channels that chilled silicone oil (-20°C) was pumped through for active cooling. Both the active heating and cooling systems were controlled using an Arduino microcontroller. The wire specimen was held clamped with ER collets in a MTS servohydraulic load frame and had two laser tags attached to thin metal tabs for rigidity that were epoxied onto the wire to measure the local displacements using a laser extensometer. The aluminum block was positioned using a micrometer stage as close as possible without touching the wire specimen, and afterwards Omegatherm 201 thermal paste was used to provide good thermal contact between the wire and the aluminum block. The aluminum block's thermal field was verified to be uniform (to less than ±1°C), and a K-type thermocouple was used to measure the temperature and provide a signal for PID control with the Arduino. A MTS 500 N load cell was used to measure the nominal load and for load control.

The experimental setup used in the influence of maximum temperature experiments is shown in Figure 4.2. The temperature control setup here made use of thermoelectric plates and controllers to force heat and cool wire specimen. A relatively massive aluminum block was used as a heat sink for the thermoelectric plates to draw and push heat from. A thin copper plate placed on the surface of the thermoelectric plates to create a uniform distribution of temperature. A laser extensometer was similarly used for a non-contact local displacement measurement of the NiTi wire samples.

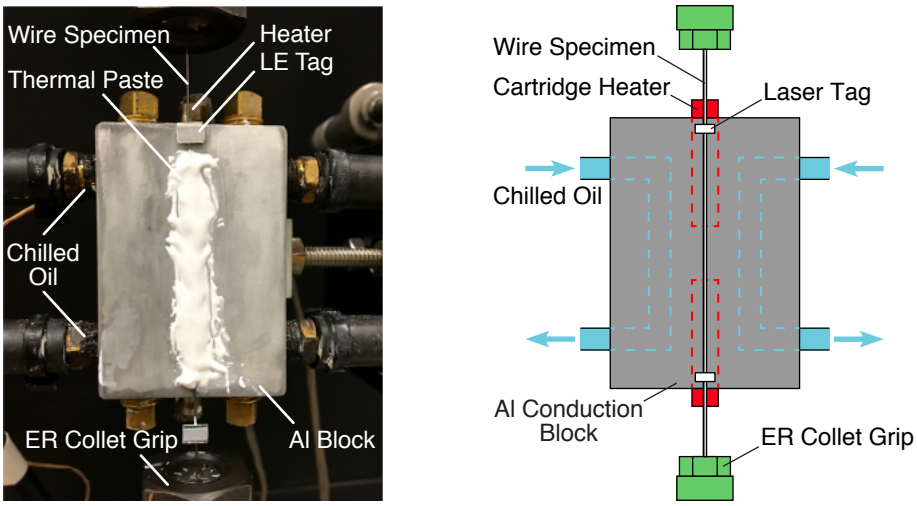

(a) Photograph (front view) (b) Schematic

Figure 4.1: Experimental setup for temperature-controlled mechanical testing of an SMA wire specimen, used in majority of experiments.

Nomenclature and the specimen schematic are explained in Figure 4.3a. During the experiments, the specimens were held in clamped-clamped grips with initial free length L with an applied axial load P, causing a grip displacement δ. To avoid grip slippage and stress concentration effects, local displacements δ_e measured outside of grip effects at a gage length L_e along with the specimens' temperature T. A typical experiment's measurement history for the first three cycles is shown in Figure 4.3b. An experiment began at 140°C and with a close to stress free load (to be exact, a 10 MPa end load was used to keep the wire straight). For the dead load experiments, the load was then increased to its prescribed value over 30 seconds and held fixed in load control for the remainder of the thermal cyclic experiments. After the load reached its prescribed value, the temperature began ramping down at 12°C/min down to 5°C. At this point the temperature ramp was reversed, and now increased at 12°C/min back towards 140° to complete one thermal cycle. The nominal strain response was recorded throughout the cycling and showed a forward transformation and reverse transformations with corresponding increase and decrease in strain.

To characterize the shakedown behavior of NiTi wire the path independent parameters that affect the thermal actuation behavior, namely the applied load and maximum temperature, will first be presented. The dependence on the applied load has been well stated in literature, but the effect of maximum temperature is new information. Further, the experiments showing the dependence of the applied load have been presented in Chapter 3 for comparison with actuator cables, but are repeated here to serve as a basis for comparison with the more complex path dependent shakedown phenomena.

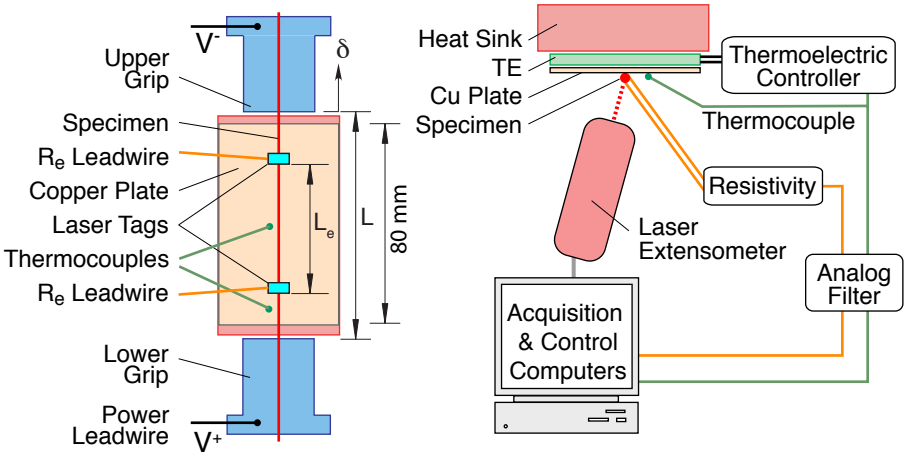

Figure 4.2: Experimental setup used in the influence of maximum temperature set of experiments.

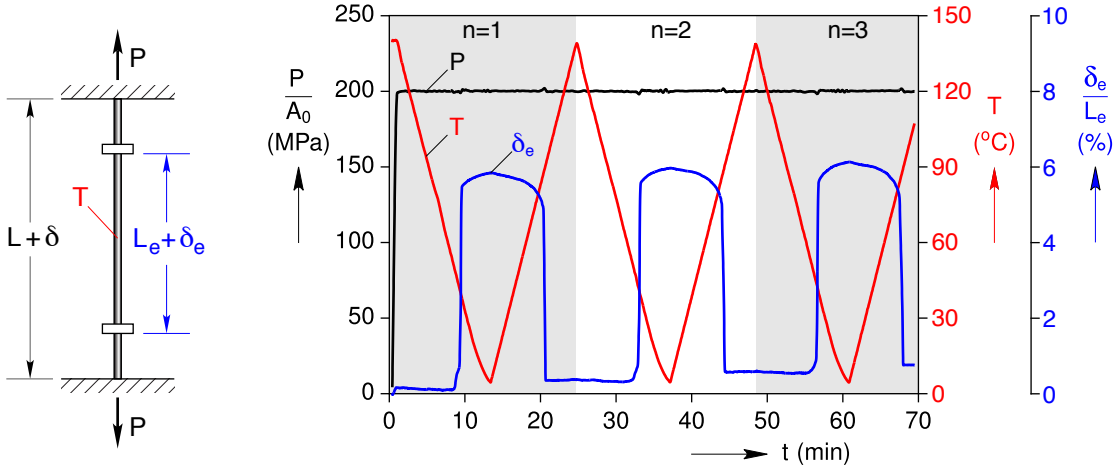

(a) Specimen (b) Measurement histories

Figure 4.3: Specimen schematic and example time history showing temperature and load control data with normalized displacement response data.

4.2 Influence of Nominal Load

Typically, an NiTi actuator requires a bias load to enable a strain increase with its forward transformation to martensite. This can be accomplished by a dead load (such as hanging a weight) or a bias spring. A dead load is the simplest case because it does not couple the load and displacement like a bias spring would, and is considered here.

The mechanical responses for four experiments with four different load values (50, 100, 200, and 400 MPa), each with a new as-received specimen, are shown in Figure 4.4, with cycle 1 and 25 summarized in Figure 4.5. Clearly, increasing the applied load increases the maximum strain in martensite at 5°C, but also increases the amount of strain ratcheting and narrowing of hysteresis with cycling. For this alloy there is also a distinct R-phase transformation around 40°C for the 50, 100, and 200 MPa experiments. By the 25th cycle this R-phase knee disappeared for all but the 50 MPa case.

It is useful to quantify two specific values from the mechanical responses to use as a comparison across experiments and cycle number. Shown in Figure 4.5a, the *actuation stroke* (ε_s) is the difference between the maximum strain in martensite and the strain at the end of the cycle in austenite. The *residual strain* (ε_r) is the accumulated and unrecovered strain in austenite, with the elastic strain (as measured on the first cycle) subtracted.

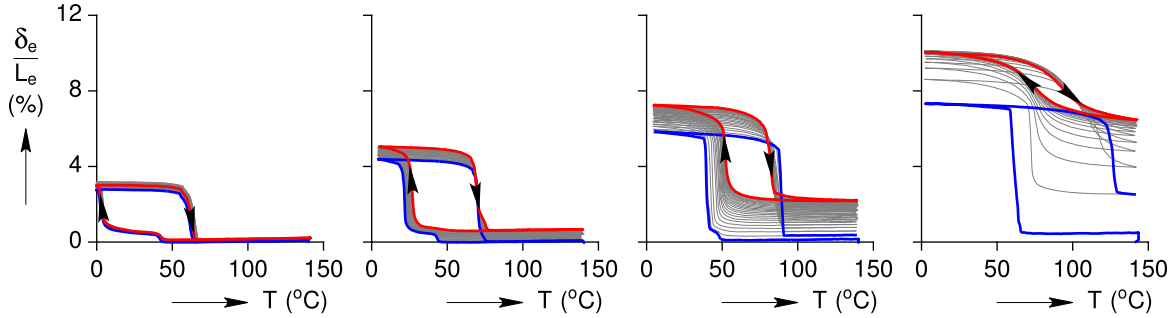

(a) 50 MPa (b) 100 MPa (c) 200 MPa (d) 400 MPa

Figure 4.4: Straight wire actuation data under dead load.

Figure 4.6 shows ε_s and ε_r for the four dead load experiments. The ε_r increases monotonically and has a strong dependence on the applied load. However, ε_s is shown to be non-monotonic with a maximum at approximately 200 MPa. At lower loads there is lower transformation strain because there is only sufficient driving force to transform favorably oriented grains in the loading axis direction. At higher loads the majority of grains are transforming in the loading axis direction, but damage begins accumulating quickly causing a loss of stroke. Thus, the optimum is understood to be caused by a competition between

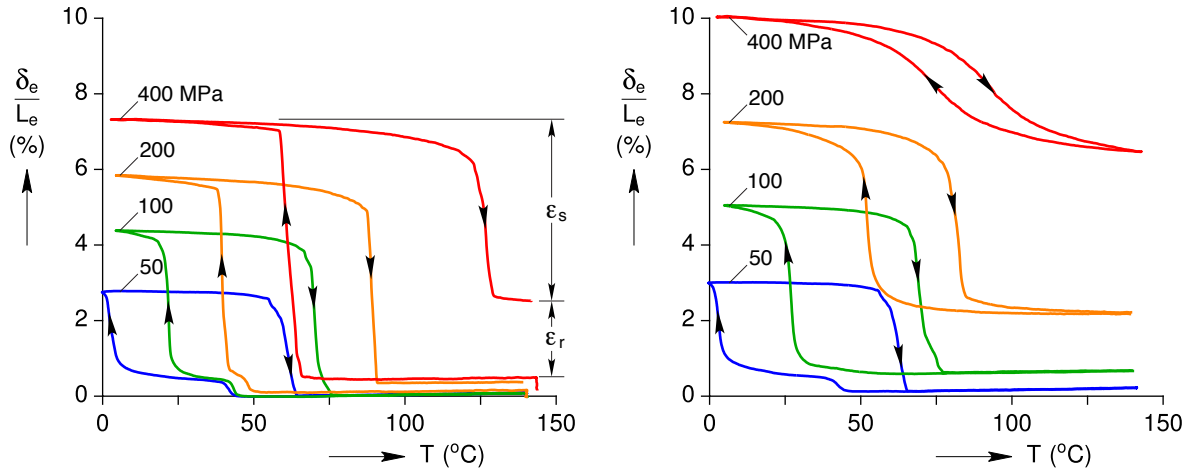

(a) Cycle 1 (b) Cycle 25

Figure 4.5: Comparison of actuation responses under different dead loads.

these two effects.

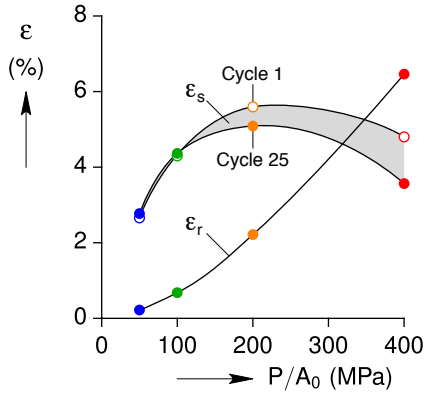

Figure 4.6: Residual strain and stroke dependence on applied load.

The difference in ε_s between cycle 1 and cycle 25 (or the loss of stroke) is larger for higher loads, and appears to be directly proportional to the increase in ε_{r}. While this relationship is intuitive, it is an important point because it will be shown for the maximum temperature experiments in the following section that the inverse relationship is also possible.

A two term exponential of the form

$$\varepsilon_{\mathrm{r}}(n) = \sum_{i=1}^{2} \varepsilon_i^{\infty}(1 - \mathrm{e}^{-n/\tau_i}) \tag{4.1}$$

can be used to fit the ε_{r} data well, as shown in Figure 4.7. This fit uses two fit parameters per exponential term: the asymptotic residual strain (ε_∞), and the time constant in cycles

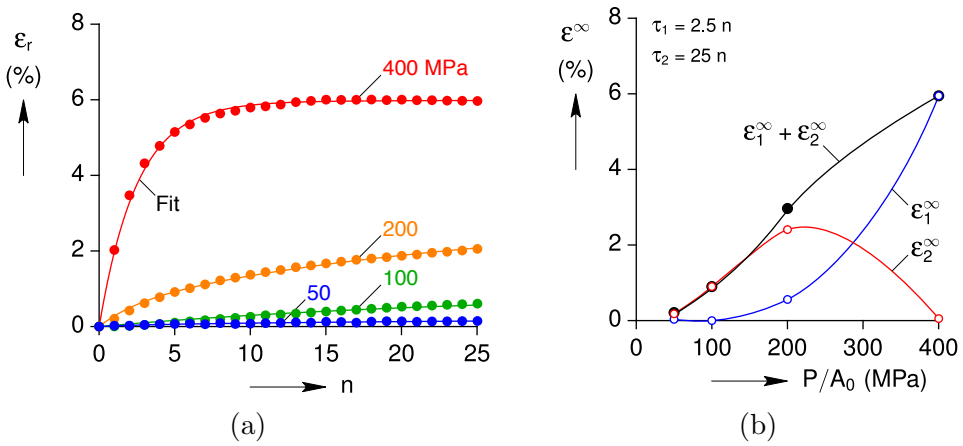

Figure 4.7: Residual strain data fit with two term exponential series. (a) Data with fit. (b) Asymptotic strain fit parameters.

(τ). For all four experiments, the same τ_1 and τ_2 values of 2.5 n and 25 n (respectively) were used to fit the ε_r data. This fit, in essence, decomposes the ε_r shakedown data into different time regimes allowing for additional insight into the degradation.

The sum $\varepsilon_1^\infty + \varepsilon_2^\infty$ increases monotonically with applied load, as expected. Interestingly, the fits for the lower load experiments are comprised primarily of ε_2^∞ which is associated with the longer time constant. In contrast with the other experiments, the 400 MPa case experiences much faster shakedown, with its fit comprised of almost entirely the ε_1^∞ component. A larger P/A_0 not only increases the degradation, but increases the rate at which it degrades to its steady state value. This conclusion is intuitive because there is additional driving force for plasticity when there is a higher load, and the material is building up a dislocation network faster with higher load.

4.3 Influence of Maximum Temperature

This second set of experiments shows the strain response's dependence on the maximum temperature of each thermal cycle. As it was stated previously, these experiments were conducted by Chris Churchill using a slightly higher temperature NiTi alloy produced by Dynalloy (0.015in wire diameter, 90°C austenite finish temperature) and on a slightly different experimental setup which utilized thermoelectric plates for forced heating and cooling (Fig. 4.2). This set of experiments are included here because it complements the rest of the wire shakedown data nicely by showing the additional dependence to maximum cycle temperature. In a typical test or application found in literature, the maximum temperature

is held constant or allowed to be sufficiently high to saturate transformation. This novel set of experiments shows that in fact the shakedown strongly depends on the maximum temperature a specimen is taken to each cycle, and it cannot be neglected.

Seven NiTi wire specimens were cycled 150 times under constant 20N load (175.4 MPa) to different maximum temperatures (136, 145, 153, 163, 174, 181, and 197°C), as shown in Figure 4.8. The mechanical behavior for the 1^{st} and 150^{th} cycles are shown in Figure 4.9a. On the 1^{st} cycle the different cases exhibit the same strain response, but by the 150^{th} cycle the amount of shakedown is largely different. The specimen that was taken to the highest temperature exhibits the largest amount strain ratcheting. Surprisingly, the hysteresis of the lowest temperature experiment is apparently smallest, even though it has the smallest amount of strain ratcheting. This is contrary to what occurred when comparing different applied loads, where the specimen with the highest damage had the smallest hysteresis.

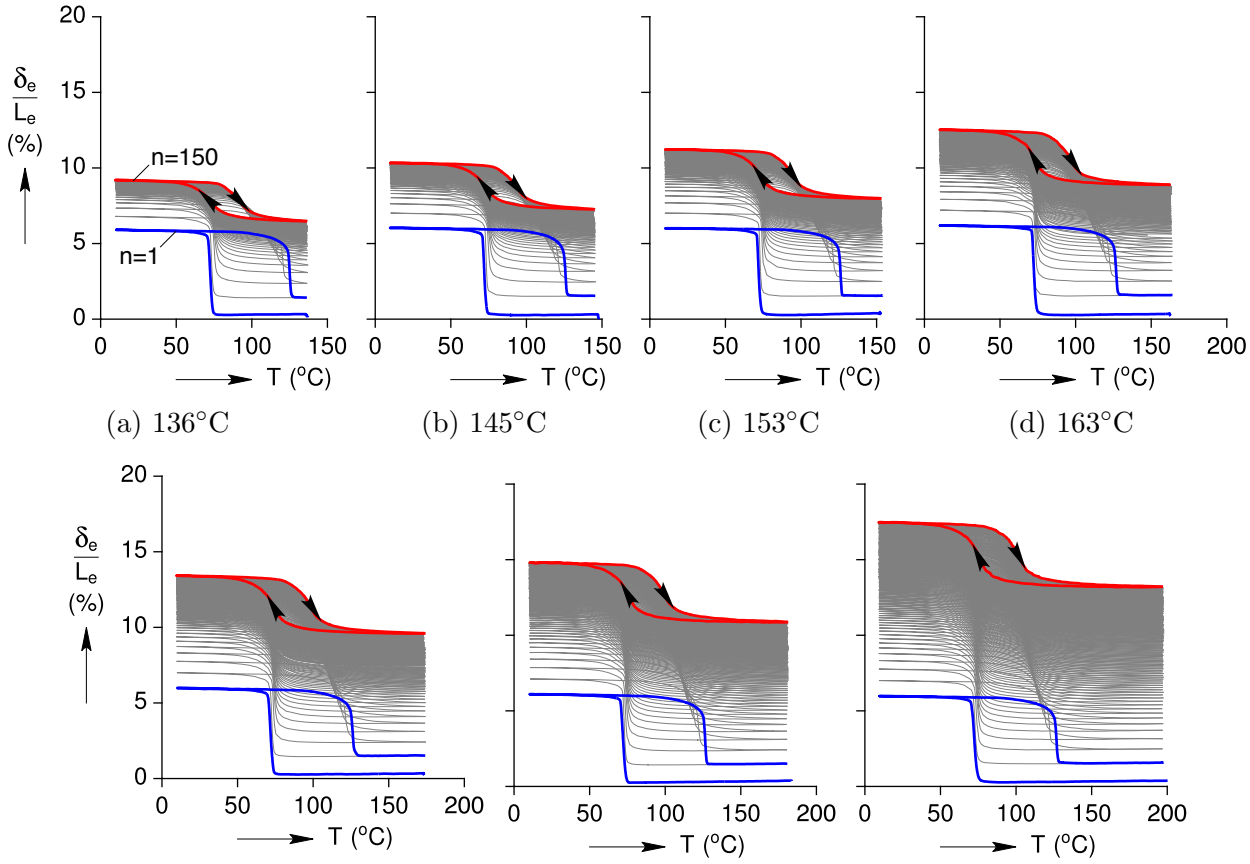

Figure 4.8: Actuation responses at $P/A_0 = 175$ MPa for 150 cycles (each), varying maximum temperature ($T_{\max}$)

Figure 4.9b highlights the effect of maximum temperature on ε_r and ε_s. Specimens

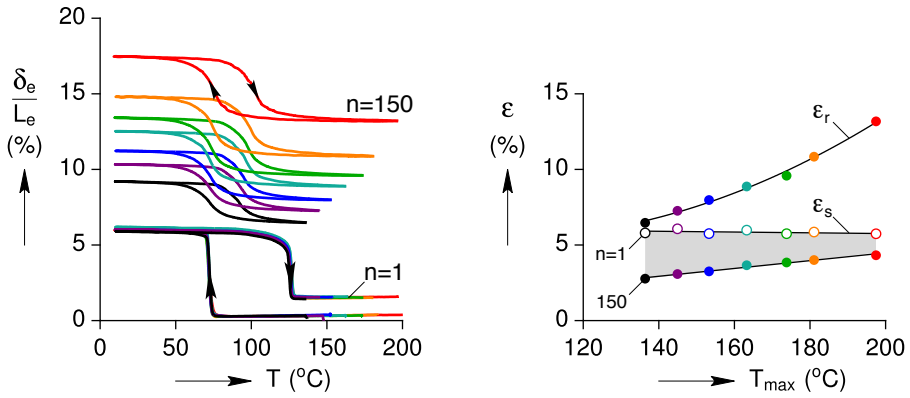

(a) (b)

Figure 4.9: Summary of additional shakedown at $P/A_0 = 175$ MPa caused by cycling specimens to progressively higher temperatures ($T_{\max}$).

that were taken to higher maximum temperatures are shown to have increased ε_{r} indicating greater degredation. On cycle 1, ε_s is again roughly constant, as would be expected, but by cycle 150 the stroke is apparently larger for the higher temperature cases. Finally, ε_s decreases the most for the low temperature 136°C experiment but the least for the 197°C experiment.

This data appears to indicate that taking a NiTi wire to a higher temperature (under load) forces the last few percent of residual martensite to reverse transform into austenite, but in doing so increases the degradation. This can be explained by considering how poorly oriented grains would respond to cycling. As residual stresses develop from a built up dislocation network, certain poorly oriented grains would require an increasingly large driving force (higher temperature) to transform back to austenite. However, when these grains now transform they are doing so under an elevated local stress state which causes additional damage and plasticity. Thus, taking a NiTi wire specimen significantly past the bulk transformation temperature would greatly increase the accumulated damage and reduce the life of an actuator.

These shakedown ε_{r} data can be fit well by a three term exponential series,

$$\varepsilon_{\mathrm{r}}(n) = \sum_{i=1}^{3} \varepsilon_i^{\infty}(1 - \mathrm{e}^{-n/\tau_i}) \tag{4.2}$$

with three asymptotic strain parameters $(\varepsilon_1^{\infty}, \varepsilon_2^{\infty}, \varepsilon_3^{\infty})$ that are allowed to vary to fit each experiment, and three time constant parameters (τ_1, τ_2, τ_3) that were set to be constant for all experiments. The fit and fit parameters are shown in Figure 4.10. The first exponential

term's ε_1^∞ is relatively constant with respect to T_{max}, ranging from 4.25 to 3.74. The second and even more so the third exponential terms' ε_∞ parameters have a strong dependence on T_{max}, with ε_2^∞ ranging from 1.86 to 4.59, and ε_3^∞ ranging from 0.74 to 10.70. It appears that the first exponential term is roughly responsible for the shakedown occurring from the transformation of the bulk of the material, while the second and third terms account for additional shakedown due to taking each specimen to elevated temperatures past the bulk transformation.

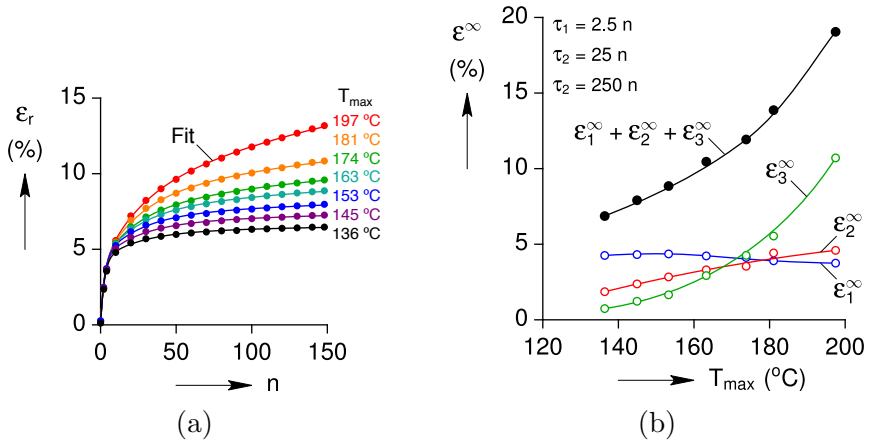

Figure 4.10: Residual strain data fit with two term exponential series. (a) Data with fit. (b) Asymptotic strain fit parameters. (c) Time constant fit parameters.

The T_{max} dependence has the opposite trend between quantity and rate of degradation to what was seen when varying P/A_0 in Section 4.2. Here, increasing T_{max} increases the steady state ε_r value, but also increases the number of cycles it takes to reach that long term value. The data suggest that this is due to the additional transformation that occurs when the temperature is increased. As the material is cycled, poorly oriented grains' transformation temperatures are pushed higher due to residual stresses, and if T_{max} is kept lower, these grains no longer contribute to the material's transformation. When T_{max} is pushed higher, the poorly oriented grains keep transforming (at higher and higher temperatures), promoting more plasticity and elongating the time to reach a steady state ε_r.

4.4 Path Dependence

The previous sections showed how the shakedown of a NiTi wire strongly depends on the applied load and the maximum temperature. This section now explores effects of varying the stress-temperature path or history while maintaining constant temperature and load limits, namely 140°C maximum temperature and 300 MPa maximum stress. Furthermore,

each cycle is prescribed to begin and end at the same reference point of 140°C and 10 MPa (which is approximately zero, but required to hold the wire in tension). It will be shown that even when holding the applied load and maximum temperature fixed, a wide range of shakedown behavior can be witnessed by varying the path in stress-temperature space.

4.4.1 Dead Load with Intermittent Unloading

The first experiment is the dead load with unloading experiment, which serves as a baseline to compare subsequent experiments. It is very similar to the previous path independent experiments, but has an additional unloading after every cycle to return to the reference point of 140°C and 10 MPa.

Figure 4.11c shows the stress-temperature path that the specimen was subjected to (note that this figure shows actual experimental data and is not a schematic). The dead load experiment begins at reference ⓪ (140°C and 10 MPa) and is loaded isothermally to ① (140°C and 300 MPa). Holding the load constant, the specimen is cooled to ② (5°C and 300 MPa), after which it is heated back to ③ (140°C and 300 MPa). Finally, the specimen is unloaded isothermally to ④, completing one cycle. This routine was completed 25 times per experiment.

The data from this experiment are shown in Figures 4.11b-d. On the first cycle, the specimen exhibited very abrupt transformations on cooling and heating, has a fairly large amount of transformation strain (approx. 6%) in martensite, and has a noticeable amount of residual strain after a single cycle. The specimen apparently had further reverse transformation on unloading from ③ to ④, which is apparent from the beginning of the second cycle in Figure 4.11b and Figure 4.11d where the strain at the start of the second cycle is smaller than at the end of the first.

On the 25^{th} cycle, the forward and reverse transformations have smoothed out significantly, indicating built up plasticity and residual stresses, there is a large reduction in the hysteresis in the transformation temperatures with a shift towards higher temperatures, and there is no visible open loop strain at the end of the cycle. The final residual strain totaled 4.37%.

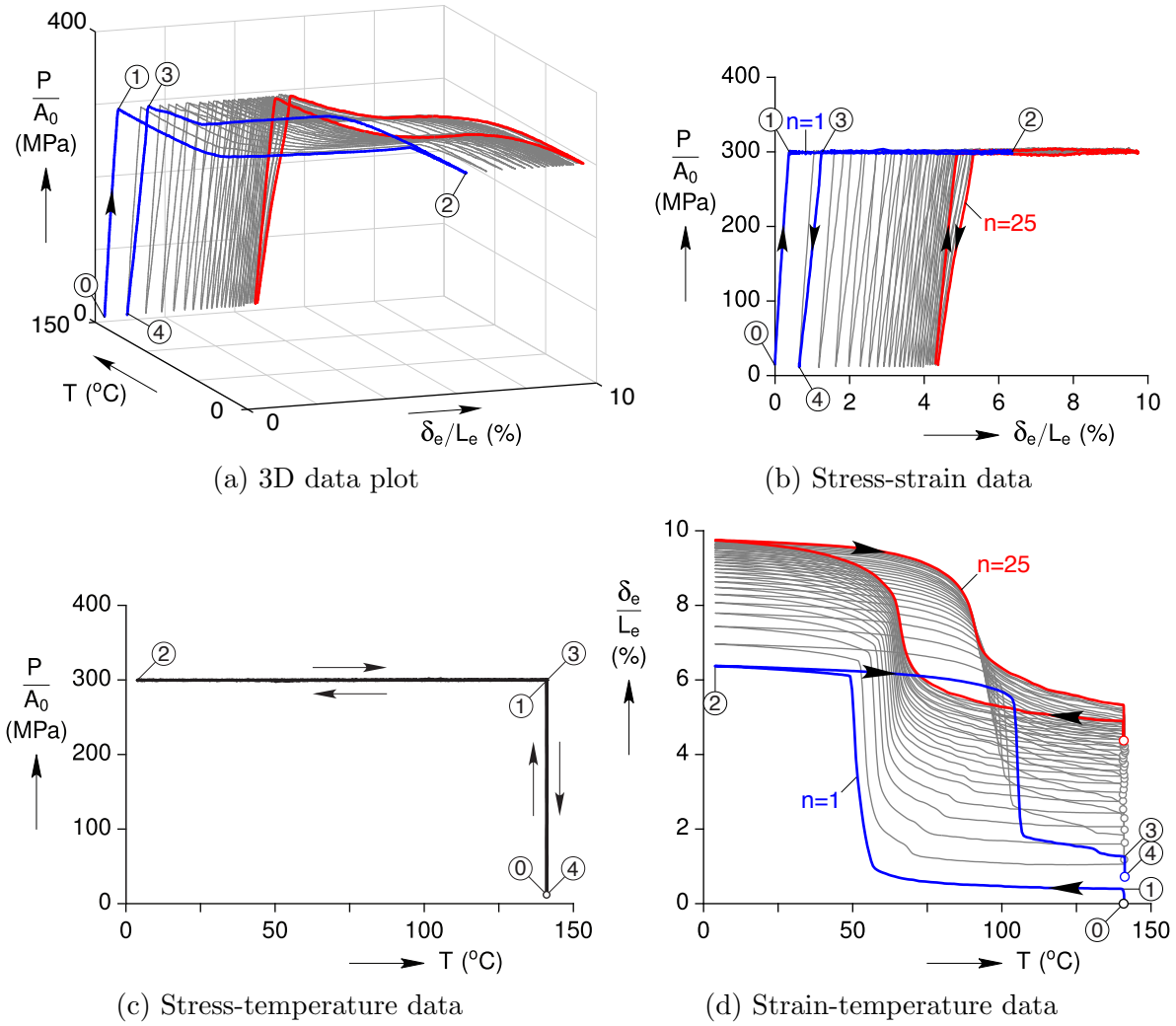

(a) 3D data plot

(b) Stress-strain data

(c) Stress-temperature data

(d) Strain-temperature data

Figure 4.11: Dead load experiment with intermittent unloading.

4.4.2 Clockwise Cycling

The second experiment is called the clockwise experiment because of the clockwise manner in which a box in stress-temperature space is traversed. The main distinction for this experiment is that each cycle the specimen is first cooled under a very small load and then is heated under a relatively high load.

The stress-temperature path for the clockwise experiment is shown in Figure 4.12c. The experiment begins again at the reference ⓪ (140°C and 10 MPa), but is now immediately cooled to ① (5°C and 10 MPa) while holding the initial load constant. The specimen is then isothermally loaded to ② while cold (5 °C and 300 MPa), before heated under constant load to ③ (140 °C and 300 MPa). The cycle is finished by unloading the specimen isothermally

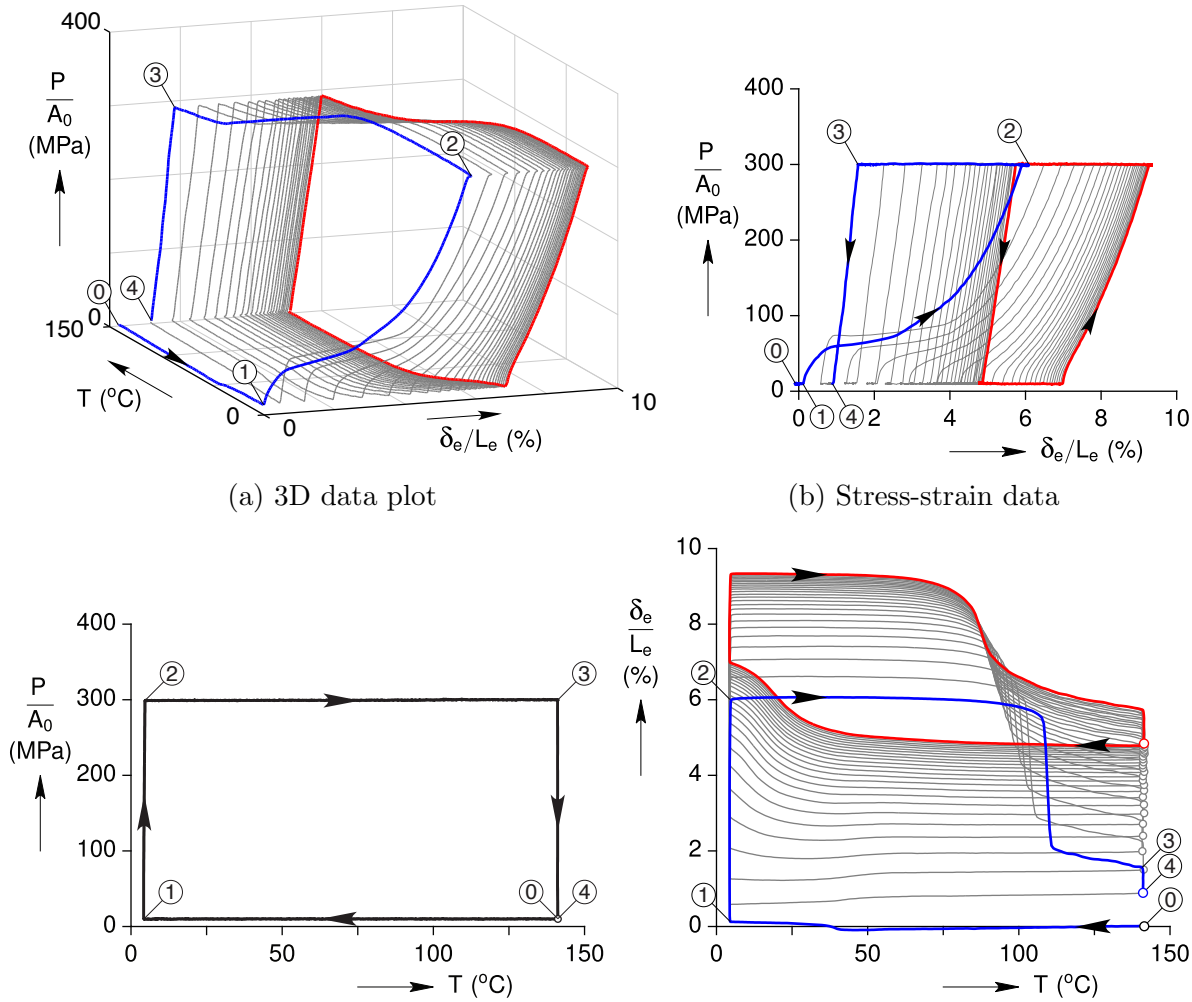

(a) 3D data plot

(b) Stress-strain data

(c) Stress-temperature data

(d) Strain-temperature data

Figure 4.12: Clockwise experiment.

to ④ (140°C and 10 MPa).

The data from this experiment are shown in Figures 4.12b-d. On cooling from ⓪ to ①, there is only a slight R-phase knee around 40°C on the first cycle, which progresses into a large two-way shape memory effect by the 25^{th} cycle. From ① to ② also shows an interesting progression of isothermal deformation and detwinning of martensite. On the first cycle this segment shows a large amount of strain increase from detwinning, but on the 25^{th} cycle as the two-way effect builds up the amount of detwinning correspondingly decreases.

There is what appears to be a significant hysteresis in the transformation temperatures between heating and cooling, but this is exaggerated by the fact that the specimen is heated and cooled under very different loads. The heating portion of each cycle proceeds as expected, with a smoothing out of what is originally an abrupt transformation, and a slight decrease

in transformation temperature. The open loop strain, which is substantial on cycle one, is again completely closed by cycle 25. The accumulated residual strain is 4.84%, surprisingly larger than the dead load with unloading experiment.

4.4.3 Counter-Clockwise Cycling

The counterclockwise experiment is in theory very similar to the clockwise experiment. Both experiments map out precisely the same box in stress-temperature space and have the same reference start and end point. However, the counterclockwise experiment progresses in reverse order compared to the clockwise experiment. Specifically for this experiment, the specimen was cooled under a considerably high load and then heated under a very small load. The results as shown here are remarkably different.

Figure 4.13c shows the stress-temperature path for the counterclockwise experiment. Again starting at reference ⓪ (140°C and 10 MPa), the specimen is first loaded isothermally to ① (140°C and 300 MPa). Second, the specimen is cooled under constant load to ② (5°C and 300 MPa). Up through this point the experiment routine is identical to the dead load with unloading experiment, but here the counterclockwise experiment is unloaded isothermally to ③ (5°C and 10 MPa). Finally, the specimen is heated under constant load to ④ (140 °C and 10 MPa) to finish the cycle.

The data for the counterclockwise experiment are summarized in Figures 4.13b-d. The data clearly show that there is very little shakedown and evolution of transformation behavior when the specimen is cycled this way. Similar to the dead load cycle, the specimen transforms to a relatively large strain in martensite of greater than 6%, but by being unloaded before heating, is able to completely recover the strain even on cycle 1. In fact, there is only a slow increase in residual strain with cycling, and it totals a very small 0.89% after cycle 25.

The hysteresis appears unusually small in this experiment, but that is again because the specimen is heated and cooled under very different loads, which makes interpreting the hysteresis less intuitive. The transformation temperature on cooling shifts up around 10°C, while the transformation temperature on heating has very little change. The transformations are also still relatively abrupt on cycle 25.

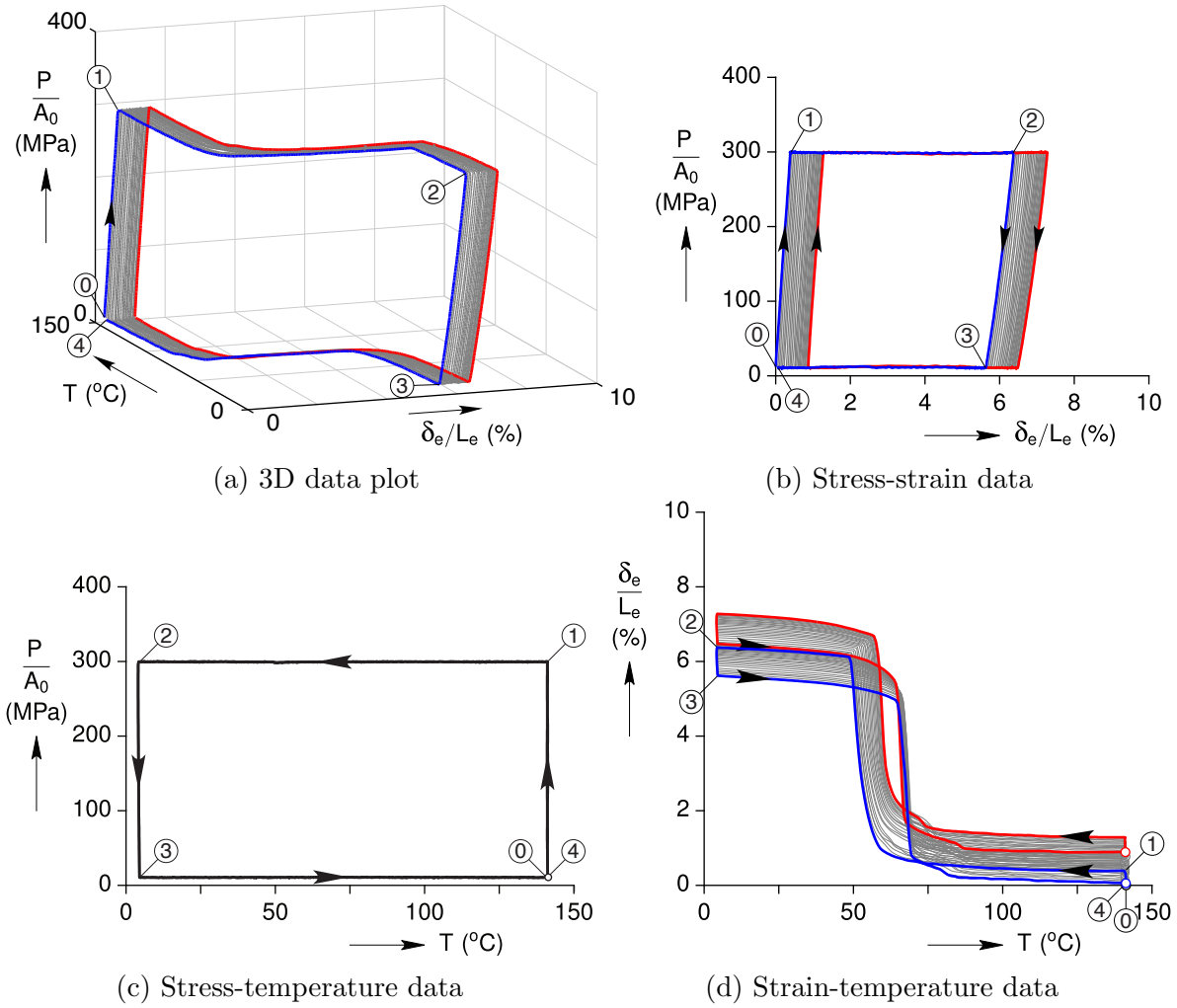

(a) 3D data plot

(b) Stress-strain data

(c) Stress-temperature data

(d) Strain-temperature data

Figure 4.13: Counterclockwise experiment.

The strain-temperature responses of the path dependent experiments are summarized for comparison in Figure 4.14, and the residual strain is shown in Figure 4.15. There is one additional experiment shown here that was not previously mentioned, called the stress free experiment. In this experiment the load was held fixed at 10 MPa for the entirety of the 25 thermal cycles, which resulted in negligible change in macroscopic strain. This experiment was conducted to show that there is no strain evolution in the absence of load, meaning that the material's transformation is macroscopically stable to thermal cycles.

These four experiments were devised to explore the path dependence of shakedown. The start point, end point, and limits in stress-temperature space were held fixed, while different paths were traversed. Previous results showed that the maximum temperature and applied load strongly influence the shakedown behavior. However, this set of experiments shows that even when holding the maximum temperature and maximum applied load fixed, by altering

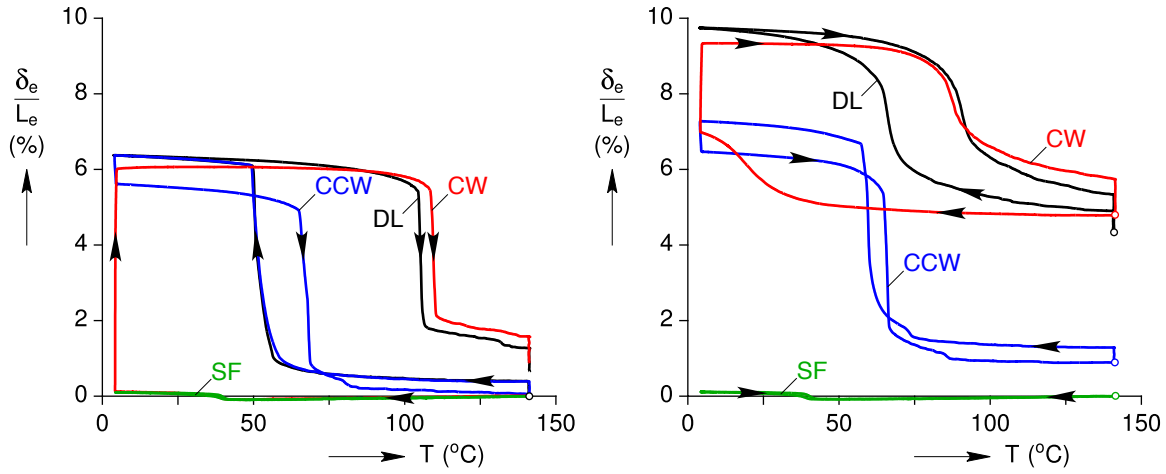

(a) Cycle 1 (b) Cycle 25

Figure 4.14: Comparison of path dependent experiments.

the temperature and load histories very different shakedown behavior can be observed.

The primary result regarding shakedown is that the damage (plasticity and built up dislocation networks) is forming while heating up the material. This is evident when comparing the clockwise to counterclockwise experiments. In the counterclockwise case, the specimen was heated under little stress, and resulted in little strain ratcheting and shakedown. The clockwise case, however, was heated under a large stress and resulted in significant strain ratcheting and shakedown. This is also evident when comparing the counterclockwise and dead load experiments. Through the first half of the first cycle of each experiment, the strain response is identical until the counterclockwise experiment is unloaded isothermally at 5°C. When both specimens are subsequently heated to 140°C, the counterclockwise experiment fully recovers the transformation strain while the dead load experiment has an open loop strain of 0.65%. These data indicate that the transformation induced plasticity is occurring on heating when the material is reverse transforming from the low symmetry martensite phase into the high symmetry austenite phase.

It is interesting to note that in the clockwise experiment over one cycle the work exerted by the specimen is positive, in the counterclockwise experiment the work is negative, and the dead load experiment the work is slightly negative but close to zero. While some plasticity occurring when heating under load is unavoidable for an actuator which needs to perform positive work on its environment, it may be possible to harness this new finding to reduce the level of degradation. Nevertheless, it is an important insight into the damage mechanics at the material level.

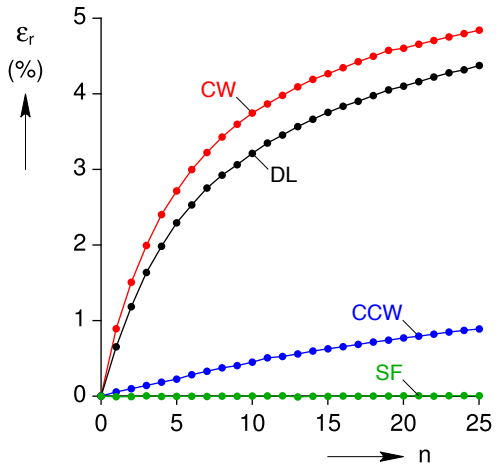

(a)

Experiment	ε_r (%)
Clockwise	4.84
Dead load	4.37
Counterclockwise	0.89
Stress free	0.01

(b)

Figure 4.15: Comparison of residual strain. (a) Residual strain growth with cycling. (b) Final residual strain on Cycle 25.

The additional damage seen in the clockwise experiment relative to the dead load experiment is also very peculiar. The dead load specimen is under high stress for both cooling and heating, while the clockwise experiment is only under high stress on heating, but low stress on cooling. Even though the clockwise experiment is under high stress for half of the time the dead load experiment is, it accumulates more residual strain! Furthermore, the clockwise experiment has lower transformation strain in martensite, which further confounds the interpretation. The tangent slope in strain-temperature space is negative on heating before the bulk transformation for the dead load experiment, but close to zero (and slightly positive) for the clockwise experiment. This indicates that the dead load experiment has some grains that begin reverse transforming much earlier than the bulk transformation, but the clockwise experiment apparently only exhibits thermal expansion before the bulk reverse transformation.

Lastly, the reverse transformation temperature of the clockwise experiment is higher by approximately 4.3°C than the dead load experiment, even though they are heated under the same 300 MPa load. This indicates that there is an additional energy barrier delaying the onset of the reverse transformation in the clockwise experiment. Clearly, two experiments are insufficient to adequately explain all of these phenomena. The goal of the following section is to present a sweep of experiments to explore these differences between the clockwise and dead load experiments.

4.4.4 Clockwise Cycling with Varying Cooling Stress

The final set of experiments explores the differences between the clockwise and dead load experiments by systematically varying the applied load on cooling (σ_{cool}) from 10 MPa to 400 MPa (with a different σ_{cool} and fresh specimen for each experiment). As before, in each experiment the specimen was heated to 140°C under 300 MPa load, and unloaded to 10 MPa after each cycle. The data from the stress-temperature paths are shown in Figure 4.16. The red and black curves with corresponding $\sigma_{\text{cool}} = 10$ and 300 MPa are the clockwise and dead load experiments presented in the previous section. By filling in the multiple experiments between these cases (and supplying an additional 400 MPa experiment), the degradation is shown to be smooth and non-monotonic with σ_{cool}. Microstructural effects are then considered in a discussion pertaining to the cause of this newly discovered phenomenon.

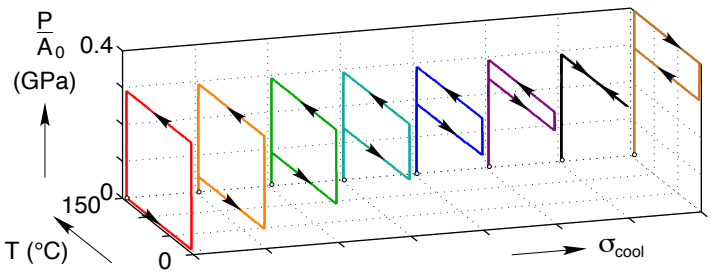

Figure 4.16: Prescribed stress-temperature path data from experiments with varying σ_{cool}.

The strain response results for this sweep of experiments showing all 25 cycles for each experiment can be seen in in Figure 4.17. From these data, there are several progressions of mechanical behavior visible as σ_{cool} is varied. Most notably, the hysteresis is very large when $\sigma_{\text{cool}} = 10$ MPa, but decreases substantially when $\sigma_{\text{cool}} = 400$ MPa. There are several other effects, such as shift in R-phase, transition temperatures, transformation strains, and residual strain, all of which will be shown with more clarity subsequently.

The cycle 1 and cycle 25 data are shown in Figure 4.18 for comparison. As σ_{cool} is increased, there is an increase in transformation strain in martensite, and an increase in forward transformation temperature. There is also a distinct R-phase transformation that appears around $\sigma_{\text{cool}} = 50$ MPa, but is only faintly visible by 200 MPa. On heating, the reverse transformation has a surprisingly large variance in recovered strain and reverse transformation temperatures, even though all specimens were under 300 MPa on heating. Similar trends can be seen on cycle 25, including a variety of residual strains.

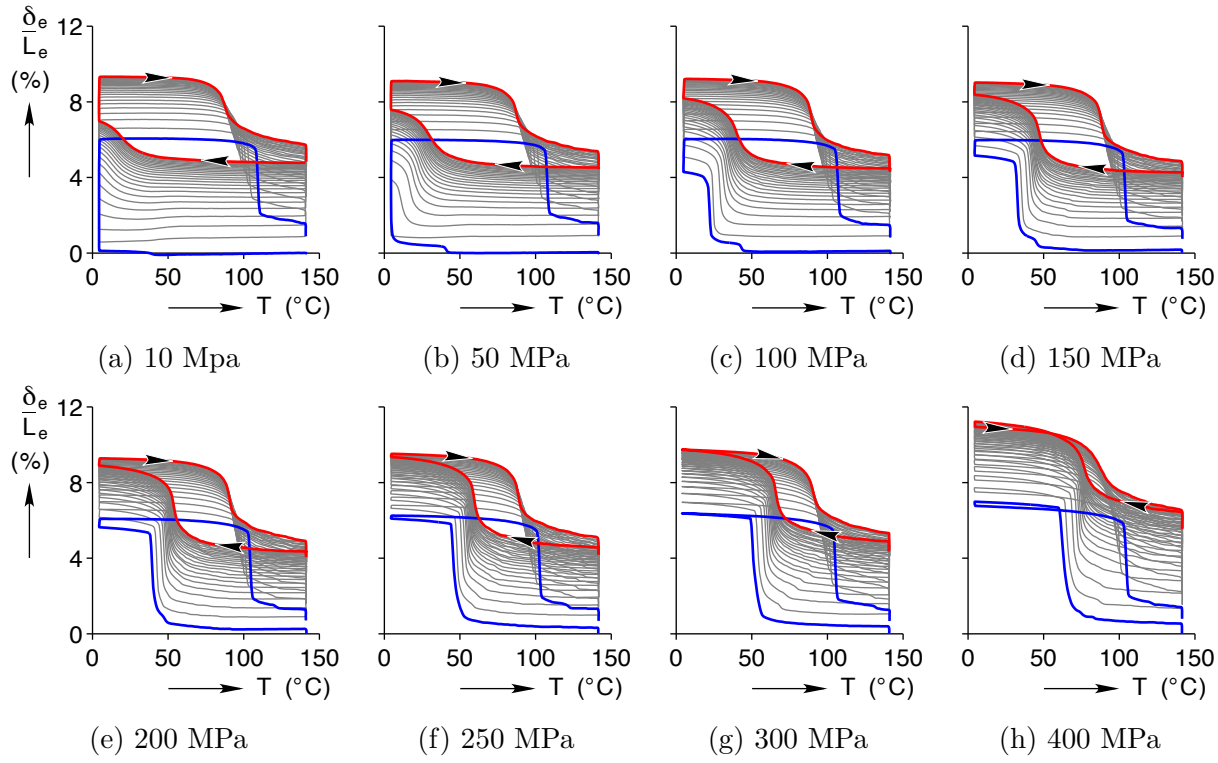

(a) 10 Mpa (b) 50 MPa (c) 100 MPa (d) 150 MPa

(e) 200 MPa (f) 250 MPa (g) 300 MPa (h) 400 MPa

Figure 4.17: Actuation response at constant heating stress (300 MPa) but varying cooling stress.

The transformation strains (ε^*) on cooling, shown in Figure 4.19, summarize the dependence of the strain response with σ_{cool}. On cycle 1, the 10 MPa case had a ε^* close to zero, but developed a two-way shape memory effect by cycle 25 with ε^* slightly over 2%. From 100 MPa and higher, the specimens had the largest ε^* on cycle 1 which deteriorated upon cycling. The 10 through 200 MPa experiments also showed a distinct R-phase transformation on cycle 1, but by cycle 25 it was no longer apparent.

The ε_s data, which are the amount of recovered ε^*, for this set are shown in Figure 4.20a. On cycle 1, ε_s was monotonic with σ_{cool}, although the concavity of the polynomial fit changes from concave up to concave down, with an inflection point around 200 MPa. The 10 MPa experiment had the smallest stroke of approximately 5%, and the 400 MPa had the largest stroke of almost 6%. By cycle 25 ε_s became non-monotonic with respect to σ_{cool}, with a maximum ε_s at approximately 250 MPa. The 200 MPa case had the smallest decrease in ε_s after cycling, making it an ideal load for minimizing degradation of ε_s. The outer load cases (10 and 400 MPa) had the largest decrease in ε_s, leading to the hourglass-like shape in ε_s data.

Figure 4.20b shows that the ε_{r} data are both smooth between $\sigma_{\text{cool}} = 10$ and 300 MPa

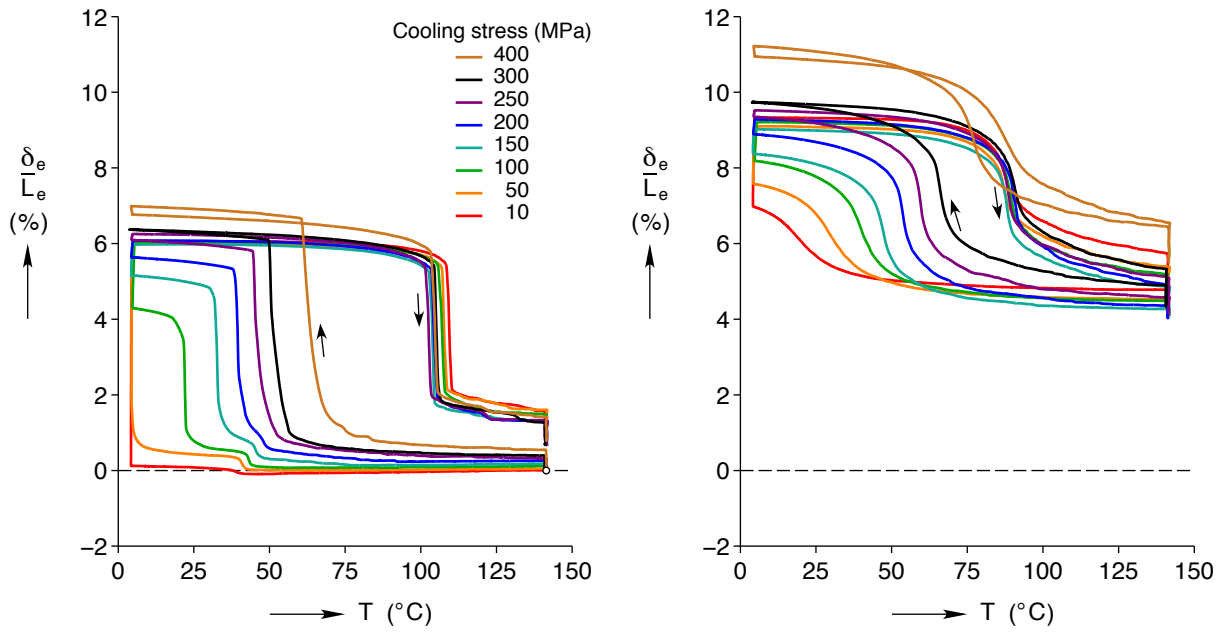

(a) Cycle 1

(b) Cycle 25

Figure 4.18: Comparison of first and last cycle of experiments with varying σ_{cool}.

cases, and furthermore non-monotonic. These data have a local minimum at $\sigma_{\text{cool}} = 200$ MPa, agreeing with the ε_s data as an ideal load condition that minimizes degradation. The outer cases (10 and 400 MPa) have noticeably larger ε_{r} and strain ratcheting. This is notably a non-intuitive result because conventional plasticity theory dictates that plasticity increases with increasing load. These data show that for NiTi the transformation induced plasticity initially decreases with increasing σ_{cool} until 200 MPa, then begins to increase again with further increasing σ_{cool}. The reason that the minimum is at 200 MPa is not immediately obvious. It was shown previously in this study that the damage occurs on heating, but now it is also shown that the amount of damage occurring is dependent on the cooling path. Clearly, this material is strongly path dependent and hysteretic in both thermal actuation response and degradation.

As done with previous data sets, these ε_{r} data can also be fit well by a three term exponential of the form,

$$\varepsilon_{\text{r}}(n) = \sum_{i=1}^{3} \varepsilon_i^{\infty}(1 - \mathrm{e}^{-n/\tau_i})\,. \tag{4.3}$$

The fit is shown in Figure 4.21. Again, the time constants τ_i are held constant across all the experiments, while the asymptotic strains ε_i^{∞} are allowed to vary. The first exponential term's ε_3^{∞} appears to be roughly independent of σ_{cool}, with values ranging from 2.7 to 3.4.

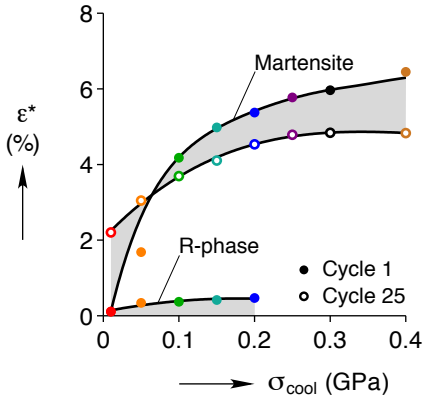

Figure 4.19: Transformation strain on cooling.

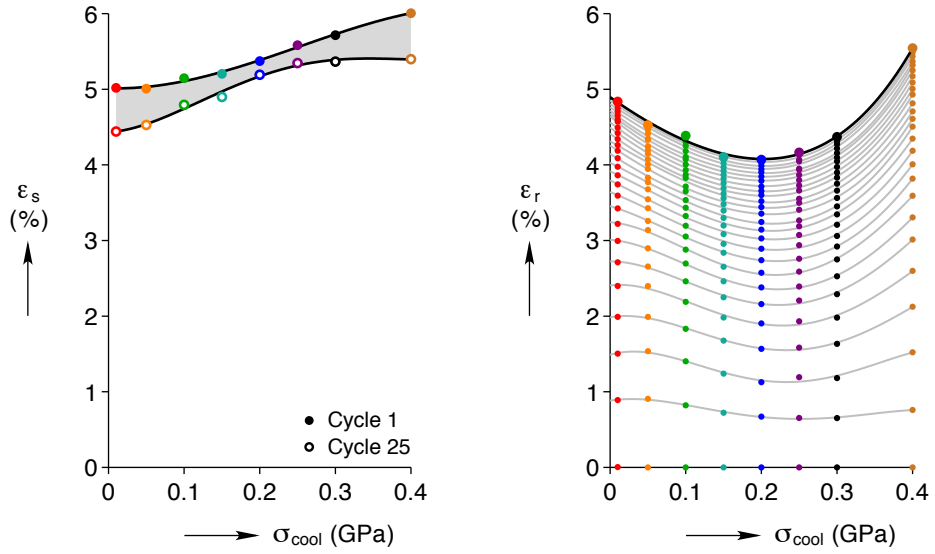

(a) Stroke (b) Residual strain

Figure 4.20: Stroke and residual strain for σ_{cool} experiments with polynomial fits.

The other two asymptotic strains, ε_1^∞ and ε_2^∞ have a less obvious dependence on σ_{cool}. What is clear is that the ε_3^∞ is associated with a time constant that is much larger than the other two ε_∞ parameters. What this shows is that the long term strain ratcheting behavior for each σ_{cool} case is equivalent. The differences from varying σ_{cool} are initial transient shakedown leading to a long-term offset in strain. In other words, the stress on heating (which is constant across these experiments) drives the long-term shakedown, but the various cooling stress have a noticeable impact on the initial shakedown of this material.

A major clue to why the material exhibits the non-monotonic residual strain behavior with σ_{cool} was found in the transformation temperatures. The peak transformation temperatures on cooling (T_m^*) were picked off on both cycle 1 and cycle 25, as shown in Figure 4.22a.

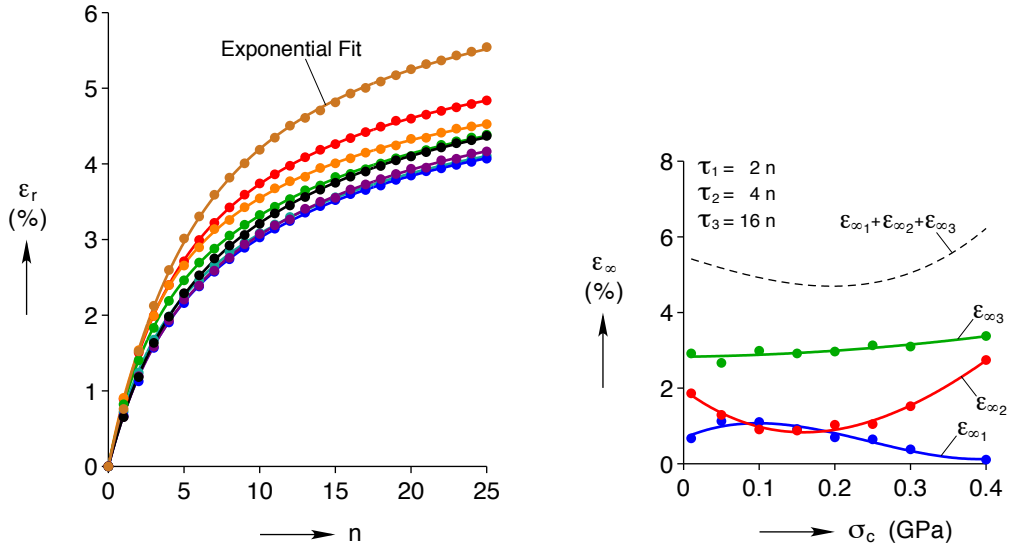

(a) (b)

Figure 4.21: Residual strain data fit with two term exponential series. (a) Data with fit. (b) Asymptotic strain fit parameters.

The Clausius-Clapeyron slope was measured to be 8 MPa/°C on both cycle 1 and cycle 25, with an interesting 14.5°C horizontal shift in the transformation temperatures with cycling but little change in slope. While it may be obvious, to be clear, this means that for every additional 8 MPa of applied dead load, the transformation temperature will increase by 1°C. This relationship applies to both A→M and M→A transformations (i.e. on heating and cooling). Given that on heating the applied load was held at a constant 300 MPa across each of these experiments, the M→A transformation temperatures (T_a^*) were expected to be the same. Contrary to that expectation, however, there was a change in T_a^* with σ_{cool} and a difference of −6.8°C measured between the σ_{cool} =10 MPa and σ_{cool} =250 MPa experiments, as shown in Figure 4.22b. By invoking the measured 8 MPa/°C Clausius-Clapeyron relationship for this material, the σ_{cool} = 10MPa case has an apparent 54 MPa increase in stress (from residual stresses) relative to the σ_{cool} = 250MPa case. There is clearly an unexpected energy barrier that the material must overcome in order to reverse transform in the lower σ_{cool} cases.

In an attempt to better explain this observed phenomenon, it is worth noting the idealized microstructures of NiTi, shown in Figure 4.23. The reader is referred to Bhattacharya ([10]) for a thorough background on the microstructures of NiTi, but in brief, the compatibility between austenite and martensite dictates the microstructures that develop in martensite when transforming from A→M. Austenite has a highly symmetric and ordered cubic crystal

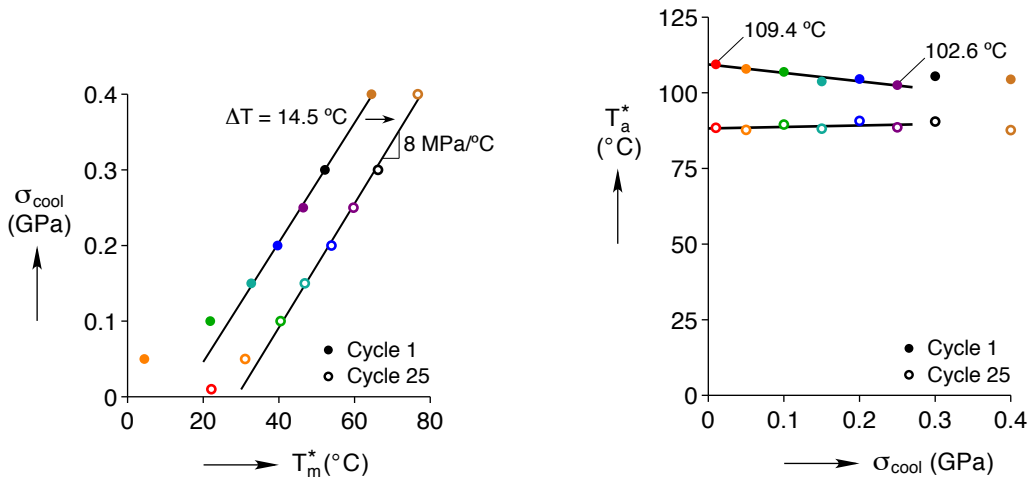

Figure 4.22: Elevated transition temperature on heating from apparent 54 MPa residual stress in $\sigma_{\text{cool}} = 10$ MPa experiment on cycle 1. (a) Clausius-Clapeyron slope as measured on cooling. (b) Shift in temperatures for constant $\sigma_{\text{heat}} = 300$ MPa.

structure, and as it only has one variant, is represented by a single color red in Figure 4.23a. Martensite, with its lower symmetry and less ordered monoclinic crystal structure, has 12 symmetry-related *lattice correspondent variants* (LCVs). Any single variant of martensite is not kinematically compatible with austenite, but pairs of martensite variants can be kinematically compatible on average (called a *habit plane variant*, HPV). These HPVs are highly twinned microstructures, and represented here schematically as two different blue colors, shown in Figure 4.23d. We must also distinguish between *thermal martensite* and *stress-induced martensite*. Thermal martensite is formed when austenite transforms to martensite in a (relatively) stress-free environment and forms a *self-accommodated* (no macroscopic shape change) microstructure. As any single HPV does not satisfy self-accommodation, multiple groups of HPVs are required as shown in Figure 4.23c. When austenite transforms to martensite under stress, the material transforms directly to a single HPV that can accommodate an axial elongation along the loading axis, and minimize the system's energy (see Fig. 4.23b). Finally, a highly twinned martensite can undergo what is called *de-twinning* when loaded axially above a load threshold. This process reorients the crystal structure into a single LCV, shown schematically in Figure 4.23e. Using these definitions and current understanding of the microstructure, two specific experiments will be examined.

The original clockwise experiment, which had $\sigma_{\text{cool}} = 10$ MPa, is now examined closer taking into consideration the idealized microstructures of the material. Shown in Figure 4.24a are the stress-temperature data of the prescribed experimental path. Starting

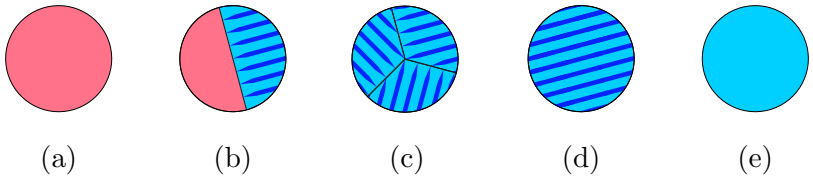

(a) (b) (c) (d) (e)

Figure 4.23: Idealized microstructures of NiTi. (a) Austenite. (b) Austenite interfaced with a single habit plane variant of martensite. (c) Self-accommodated thermal martensite with multiple habit plane variants. (d) Single habit plane variant of martensite. (e) Single lattice correspondent variant of martensite.

from ⓪ (140°C, 10 MPa), the specimen was cooled to ① (5°C, 10 MPa), then subsequently loaded to ② (5°C, 300 MPa). The stress-strain response data are shown in Figure 4.24b. Initially at ⓪, the material is fully austenite. Cooling to ① (relatively) stress free, the material transforms to thermal martensite and has relatively little macroscopic strain change. From ①–② the material is loaded isothermally, and shows the martensite deformation and de-twinning response. Through this loading the material is reoriented into a single LCV microstructure. So far, the current understanding of the microstructure adequately explains the phenomenon. Where the theory breaks down is shown next.

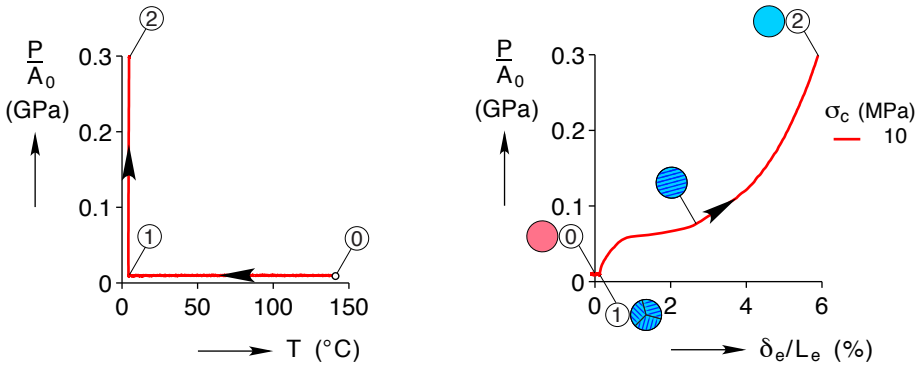

(a) (b)

Figure 4.24: Experiment with $\sigma_{\text{cool}} = 10$ MPa, showing cooling half of cycle 1 data. (a) Prescribed stress-temperature path data. (b) Stress-strain response data.

An intermediate experiment at $\sigma_{\text{cool}} = 150$ MPa is similarly shown in Figure 4.25 above the previous $\sigma_{\text{cool}} = 10$ MPa data. In this intermediate experiment, starting from ⓪ (140°C, 10 MPa) the wire was first loaded isothermally to ① (140°C, 150 MPa), before cooled to ② (5°C, 150 MPa). The wire was then loaded again isothermally to ③ (5°C, 300 MPa). In the stress-strain response (Fig. 4.25b) there is elastic loading from ⓪–①, then a strain increase from ①–② due to the forward transformation under stress. From ②–③, there is additional loading that is part elastic and part detwinning of the HPV system into a LCV.

Comparing the 10 MPa and 150 MPa experiments at ② in Figure 4.25a reveals an unexpected trend. At ②, both specimens are at 150 MPa and 5°C, the only difference being the path that they reached this ② point. However, the strain at this point, shown in Figure 4.25b is significantly different (+0.7%) between the $\sigma_{\text{cool}} = 10$ MPa and 150 MPa experiments. This cannot be explained by plasticity, because it has been shown that on the first cycle no plasticity develops prior to heating. Thus, the microstructure in the 150 MPa experiment is very different than that in the 10 MPa experiment, simply due to the difference in paths taken to ②.

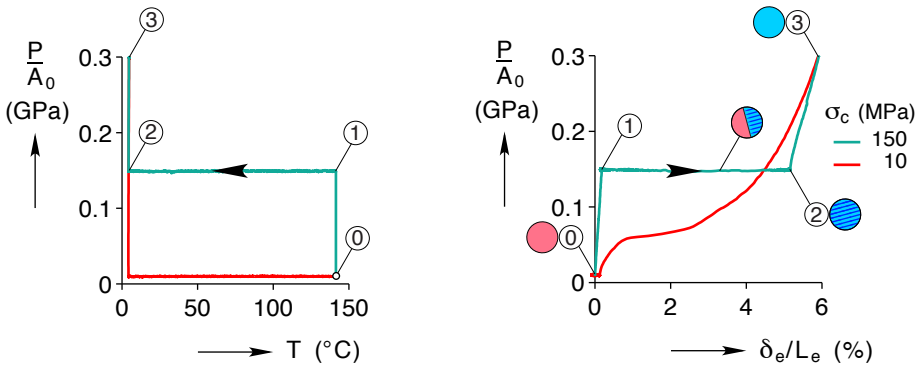

(a) (b)

Figure 4.25: Experiment with $\sigma_{\text{cool}} = 150$ MPa, showing cooling half of cycle 1 data and overlaid over 10 MPa experiment. (a) Prescribed stress-temperature path data. (b) Stress-strain response data.

Furthermore, this trend is visible in all of the stress-strain data for the σ_{cool} experiments, and is shown in Figure 4.26a. The strain overshoot (relative to the 10 MPa baseline experiment) is consistently apparent in all of the experiments. The overshoots appear to trace out another martensite deformation curve parallel to that of the 10 MPa experiment. Another surprising trend, apparent mostly in the 50 MPa experiment, but also in the 100 MPa experiment, is the initially very stiff tangent modulus these specimen had when isothermally loaded after the temperature induced transformation. After this initially stiff portion, the 50 MPa experiment then traces the 10 MPa experiment's curve exactly up through 300 MPa. The strain overshoots ($\Delta\varepsilon$) are summarized in Figure 4.26b, and shown to be monotonic and continuous with σ_{cool}. The $\Delta\varepsilon$ also appears to asymptote around 0.5% strain at 300 MPa.

These data show that not only do the various experiments have different microstructures when cooled under load than that of the 10 MPa experiment, but there is a continuous spectrum of microstructures based on σ_{cool}. One possible explanation is that if one assumes the 10 MPa experiment is 100% volume fraction thermal martensite and the 300 MPa ex-

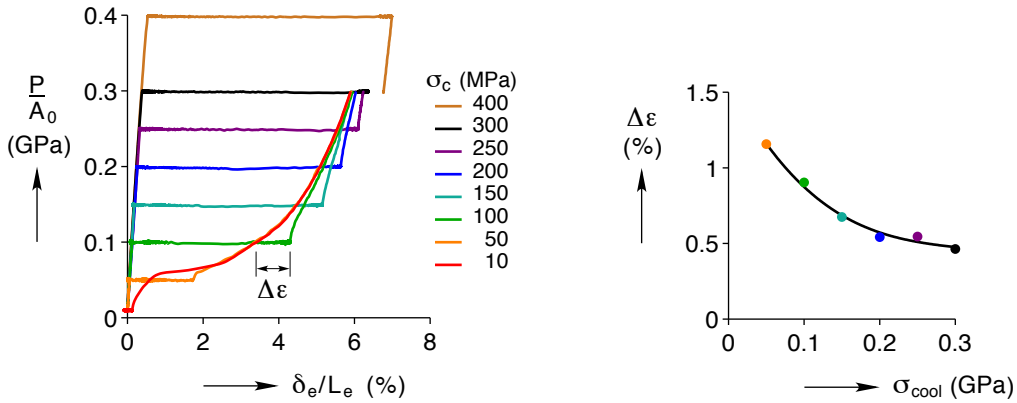

Figure 4.26: Resulting transformation strain under constant load differs from isothermal martensite curve. (a) Stress-strain response data. (b) Strain overshoot.

periment is 100% stress-induced martensite, then the intermediate stress cases could have a varying volume fraction of thermal and stress-induced martensite. The required energy to transform directly into a stress-induced martensite microstructure is apparently lower than the energy to de-twin a thermal martensite microstructure into a similar single HPV dominated microstructure, as shown by the $\Delta\varepsilon$ trend.

What remains is an explanation for why the lower σ_{cool} experiments accumulate a higher amount of plasticity and degradation. One possible explanation can be given by considering again the path each specimen is taken through, and the kinematic compatibility between austenite and martensite. The microstructure that forms when cooling from austenite to martensite is such that during transformation, there is as little mismatch in atoms across the A-M interface as possible (thus forming the HPV system). It stands to reason that after transforming to martensite, if the material is then heated back to austenite without changing stress state, then it should have a relatively low energy barrier. This is because the habit plane could simply follow the same path created by the forward transformation, but in reverse.

However, if the microstructure was changed through additional loading and reorientation of the lattice structure prior to reverse transformation, this reverse path for the habit plane would be altered. The amount it is altered would depend on the amount the lattice structure was reoriented; i.e. the amount of detwinning. Thus, σ_{cool} determines the volume fraction of thermal martensite that forms upon cooling and in turn the amount of crystal reorientation (detwinning) that occurs when loaded to 300 MPa. Larger amounts of detwinning further shifts the microstructure away from one that is favorable for the reverse transformation.

4.5 Conclusions

This study provided three major conclusions which further the understanding of the process of shakedown in NiTi wires undergoing thermal actuation:

- Raising the maximum temperature of each thermal cycle increases the amount of degradation by transforming a larger volume fraction of material at progressively higher temperatures. This causes more plasticity and a prolonged shakedown that requires increasing number of cycles to reach an asymptotic limit.
- The transformation-induced plasticity was discovered to occur during heating when martensite reversely transforms to austenite, and the plasticity could be avoided on the first cycle by unloading before heating. This revealed a large path dependence to the shakedown of shape memory wire.
- Varying σ_{cool} between 10 and 400 MPa, but maintaining a constant σ_{heat} of 300 MPa, revealed non-monotonic shakedown behavior with the minimum shakedown occurring at 200 MPa. The transformation strain was largely different than what the martensite deformation curve would have dictated, indicating that the microstructure that formed upon transforming to martensite was different based on the stress state during transformation. It is thought that this is caused by a varying volume fraction of thermal and stress-induced martensite, and through the detwinning process the reverse transformation is met with an additional energy barrier (as shown by the transformation temperatures), effectively causing additional plasticity to develop.

These contributions advanced our general scientific understanding of transformation induced plasticity and shakedown of thermal actuation by revealing new dependencies outside of the typical magnitude of bias load. Some interesting implications on how to design an actuator based on this information include emphasizing careful control of maximum cycle temperature, and having a stress differential between heating and cooling to enhance strain output while minimizing shakedown.

CHAPTER 5

Characterization and Modeling of 1×3 Superelastic Twists

This chapter presents work exploring the behavior of a reduced order superelastic cable: a 1×3 twist. The 1×3 twist exhibits similar local mechanics (contact, bending, and twisting) seen in a more complex cable, such as a 7×7. However, the 1×3 lends itself to easier analysis and interpretation because of its simplified geometry. The behavior of three twist specimens of varying helix angle (10.1°, 17.8°, and 21.5°) was explored.

The motivation for this study begins with work done by Reedlunn et al. [75, 76, 72] on two superelastic cables, a 7×7 and 1×27. They showed that the 7×7 exhibits mechanical behavior similar to that of a straight wire, with propagating transformation fronts and a distinct stress plateau. The 1×27 in contrast, had a compliant and stable response, with a gradual transformation and no distinct stress plateau. It was theorized that the increased curvature of the wires in the 1×27 was responsible for the change in transformation behavior. This could be due to increased friction or increased triaxiality from increased bending and torsion at the wire level. Through lubrication tests, however, friction was not seen to have a large effect on the isothermal mechanical response. The increased triaxiality from increased local bending and torsion could explain the different propagating behavior [75].

While the majority of research has focused on uniaxial tension, there have been notable advances to combined modes of deformation in NiTi. The material's response in bending, in particular, has been of large interest to many researchers [7, 12, 77], because of its implications for many products that make use of that mode of deformation. Torsion of thin-walled tubes, which produces a well-defined shear stress state, has also been the attention of several researchers [8, 90, 42, 93]. Two recent works, one by Bechle et al. [6] and one by Reedlunn et al. [73], showed varying strain localization events in the bending of NiTi tubes after the onset of phase transformation. The first showed a propagating localized curvature, while the

second showed diamond pattern strain localizations on the tension side of the tube. These results appear to corroborate with the hypothesis that the local bending and torsion are the cause of the shift in behavior between the 7×7 and 1×27 cables.

The goal then of this work was to have several specimens of the same material and construction, but with different helix angles to study the effect of increasing the curvature of the wires in a cable. It was thought that this should have a measurable impact on the phase propagating behavior. As it will be shown, the smallest helix angle twist (10.1°) exhibited wire like behavior with a single propagating transformation front and a distinct, smooth stress plateau as anticipated. However, the largest helix angle twist (21.5°) had an unexpected and new transformation behavior. There were many nucleation events with pockets of untransformed material along the axial length of the specimen, yielding a periodic and heterogeneous strain field. The stress history along the stress plateau was correspondingly unsteady. While additional lubrication tests also appeared to provide evidence that friction is not the culprit, finite element analysis simulations showed that the contact mechanics and friction were the dominant cause of the shift in transformation behavior between the three twists.

5.1 Specimens and Experimental Setup

Nickel titanium (NiTi) twist specimens with three different helix angles and straight wire were obtained from Fort Wayne Metals, Research Products Corp. (Fort Wayne, Indiana). All material was fabricated from the same NiTi ingot lot and had the same heat treatment processing to ensure as identical material properties as possible. The NiTi material's austenite finish temperature (A_f) was reported to be -5.0°C. The material is then fully austenite at room temperature and exhibits superelastic properties. Photographs of the three specimens (painted for digital image correlation and thermography) along with a schematic of the geometry are shown in Figure 5.1. Here, the helix angle (α) is measured from the vertical loading axis, and varied from 10.1° to 21.5°, d is the helix diameter, and d_w is the wire diameter.

The d_w was measured with a micrometer to be 1.020 mm. The axial length of one full turn, or pitch (p), of each specimen was measured to be 9.576 mm, 11.684 mm, and 20.904 mm also with a micrometer and by averaging over multiple turns, as advised by Reedlunn et al. [75]. The measured pitch lengths were the same as reported by the supplier Fort Wayne Metals for the two longer p specimens, but the shortest pitch (reported to be 7.620 mm)

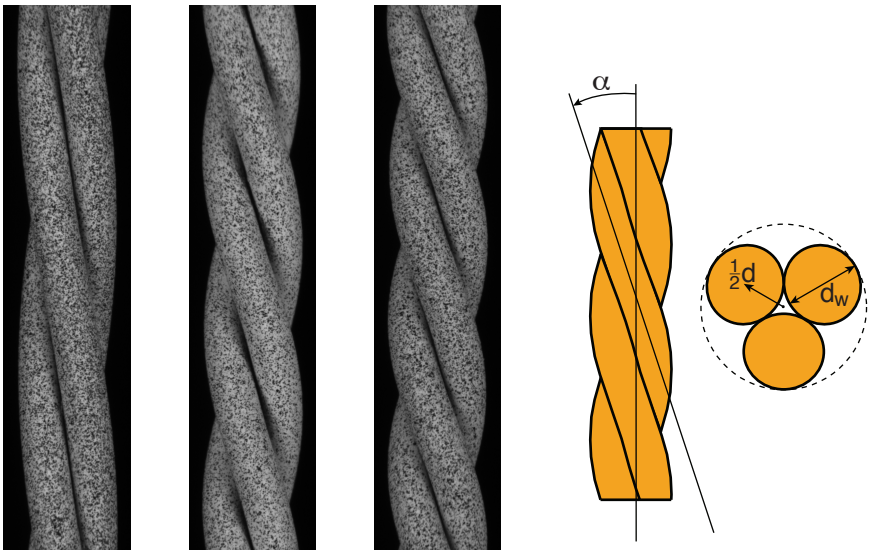

(a) (b) (c) (d)

Figure 5.1: Twist specimens speckled for digital image correlation and IR measurement. (a) 10.1° twist, (b) 17.8° twist, (c) 21.5° twist, (d) Schematic highlighting helix angle (α), wire diameter (d_w), and radius of helix (d).

was not. Fort Wayne Metals communicated difficulty in setting the pitches of very tightly twisted NiTi wires. To calculate the α for each specimen, the d is required but measuring this proves challenging. In a cable with a straight core wire, there is no unknown unknown gap between the wires in the center. In contrast, these 1×3 specimens have no central wire. The values of d and α were found for by solving the following equations in Costello [27]:

$$d = d_w \sqrt{1 + \frac{1}{3\sin^2\alpha}}$$

$$p = d\,\pi\,\tan\alpha$$

The first equation uses an approximation that in the horizontal cut plane, the wires' surface area are perfectly elliptical. This is not exactly the case, but it is a reasonable assumption for the 1×3 twist geometry [27]. The resulting helix angles are then calculated to be 21.5°, 17.8°, and 10.1°.

The samples were delivered in straight 0.3048 m (1 ft.) segments, and to prepare the individual samples they were first cut to approximately 100mm lengths with cable cutters. The samples were then airbrushed first with a background coat of a matt white paint (Golden Airbrush Titanium White #8380), and then speckled with a matt black paint (Golden Airbrush Carbon Black #8040). Both matt paints have an emissivity of $\epsilon = 0.91$ which

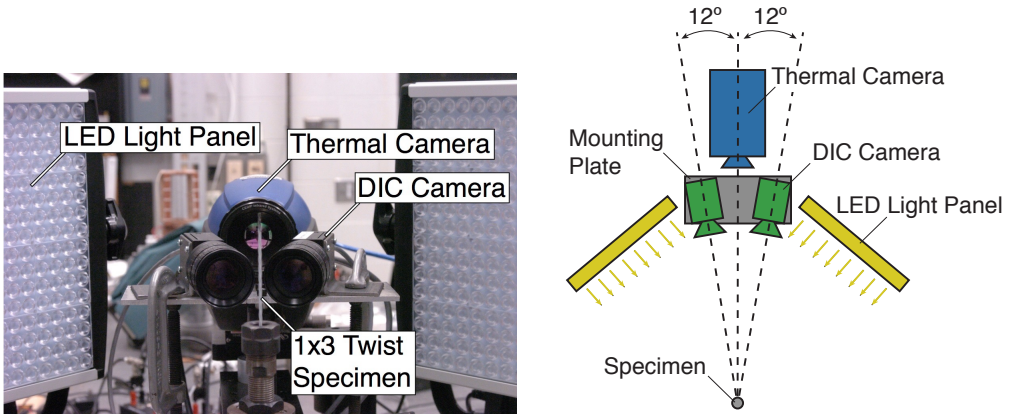

(a) (b)

Figure 5.2: Digital image correlation and thermography setup for 1x3 twists experiments. (a) Photograph, (b) Schematic.

allows for good IR temperature measurements. The speckle pattern is required for digital image correlation (DIC), which allows the measurement of full field displacements and in-plane strain calculations from digital images captured during an experiment. An overview of the mathematical background and experimental technique for DIC can be found in [74]. The DIC procedure was accomplished by using a commercially available software package made by Correlated Solutions [25, 26, 24], with additional post-processing done in Matlab [62].

The experimental setup for digital image correlation and thermography is shown in Figure 5.2. The experiments were conducted on an MTS servo-hydraulic load frame capable up to 15kN, with a 5kN MTS load cell and 400 in-oz Futek torque cell. The twist specimens were gripped with ER collets to provide radially symmetric grip force, and were sand blasted to minimize slip. For stereo DIC measurements, two Research Grasshopper CCD cameras (GRAS-50S5M-C) were mounted to a rigid steel plate and used to capture stereo digital images. The Grasshopper cameras have a 2048x2048 pixel array with square pixel size of 3.45 μm. Mounting both cameras on a steel plate was found to be very effective in preserving a good calibration over longer period of time, which was necessary for the longer cycling experiments. The two cameras made a stereo angle of 24° , which was large enough to allow room for the FLIR infrared camera to have full visual of the specimen. Two LED light panels (Litepanel Astra 1x1 Bi-Color LED Panel) which output 4577 lux at 1.5 m each were used at approximately 80% brightness to provide very uniform, non-flickering, and non-heating light on the specimen. This would have been an excessive amount of light in many circumstances, but allowed the cameras' exposure time to be minimized at 5 ms and overcome the natural

vibrations of the servo-hydraulic load frame. At long exposure times, the digital images were found to have noticeable motion blurring which was undesirable.

Before each experiment, after the specimen was carefully speckled, the specimen was loaded into the bottom grip and the camera focus and f-stop was adjusted. From this point on, the utmost care was taken to not touch the cameras or optical table to ensure a good stereo camera calibration. The specimen was then removed from the grip and a laser etched glass calibration grid (9×9 grid with 1.34mm spacing) was used to calibrate the stereo cameras with VIC 3D software [25]. After the experiment, this calibration was then used in conjunction with the digital images captured during the experiment in VIC 3D to calculate the in-plane strain fields.

5.2 Isothermal Experiments

This first experimental section describes the isothermal tension experiments on each twist specimen. The mechanical responses in a single load-unload cycle under a strain rate of $2 \times 10^{-5}\ s^{-1}$ are shown in Figure 5.3. The slow isothermal experiment suppresses the rate and latent heat related thermo-mechanical coupling, helping to isolate the underlying purely mechanical behavior. In Figure 5.3a, the axial load (P) is normalized by an idealized reference area ($A_0 = n\,\pi\,d_w^2/4$), calculated from the number of wires (n) and d_w. In Figure 5.3b, the axial torque (M_z) is normalized by the polar moment of inertia of an idealized cross-section as recommended by Reedlunn et al. [75] and given by,

$$J_0 = n\frac{\pi d_w^4}{32} + \sum_{i=1}^{n} \frac{\pi d_w^2 d^2}{16}\,.$$

The ratio J_0/R is then used to normalized the axial torque, where $R = \frac{1}{2}(d_w + d)$. The normalized axial strain (δ_e/L_e) is calculated by creating a virtual extensometer from specified material points in the post-processed DIC data and tracking those material displacements throughout the experiment. For these experiments, the grip-to-grip free length was around 29mm, the DIC field of view was 18.5mm, and the DIC virtual extensometer was around 16mm.

On loading, the 10.1° twist has the apparently stiffest response and smoothest transformation plateau. This twist has initial linear elastic tangent modulus of 66.7 GPa and has a transformation plateau at 0.476 GPa that is accompanied by a axial strain increase of

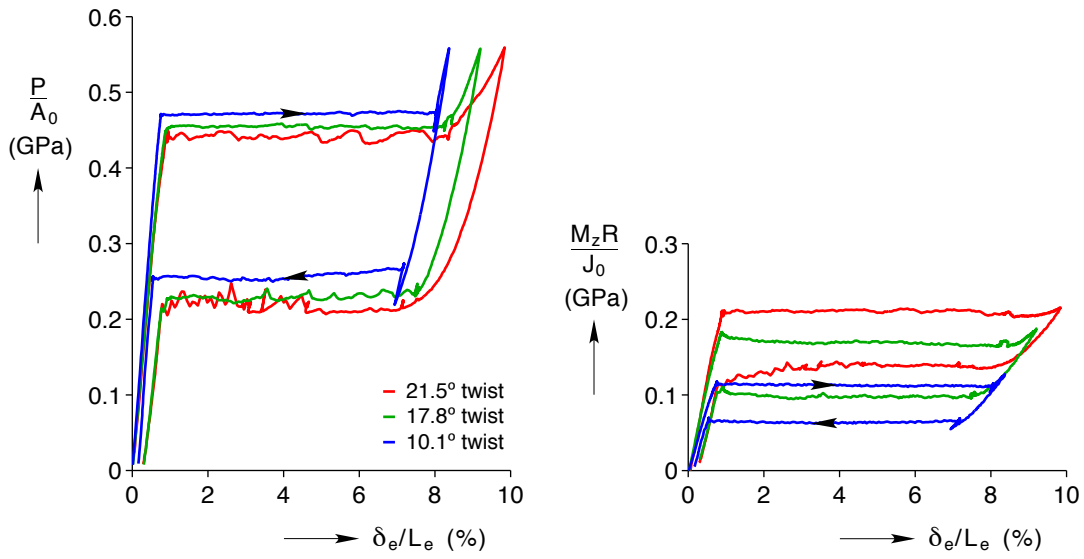

(a) (b)

Figure 5.3: Isothermal mechanical behavior of the three twists. (a) Normalized axial load, (b) Normalized axial torque.

7.38%. The 17.8° twist has an initial modulus of 57.7 GPa, a plateau stress of 0.459 GPa, and a plateau length of 7.92%. The 21.5° twist had the most flexible response, with a initial modulus of 55.0 GPa, a plateau stress that fluctuated between 0.454 GPa and 0.435 GPa, and the longest plateau length of 8.52%. From these data, it is clear that increasing the helix angle creates a more compliant structure. There is a trade-off of decreasing the plateau stress while correspondingly increasing the plateau length.

On unloading, the 10.1° twist reverse transforms at around 0.26 GPa and again had a relatively smooth reverse transformation. The 17.8° twist (which reverse transformed at around 0.23 GPa), and even more so the 21.5° twist (which reverse transformed at around 0.21 GPa), had a very unstable reverse transformation. Note that these apparently 'jagged' stress jumps are not random noise, but are in fact real effects due to the reverse transformation. Each spike corresponds to a de-nucleation event of a transformed martensite region reverting to an austenite parent phase. This is shown more clearly in the DIC images shown subsequently in this section.

As it should be expected, the 21.5° largest helix angle twist has the strongest axial torque response. During the transformation plateau, this twist maintains a normalized axial torque of around 0.20 GPa. The 10.1° twist in contrast only generates half the normalized torque at 0.11 GPa.

The axial load data plotted with respect to time for these isothermal experiments are

shown in Figures 5.4a, 5.4c, and 5.4e. The DIC virtual extensometer strain (δ_e/L_e) and grip strain (δ/L) histories are shown in Figures 5.4b, 5.4d, and 5.4f. Here, ①-② is the initial elastic loading portion of the stress data. There is curvature to the stress data when viewed in time because of noticeable grip slippage. The grip slippage is most apparent in the δ_e/L_e strain and δ/L comparison, where the δ_e/L_e strain approaches nearly zero after the experiment while the δ/L ends at upwards of 3-4%. This highlights the essential reason for using a local strain measurement and not a grip based measurement, because a grip based measurement would have substantial error.

One consequence of using ER collets is they suppress any nucleation peak. Nucleation peaks for stress-induced martensite can typically be measured as large as 100 MPa, but often require special setups that prevent large stress concentrations at the grips. In the present experiments, the ER collets provide a radially symmetric clamping force on the twists, but have a very sharp edge in contact with the specimen. This leads to a large stress concentration that suppresses any nucleation peak. The specimens are shown in these data to smoothly transition to a transformation region past ②. There are some nucleation or de-nucleation events visible. For instance in Fig. 5.4a between ⑦ and ⑧ there is a front coalescence event here shown by a 35 MPa drop in the load. This typically occurs when two fronts merge outside of the grips. On unloading at ⑨, there is also a 50 MPa jump in load caused by a nucleation event beginning reverse transformation. This occurred outside of the DIC field of view, but most likely the nucleation event on unloading initiated in the same location that there was the coalescence event on loading.

As each specimen undergoes a forward transformation from ② past ⑦, and again on its reverse transformation from ⑨ past ⑪, there are also localization events in the strain. This is evident again when comparing the strain fields. While δ/L has an steady positive ramp on loading, the δ_e/L_e only increases rapidly when the localized transformation region is within the DIC virtual extensometer's gage length.

The stress histories shown in Figure 5.4 have circled time labels that correspond to DIC images of axial strain component in the loading direction (ε_{zz}), shown in Figure 5.5. The labels ① through ⑧ correspond to loading, and ⑧ through ⑫ are the unloading portions of the tension experiments. Images ③ through ⑥ were chosen to highlight the varying ways the transformation fronts propagate between the three twists. Then images ⑩ and ⑪ show the reverse transformation on unloading.

The 10.1° twist, as shown in Figure 5.5a, transforms in a similar manner to that of a single straight wire. A single front per wire, at roughly the same axial position propagates from the

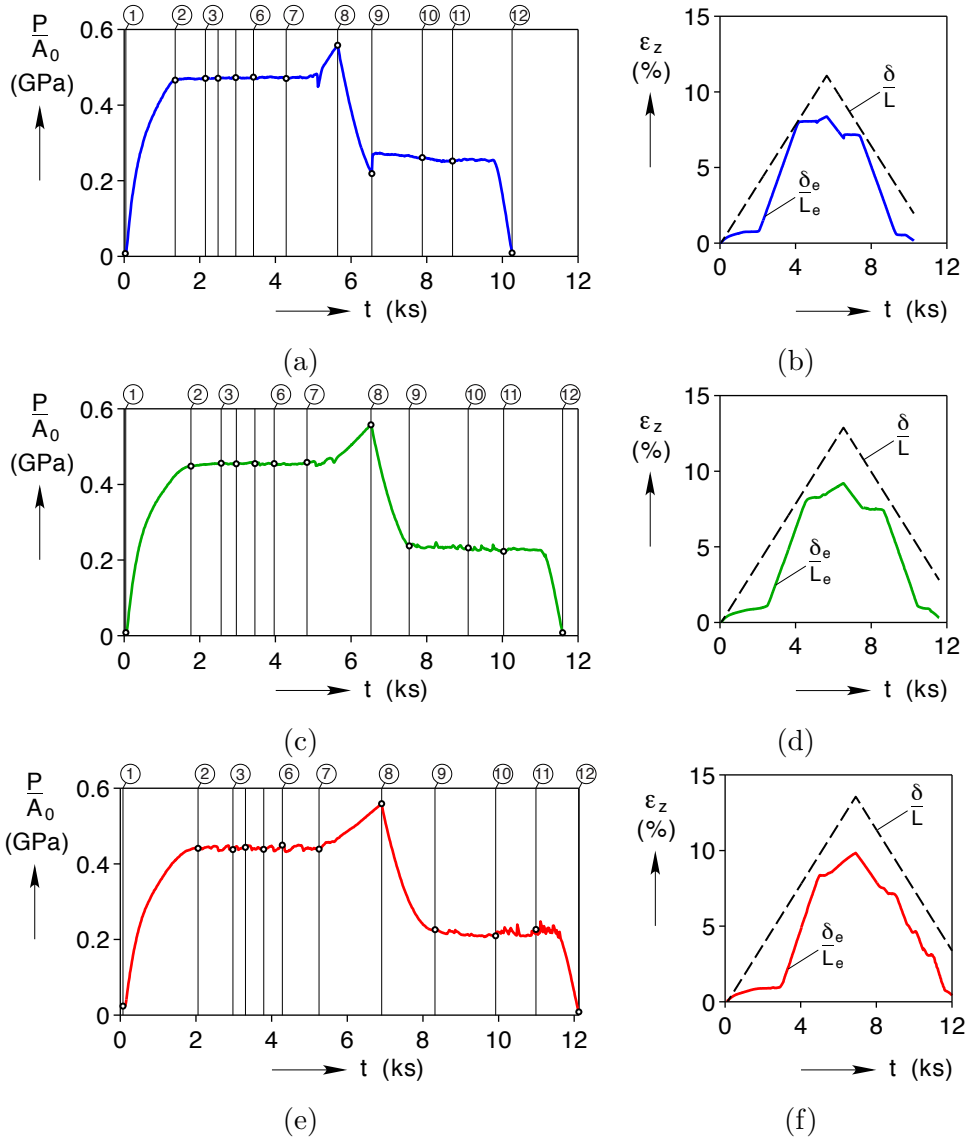

Figure 5.4: Isothermal stress history. (a) 10.1° twist, (b) 17.8° twist, (c) 21.5° twist. Circled time labels correspond to DIC strain images in Fig. 5.5.

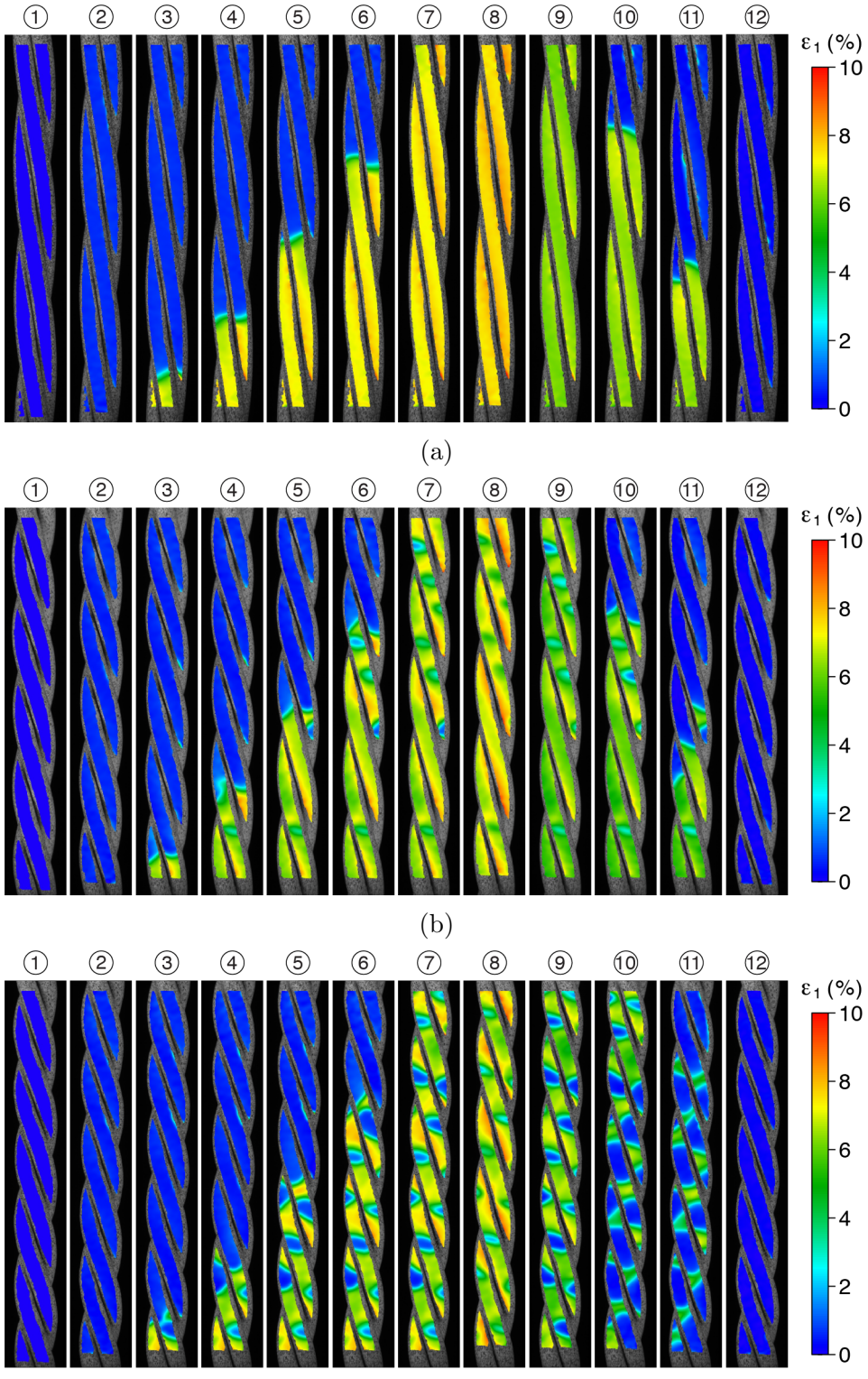

Figure 5.5: Snapshots of digital image correlation strain fields. (a) 10.1° twist, (b) 17.8° twist, (c) 21.5° twist. Circled image labels correspond to time labels in Fig. 5.4.

bottom grip towards the top grip from ③-⑥. Across the front, the ε_{zz} jumps from around 0.7% to 6.7%. Note that, because of the curvature of the wires, there is some bending even in this small helix angle twist. The strains are expected to be slightly higher on the interior surface of the wire, which is hidden from DIC. The transformation front has finished crossing the DIC field of view by ⑦, and the specimen is loaded an additional 80 MPa, peaking at ⑧, before unloading begins. The specimen then unloads without any transformation fronts until ⑨. The specimen then reverse transforms again with a propagating front, now traversing in the opposite direction starting from the top grip and ending at the bottom grip (⑩-⑪). The specimen is finished unloading in the final image ⑫.

In Figure. 5.5b, the intermediate 17.8° twist has in general the same progression of transformation fronts. On loading, the front begins at the bottom grip and propagates to the tip grip. Then on unloading, the front reverses direction and propagates to the bottom grip. Most evident in image ⑧ is the increased bending of each wire. From the surface area visible, ε_{zz} ranges from as low as 3.4% to above 9%. It is safe to assume that the ε_{zz} are even higher on the interior surface of the wires. There are also elliptical regions or pockets of low strain, untransformed material visible in the DIC. These untransformed pockets appear concentrated on specific wires, but are absent on others.

The trend in shifting propagating behavior continues to the 21.5° twist, show in Figure 5.5c. The phase transformation propagates in the same direction on loading, starting from the bottom grip, but the progression was now dominated by nucleation events as opposed to steady front progression. Each new nucleation created a discrete region of transformation, apparently to jump past a region of untransformed material. After the transformation plateau saturated, shown in ⑦, the resulting strain field shows again a large amount of bending and many periodic pockets of low strain. When the specimen is loaded an additional 125 MPa past the transformation plateau (in image ⑧, to the same maximum 1400 N as the other specimens), these low strain pockets are still distinctly visible.

On unloading, the 21° twist has a very different transformation. There was no nucleation event, because many austenite-martensite interfaces were retained through the whole loading sequence. As the specimen reverse transforms (⑨ – ⑪), each of these interfaces (the boundaries of each low strain regions) grew outwards until the regions of high strain austenite became increasingly thin. Following that, the transformation fronts began to coalesce in a very dynamic fashion. The transition from growth of low strain regions to coalescence events is clearly visible in the stress history, shown in Figure 5.4e. The first region of growth has a very smooth load history, while each coalescence event causes a load spike (20 – 30 MPa) resulting in many abrupt load fluctuations.

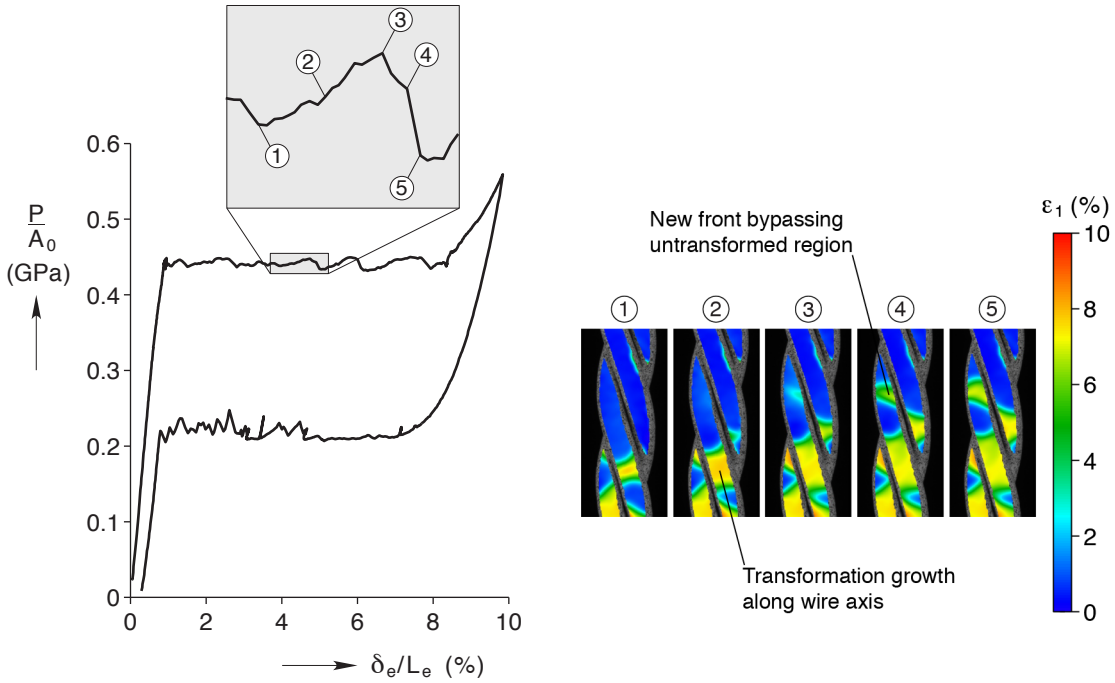

(a) (b)

Figure 5.6: Close-up view of load fluctuations in the transformation plateau during loading of the 21° twist.

Figure 5.6 shows a close-up view of the transformation plateau and corresponding DIC images on loading of the 21° twist. Points ① – ③ show an increasing trend in the normalized load, and have a corresponding transformation growth along the wire axis (similar to a single straight wire). Points ③ – ⑤, however, show a steep decreasing trend in the normalized load, during which time a new finger-like front appears on the left wire, that bypasses an elliptical region of low-strain, untransformed material. The same order of events can be traced to the other load fluctuations on the loading portion of this transformation plateau. These order of events can be explained by considering the friction and local stiction between the three wires. As one particular wire elongates axially, it appears to build up local stresses and requires an increasingly large macroscopic stress to continue propagating. This reaches a limit, at which point a new finger-like front nucleates, bypassing a region of stuck material (due to friction). This new front relieves the built-up stresses and has a corresponding drop in macroscopic load.

Previously Reedlunn et al. showed that applying a penetrating lubricant (Grignard TN-3, composed of a non-petroleum group of synthetic di-esters) to a 7×7 and a 1×27 cable created no net change in macroscopic mechanical response. This provided evidence that friction did not a dominant role in the transformation of a NiTi cable. This experiment was

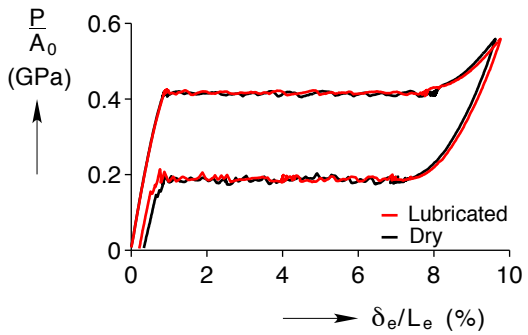

Figure 5.7: Isothermal mechanical responses two 21° twist specimens, with one specimen coated in a penetrating lubricant.

repeated here with a 21° 1×3 twist, using a mechanical MTS extensometer (25.4 mm gage length, +22.5%/-12.5% strain reading). The mechanical responses of two specimens, one dry and one lubricated, are shown in Figure 5.7. These data show that, again, the penetrating lubricant had no real impact on the macroscopic behavior on a NiTi cable or twist. However, we feel this does not invalidate the role of friction as previously discussed, but rather brings to question whether or not the penetrating lubricant is having any impact on reducing the friction between the wires in the 1×3 twist.

5.3 Cyclic Shakedown Experiments

The first cycle of an isothermal tension experiment on these 1×3 twists in Section 5.2 showed interesting differences in the mechanical responses and the transformations' propagation. How the varying α of the three 1×3 twists affects the cyclic shakedown or functional fatigue is explored in this section. Three additional experiments are presented here, where 50 tension cycles to a constant peak load of 1275 N (524.2 MPa) at a strain rate of $1.5 \times 10^{-4}\ s^{-1}$. This is about an order of magnitude faster than the previous isothermal experiments, and the latent heat release becomes an important factor bringing in additional thermomechanical coupling. For these experiments, DIC and IR imaging was utilized on the select cycles[1] of 1, 2, 5, 10, and 50 to measure the local changes in propagating behavior with cycling.

The mechanical behavior for these cycling experiments on all three 1×3 twists are shown in Figure 5.8. The normalized axial load and axial strain responses, shown in Figures 5.8a, 5.8c, and 5.8e show a similar trend as the twists shakedown. After 50 cycles, the plateau stress drops by 130-140 MPa, the plateau strains have decreased by approximately 2%, and there

[1]Collecting DIC and IR images on all 50 cycles would have been an excessive quantity of data and was omitted for practicality.

is a final residual strain of around 2-2.5%. The normalized axial torque response (Figs. 5.8b, 5.8d, and 5.8f) with a similar drop in the twisting moment, but with an interesting trend in what is apparently a residual twisting moment then the axial load is removed (most visible in the 17.8°and 21.5° twists). The twists were in a torsionally clamped fixture and did not have the ability to freely rotate after each cycle. Thus as an axial residual strain accumulated, it appears there was also a corresponding built-up torque in the specimen.

To better summarize the cycling data, key parameters are picked off from the normalized load-displacement curves. These values are plateau strain (ε_p), plateau stress (σ_p), residual strain (ε_r), and specific work (w). Linear fits were used to measure these values, and an example of the fits used are shown in Figure 5.9. The specific work is meant to be a measure of the work associated with the loading plateau, and is calculated by,

$$w = \frac{1}{\rho\, c}\, \sigma_p\, \varepsilon_p\,.$$

Here ρ is the mass density of NiTi (6.5×10^6 g/m^3). Note that $\sigma_p = P/A_0$, and A_0 was the idealized area calculated by an equal number of straight wires. Thus, $A_0 \times L_e$ does not represent the actual volume of any given twist. A correction factor c is applied to account for the additional length of helical wires in a cable, and represents the increase in mass per length per wire relative to the single straight wire. This factor was calculated by dividing the weight of a unit length of a twist by the number of wires and the weight of a unit length of a single straight wire. The values found for c are 1.015, 1.050, and 1.075 for the 10.1° 17.8° and 21.5° twists, respectively.

A summary of the shakedown data is shown in Figure 5.10. As mentioned before, DIC data was only available on cycles 1, 2, 5, 10, and 50. Thus, data were only available on these cycles for ε_p, σ_p, and w. To aid visualization, an exponential fit of the form $\{a - b(1 - \mathrm{e}^{-n/c})\}$ was used to fit and interpolate the data. An inverse relationship between ε_p and σ_p with α is again apparent here. The larger α twist is again shown to have a more compliant response, with a larger ε_p with a smaller σ_p. Interestingly, the rate at which ε_p and σ_p shakedown with cycle number (n) appears to be consistent between the different α twists.

The residual strain, shown in Figure 5.10c, has an unexpected conclusion. The 10.1° twist has a final ε_r of 2.00%, while the 17.8° and 21.5° twist each have ε_r of 2.40% and 2.37%. Clearly, there is additional plasticity associated with the larger two α twists compared to the 10° twist, but between these two twists there is no significant difference. The w with cycling, shown in Figure 5.10d, is nearly identical between the three twists. By cycle 50, the differences in w are indistinguishable. This shows that there exists an interesting proportional

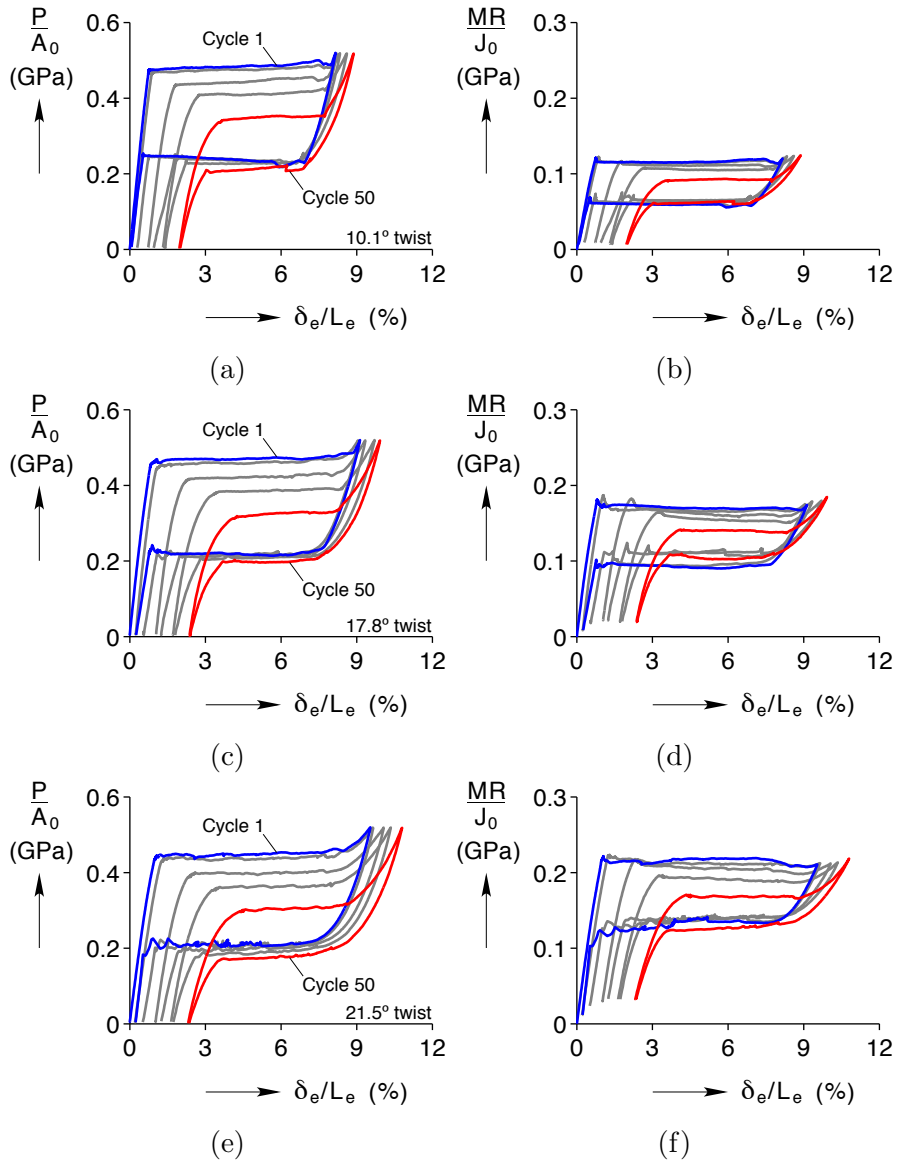

Figure 5.8: Mechanical behavior over 50 cycles (showing cycle 1, 2, 5, 10, 50) at 1.5×10^{-4} s^{-1} strain rate. (a) 10.1° twist normalized axial load, (b) 10.1° twist normalized axial torque, (c) 17.8° twist normalized axial load, (d) 17.8° twist normalized axial torque, (e) 21.5° twist normalized axial load, (f) 21.5° twist normalized axial torque.

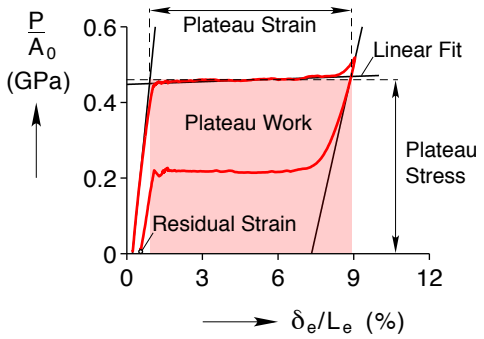

Figure 5.9: Cycle 2 of 17.8° twist shakedown specimen with linear fits to aid measurement of key values.

relationship between ε_p and σ_p. This is reminiscent of the Clausius-Clapeyron equilibrium thermodynamic relationship, where derivative of stress ($\mathrm{d}\sigma_P/\mathrm{d}T$) is related to ε_p instead of simply σ_p as suggested here.

The latent heat released upon transformation (and absorbed upon reverse transformation) for each 1×3 twist are shown in Figure 5.11 and had interesting differences as well. The IR temperature field was recorded on cycles 1, 2, 5, 10, and 50 (the same cycles as DIC), and what is shown here are time lapses of the surface temperature. Each vertical line of pixels represents one IR snapshot in time, and each pixel is the averaged temperature across the width of each specimen. When these vertical lines are stacked together, it creates a smear or time lapse of the temperature field. The stress history is then overlaid as a black line to serve as a reference.

For the 10.1° twist shown in Figure 5.11a, on cycle 1 there were two transformation fronts (visible by localized elevated temperature) that propagate from the top and bottom grips and coalesce in the middle of the specimen causing an elevated temperature of approximately +5°C. On unloading, this process reverses direction and the two reverse transformation fronts nucleate in the middle of the specimen and propagate towards either end of the specimen. With cycling, the two transformation fronts gradually shifts to a single front on loading and unloading, but the latent heat released appears to remain consistently high with a distinct transformation front even on cycle 50.

The temperature data for the 21.5° twist shown in Figures 5.11c are remarkably different. On cycle 1, in contrast with the two steady fronts, there a many nucleation events that each cause a distinct and localized spike in temperature, and these many nucleation events coalesce towards the middle of the specimen. This trend also appears to shift to propagating in a single direction, from the bottom grip to the top grip. By cycle 50, however, there is only a

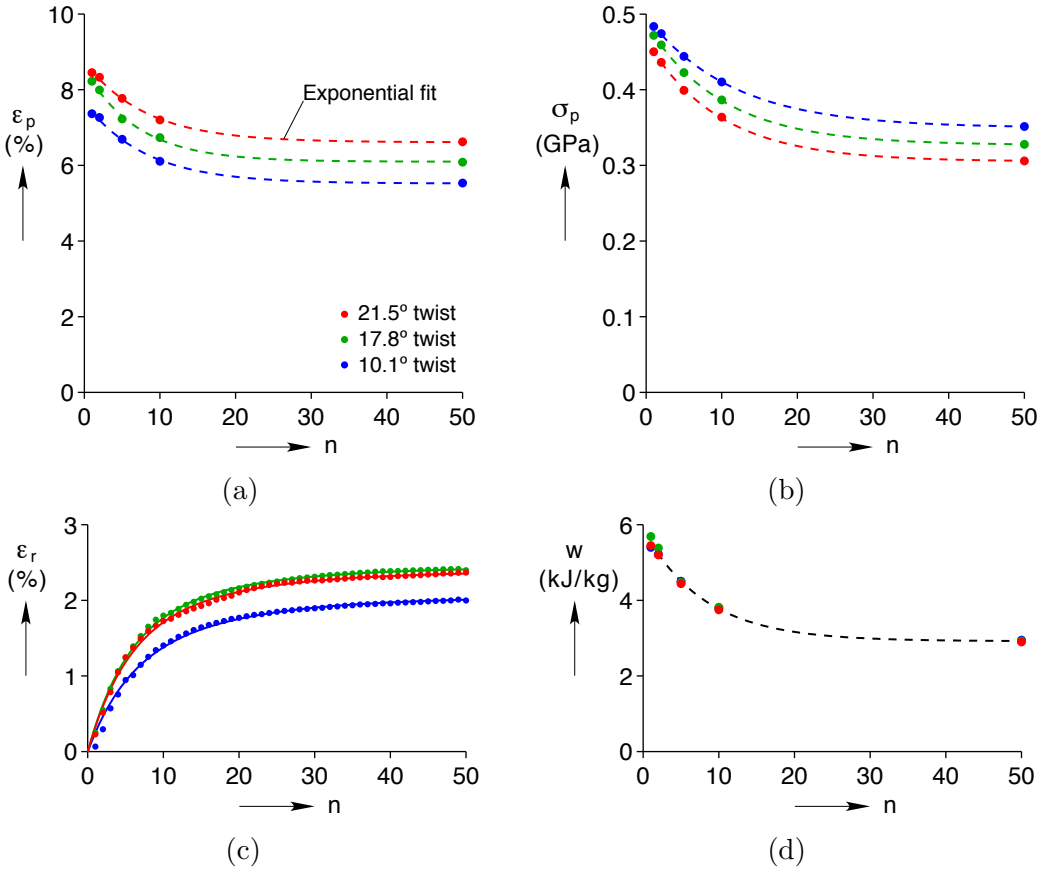

Figure 5.10: Summary of twist shakedown data. (a) Transformation plateau strain (loading), (b) Transformation plateau stress (loading), (c) Residual strain, (d) Mass normalized transformation work (loading).

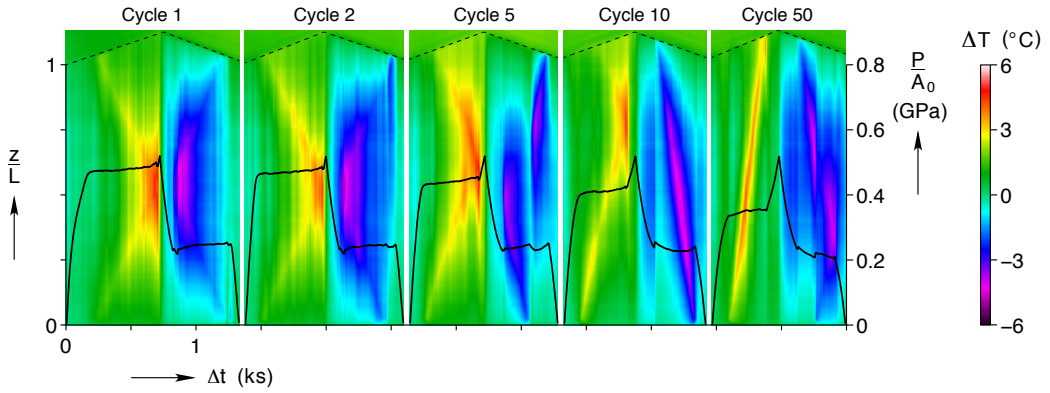

(a)

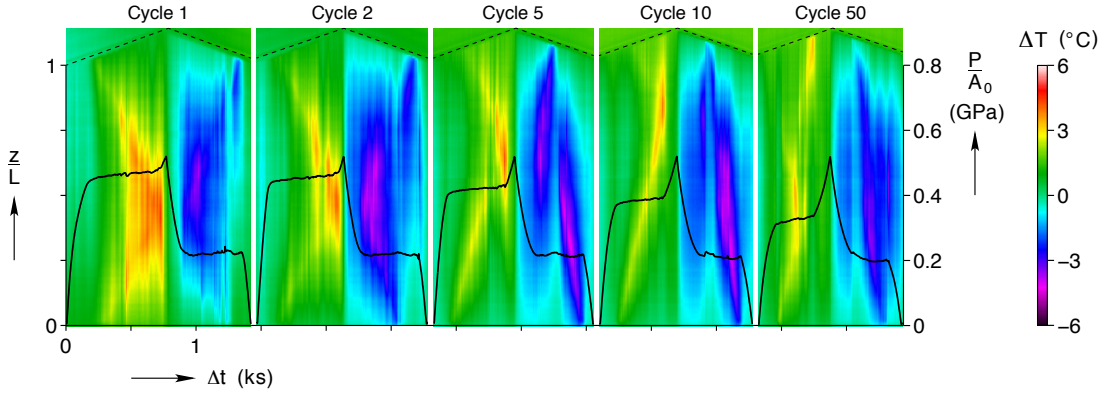

(b)

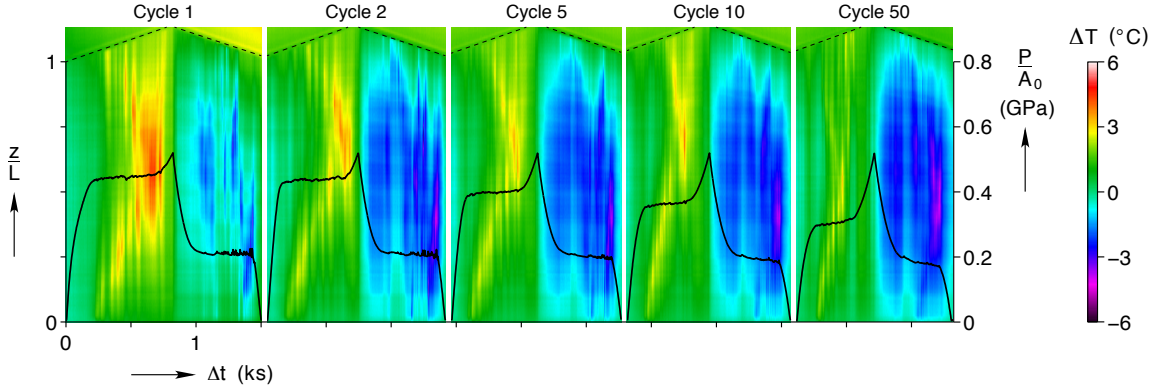

(c)

Figure 5.11: Contour plot of IR temperature field with overlaid stress history for select cycles. (a) 10.1° twist, (b) 17.8° twist, (c) 21.5° twist.

trace of visible latent heat released.

NiTi is understood to have a large amount of thermo-mechanical coupling and be very sensitive to the loading rate. This is caused by the Clausius-Clapeyron relation which couples transformation stress with temperature, and as latent heat is released with transformation the transformation stress also rises. The 10.1° twist which has a single distinct transformation front on cycle 50, would still have this large amount of thermomechanical coupling. The 21.5° twist, on the other hand, is shown to not have the same local heating on cycle 50. This means the 21.5° twist would have a reduced thermomechanical coupling and a reduced loading rate dependence. The reason for this is that the transformation becomes much more diffuse and uniform in the 21.5° twist. While the total latent heat released may remain constant, if the specimen is transforming over a larger spacial volume at any given instant, the latent heat is likewise distributed over a wider volume causing reduced local temperature increase. This conclusion is more evident in the subsequent DIC snapshots on cycle 50.

The stress and strain histories on cycle 50 of the cyclic shakedown experiment for each specimen are shown in Figure 5.12. The circled time labels in the stress histories (Figs. 5.12a,5.12c,5.12e) correspond to the DIC strain images in Figure 5.13. In the isothermal stress histories (Fig. 5.4), the initial rounding prior to the nucleation of the high strain martensite was attributed to primarily grip slippage, which was apparent from the strain histories. Here, on cycle 50 of the cyclic shakedown experiments, there is also initial rounding of the stress history. However, from the strain histories it is apparent that little grip slippage is occurring, but rather the majority of grip slippage occurred on the first cycle, creating a constant offset between the grip strain (δ/L) and virtual extensometer strain (δ_e/L_e). The reason for initial rounding in the stress history shown here is actually initial diffuse transformation prior to the transformation plateau.

Figure 5.13a shows the selected snapshots of the ε_{zz} strain field for the 10.1° twist on cycle 50 of the cyclic shakedown experiment. As mentioned previously, there is initial diffuse transformation from ① – ②. From ③ – ⑥ a distinct transformation front propagated from the bottom grip to the top grip, and the load peaked at ⑦. On unloading past ⑦, a single front began to propagate in reverse fashion from the top grip down towards the bottom grip, until a second front nucleated at the bottom grip at ⑨ and began propagating upwards. This second nucleation event is visible in Figure 5.12a at ⑨ as a small jump in the load.

The 17.8° twist shown in Figure 5.13b had two fronts propagating from either grip and coalescing towards the center of the field of view. There were only several diffuse low strain pockets visible, and a large amount of bending apparent at peak load in ⑦. Unloading (⑧

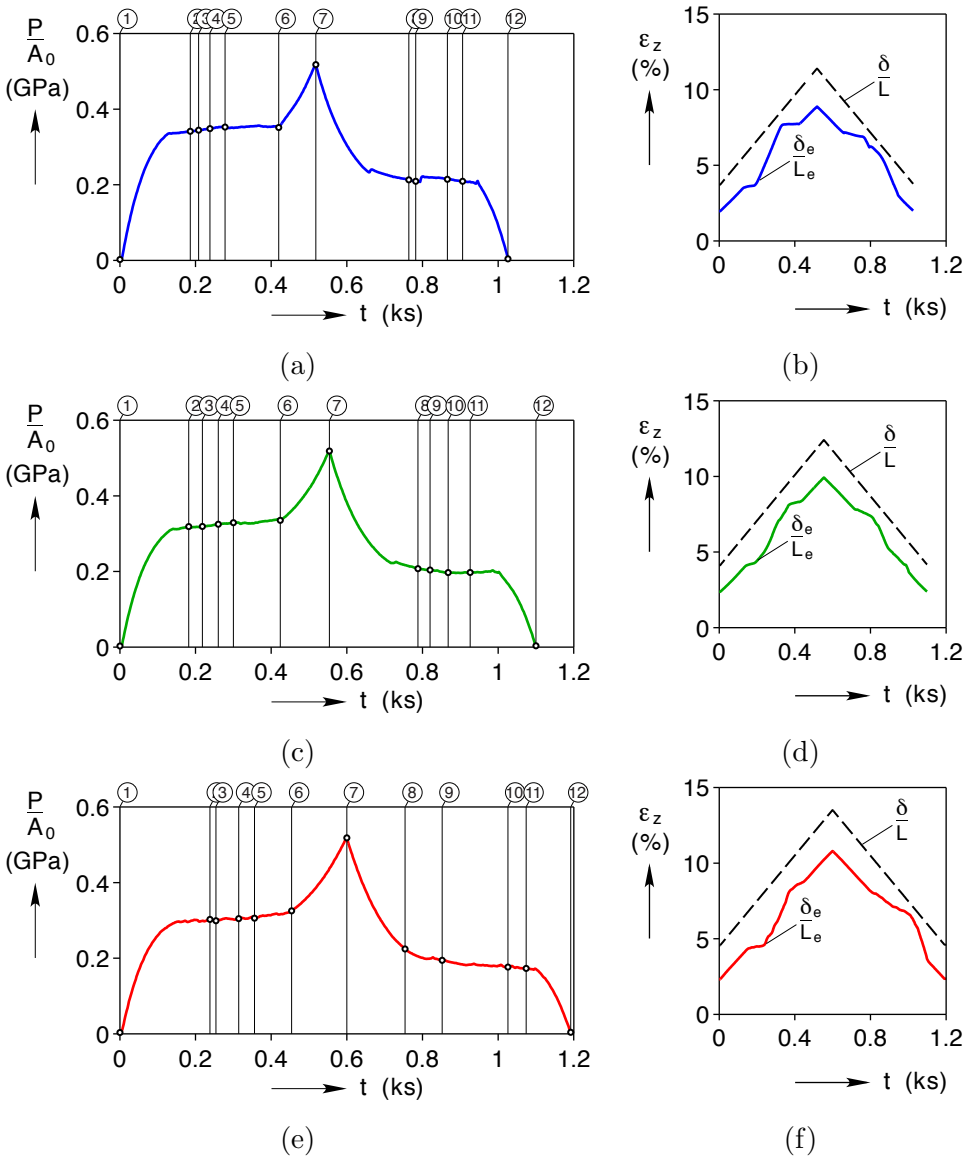

Figure 5.12: Stress history on cycle 50 of the cyclic shakedown experiments. (a) 10.1° twist, (b) 17.8° twist, (c) 21.5° twist. Circled time labels correspond to DIC strain images in Fig. 5.13.

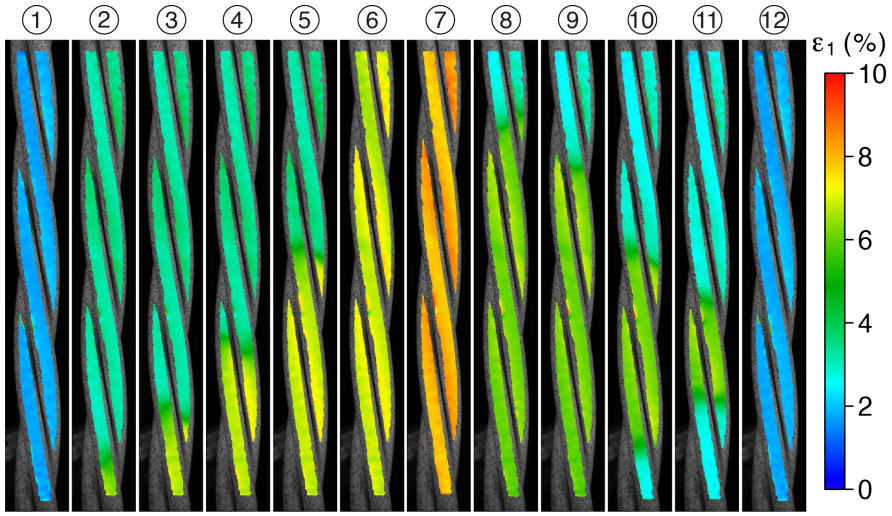

(a)

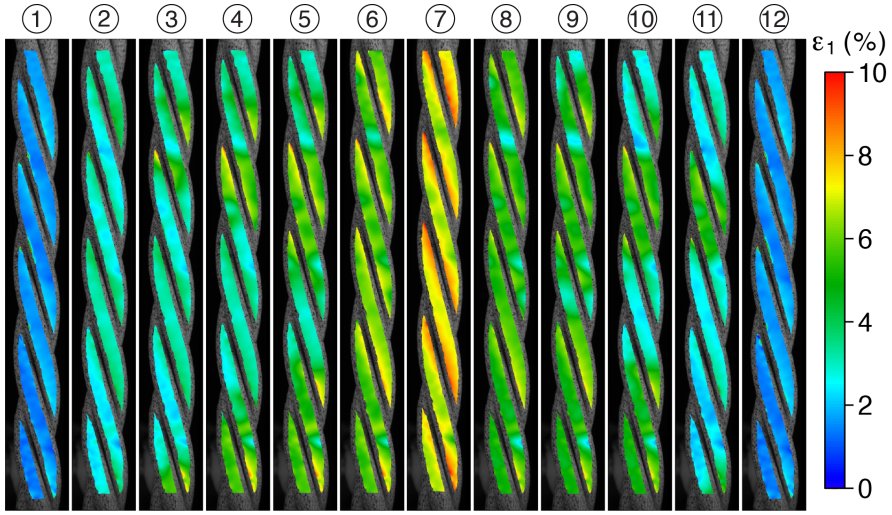

(b)

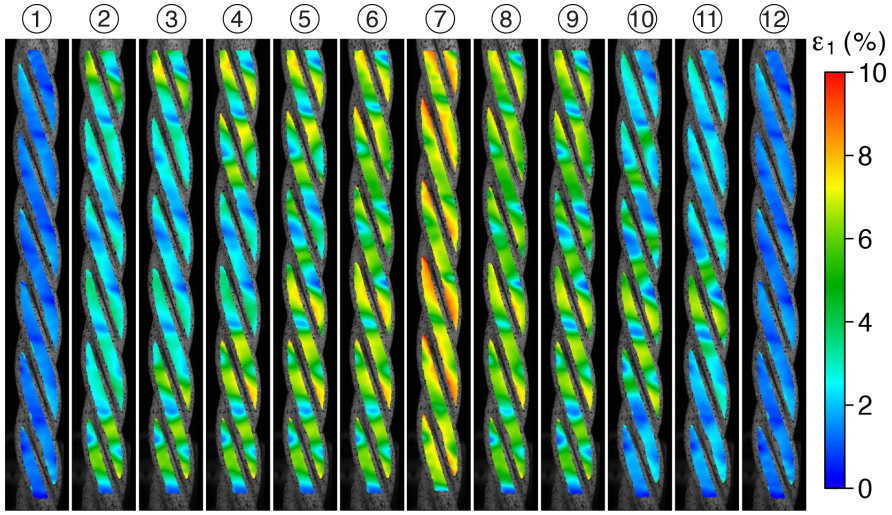

(c)

Figure 5.13: Snapshots of digital image correlation strain fields on cycle 50. (a) 10.1° twist, (b) 17.8° twist, (c) 21.5° twist. Circled image labels correspond to time labels in Fig. 5.12.

– (11)) progressed in a similar manner to loading. Overall, the 17.8° twist's strain response had less distinct transformation fronts than the 10.1° twist (as would be expected from the temperature fields).

Finally, the 21.5° twist shown in Figure 5.13c had the most diffuse transformation. While the material is in general transforming from both the top and bottom grips and progressing towards the center, there is no distinct front which can be identified. Rather, the transformation snakes between low strain pockets (which have stayed prominent and in the same positions since cycle 1), in a much smoother fashion relative to cycle 1. This twist, which was characterized by many nucleation events on loading on cycle 1, now has no visible nucleations and is transforming much more uniformly along the length of the specimen. This corroborates with the temperature data indicating that the transformation is occurring in a spatially more distributed nature. This increase in transformation uniformity reduces the thermo-mechanical coupling and rate sensitivity of the 21.5° twist relative to the other twists.

There has been a longstanding question of whether or not relative sliding is occurring between wires in a strand or cable. Reedlunn indicated that, based on lubrication tests, relative sliding was not thought to be present [72]. To investigate whether or not there were signs of relative sliding or even fretting occurring between the wires of these 1×3 twists, the cycled twist specimens and additional as-received and untested specimens were disassembled and examined in a scanning electron microscope (SEM) to view the contact area. Figure 5.14 shows SEM images of the 10.1° twist with a zoomed view of the contact region, for both the as-received and cycled samples. In the as-received specimen, the contact region has an apparent difference in surface roughness (with the smoother dark region being the contact region) that is thought to be caused by the fabrication process of the twist. The cycled specimen, in contrast, has signs of abrasion in the contact region indicating that there is relative motion between the wires and mild fretting in this shallow angle twist.

Similar SEM images for the 21.5° twist are shown in Figure 5.15. In this larger helix angle twist, it is clear that there is an increased amount of sliding and fretting indicated by the additional abrasion. Here, the contact region now showed additional discoloration as well as multiple scratch lines in loading axis direction indicating more of the oxide layer being worn away.

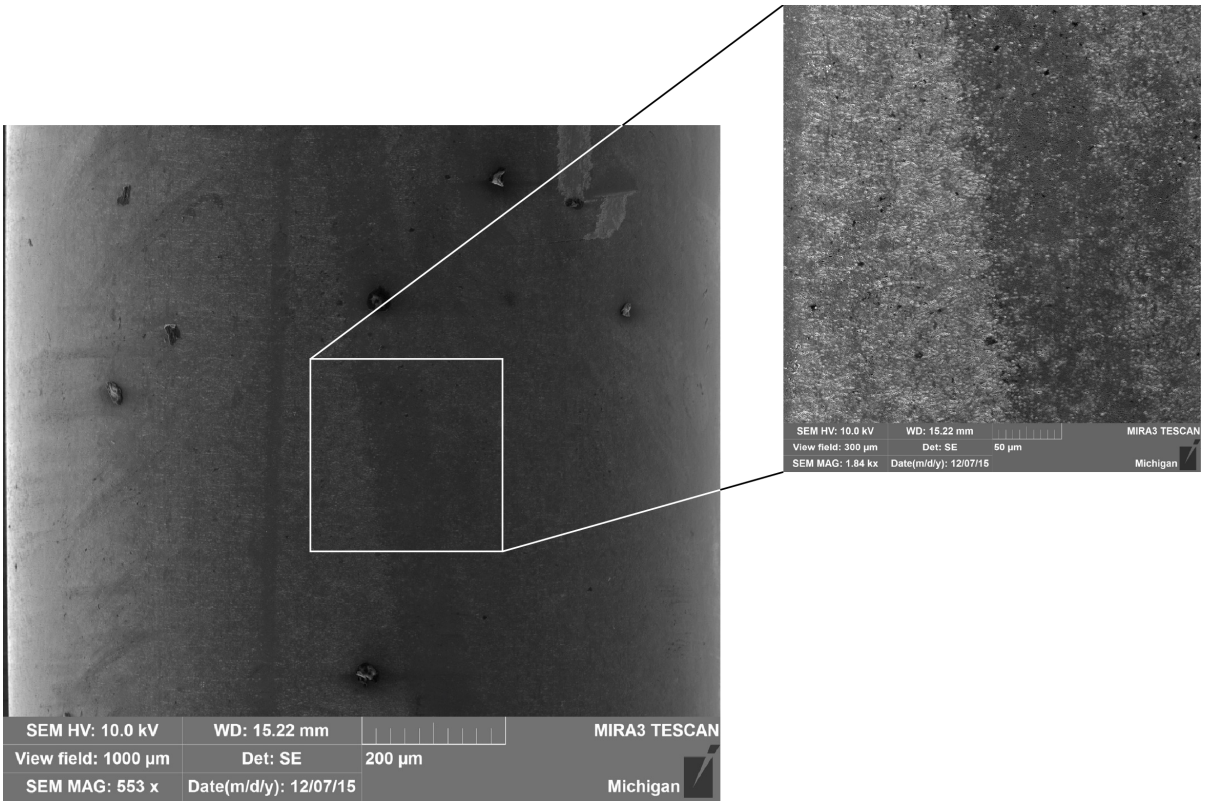

(a)

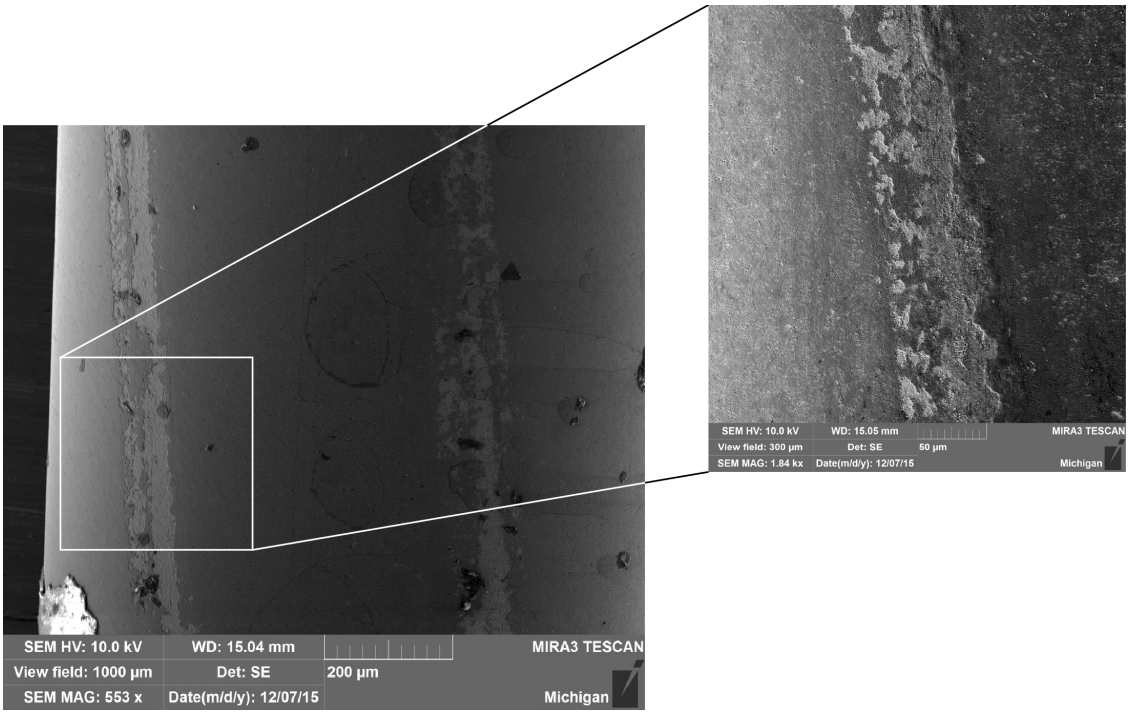

(b)

Figure 5.14: SEM images of 10.1° twist contact region. (a) As-received and not cycled. (b) After 50 cycles.

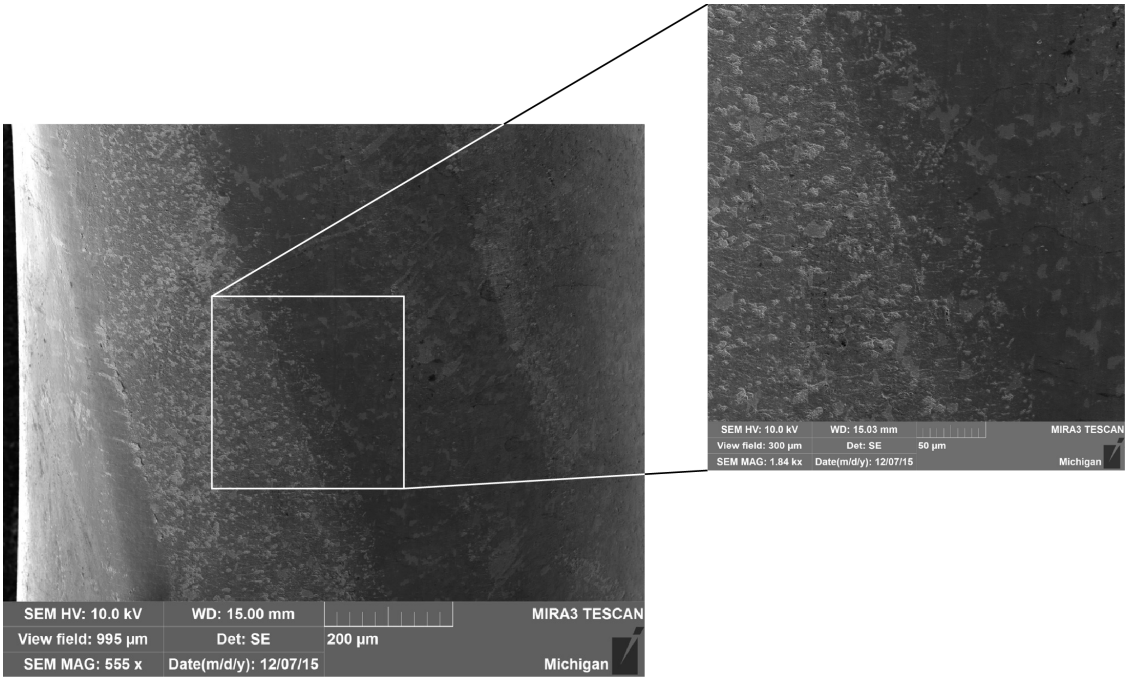

(a)

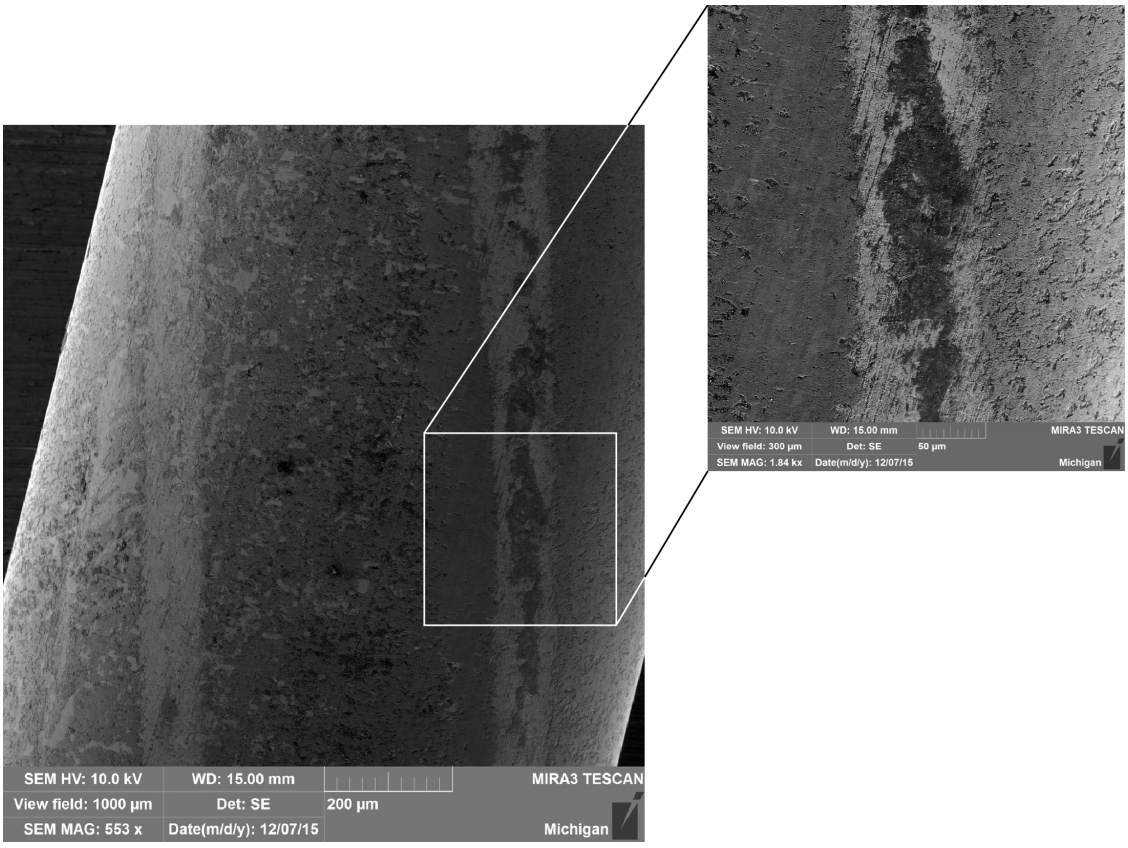

(b)

Figure 5.15: SEM image of 21.5° twist contact region. (a) As-received and not cycled. (b) After 50 cycles.

5.4 Finite Element Simulations

This section describes finite element simulations conducted using the Abaqus FEA [23] software package to explore the local contact behavior in the 1×3 twists. In section 5.2, experimentation revealed a periodic transformation pattern in the 21.5° twist that appeared to be caused by wire-to-wire friction and sliding. The finite element simulations were used as a method to better understand the role of friction and sliding, as well as the shift in transformation propagation behavior from a single front to a nucleation dominated one with increasing α. It has been shown by several researchers that a J2 plasticity model can capture many features of the stress induced phase transformation in NiTi [85, 82, 38, 53]. The superelastic transformation has many similarities with classic metal plasticity including a yield surface that can be modeled adequately well by the Von Mises stress and netting inelastic strains that are accompanied by no dilatation. This lends itself well to superelasticity, because the phase transformation is itself volume preserving. Our goal here is thus to model the loading portion of the superelastic tensile curves using a simple J2 plasticity model while capturing the local contact mechanics in order to explain the periodic propagating fronts witnessed in the 21° twist.

5.4.1 Material Model

To calibrate the J2 plasticity model, a uniaxial tension experiment was conducted on a straight NiTi wire of the same material as the twists (same ingot and lot number, and identical processing). Using the same setup as for the twists, the local strain field was captured using DIC and a virtual extensometer used to measure the axial strain. The straight wire experimental data, shown in Figure 5.16a, are overlaid with a simplified a series of non-monotonic fits to capture the material's unstable constitutive behavior [43, 94, 95]. This fits are close to trilinear, but have slight softening in the post-transformation region to better match the experimental data. The 20°C fit was made to approximate the constitutive material response of the experimental wire data, while the 10, 30, and 40°C curves add the temperature dependence. These additional fits are essentially adjusted 20°C curves based on the Clausius-Clapeyron relation, using 7 MPa/°C to shift the plateau stress. The motivation for adding in the temperature dependence was to stabilize the convergence of the simulations. Many investigators turn to artificial numerical damping to stabilize the problem, which does yield satisfactory results. It was decided, however, to use thermal effects as a source of damping because it yields a similar result while also having a more physical basis for the dissipated energy. Note that, in the simulations presented subsequently, the temperature

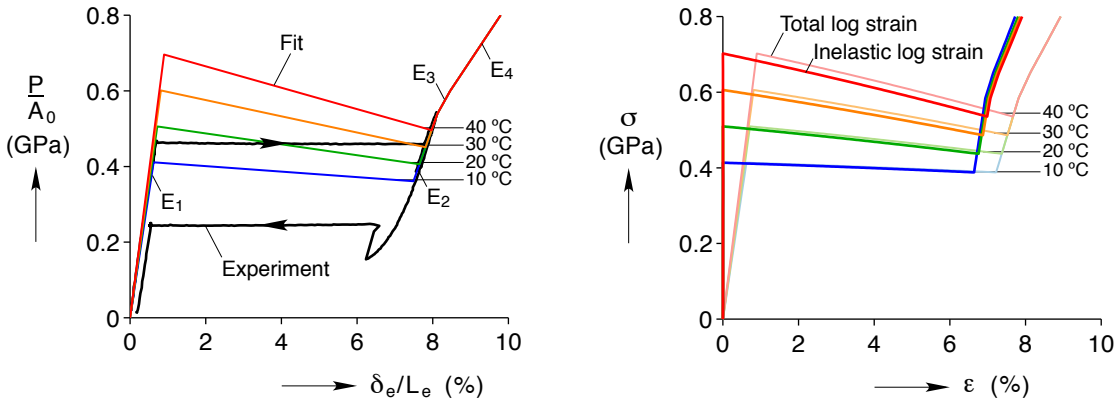

(a) (b)

Figure 5.16: Material model calibrated from a straight wire experiment. (a) Isothermal tension experiment on a single straight wire overlaid with a simplified material model fit, (b) Fit used for a material model showing total logarithmic strain and inelastic strain component.

Table 5.1: Material parameters using nominal stress and strain measures.

T (°C)	E_1 (GPa)	E_2 (GPa)	E_3 (GPa)	E_4 (GPa)	σ_p (MPa)	$\Delta\sigma_p$ (MPa)	ε^* (%)
10	66.0	28.0	18.0	15.0	386	25	6.2
20	70.5	28.0	18.0	15.0	456	50	6.2
30	74.0	28.0	18.0	15.0	526	75	6.2
40	77.5	28.0	18.0	15.0	596	100	6.2

rise was less than 1°C, and the net impact of the higher temperature material properties was quite small. The parameters used in the fits are summarized in Table 5.1. Here, σ_p represents the mean plateau stress, $\Delta\sigma_p$ is the difference between the nucleation stress and σ_p (with $2 \cdot \Delta\sigma_p$ being the total drop in stress across the transformation region), and ε^* is the transformation strain.

The J2 plasticity model requires the plastic (transformation) strain at corresponding Cauchy stress levels. The nominal stress and nominal strain of the fit can be converted to Cauchy stress and logarithmic strain through the equations

$$\sigma = \frac{P}{A_0}(1 + \frac{\delta_e}{L_e})$$

and

$$\varepsilon = \ln(1 + \frac{\delta_e}{L_e})\,.$$

Table 5.2: Material properties used in simulating thermal effects.

Property	Value	Units
Thermal conductivity (k)	3.6	W/m-K
Mass density (ρ)	6500	kg/m^3
Thermal expansion coefficient (α)	10	10^{-6}/K
Specific heat (C)	90	J/kg-K
Surface convective film coefficient (h)	50	W/m^2 K

The plastic component of logarithmic strain can then be calculated by,

$$\varepsilon_p = \varepsilon - \frac{\sigma}{E}\,.$$

The logarithmic strain and plastic component of the logarithmic strain are shown in Figure 5.16b. Other material properties that were constant in temperature are listed in Table 5.2. Note that the specific heat, thermal conductivity, and convective film coefficient were all scaled to limit the temperature rise to less than 1°C. This is similar to what was done by Shaw to correct for the latent heat (modeled as inelastic heat fraction) having a maximum of unity in Abaqus [82]. This work could be easily extended to model the thermal and loading rate dependent effects, but for now is limited to supplying a source of damping with a physical basis.

5.4.2 Mesh and Boundary Conditions

The meshes used for the straight wire and 1×3 twists are shown in Figure 5.17. The wires were partitioned in the center by a smaller wire (of one third diameter), to allow for two element types to be used. The outer partition used hexahedron (brick) elements, while the inner partition used wedge elements. This allowed for a uniform mesh to be generated while keeping the number of elements through the thickness lower than if only brick elements were used. Both element types were linear coupled temperature-displacement formulations, with the brick elements also having reduced integration (C3D6T and C3D8RT in Abaqus). The number of elements per wire was kept consistent between all the geometries. Each wire had 32 elements along the circumference of the circular cross-section, 6 elements through the thickness, and 150 elements along the length of the wire. This totaled 9600 brick elements and 4800 wedge elements, totaling 1440 elements. There were two imperfections imposed in the mesh. First, at the bottom of each wire in the twists, a 0.1mm chamfer was placed to create a stress concentration to promote transformation at that end first. Second, each

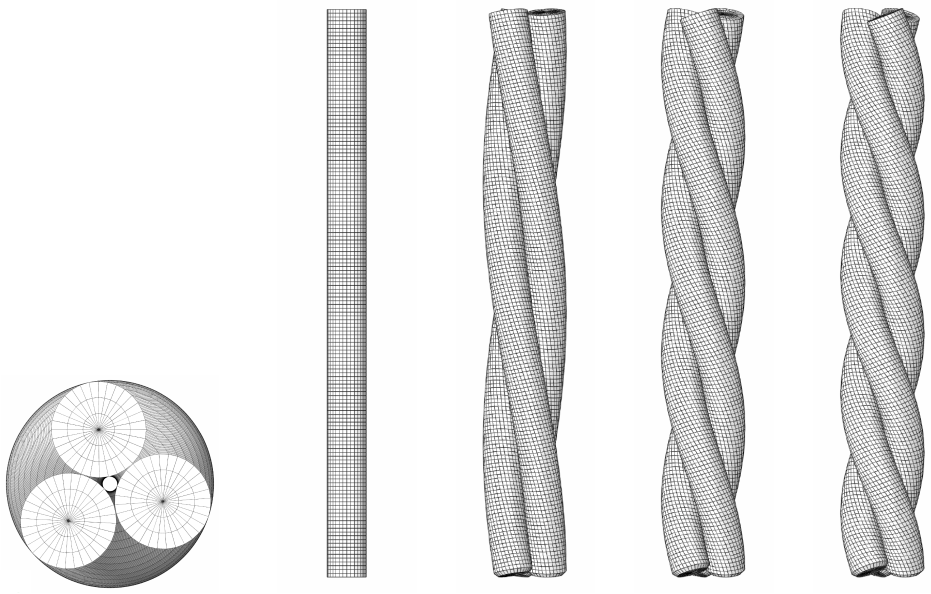

(a) (b) (c) (d) (e)

Figure 5.17: Meshes used in the finite element simulations. (a) Top view of 10.1° twist showing circular cross-section with wedge and brick elements. (b) Straight wire. (c) 10.1° twist. (d) 17.8° twist. (e) 21.5° twist..

wire diameter was made 0.5% larger (1.0251 mm) than reality, in order for the wire surfaces to initially penetrate each other in the twist. This triggered Abaqus to make strain-free adjustments to the nodes that were penetrating surfaces prior to the loading step, effectively establishing initial contact. If this was not triggered (by having no penetrating nodes), the twists were found to have additional artificial flexibility during the loading step as Abaqus' solver made contact.

Enforcing boundary conditions to exactly match the grips used in the experiments is complex, and more simple boundary conditions were chosen for simplicity. The bottom surface of each wire was clamped in all directions, and on the top surface a displacement was specified on a specific node in the axial direction with displacements in the other two directions being held clamped. A kinematic constraint tied the top surface nodes displacements together, allowing for the total end load to be measured at the node where the displacement was specified. To measure the macroscopic strain in a similar manner to experiments, the coordinates of surface nodes approximately 9mm apart (1.5mm from either grip to eliminate grip effects) were tracked on each wire and used as a virtual extensometer. Thermally, the end surfaces were fully insulated, and the outer surface had convective heat transfer enabled. For the twists, general contact was used with penalty friction ($\mu = 0.4$) enforced in the tangential direction, and hard contact enforced in the normal direction.

5.4.3 Straight Wire Simulation

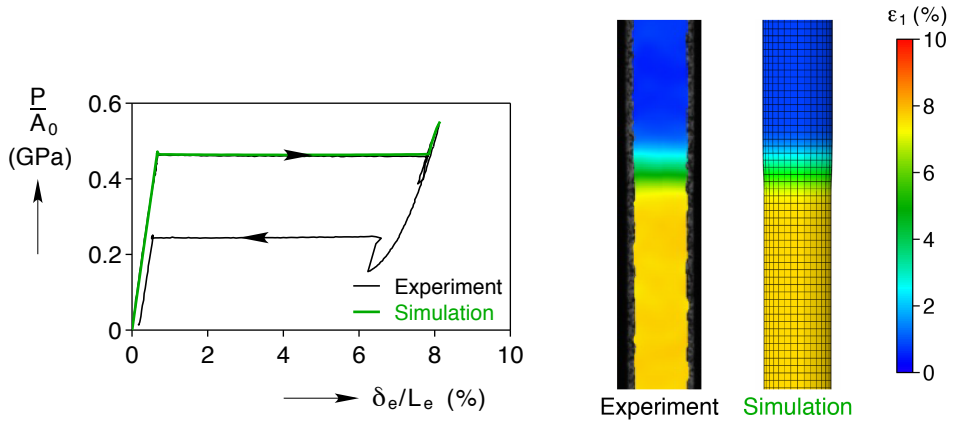

(a) (b)

Figure 5.18: Comparison of tensile response of straight wire experiment and simulation. (a) Mechanical response showing normalized force and normalized displacement, (b) Local strain field (nominal strain) during transformation plateau (at approx. 4% macroscopic strain and showing 11% of the free length for the experiment and 40% for the simulation).

The straight wire experimental data (which was used to calibrate the material model), is shown to be reproduced by the simulation very well, as shown in Figure 5.18. The elastic, plateau, and post-plateau macroscopic mechanical responses all match the experimental data. The localized transformation front (Fig. 5.18b) and strain gradient also appears consistent. Both experiment and simulation had a single localized front that propagated from the bottom to top grip. In the experiment, the bottom grip was likely a favorable nucleation spot due to the grip stress concentration. The simulation had an imperfection implanted at the bottom edge of the wire, in order to make that end slightly favorable for nucleation. Note that the constitutive material model had a non-monotonic trilinear (up-down-up) behavior, the wire exhibits a structural response with a smooth, flat transformation plateau. This is because the negative tangent modulus of the transformation region is unstable, and similar to a snap-through buckling problem, material points jump from one stable branch to the next causing a strain localization and discontinuity. While the straight wire is a comparatively simple case, having shown that straight wire data can indeed be reproduced well provided some confidence in the model before adding in the additional complexities of the 1×3 twists including: contact, friction, and increased bending and twisting of the material.

5.4.4 1×3 Twist Simulations

The 1×3 twist simulation data are summarized in Figure 5.19. Overall, the data shows an interesting progression from 10.1° to 21.5° twists. All three twists exhibit a flat transformation plateau, but there is an increased rounding in towards the end of the plateau and a lower tangent modulus in the 21.5° twist (Figs. 5.19a, 5.19c, and 5.19e). The 10.1° twist's strain field (showing major principal strain ε_1) in Figure 5.19b had a wire-like response. This is evident from only a small amount of bending and a single localized transformation front in each wire. The 17.8° twist (Fig. 5.19d) had similarly only a single transformation front per wire, but exhibits a large amount of bending. The 21.5° twist's response bifurcates from the single front behavior of the other twists, and had multiple nucleation fronts along the length of the twist, as shown in Figure 5.19f. These nucleation regions leave behind pockets of untransformed material, shown by the low strain values. Outside of the pockets and in the nucleated regions, the strain is rather large and comparable to the strain in the 10.1° twist (approx. 7.5%), and appears to have little bending through the thickness. After the periodic nucleations have fully traversed the length of the twist, the transformation continues by growing the nucleated regions into the untransformed pockets (⑤–⑥).

The 1×3 twists simulation data are shown to have good agreement with the experimental DIC data in Figure 5.20. Here, the end twisting moment ($M_z R/J_0$) and nominal stress (P/A_0) are cross-plotted against the normalized axial strain (δ_e/L_e) to compare the macroscopic mechanical responses, and the strain field showing ε_1 compared between experiments and simulations. The macroscopic stress-strain responses have good agreement and appear to capture the effects of increasing the helix angle well, including drop in plateau stress. The initial elastic tangent modulus deviates in the experiments because of some early transformation of well-oriented grains that is not accounted for in the simulations. The twisting moment data have reasonable accuracy between the simulations and experiments, but the 10.1 and 17.8° twists do have slightly higher plateau moments. It will be shown later that the twisting moment during the plateau is very sensitive to how friction is modeled (and the coefficient of friction μ). As friction is very complicated and only a simple Coulomb model was applied here, it is not surprising that there is less accuracy in how close the simulation twisting moment data matches experiment data during the transformation.

There is also very good agreement in the strain fields, shown in Figures 5.20b, 5.20d, and 5.20f. In both experimental DIC and simulation strain fields, there is mostly uniaxial tension in the 10.1° twist, but increased bending deformation in the 17.8° twist. In the 21.5° twist there again are the periodic nucleations and distinct low strain pockets. Through the

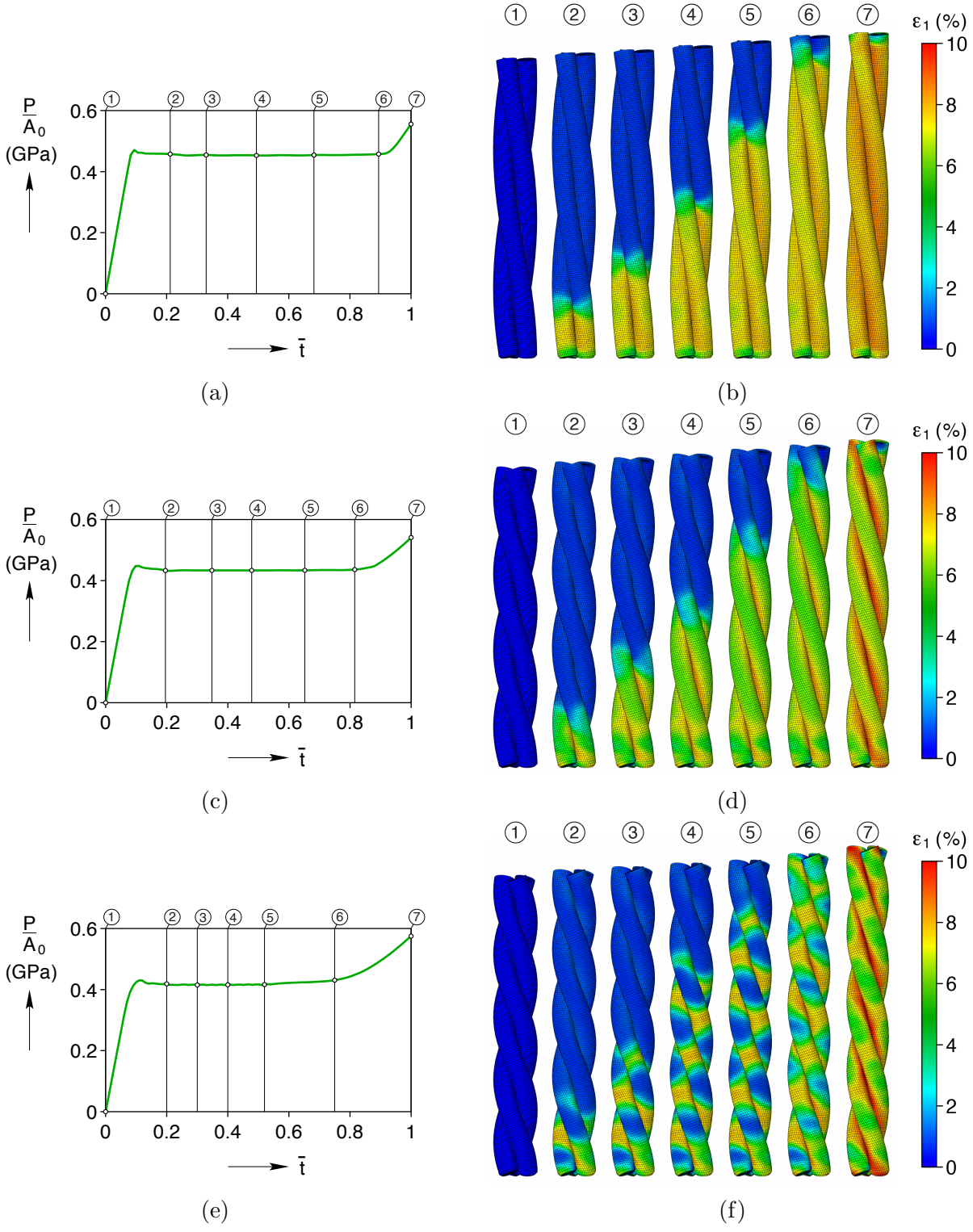

Figure 5.19: Simulation load history and strain field images. (a) 10.1° twist, (b) 17.8° twist, (c) 21.5° twist. Circled time labels correspond to the simulation image labels.

comparison of the mechanical responses and strain fields, it is shown that the finite element simulations and material model are indeed predicting the mechanical and transformational behavior of the NiTi 1×3 twists very well. Having shown this, local contact mechanics behavior can be examined with more confidence to better explain the role of friction in influencing the shift in propagating behavior shown in the twists.

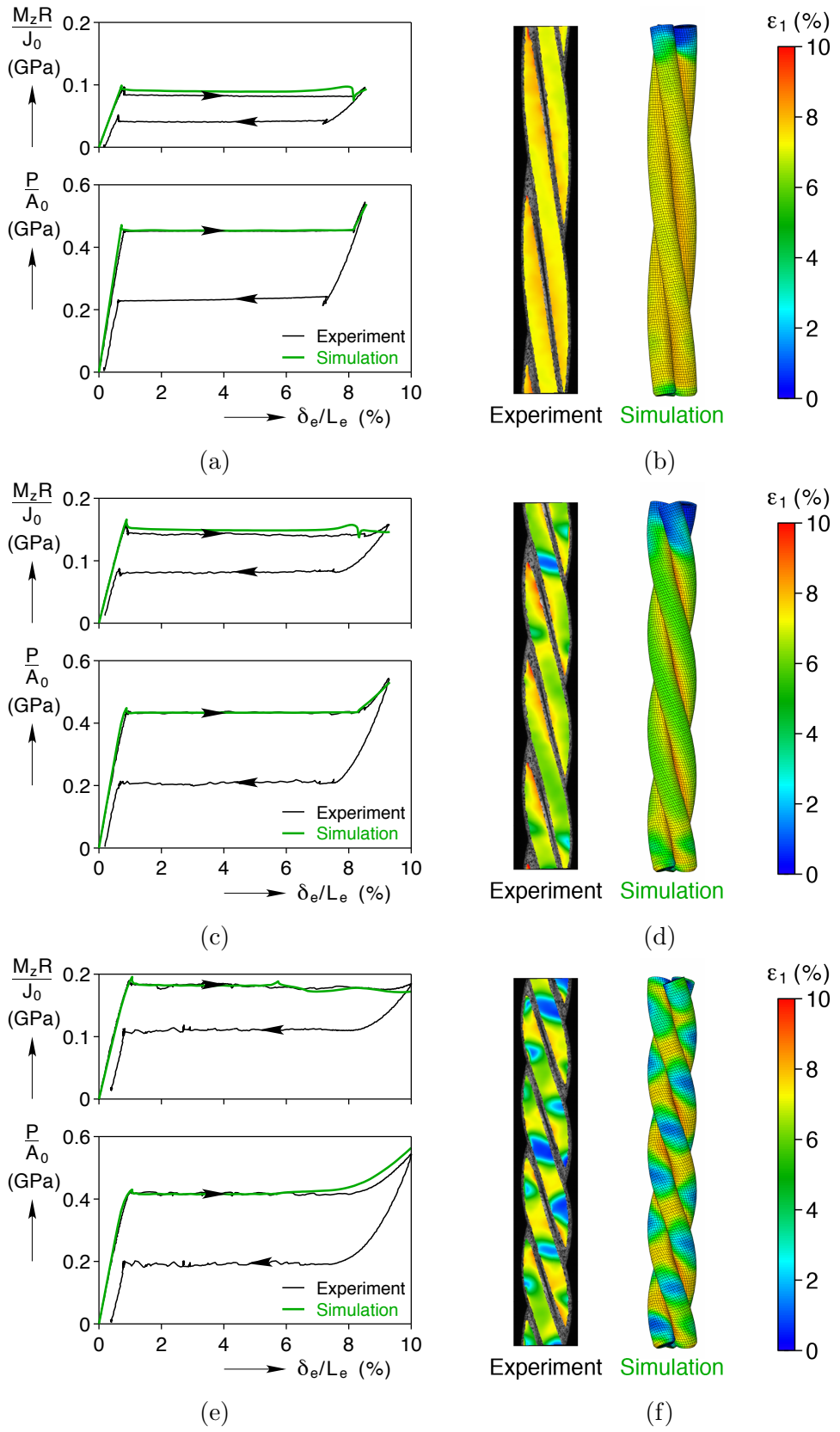

Figure 5.20: Comparison of simulation and experiment data. (a) 10.1° twist, (b) 17.8° twist, (c) 21.5° twist.

5.4.5 Contact in the Twists

To facilitate better interpretation and visualization of the contact area, the outer surface of a wire in a given twist was mapped from cartesian coordinates to a 2D planar surface using unit vectors defined in an orthonormal frame (*Frenet frame*). The unit vectors, $\mathbf{t}$, $\mathbf{n}$, and $\mathbf{b}$, are called the *tangent*, *normal*, and *binormal* vectors that can follow any smooth curve through 3-dimensional space. The $\mathbf{t}$ unit vector, as the name implies, points in the tangent direction of the curve. The $\mathbf{n}$ unit vector is related to the derivative of $\mathbf{t}$, and if the curve is a helix, points inwards to the center of the helix. The last unit vector, $\mathbf{b}$, points in an orthogonal direction to the previous two.

A helical curve describing the centerline of a wire in its reference state in any given twist can be defined in cartesian coordinates as,

$$\mathbf{r}(s) = \frac{d}{2}\sin(2\pi\frac{s}{\Delta s})\,\mathbf{i} + \frac{d}{2}\cos(2\pi\frac{s}{\Delta s})\,\mathbf{i} + s\cos\alpha\,\mathbf{k}\,. \tag{5.1}$$

Note that curve has been parametrized by the arc-length parameter s (with Δs being the length of one coil). The unit vectors in the orthonormal frame are then found by taking derivatives and normalizing to unit magnitudes,

$$\mathbf{t}(s) = \frac{\mathbf{r}'(s)}{||\mathbf{r}'(s)||} \tag{5.2}$$

$$\mathbf{n}(s) = \frac{\mathbf{t}'(s)}{||\mathbf{t}'(s)||} \tag{5.3}$$

$$\mathbf{b}(s) = \mathbf{t}(s) \times \mathbf{n}(s)\,. \tag{5.4}$$

The plane created by the unit vectors $\mathbf{n}$ and $\mathbf{b}$ create what is called the *normal plane*. In the normal plane, the cross-section of a wire in a twist is perfectly circular, and the circumference can be written as,

$$\mathbf{D}(s,\psi) = \frac{d_w}{2}\cos\psi\,\mathbf{b} + \frac{d_w}{2}\sin\psi\,\mathbf{n}\,, \tag{5.5}$$

which is parametrized by the angular coordinate ψ. Finally, the reference coordinates of any material point on the surface of a wire in any given twist can be found by the arc-length and polar coordinates s and ψ by the relation,

$$\mathbf{R}(s,\psi) = \mathbf{r}(s) + \mathbf{D}(s,\psi)\,. \tag{5.6}$$

In order to map the data (i.e. strain tensor or contact pressure) from the wire surface to a 2-dimensional $s - \psi$ plane, the data at each material point on the surface of a wire, together with the reference material coordinates, was first output from Abaqus FEA. These reference coordinates were then used to inversely solve Eqn. 5.6 for the reference s and ψ coordinates. In short, this provided the link between the finite element node numbers and the reference coordinates in the s-ψ space. The strain tensor data was then first rotated from cartesian coordinates (i, j, k) to the orthonormal frame coordinates (t, n, b), and then to a polar-orthonormal frame (t, r, ψ), where r is the radial direction. For plotting in dimensional units, ψ was multiplied by d_w to express the polar angle in terms of the position along the circumference, c.

The strain in the arc-length direction (ε_{ss}) on surface of a wire in the 10.1° twist is shown in Figure 5.21a. Five instances in time ($\bar{t} = 0.30, 0.35, 0.40, 0.45, 0.50$) were selected to show progression of the localized transformation front. The contact pressure (σ_{press}) for these same instances (Fig. 5.21b) shows two lines of contact on the wire surface, with two points of large stress concentrations.

The σ_{press} and radial strain (ε_{rr}) data were extracted from the left line of contact (at approx. c = 1.15mm), and shown in Figure 5.22. With each time shown, there is a single large contact stress peak (with several smaller oscillations). The material transforms in an isochoric manner, causing inward contraction of the wire and negative ε_{rr}. These data show that there is a stress concentration occurring near but slightly leading the transformation front. As the twist is pulled in tension, the bending deformation of the wires causes inward pressure to be applied between the wires at the contact area. However, as the wires transform, there is radial contraction *away* from the point of contact. This causes a decrease in contact stress just behind the transformation front, and in reaction an increase in contact stress just before the transformation front. The finding that a transformation front is accompanied by a local peak in σ_{press} is an important finding for explaining the behavior of the 21° twist subsequently.

Sequential images of the 21° twist showing ε_{ss} and σ_{press} in Fig. 5.23 show a nucleation event unfolding in time. The 21° twist is characterized by these periodic transformed and untransformed regions, that appear as a diamond-pattern in the arc-length space. The contact area (marked by two parallel vertical lines of high σ_{press} magnitude) is now shown to have multiple large stress concentrations, rather than one distinct concentration seen in the 10.1° twist. It is difficult to conclude much from the multiple σ_{press} concentrations, but one region is circled for emphasis. There is a stress concentration circled in the first image at $\bar{t} = 0.34$, which, with progression in time, first moves in the positive s direction then

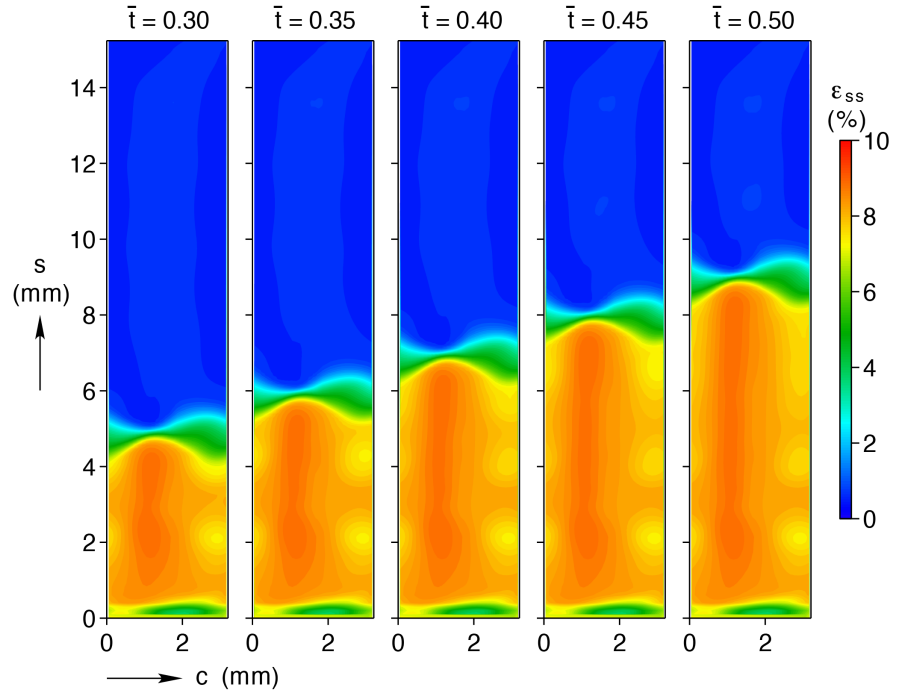

(a)

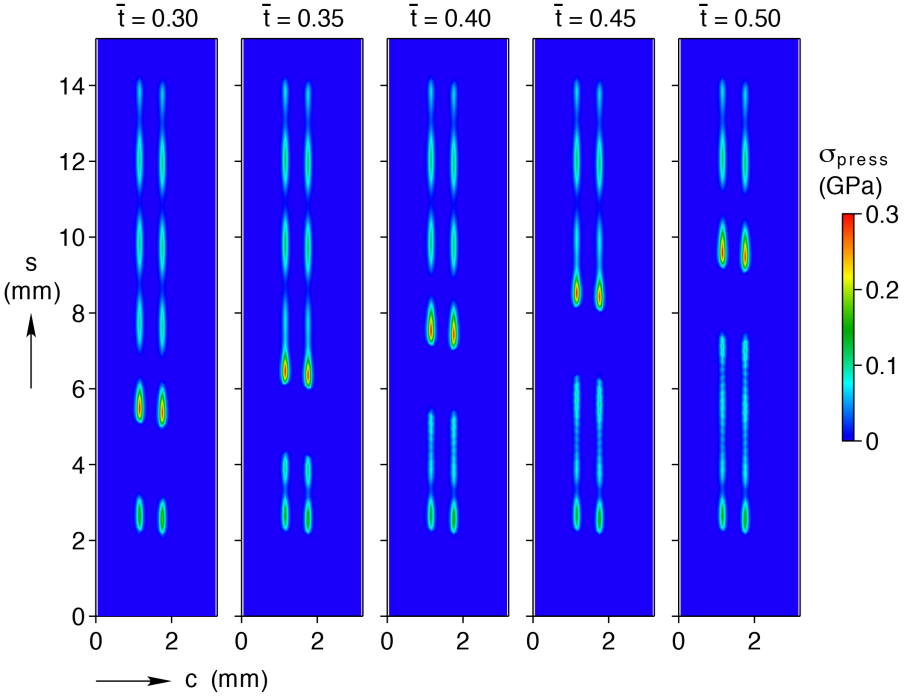

(b)

Figure 5.21: The surface of one wire in the 10.1° twist mapped to the arc-length parameter s and circumference parameter c space. (a) Strain in arc-length direction. (b) Contact pressure.

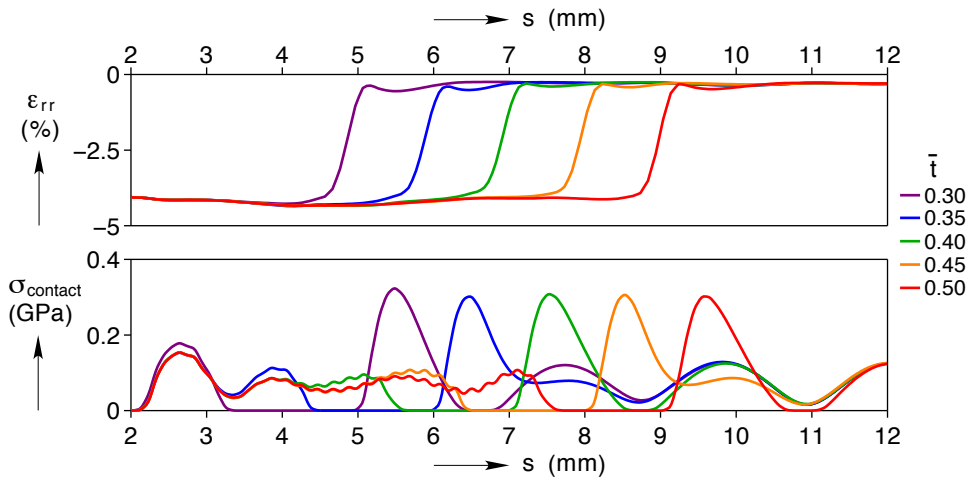

Figure 5.22: Data extracted from the surface of the 10.1° twist along the line of contact at approximately $c = 1.15$ mm showing contact stress and the radial strain component.

disappears from view by $\bar{t} = 0.39$. This transition corresponds to a nucleation event when viewing the ε_{ss} field.

The σ_{press} and ε_{rr} data of one wire in the 21° twist along the line of contact at $c = 1.15$ mm are compared in Fig. 5.24. Here, ε_{rr} shows a front that progresses in the $+s$ direction from $\bar{t} = 0.34$ to $\bar{t} = 0.37$, but is then arrested and a nucleation event skips over the arrested region of material. Note that the single local peak in ε_{rr} around $s = 0.57$ is the untransformed region between two transformation fronts. In the σ_{press} data near this peak, there are two local pressure peaks (one for each transformation front). The peak in σ_{press} located at approximately $s = 7$ mm grows towards an asymptotic limit as the progressing front reaches its corresponding limit.

Moreover, there is a non-monotonic σ_{press} peak around $s = 9$ mm, corresponding to where the progressing front was arrested and new transformation front was nucleated. From $\bar{t} = 0.34$ to $\bar{t} = 0.36$ the σ_{press} steadily increases, but from $\bar{t} = 0.36$ to $\bar{t} = 0.39$ there is a marked drop in pressure with the nucleation event.

These data indicate that, for the 21° twist, there is a correlation between the height (in s) of a transformed region of material, and contact pressure at the transformation fronts on either end. This is caused by the transformed region, which has a large negative ε_{rr}, being suspended out of contact with the neighboring material. The more material there is which is out of contact, the higher the reaction force that is required to maintain equilibrium. Thus the contact pressures on either end of the transformed region grow, until the energy required to progress the current front is higher than the energy to required create a new

transformation front. By nucleating a new transformation region, the contact pressure is then split between the old arrested front and the new nucleated front, causing the drop shown in the data. The contact pressure directly increases the resistance to sliding through friction, and the contact shear stresses developing are thought to suppress the continuation of the multiple transformation fronts.

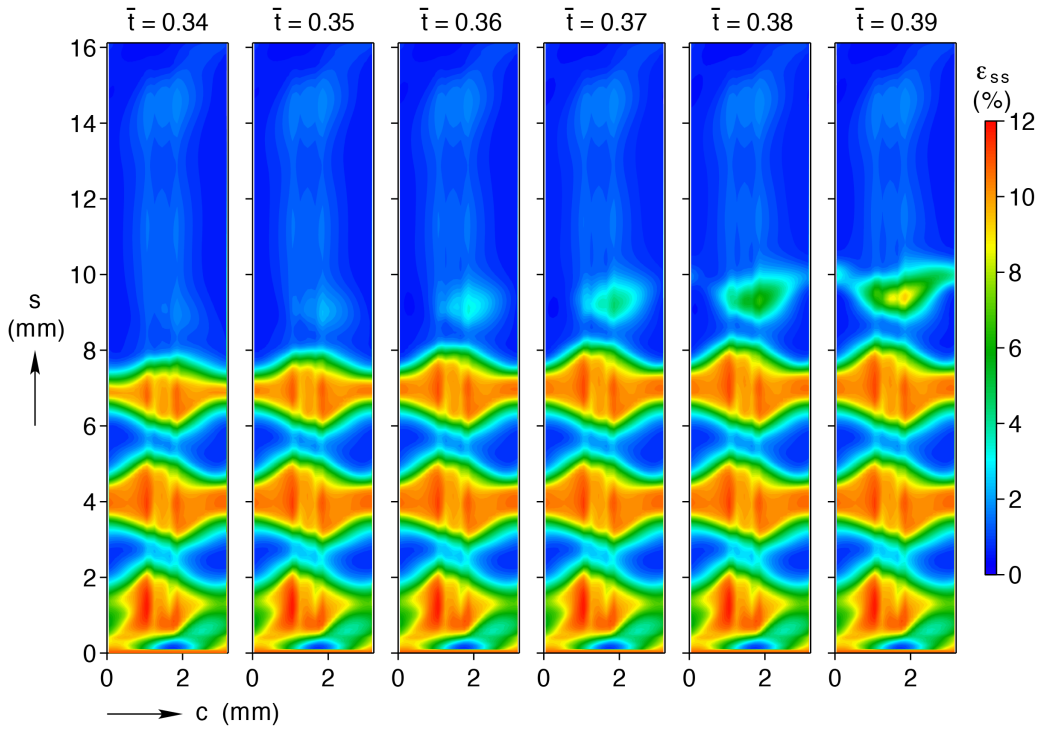

(a)

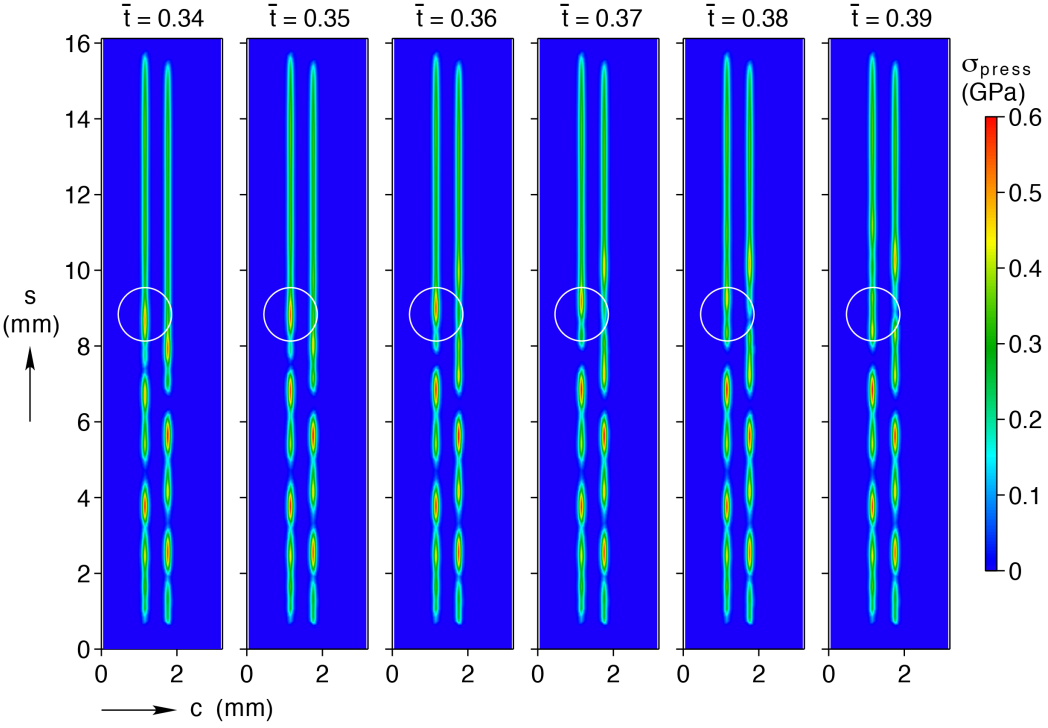

(b)

Figure 5.23: The surface of one wire in the 21.5° twist mapped to the arc-length parameter s and circumference parameter c space. (a) Strain in arc-length direction. (b) Contact pressure.

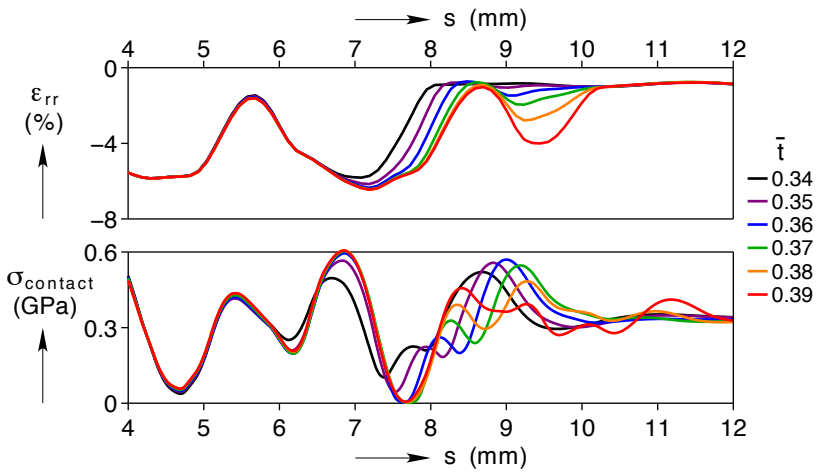

Figure 5.24: Data extracted from the surface of the 21.5° twist along the line of contact at approximately $c = 1.15$ mm showing contact stress and the radial strain component.

5.4.6 Effect of Friction

Additional friction coefficients of $\mu = 0$ and $\mu = 4$ were tested with the 21.5° twist model to study the role of friction in both the macroscopic mechanical response and the periodic strain localizations. The results are summarized in Figure 5.25.

The primary effect of μ in the macroscopic mechanical response data is shown to be a shift in the axial transformation plateau stress, and change in slope in the post-plateau region. The reaction torque data was very sensitive to a change in μ. The frictionless case unexpectedly had the largest reaction torque during the initial nucleation, followed by a steep negative slope with progressing transformation.

The most notable difference in the strain fields was in with the frictionless case, which almost entirely lacked the low strain pockets shown in the cases with friction. This corroborates the finding that the σ_{press} and friction are the primary cause of the periodic strain localizations found in the 21° twist.

5.5 Conclusions

This study of superelastic 1×3 twists was motivated by the desire to better understand the role that different modes of deformation (such as bending and twisting) and contact mechanics had in the unstable stress-induced transformation of cable-like structures. In that effort, twists with varying helix angles were studied using detailed experimental measurements and

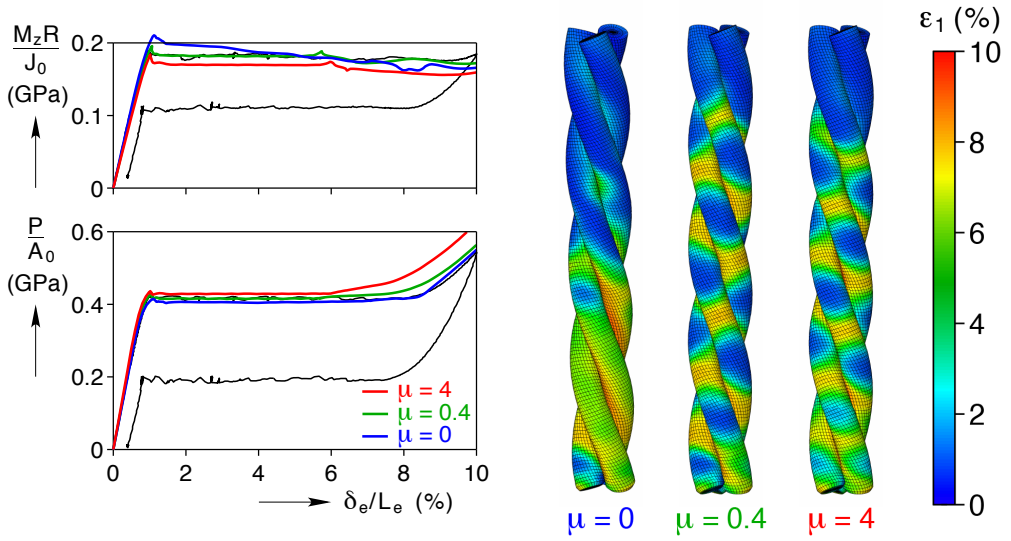

(a) (b)

Figure 5.25: The effect of varying the friction coefficient. (a) Macroscopic mechanical response. (b) Strain field.

numerical simulations. Periodic transformation instabilities in the largest helix angle twist were discovered, which initially appeared to be caused by local friction and sliding between the wires in the twist. Cyclic tests at a faster rate showed a reduced rate sensitivity and local heating in the 21.5° twist during later cycles compared to the 10.1° twist, while SEM images revealed increased fretting in the same twist.

Finite element analysis was utilized to model the unstable phase transformation using a J2 yield criterion, which was calibrated off of straight wire experimental data. When this model was applied to the 1×3 twists, the macroscopic mechanical responses and local strain effects were shown to be predicted with good accuracy. Further investigation into the contact areas between the wires revealed stress concentrations at the transformation fronts, which are thought to be responsible for the periodic instability in the 21.5° twist. Simulations with varying friction coefficient further corroborated this claim, by showing that the periodic instability could be suppressed when there is frictionless sliding.

CHAPTER 6

Convective Heat Transfer of Springs

Helical wires represent a basic geometric structure in ubiquitous use in consumer and industrial applications, many of which depend on heat transfer between the helix and ambient fluid. Some examples are resistive heating elements in air heaters and automotive springs under heavy use [58, 30]. Numerous references exist for the heat transfer of straight wires and cylinders in forced-convection crossflows, applicable to hot-wire anemometry [81, 88] and tube-bundle heat exchangers [99, 98]. We were unable, however, to find in the open literature any heat transfer data or correlations for helical objects in a cross-flow.

A more recent application of helical heat transfer involves the use of shape memory alloy (SMA) springs as both thermal actuators and energy harvesters. An SMA waste heat engine can be constructed from a continuous loop of SMA spring, which generates power through expansion and contraction as it is drawn through a sequence of hot and cold airflows [56]. Heat transfer between the SMA spring and these crossflows was quickly determined to be a critical limiting feature of the engine power. Furthermore, the problem was complicated by two facts: (1) relative motion of the SMA spring and the airflows induced an effective angle of attack (oblique crossflow) that changed with position, and (2) the spring underwent periodic stretching and contraction as it moved through the engine, making the effective angle of attack vary with location within the loop. Thus, a need existed for experimental data across a large parameter space, spanning various flow velocities, angles of attack and spring stretch ratios. This motivated the experimental program described herein to measure the effective heat transfer coefficients and to establish a dimensionless heat transfer correlation suitable for simulation models of the heat engine [19].

This chapter presents heat transfer experiments performed on straight wires and springs made of steel, with known electrical resistance-temperature properties, across a moderate range of airflows for a range of spring stretch ratios (spring pitch) of a selected spring index.

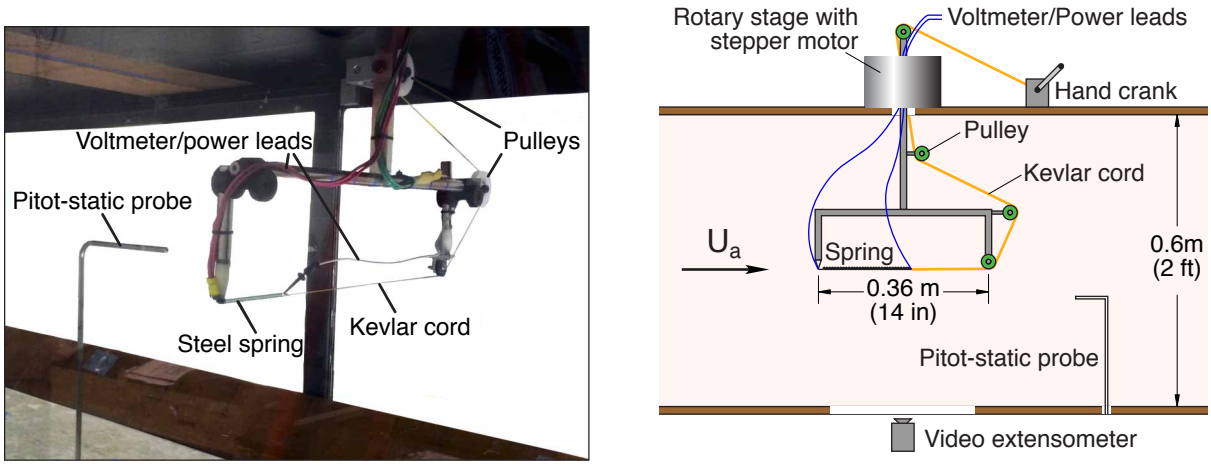

(a) Photograph of wind tunnel setup

(b) Schematic of setup (side view)

Figure 6.1: Experimental setup in the wind tunnel.

To validate our setup, heat transfer data is first reported on straight wire of several wire diameters, angles of attack from perpendicular to parallel flow, and flow speeds (Reynolds numbers from 2 to 500) and compared to known theoretical and empirical correlations. Heat transfer data on springs are then shown under various spring stretch ratios, angles of attack, and flow speeds. In particular, an interesting non-monotonic dependency on angle-of-attack is discovered.

The heat transfer data on springs are then analyzed using three different methods.. First, a simplistic heat transfer model is attempted, based solely on the projected frontal area, that captures the heat transfer to first order accuracy. Second, a large number of computational fluid dynamics (CFD) simulations (using no fitting parameters) are shown to validate the measurements, gain further insight into the spring's non-monotonic heat transfer phenomena, and to visualize the nonuniform heat transfer coefficient on the surface of the spring. Third, a dimensionless empirical correlation is developed and fitted to the CFD data that accurately captures the heat transfer dependencies across the range of experimental parameters studied. Note that the majority of the effort for this third aspect involving an empirical correlation was completed by John Shaw.

6.1 Experimental Setup and Procedure

Our approach to measure forced-convection heat transfer was similar to the calibration step used in hot-wire anemometry. That is, the remote air flow speed was measured by a pitot-

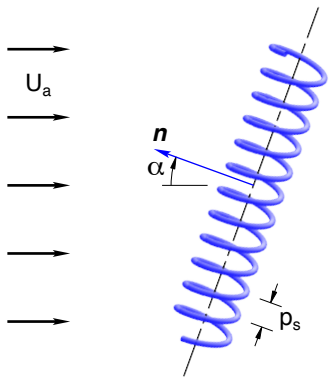

Figure 6.2: Schematic of spring in crossflow (top view).

static probe, a wire or spring specimen was heated by electric current, and the temperature rise was inferred from steady-state measurements of voltage and electrical current using a calibrated electrical resistivity–temperature correlation. The average heat transfer coefficient (h) was then calculated at a selected temperature rise (100 ℃) using the measured dissipated electrical power. The voltage drop was measured across the specimen, and the electric current was measured using a high-quality shunt resistor (0.10 Ω) in series. The histories of voltage, current, and pressure transducer signals were simultaneously captured by a computer at 0.1 s intervals during each experiment.

6.1.1 Wind Tunnel Setup

The experiments were performed in a 0.6 m×0.6 m wind tunnel in the Aerospace Engineering Department at the University of Michigan (UM) at airflow speeds in the range $4 \leq U_a \leq 16$ m/s. Figure 6.1 shows a photograph and schematics of the setup in the wind tunnel. An inverted U-shaped bracket held a steel wire or spring specimen in a horizontal orientation, which could be swiveled about the vertical axis (as controlled by a rotary stage and stepper motor above the wind tunnel) to change the angle of attack ($0^o \leq \alpha \leq 90^o$) relative to the airflow direction between experiments. We defined the angle of attack α relative to the normal of the specimen axis (Fig. 6.2), so $\alpha = 0^o$ was perpendicular flow and $\alpha = 90^o$ was parallel flow. For spring specimens, one end of the spring was attached to a kevlar cord, which was routed to a hand crank to allow the stretch ratio, defined as the ratio of current pitch to reference (tightly coiled) pitch ($\lambda = p_s/P_s$, $P_s = d$), to be varied systematically between experiments. (Variable subscripts 's', 'a', 'e' denote spring, air, and electrical quantities, respectively.) A digital camera took photographs of the spring from underneath the wind tunnel, and the photographs were used as a digital extensometer to measure the stretch ratio

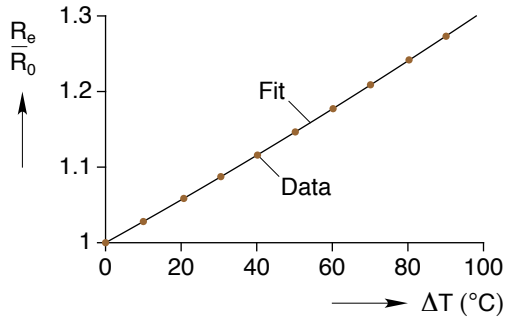

Figure 6.3: Normalized electrical resistance-temperature calibration for steel springs.

λ of the spring (approximate resolution of $\Delta\lambda = 0.01$).

The ambient air temperature (T_a), relative humidity (RH), and static pressure (p_a^0) were recorded at the start of each experiment using a handheld temperature and humidity sensor, and a mercury manometer. The relevant air properties, density (ρ_a), dynamic viscosity (μ_a), thermal conductivity (k_a), and specific heat (c_a^p), were then calculated using the measured values. The relative humidity was not found to play a significant role for nominal room temperature air. The air density was calculated using the ideal gas law, $\rho_\mathrm{a} = p_\mathrm{a}^0/(RT_\mathrm{a})$, while the rest were calculated using compiled air data [51].

6.1.2 Test Specimen Resistivity Calibration

The specimen material used in the experiments was standard AISI 1080 carbon steel (matte finish, phosphate coated) with mass density $\rho = 7850$ kg/m^3. As-received spring specimens were close-coiled (about 58 coils) with a wire diameter $d = 0.305$ mm and outer spring diameter $D_\mathrm{s}^\mathrm{o} = 3.18$ mm. The spring index was $C_\mathrm{s} = D_\mathrm{s}/d = 9.433$, based on the nominal (midline) spring diameter $D_\mathrm{s} = D_\mathrm{s}^\mathrm{o} - d$. The theoretical maximum stretch ratio to a straight configuration, assuming the midline remains inextensional, can be calculated from $\lambda_\mathrm{max} = \sqrt{1 + (\pi C_\mathrm{s})^2} = 29.65$. Prior to the wind tunnel experiments, springs were immersed in a temperature-controlled silicone oil bath to establish the electrical resistance R_e versus temperature correlation. The springs were tested in the temperature range $20 \leq T \leq 110$ ℃ in 10 ℃ increments. This was repeated at three different spring stretch ratios, $\lambda = \{2.2, 4.2, 8.0\}$, but the deformation had no noticeable affect on the resistance-temperature curve. Figure 6.3 shows the data normalized by the measured resistance at 20 ℃ ($R_0 = 1.38$ Ω) plotted against the temperature change (ΔT) relative to 20 ℃. The data is nearly linearly dependent on temperature, although a slightly quadratic correlation (as shown)

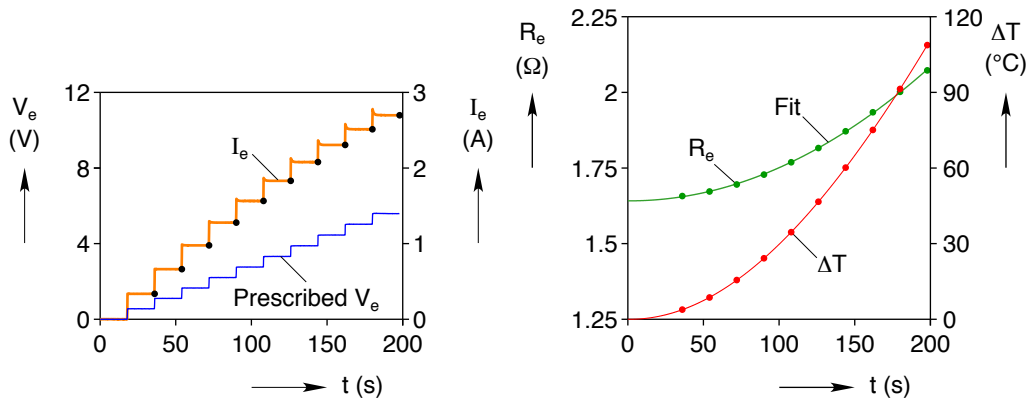

(a) Applied voltage & electrical current (b) Electrical resistance & temperature rise

Figure 6.4: Example wind tunnel data for spring at airspeed $U_a = 4$ m/s, angle of attack $\alpha = 0^o$, and stretch ratio $\lambda = 4$.

provides a more precise fit,

$$\frac{R_e}{R_0} = 1 + 0.00277 \left[\frac{\Delta T}{^\circ\text{C}}\right] + 2.92 \times 10^{-6} \left[\frac{\Delta T}{^\circ\text{C}}\right]^2 . \tag{6.1}$$

The resistivity is calculated from $\rho_e = R_e A/L$, where $A = \pi d^2/4$ is the cross-sectional area of the wire and $L = \lambda_{max} L_s$ is the total arclength of wire in the spring, giving the resistivity correlation

$$\frac{\rho_e}{\Omega\text{-}\mu\text{m}} = 0.176 + 4.93 \times 10^{-4} \left[\frac{T}{^\circ\text{C}}\right] + 5.40 \times 10^{-7} \left[\frac{T}{^\circ\text{C}}\right]^2 . \tag{6.2}$$

The resistivity $\rho_e = 0.186$ Ω-μm at 20 °C is close to the nominal handbook value (0.180 Ω-μm, [1]). The steady-state convective heat transfer coefficient is then

$$h = \frac{V_e^2/R_e}{A_s \, \Delta T}, \tag{6.3}$$

where the electrical power input is V_e^2/R_e, the total surface area of the wire is $A_s = \pi d L$, and $\Delta T = T - T_a$ is the temperature difference between the spring and the ambient air.

6.1.3 Procedure

For each selected combination of U_a, α, and λ, the histories of applied voltage and electrical current across the spring were recorded (see example in Fig. 6.4). The power supply, con-

trolled by Matlab software, incremented the voltage in 10 equal steps with 18 second pauses between each step (Fig. 6.4a). As can be seen late in the experiment at larger voltages, a transient decay occurred in the measured electrical current I_e after each voltage step. This was caused by the increasing resistance during the rising temperature transient. The pause between voltage steps was selected to allow the specimen to reach an equilibrium temperature and resistance. A quadratic polynomial curve was then fit to the steady state resistance points (Fig. 6.4b) as calculated by Ohm's law. Next, applying the resistivity-temperature correlation Eq. (6.2) to find the temperature, the heat transfer coefficient was calculated at a temperature rise of $\Delta T = 100$ ℃ using the corresponding electrical power.

Finally, bulk air properties were used to convert h and U_a to their dimensionless counterparts, the average Nusselt number $\mathrm{Nu} = hd/k_a$ and Reynolds number $\mathrm{Re} = \rho_a U_a d/\mu_a$ using the wire diameter d as the characteristic length. Some disagreement exists in literature whether to use 'film temperature' or total temperature in a heat transfer correlation [88]. Following the recommendation of Zukauskas [98], we chose the free-stream (remote) air temperature (negligibly different from total temperature at low Mach number) as our reference for all air properties.

6.1.4 Thermal End Effects

For straight wire, L was held constant near 280 mm, based on specimen availability and size constraints in the 0.6 m × 0.6 m wind tunnel. The aspect ratio of the straight wire ranged between $L/d = 550$ and 1100, depending on the wire diameter. For the spring, the aspect ratio was about $L/d = 1730$, based on the total arclength L of wire.

Due to thermal conduction with the relatively massive support posts and power cables, the specimen temperatures at the ends were likely close to the ambient air temperature, creating a non-uniform temperature distribution. Since the Biot number is small, $\mathrm{Bi} = hd/(4k) = 1.3 \times 10^{-3}$ (based on a maximum heat transfer coefficient $h \approx 500$ W/(m^2-K), the largest diameter wire $d = 0.508$ mm, and the thermal conductivity of steel $k = 48.1$ W/(m-K)), any temperature gradient normal to the wire midline can be reasonably neglected. This allows the use of the 1-D steady state heat equation,

$$\dot{q}_e + k\,\Delta T''(x) = \frac{4h}{d}\Delta T(x), \tag{6.4}$$

where $\Delta T(x) = T(x) - T_a$ is the temperature difference relative to ambient temperature, $\dot{q}_e$ is the internal (electrical) heat generation rate density, and x is an arclength coordinate

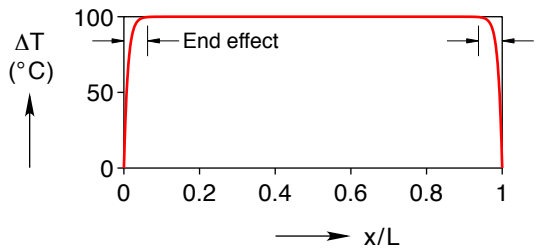

Figure 6.5: Calculated wire temperature profile accounting for end conduction.

along the wire midline.

The solution to Eq. (6.4) with end temperatures fixed at ambient, $\Delta T(0) = \Delta T(L) = 0$ [13], is

$$\Delta T(x) = \Delta T_{\max}\left[1 - \cosh\left(\frac{L-2x}{L^*}\right)\operatorname{sech}\left(\frac{L}{L^*}\right)\right], \tag{6.5}$$

where $L^* = \sqrt{kd/h}$ is a characteristic thermal length scale and the maximum temperature rise is $\Delta T_{\max} = \Delta T(L/2) = \dot{q}_e d/(4h)$. A typical temperature profile according to Eq. (6.5) is shown in Fig. 6.5 for $h = 450$ W/(m^2-K), $\dot{Q} = 12$ W, $d = 0.305$ mm, $L = 280$ mm. The experimental method measured the average temperature $\overline{\Delta T}$ across the specimen length, which can be found by integration

$$\overline{\Delta T} = \frac{1}{L}\int_0^L \Delta T(x)\,\mathrm{d}x = \frac{\dot{q}_e d}{4h}\left[1 - \frac{1}{\ell}\tanh\ell\right], \tag{6.6}$$

where $\ell = L/L^*$ is defined as a thermal aspect ratio. Using Eq. (6.6), the relative measurement error is then

$$\frac{\overline{\Delta T}}{\Delta T_{\max}} - 1 = -\frac{\tanh\ell}{\ell}. \tag{6.7}$$

The error is always negative, a systematic bias making the heat transfer coefficient h appear larger than it actually is. The minimum thermal aspect ratio for the spring was about $\ell = 98$ (at $h = 500$ W/(m^2-K)), while the corresponding value for the largest diameter straight wire was about $\ell = 40$. According to Eq. (6.7), these give worst case relative errors of -1% for the spring and -2.5% for the straight wire. These are small errors, but the correction was simple, so it was done in the post-processing of all the springs and wire data.

Table 6.1: Experimental parameters.

Specimen	d (mm)	D_s (mm)	L (mm)	U_a (m/s)	α (°)	Nominal λ
Wire	$0.254, 0.305, 0.356, 0.508$	–	283	$4, 8, 16$	$0, 10, 20, ..., 90$	–
Spring	0.305	2.88	528	$4, 8, 16$	$0, 10, 20, ..., 90$	$4, 6, 8, ..., 20$

6.1.5 Scope of Experiments

The heat transfer of straight cylinders in a crossflow is well understood and documented in the literature, and since forced-convection heat transfer correlations exist, we sought to determine if these correlations (applicable to straight wire) could be applied to more complex geometries such as helical springs. To enable a direct comparison of spring and wire data, both straight wire and spring data were collected in the same experimental setup. The scope of the wire and spring experiments are listed in Table 6.1. In both cases, U_a was varied from 4 to 16 m/s, and α from 0 to 90°. Heat transfer experiments experiments were performed on four different straight wire diameters d from 0.254 to 0.508 mm and nine different spring stretch ratios λ from 4 to 20 (using a spring made of one of the straight wire diameters). Thus, the experimental program generated $4 \times 3 \times 10 = 120$ straight wire and $3 \times 10 \times 9 = 270$ spring heat transfer measurements. As discussed later, a special set of experiments (not listed in the table) was also performed on a spring at one flow speed and stretch ratio, but at finer increments in angle of attack.

6.2 Heat Transfer of Straight Wire

An example of the measured straight wire data ($d = 0.305$ mm) is shown in Fig. 6.6a in terms of the (specimen averaged) dimensionless heat transfer coefficient (Nusselt number, Nu) against angle of attack (α) for three dimensionless flow speeds (Reynolds numbers, Re). As expected, Nu increases monotonically with Re and decreases with α. It is well known that heat transfer due to parallel flow is negligible compared to perpendicular flow across a cylinder [78], so this data (and similar data from the other wire diameters d) can be combined into a master plot using the normal component of Re,

$$\mathrm{Re}_n = \mathrm{Re} \cos \alpha. \tag{6.8}$$

Figure 6.6b includes all of the experimentally measured data on straight wire except those at $\alpha = 90°$. The wire correlation does not hold at 90° for two well-known reasons. First, the

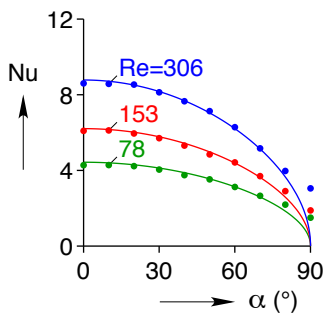

(a) Wire diameter d = 0.305 mm

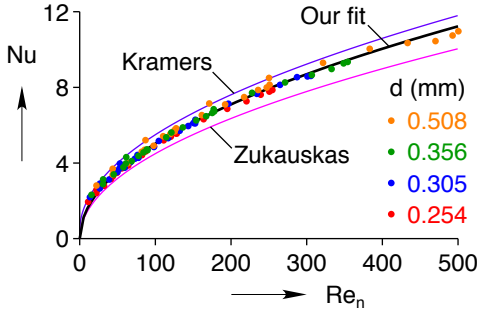

(b) All wire data, excluding data at $\alpha = 90^o$

Figure 6.6: (a) Plot of Nusselt number (Nu) versus angle of attack (α) for experiments on straight wire (solid circles) and correlation Eq. (6.9) (solid lines), showing the expected monotonic decrease of Nu with angle of attack (α); (b) Data for all wire diameters versus the normal component of Reynolds number ($\mathrm{Re_n}$) exhibit a square root dependence, agreeing with selected correlations (bold line is Eq. (6.9)).

specimen support post at each end disturbs the flow field. These disturbances only interact with the specimen at very high α, but in this case artificially increase heat transfer to the airflow. Second, the correlation only captures forced convective heat transfer, which predicts $\mathrm{Nu} \to 0$ as $\mathrm{Re_n} \to 0$ ($\alpha \to \pi/2$). However, for very low $\mathrm{Re_n}$, natural convection becomes important, so even with ideally thin supports the heat transfer never quite reaches zero.

Overall, the combined straight wire data set is nicely fit by the one parameter correlation

$$\mathrm{Nu} = 0.502\sqrt{\mathrm{Re_n}}. \tag{6.9}$$

This is consistent with the prevalent correlations in the literature for a heated solid cylinder in subsonic, incompressible (and perpendicular) fluid flow of the form $\mathrm{Nu} = a + b\,\mathrm{Re}^m$, where a accounts for natural convection, b accounts for forced convection, and the exponent m is equal or near to 1/2. A few notable correlations exist for our Reynolds number range, including the one by Kramers [59],

$$\mathrm{Nu} = 0.42\,\mathrm{Pr}^{1/5} + 0.57\,\mathrm{Pr}^{1/3}\mathrm{Re}^{1/2} = 0.393 + 0.510\sqrt{\mathrm{Re}}, \tag{6.10}$$

where the Prandtl number is taken as $\mathrm{Pr} = 0.713$ at 20 °C for dry air. Another correlation proposed by Zukauskas [98] is

$$\mathrm{Nu} = 0.449\sqrt{\mathrm{Re}}, \tag{6.11}$$

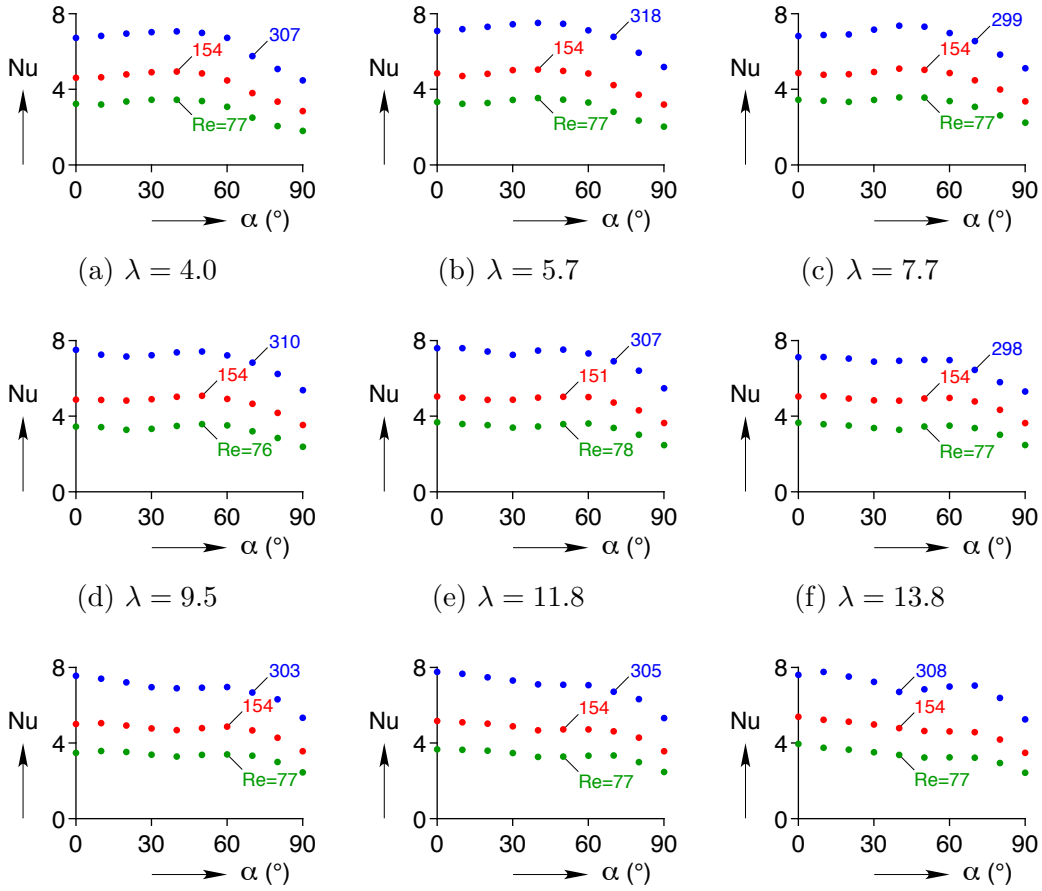

(a) $\lambda = 4.0$ (b) $\lambda = 5.7$ (c) $\lambda = 7.7$

(d) $\lambda = 9.5$ (e) $\lambda = 11.8$ (f) $\lambda = 13.8$

(g) $\lambda = 15.8$ (h) $\lambda = 17.8$ (i) $\lambda = 20.0$

Figure 6.7: Experimentally measured convective heat transfer (Nu) of springs versus angle of attack (α) at nine stretch ratios (λ).

for $40 < \mathrm{Re} < 1000$ room temperature airflows. As shown in Fig. 6.6b, Kramers' correlation provides a tight upper bound to our data, Zukauskas' correlation falls somewhat below the data, and our fit Eq. (6.9) lies in between.

6.3 Heat Transfer of Springs

A summary of the experimentally measured spring convective heat transfer data is plotted in Fig. 6.7, showing data at nine different stretch ratios. While the heat transfer coefficient (Nu) increases monotonically with the flow velocity (Re) for a given angle of attack α and stretch ratio λ, Nu has an interesting non-monotonic dependence on α and an unclear dependence on λ, both of which will be discussed below. Unlike a straight wire, it is remarkable that a spring in a crossflow has a 'plateau', where Nu is relatively insensitive to α across a large

range (say 0^o to 60^o), only dropping significantly at larger angles of attack. In fact, at the three smallest stretch ratios the maximum heat transfer does not occur at $\alpha = 0^o$ (for example, Nu is largest at $\alpha = 45^o$ in Fig. 6.7a).

Below, the convective heat transfer of springs are analyzed three ways. The first method uses the straight wire correlation with a geometric scaling based on the projected frontal area of the spring. The second method involves computational fluid dynamics (CFD) simulations. The third method developes an empirical correlation to enable relatively fast calculation.

6.3.1 Projected Frontal Area Model

A simplistic approach that provides a first-order approximation of the spring's heat transfer is to use the straight wire correlation but account for the 'viewable' frontal area of spring. This method is inspired by the notion that trailing edge coils are 'shadowed' by upstream coils and would see reduced flow and heat transfer. The angle of attack dependence in the straight wire correlation Eq. (6.9) was modeled by taking the normal component of the Reynolds number, Eq. (6.8), which is equivalent to scaling the flow speed by the ratio of the projected frontal area of wire (onto a plane normal to the flow) to total frontal area. Accordingly, an area knockdown factor is defined here as

$$\eta = \frac{A_\mathrm{p}}{d\,L}, \tag{6.12}$$

where $A_\mathrm{p} = A_\mathrm{p}(\alpha, \lambda)$ is the projected (frontal) surface area of the spring, and the normalizing factor dL is the total frontal area of the wire as if fully uncoiled (straightened) and oriented perpendicular to the flow ($\alpha = 0^o$). For straight wire, Eq. (6.12) simplifies to $\eta = \cos\alpha$ consistent with Eq. (6.8). For the spring, however, A_p is a complicated function of α and λ with numerous kinks arising from disjoint shadowing between coil segments, making an analytical approach intractable. We instead calculated A_p numerically using computer aided design (CAD) software and high resolution image analysis for a multitude of spring configurations, a few of which are shown in Fig. 6.8a. Figure 6.8b plots the calculated η versus α for five different stretch ratios. Thus, using the straight wire correlation and replacing $\cos\alpha$ by η, the effective Nusselt number for the spring is

$$\mathrm{Nu} = 0.502\sqrt{\mathrm{Re}\,\eta}. \tag{6.13}$$

As shown in the example ($\lambda = 11.8$) of Fig. 6.8c the model gives reasonable estimate,

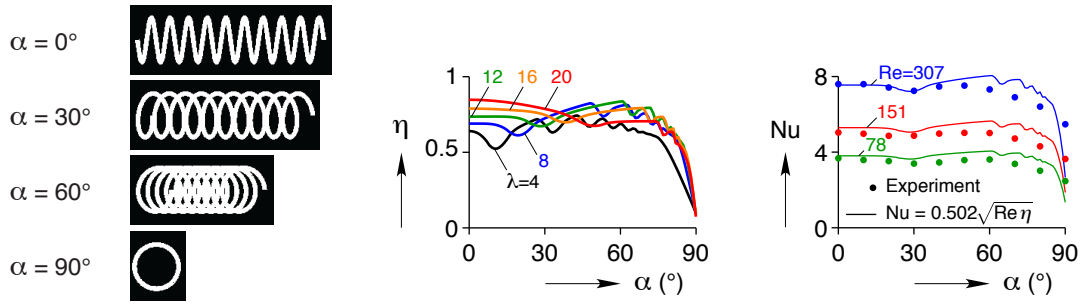

(a) Projected frontal areas for $\lambda = 4.0$ (b) Area knockdown factor (c) $\lambda = 11.8$

Figure 6.8: Projected frontal area model and example comparison to experimental data.

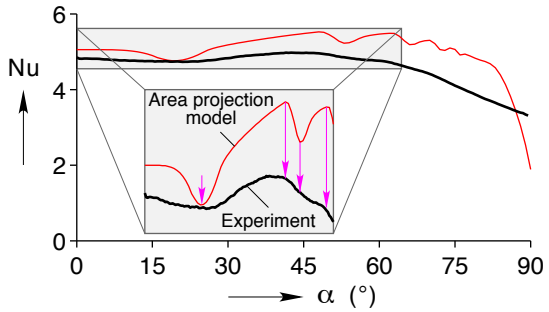

Figure 6.9: Comparison of frontal area model and experimental data (solid line) on a spring specimen at $\lambda = 8$ and Re = 147 taken over fine increments ($\Delta\alpha = 0.5^o$).

considering the complexity of the flow field (shown later) and the fact that the model has no fitting parameters (once calibrated to straight wire data). It satisfactorily captures the general 'plateau' behavior for small to moderate attack angles, achieving quantitative agreement with the experimental data for the lower half of α cases and even capturing the first dip in Nu near $\alpha = 30^o$. Admittedly, the prediction overshoots the heat transfer for $45^o < \alpha < 80^o$ and contains larger oscillations than seem to exist in the experimental data. This 'line-of-sight' approach, however, provides a reasonable first estimate of the heat transfer coefficient of helical springs, which we believe would perform similarly well for other complex wire geometries.

The most serious limitation of this model is the seemingly spurious oscillations at large α's, yet the data increments just shown ($\Delta\alpha = 10^o$) are too sparse to decide if they are real. As shown in Fig. 6.9, we performed one additional series of experiments with finer angle of attack increments ($\Delta\alpha = 0.5^o$) at a single stretch ratio ($\lambda = 8$) and Reynolds number (Re = 147) to see if any evidence of these oscillations truly exist. Clearly, the experimental data do not exhibit the same fluctuations with α, at least to the same magnitude, as predicted by the model. Small oscillations do exist in the data at the appropriate α's, but they are subtle and

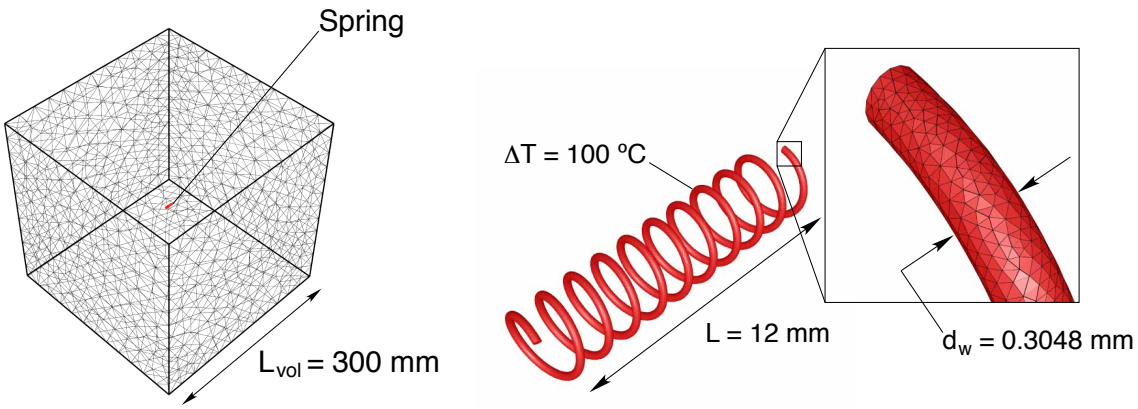

(a) Control volume mesh

(b) Spring mesh

Figure 6.10: CFD mesh at $\lambda = 4$.

require a magnified view to detect them. Thus, while the model exaggerates the effects of self-shadowing, it seems to capture the correct qualitative trends. Both the agreement and discrepancies can be rationalized, knowing the heat transfer is larger on upstream exposed wire surface elements than oppositely-faced or shadowed surfaces (consistent with the model), yet the flow certainly fills in these downstream regions so the heat transfer is not zero there (contrary to the model).

6.3.2 CFD Simulations

As a more rigorous approach, computational fluid dynamics (CFD) simulations were performed to capture the entire parameter space (including stretch ratio (λ) regimes outside our experimental data) and to study details of the flow field and heat transfer distributions on the spring surface. An advantage of CFD simulations is the ability to prescribe consistent ambient air properties; whereas, the ambient temperature and static pressure varied from day to day in the wind tunnel, making it difficult to prescribe precise Reynolds numbers. Furthermore, the tensile force required to elongate steel springs beyond $\lambda > 20$ would have required an excessively bulky support structure, while CFD simulations could be run to fill in the data gap $20 < \lambda < 29.6$.

The 3-dimensional Navier-Stokes equations were solved using a second-order upwind solution method by Ansys Fluent [39], which has the necessary viscous terms for heat transfer simulation. The airflow was assumed to be incompressible, steady state, and laminar. Natural convection was neglected, since buoyancy effects were not modeled. The spring was modeled as a wall boundary with uniform temperature of 100 °C above the ambient air tem-

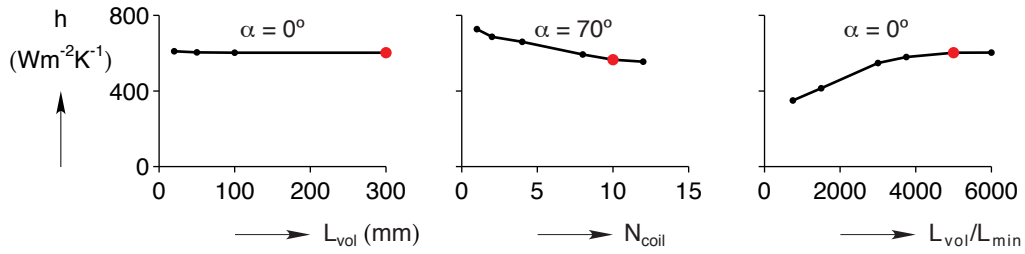

Figure 6.11: CFD convergence study for the case $U_a = 16$ m/s and $\lambda = 4.23$, showing the influence of total fluid volume side length (L_{vol}), number of spring coils (N_{coil}), and mesh density (L_{vol}/L_{min}).

perature, thereby ignoring any temperature gradients at the spring's ends or through the wire cross-section. The effective heat transfer coefficient h was then calculated from the area-weighted average of the heat flux over the spring's wall surface.

CAD drawings and meshing were generated within the Ansys Workbench environment, and the spring mesh was freely suspended (no supports) in a much larger fluid box of dimensions $300 \times 300 \times 300$ mm^3 (Fig. 6.10a). A constant flow velocity was specified on each box face to establish far-field flow conditions. Ten spring loops were modeled, using a fine mesh near its wall surface (Fig. 6.10b). The spring length varied from about 3 mm when tightly coiled to 90 mm when fully straightened. Rather than rotating the spring's mesh inside the box for each different angle of attack (α), it was more convenient to rotate the flow direction specified on the box boundary, allowing the use of one static mesh for each stretch ratio (λ) case.

The total fluid box size, number of spring loops, and mesh density were determined by a convergence study shown in Fig. 6.11. The total fluid volume size had little impact on the solution, but its effect on computation time was small, so a (larger than necessary) value of $L_{vol} = 300$ mm side length was chosen. The number of spring coils, however, had a significant effect on computation time, due to the mesh refinement near the spring. A value of $N_{coil} = 10$ was adequate to converge the solution. A calculation at $N_{coil} = 12$ showed little change in h at large attack angles ($\alpha = 70^o$ shown), where the solution was most sensitive. The mesh density, of course, also had a large influence on computational time. The mesh was spatially nonuniform with a minimum grid length L_{min}, so the ratio of the total fluid box side length to minimum element length (L_{vol}/L_{min}) was chosen as a measure of the mesh density. A value of $L_{vol}/L_{min} = 5000$ was selected as a compromise between computational time and solution convergence, which corresponded to 16 nodes around the spring's wire circumference and 151 nodes along each coil length. A test calculation at $L_{vol}/L_{min} = 6000$ showed no change in h.

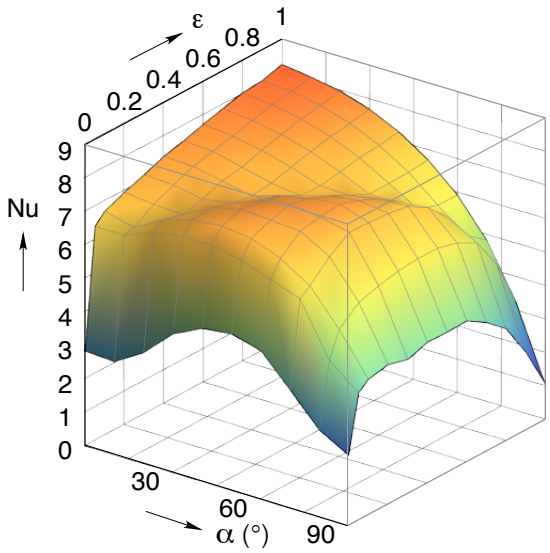

Figure 6.12: CFD simulations of spring heat transfer at Re = 300.

As shown in Fig. 6.12, CFD results at a specified Reynolds number (Re = 300) could be used to construct a 3D 'surface' for Nu across the entire ranges of λ and α. For convenience, a homogenized 'strain' measure for the spring ($0 \leq \varepsilon \leq 1$) is defined as

$$\varepsilon = \frac{\lambda - 1}{\lambda_{\max} - 1}, \tag{6.14}$$

so that $\varepsilon = 0$ corresponds to the close coiled spring ($\lambda = 1$) and $\varepsilon = 1$ corresponds to the straight wire (fully extended spring at $\lambda = \lambda_{\max} = 29.6$). The global maximum of Nu corresponds to the straight wire case in perpendicular flow ($\varepsilon = 1, \alpha = 0^{\circ}$), shown in the uppermost corner of the surface in Fig. 6.12. The upper right plane at $\varepsilon = 1$ shows the monotonic decrease of Nu with α of the straight wire. Starting from max Nu ($\varepsilon = 1, \alpha = 0^{\circ}$), the upper left plane at $\alpha = 0$ (perpendicular flow to the spring axis) shows initially a nearly linear decrease in Nu as the helix is shortened (decreasing ε) from the fully extended configuration. Eventually, however, a precipitous drop in Nu is seen at small values of strain ($0 \leq \varepsilon \leq 0.05$) as the spring becomes close-coiled and little to no air gaps exists for airflow between the coils. The previously noted trends in the experimental data are seen by tracing lines along constant ε. The non-monotonic trends with α arise from the local maximum in Nu near $\varepsilon = 0.3$ ($\lambda = 10$) and $\alpha = 50^{\circ}$, thereby enhancing the spring's heat transfer over a wide range of ε and α. A gentle crevasse in the surface exists along a diagonal line, spanning from $(\varepsilon, \alpha) = (0, 0^{\circ})$ to $(\varepsilon, \alpha) = (1, 90^{\circ})$. The global minimum is the straight wire case at $\alpha = 90^{\circ}$, although other local minimums exist in the lefthand corners of the plot at $(0, 90^{\circ})$ and $(1, 90^{\circ})$ corresponding to the close-coiled spring (like a serrated tube) in perpendicular

and parallel flow, respectively.

Until now, the heat transfer coefficient h (or Nu) has been averaged over the entire surface area of the spring wire, yet CFD provides the distributions of all field quantities, thereby providing an opportunity to better understand the underlying heat transfer behavior. Figure 6.13 shows details of an example CFD simulation of a spring at $\lambda = 4$ and $\mathrm{Re} = 300$. This case is interesting, since it has a non-monotonic heat transfer dependence on angle of attack, so results for four selected values are shown $\alpha = \{0^o, 10^o, 40^o, 70^o\}$. While a wire's average h monotonically decays relative to perpendicular flow by $\{0\%, -1\%, -12\%, -42\%\}$ at the respective α's, the spring's heat transfer changes by $\{0\%, -3\%, +9\%, -6\%\}$.

Clearly, the local h varies significantly along the surface of the spring as shown viewed from above in Fig. 6.13a. It is highest at the leading edge where the surface is directly visible to the flow, and lowest at the trailing edge surface which is hidden from the flow. Even as the angle of attack is increased, the surface area exposed to the flow does not appear to decrease until there is a large amount of shadowing of trailing coils by leading coils in the final case of $\alpha = 70^o$. This is partially due to the fact that the wire in the spring has a continuous sweep of α relative to the flow, and as α is changed some regions are turned away from the flow while other regions are turned in towards the flow.

The conclusion that wire surface elements exposed to the flow are responsible for the majority of the heat transfer, while the surface elements hidden from the flow contribute relatively little, is confirmed in Fig. 6.13b that shows h distributions viewed along the flow in both upstream and downstream directions. When viewed downstream the heat transfer on exposed (leading edge) surfaces is largely uniform at high values of h, while upstream views of hidden (trailing edge) surfaces show nearly uniform heat transfer at low values h. This corroborates the projected frontal area analysis done previously.

The discrepancy with the projected frontal area analysis at large α's is revealed in Fig. 6.14, which shows the flow velocity field in a cut-plane across the diameter of the spring. Two features can be observed. First, from $\alpha = 0^o$ to $\alpha = 40^o$, the width of the low speed wake behind the leading edge wire elements remains roughly constant (until it meets trailing edge elements), although of course the direction of the wake changes relative to the spring axis. At $\alpha = 0^o$ and $\alpha = 40^o$, the leading edge wake passes roughly between the trailing wire elements, but at $\alpha = 10^o$ it aligns with the trailing edge elements. This explains why a local minimum in heat transfer exists at $\alpha = 10^o$. Second, the width of the the wake width increases between $\alpha = 40^o$ and $\alpha = 70^o$. This means that the effective shadowing caused by the leading edge coils is actually worse at higher α than what the projected area would

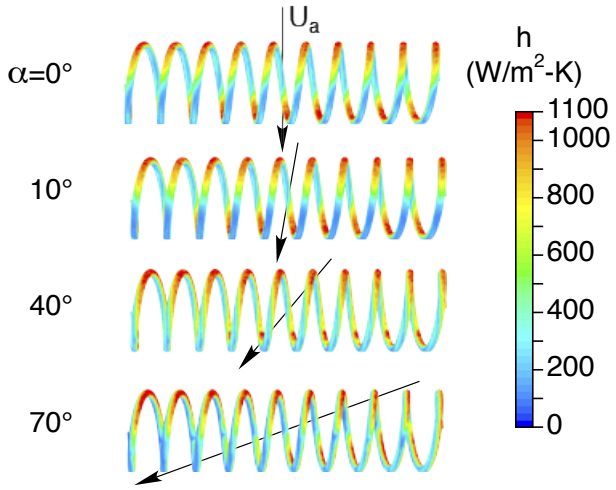

(a) h distributions top view

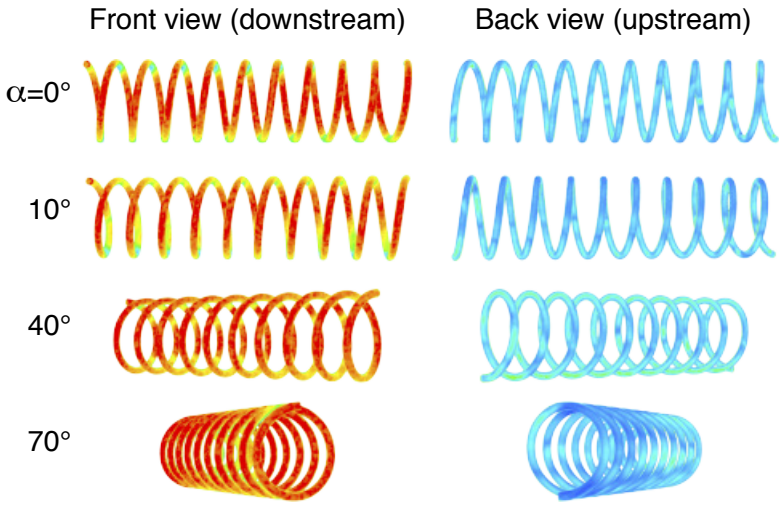

(b) h distributions viewed along flow

Figure 6.13: CFD results for $\varepsilon = 0.10$ ($\lambda = 4$) and Re = 300 ($U_a = 16$ m/s) showing local distributions of h.

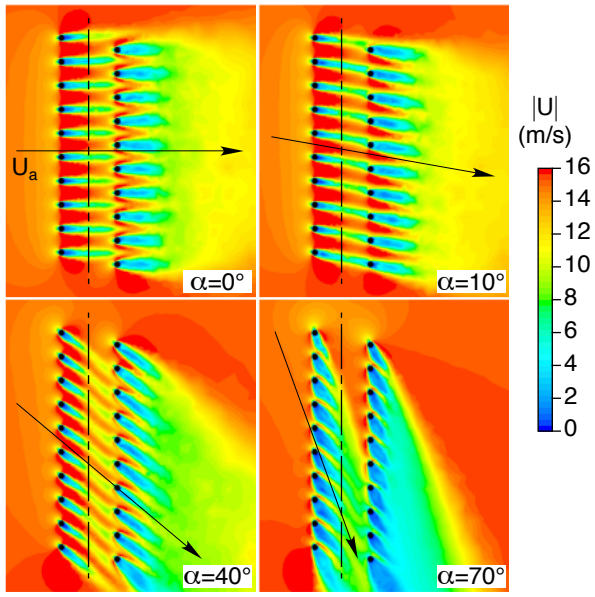

Figure 6.14: CFD results for $\varepsilon = 0.10$ ($\lambda = 4$) and Re $= 300$ ($U_\mathrm{a} = 16$ m/s) showing the velocity field ($|\boldsymbol{U}|$) in the spring cut-plane.

indicate. This explains why the measured heat transfer is lower (at high α) than predicted by the projected area ('line-of-sight') analysis.

6.3.3 Empirical Correlation

Finally, an empirical correlation is developed that captures the (specimen averaged) spring's heat transfer dependence on Reynolds number, strain (stretch ratio), and angle of attack. The correlation is fitted to the CFD data (rather than the experimental data), since this provides a more comprehensive and consistent dataset. Accordingly, any contribution of natural convection is neglected. Accurately capturing all the relevant trends in the heat transfer behavior was difficult, ultimately requiring a large number of fitting parameters, and we make no claim that ours is the simplest possible function that could be developed. Nevertheless, the correlation described below successfully fits the available data, is a smooth analytical function, and agrees with the straight wire correlation in the asymptotic limit ($\lambda \to \lambda_\mathrm{max}$ or $\varepsilon \to 1$). Overall, its purpose is to provide a computational tool for quick calculation of the heat transfer coefficient, suitable for simulations in broader applications (such as in [19]).

The correlation $\mathrm{Nu}(\mathrm{Re}, \varepsilon, \alpha)$ is a function of Reynolds number, strain, angle of attack of

the form

$$\mathrm{Nu} = b\,[\mathrm{Re}/300]^m\,, \tag{6.15}$$

where the coefficient $b = b(\varepsilon, \alpha)$ is the Nusselt number function at a selected Reynolds number ($\mathrm{Re} = 300$) and $m = m(\varepsilon, \alpha)$ is a function for the Reynolds number exponent. This form allowed b to be fitted to the CDF data of Fig. 6.12 at $\mathrm{Re} = 300$ independent of m. CFD simulations were performed at five Reynolds numbers $\mathrm{Re} = \{75, 112.5, 150, 225, 300\}$ for each case (ε, α), and exponent m values were fit from each. This provided discrete data that was subsequently fit by a 3D surface $m(\varepsilon, \alpha)$.

The chosen function b is

$$b = \sqrt{b_1 + b_2 + b_3}, \tag{6.16a}$$

$$b_1 = \left[b_{10}\,(1-\varepsilon)\left(1-(1-\varepsilon)^{b_{12}}\right) + b_{11}\varepsilon\right]\cos\alpha, \tag{6.16b}$$

$$b_2 = (1-\varepsilon)\,(b_{20} + b_{21}\varepsilon)\exp\left[-\left(\frac{\overline{\alpha} - b_{22} - b_{23}\varepsilon}{b_{24} - b_{25}\varepsilon}\right)^2\right], \tag{6.16c}$$

$$b_3 = -b_{30}\mathrm{sech}\,(b_{31}\overline{\alpha} - b_{32})\,\mathrm{sech}\,[(b_{33}\overline{\alpha} + b_{34})\,(\varepsilon - \varepsilon_1)]\,, \tag{6.16d}$$

$$\varepsilon_1 = \frac{1}{\lambda_{\max} - 1}\left[\frac{\lambda_{\max}\sin\alpha}{\sqrt{\left(\frac{\pi}{2}\right)^2\cos^2\alpha + \sin^2\alpha}} - 1\right], \tag{6.16e}$$

with $\overline{\alpha} = 2\alpha/\pi$. The fitting constants are the 14 quantities with double subscripts, and values are provided in Table 6.2. Note that in the limit $\varepsilon = 1$ the straight wire case is essentially recovered with $b_1 = b_{11}\cos\alpha$, $b_2 = 0$, and $b_3 \approx 0$. The function b_2 gives the heat transfer augmentation (local maximum) at intermediate strains and attack angles. The function b_3 gives a slight correction at small ε and small α, where the function ε_1 is the strain at which a downstream loop is first shadowed by an upstream loop. The correlation at $\mathrm{Re} = 300$ is plotted in Fig. 6.15, and the agreement with the corresponding CFD data (Fig. 6.12) is excellent everywhere, except along the edges $\varepsilon = 0$ and $\alpha = 90^\mathrm{o}$ where the correlation is less accurate but still reasonable.

Table 6.2: Correlation parameters for function b.

Param	Value	Param	Value	Param	Value
b_{10}	44.00	b_{11}	67.95	b_{12}	37.23
b_{20}	17.97	b_{21}	95.77	b_{22}	1.042
b_{23}	0.3907	b_{24}	0.6859	b_{25}	0.5017
b_{30}	5.825	b_{31}	6.560	b_{32}	1.828
b_{33}	26.93	b_{34}	5.768		

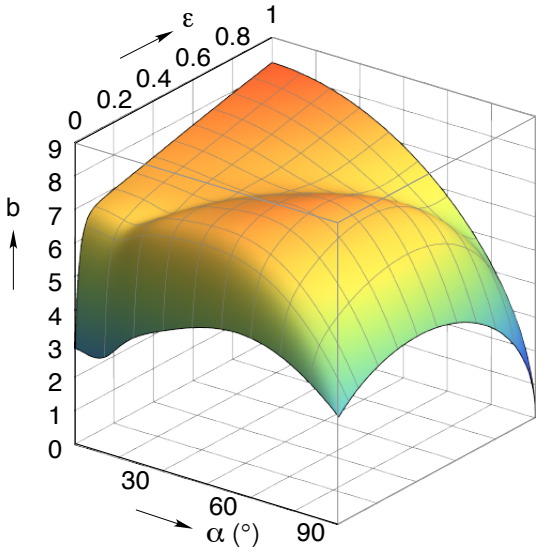

Figure 6.15: Function b in spring heat transfer correlation corresponding to Nu at Re = 300.

The chosen exponent function m is

$$m = m_0 + (m_1 - m_0 - \overline{\alpha}_1 m_3)\left(\overline{\alpha}/\overline{\alpha}_1\right)^{m_2} + m_3\overline{\alpha}, \tag{6.17a}$$

$$m_0 = m_{00} + m_{01}\left(1-\varepsilon\right)^{m_{02}}, \\ + m_{03}\left[\operatorname{sech}\left(\frac{\varepsilon - m_{04}}{m_{05}}\right) - \operatorname{sech}\left(\frac{1-m_{04}}{m_{05}}\right)\right], \tag{6.17b}$$

$$m_1 = m_{10} + m_{11}\left(1-\varepsilon\right)^{m_{12}} + m_{13}\left(1-\varepsilon^{m_{14}}\right), \tag{6.17c}$$

$$m_2 = m_{21}\left[1 - \exp\left(-m_{22}\varepsilon\right)\right]. \tag{6.17d}$$

$$m_3 = \left(m_{30} - m_{32}\varepsilon^2\right)\left(1-\varepsilon\right)^2, \tag{6.17e}$$

When $\alpha = 0$, the exponent becomes $m = m_0$, which describes the exponent's dependence on strain for perpendicular cross-flow. The exponent becomes $m = m_1$ when $\overline{\alpha} = \overline{\alpha}_1$, which describes the strain dependence at a selected large angle (chosen here as $\overline{\alpha}_1 = 8/9$ or

Table 6.3: Correlation parameters for function m.

Param	Value	Param	Value	Param	Value
m_{00}	0.5000	m_{01}	0.08277	m_{02}	18.98
m_{03}	0.1513	m_{04}	0.2975	m_{05}	1.321
m_{10}	0.4589	m_{11}	0.1221	m_{12}	2.395
m_{13}	0.1256	m_{14}	30.00		
m_{21}	10.65	m_{22}	4.145		
m_{30}	0.03674	m_{32}	0.2744		

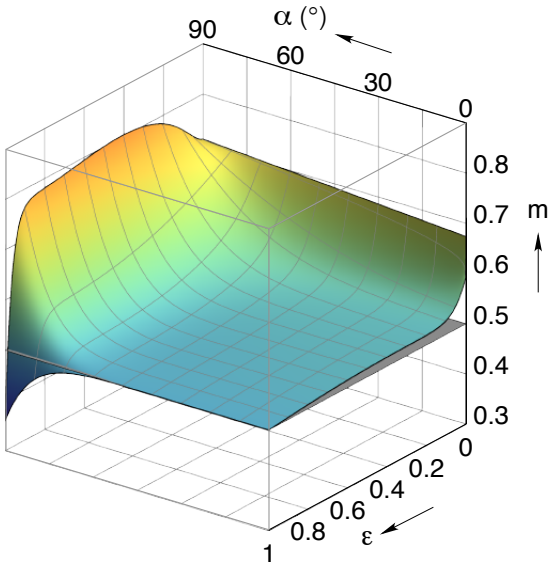

Figure 6.16: Function m in spring heat transfer correlation.

$\alpha_1 = 80^o$). The functions m_2 and m_3 serve to interpolate between these two attack angles. The m function involves 15 fitting constants with values provided in Table 6.3. As shown in Fig. 6.16, the exponent m is close to a baseline value of 0.5 over much of the range, gently increasing with decreasing strain and rising steeply as the spring becomes close-coiled ($\varepsilon \to 0$). It also rises as the angle of attack approaches 90^o except near the straight wire limit ($\varepsilon \to 1$).

Example results from CFD simulations, experimental data, and our correlation are plotted in Fig. 6.17, showing good agreement and similar trends with Reynolds number and angle of attack for a single stretch ratio. To more clearly show the influence of angle of attack, Fig. 6.18 provides CFD data, experimental data, and correlation curves for four stretch ratios and three Reynolds numbers each. Here, the CFD simulations were run with adjusted air properties to match the Re of the experimental measurements. Other stretch ratios (not shown) exhibit similarly good agreement, especially at low to moderate angles of

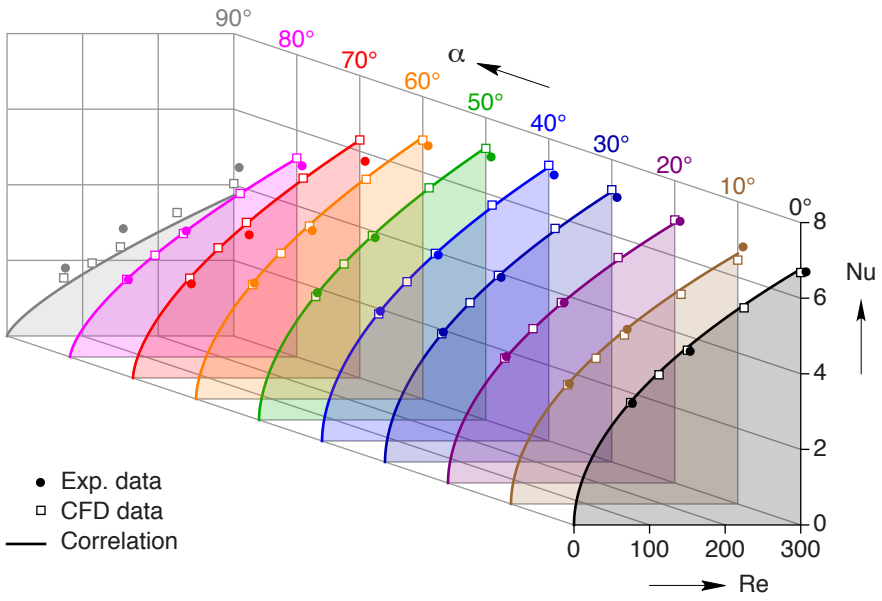

Figure 6.17: CFD data, experimental data, and empirical correlation curves versus Reynolds number for spring heat transfer at $\varepsilon = 0.105$ ($\lambda = 4.0$).

attack ($0 \leq \alpha \leq 60^{\text{o}}$). Discrepancies do exists in each set at $\alpha = 90^{\text{o}}$, where the Nu values from CFD are consistently smaller that the corresponding experimental data, but that is explained by the presence of the support posts in the wind tunnel experiments (as discussed previously) that were absent in the CFD simulations. That case aside, the good agreement seems to validate the laminar flow assumption for our range of Reynolds numbers. Table 6.4 provides the magnitude of the maximum errors in Nu (among all Re values at each (ε, α)) between the correlation and the CFD data. Across the majority of the parameter space (shaded region of the table), $0 \leq \alpha \leq 80^{\text{o}}$, $0.1 \leq \varepsilon \leq 1$, the error in Nu is 0.22 worst case (at $\varepsilon = 0.8$, $\alpha = 80^{\text{o}}$) and is 0.06 on average.

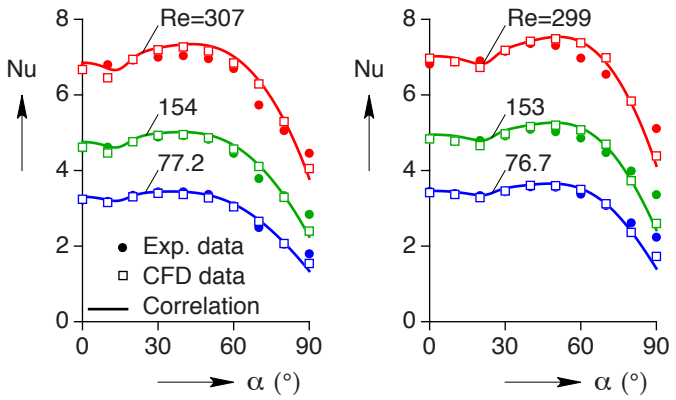

(a) $\varepsilon = 0.105$ ($\lambda = 4.0$) (b) $\varepsilon = 0.233$ ($\lambda = 7.7$)

(c) $\varepsilon = 0.377$ ($\lambda = 11.8$) (d) $\varepsilon = 0.516$ ($\lambda = 15.8$)

Figure 6.18: CFD data, experimental data, and empirical correlation curves versus angle of attack for spring heat transfer at four stretch ratios.

Table 6.4: Magnitude of maximum Nu errors between the correlation and CFD data.

		α									
λ	ε	0°	10°	20°	30°	40°	50°	60°	70°	80°	90°
1.15	0.005	0.47	0.41	0.73	0.62	0.67	0.74	0.84	1.04	1.37	1.11
2.57	0.055	0.05	0.16	0.15	0.08	0.03	0.10	0.11	0.19	0.41	0.30
4.00	0.105	0.09	0.17	0.08	0.06	0.06	0.03	0.07	0.04	0.02	0.31
6.85	0.204	0.05	0.09	0.03	0.03	0.08	0.10	0.06	0.11	0.07	0.33
9.70	0.304	0.03	0.03	0.09	0.04	0.02	0.03	0.10	0.21	0.06	0.39
12.6	0.403	0.07	0.06	0.01	0.12	0.03	0.04	0.04	0.05	0.11	0.31
15.4	0.503	0.06	0.05	0.04	0.07	0.10	0.04	0.11	0.02	0.09	0.32
18.3	0.602	0.08	0.05	0.05	0.07	0.03	0.03	0.05	0.07	0.02	0.39
21.1	0.702	0.09	0.06	0.07	0.10	0.13	0.04	0.04	0.09	0.07	0.29
24.0	0.801	0.09	0.07	0.07	0.10	0.16	0.17	0.03	0.07	0.22	0.21
26.8	0.901	0.03	0.03	0.04	0.06	0.09	0.14	0.09	0.08	0.03	0.21
29.7	1.000	0.04	0.05	0.03	0.04	0.06	0.09	0.09	0.03	0.19	1.06

6.4 Conclusion

The forced-convection heat transfer coefficients h of thin-wire tension springs were measured for the first time under varying flow conditions and spring configurations in a wind tunnel experimental setup. The experimental program spanned a large parameter space, including several air speeds $0 < U_a \leq 16$ m/s, angles of attack $0 \leq \alpha \leq 90^o$, and spring stretch ratios $1 < \lambda \leq 29.7$ (close-coiled to straight wire). The dependence of the specimen averaged h on Reynolds numbers (here $0 < \mathrm{Re} \leq 300$) followed a square root law over most angles of attack α and stretch ratios λ, only transitioning to higher exponents for small λ (approaching the close-coiled spring). The heat transfer of springs was discovered to have a non-monotonic dependence on angle of attack α, and unlike a straight wire, a plateau-like behavior existed over a wide range of α's. While the maximum heat transfer occurred for straight wire in perpendicular flow, the heat transfer of springs was more robust (relatively insensitive) to changes in angle of attack compared to straight wire. The dependence on stretch ratio λ was complex and interdependent on α, and a local maximum in h was found at intermediate values near $\alpha = 50^o$ and $\lambda = 10$.

This complex behavior was analyzed three ways:

1. A simplistic model was first attempted, using image analysis of the spring's projected frontal area combined with the straight wire correlation, that gave a reasonable first-order estimate of the spring's heat transfer. The agreement was good for moderate angles of attack ($0 \leq \alpha \leq 30^o$) but somewhat over-predicted the heat transfer and had spurious oscillations at larger angles.

2. An extensive set of steady-state computational fluid dynamics (CFD) simulations were performed that accurately reproduced the experimental measurements and could be used to fill in the parameter space where experiments were impractical. The laminar flow model used, unlike a typical turbulent flow model, had no fitting parameters, thereby providing independent confirmation of the heat transfer trends. Further, high-fidelity CFD simulations provided details of the spatial heterogenieties of the local h on the spring's surface and in the flow field, which helped to explain the non-monotonic behavior of the average h with α and λ.

3. A dimensionless empirical correlation was developed that successfully captured the experimental and CFD average Nusselt number (Nu) of springs as a function of Re, α, and λ. Its purpose was to provide a numerical tool for quick calculation of the heat

transfer behavior that can be readily utilized in larger scope models where the heat transfer of a spring plays a critical role.

All of the above provided a better understanding of the heat transfer of helical wire elements across a comprehensive range of angles of attack and stretch ratios in low Re forced-convention flows.

CHAPTER 7

Summary and Conclusions

The fundamental nature of shape memory alloys needs to be more well understood in order to effectively apply them in the aerospace and civil engineering fields. The investigations presented in this work were focused on determining key properties of NiTi, which is a commonly used SMA material, when used in new forms such as stranded cable. Wire rope technology enables the joining of fine wires to create a hierarchical structure capable of carrying large tensile loads. Doing so comes at a cost of complexity, as the mechanical behavior is no longer pure uniaxial tension (as it is in straight wire), but now has added bending, twisting, and contact mechanics. The goal of this work was thus to explore the scalability of NiTi cables and extend the understanding of the unstable phase transformation in the presence of complex local mechanics.

This work first provided a thorough characterization of superelastic NiTi cables much larger than previously tested. This provided conclusive evidence that desirable superelastic properties can be achieved in structures capable of withstanding loads excessive of tens of kilonewtons (thousands of pounds). The rate sensitivity of the large 7×7 cable was shown to reach an adiabatic limit at a slower rate than straight wire, in accordance with the heat transfer scaling. The Clausius-Clapeyron slope was found to be reduced, and the cyclic stability showed little accumulation of plasticity. The cable was also taken to failure, approximating the ultimate breaking load which is thought to exceed 32 kN.

This work was then extended to explore the novel thermal actuation of NiTi cables, with a sweep of experiments characterizing the thermo-responsive shape memory actuation behavior. Here, two cables, with 7×7 and 1×27 geometries, and straight wire were characterized under dead load condition to both understand the thermal actuation behavior of each specimen individually and compare the effect of varying the cable construction on the macroscopic mechanical response. Overall, both cables were shown to have good shape memory

properties, and had an equivalent work output to the straight wire, providing evidence that the thermal actuation behavior of a wire can be scaled up to large loads by stranding it into a cable form. The 1×27 cable had a large stroke at lower loads, and an increased reaction torque during transformation due to interactions within the various layers of its construction. The 7×7 cable mimicked the behavior of the straight wire due to its shallow helix angles. This showcases the ability to tailor the thermal actuation behavior by simply altering the cable construction, without needing to change the underlying material properties, to better optimize the performance to any given application.

As the cyclic performance is a key factor impacting the end usability of NiTi actuators, a careful suite of experiments characterizing the path dependent shakedown and formation of plasticity of straight NiTi wire was also presented. Through this work, it was discovered that transformation-induced plasticity occurs primarily on heating during the reverse transformation from M→A. Moreover, the stress on cooling was discovered to dictate the microstructure formed during the forward transformation, which in turn impacts the amount of plasticity developing on heating. It was hypothesized that the microstructure that forms on cooling is a split phase between thermal and stress-induced martensite, and the act of detwinning martensite increases the energy barrier to the reverse transformation and the corresponding amount of plasticity. These new findings shed light on where transformation-induced plasticity is forming and potential methods to avoid excessive degradation of the thermal actuation in NiTi actuators.

To better explore how the local mechanics of cables impact the unstable phase transformation, superelastic 1×3 twists were experimentally characterized and simulated using finite element analysis. The experiments utilized digital image correlation to measure the local transformation and strain fields of three 1×3 twists with increasing helix angles. The twist with the steepest helix angle was discovered to have a periodic transformation behavior with many nucleation events and pockets of untransformed material, even at loads exceeding the transformation plateau. From the experimental observations, the many nucleation events were thought to be caused by friction and contact between the wires in the twist, but a lubrication experiment showed no large difference between the lubricated and dry specimens. Finite element simulations modeling the stress-induced phase transformation as a J2 yield surface were conducted and shown to accurately reproduce the experimental data. Furthermore, these simulations revealed that the periodic instability in the largest helix angle twist was indeed caused by contact forces that impede the phase transformation and force nucleations past the arrested region of material.

The final chapter explored the convective heat transfer of helical wire in a crossflow. While

this topic diverges from the solid mechanics research in the previous sections, it fits into the larger scope of providing research to enable new shape memory alloy actuator applications. Here, wind tunnel experiments were conducted under varying flow and spring geometry conditions to measure the wide range of heat transfer conditions. This revealed a non-monotonic dependence of the heat transfer coefficient on the angle of the flow with respect to the spring axis. Computational fluid dynamic simulations matched the experimental data well, and showed that the wake's interaction with the trailing coils dictated the non-monotonic trend in the heat transfer coefficient. A detailed correlation was then presented, which provides a rapid way to implement the heat transfer data into modeling helical shape memory alloy actuators.

In conclusion, it has been shown that shape memory alloy cables provide promising capability to both scale up the adaptive properties of straight wire, and furthermore, add a new toolset to better optimize the performance and potentially overcome previous limitations of straight wire (such as low actuation strain). Further advances in shape memory alloy actuator performance can be made by bettering our understanding in the mechanics of degradation, and this work highlighted new behaviors that could be utilized in novel ways to overcome cyclic limitations in shape memory actuators. This work also revealed that relative sliding and contact mechanics are very important in shape memory cables and have a large impact on the phase transformation. While the thermo-mechanical behavior of shape memory alloys, particularly in advanced forms, is highly complex and has well known limitations, this research shows that through bettering our fundamental understanding of the mechanics of the phase transformation, new forms of adaptive structures with desirable properties are indeed possible.

7.1 Future Work

There are many ways this research could be expanded. One direct research path for improving the understanding of NiTi cables would be to develop a model, be it numerical or analytical, to explain the interactions between the layers of a cable. The reaction torque in particular has intriguing dependence on when each layer transforms. This model would ideally predict the instances when each layer undergoes a phase transformation and better explain why the reaction torque has a wide variance during transformation. These findings may provide insight for tailoring the cable geometry to create, for instance, a cable that contracts and twists a predetermined amount with thermal actuation.

While the focus of this research was on scaling up the shape memory alloy structures, small scale structures could also derive benefit from making use of cable structures. For instance, the increased bending flexibility allows the cable to be spooled in a much tighter package, further reducing the form factor of shape memory alloy actuators. The damage tolerance could also provide an increase in the long-term cyclic performance. Monolithic wires can fracture with many repeated thermal actuation cycles, with a wide variance as far as when any particular wire will fail. A cable with numerous wires could mitigate this risk and extend the lifespan of the actuator by allowing any single wire to fail without compromising the integrity of the entire structure.

Discoveries into the path dependent shakedown of NiTi wires investigated here raised many new and unanswered questions about the microstructure. Modeling advances that could predict the microstructure under the influence of an applied stress field would be an exciting avenue to pursue. This could perhaps show how the kinematically admissible HPVs which are favorable under stress-free conditions, changes once a stress field is applied. Understanding how the microstructure changes with transformation under various stress states would be crucial in predicting the occurrence of transformation-induced plasticity.

Finally, there are several avenues to extend the modeling efforts of the 1x3 twists. As the temperature-displacement formulation is already implemented, modeling the rate dependent effects would be a natural extension to the current work. A more ambitious extension would be to create a customized material model based on fundamental thermodynamic relations to model the problem more fully, including the reverse transformation. Adding in the effects of transformation-induced plasticity would also allow one to model the change in cyclic behavior with increasing helix angle.

The ideas presented are only a mere starting point to ever growing research avenues that will help us understand the vast capabilities of NiTi cables along with various advantageous industial applications. Hopefully this research helps lay the groundwork to enable the increasing prevalence of NiTi applications.

BIBLIOGRAPHY

[1] *ASM Handbook, Volume 1: Properties and Selection: Irons, Steels, and High-Performance Alloys*. ASM International, 1990.

[2] R. Abeyaratne and J. Knowles. *Evolution of Phase Transitions: a Continuum Theory*. Cambridge University Press Inc., New York, NY, USA, 2006.

[3] Y. Adachi, S. Unjoh, and M. Kondoh. Development of a shape memory alloy damper for intelligent bridge systems. *Mater. Sci. Forum (Switzerland)*, 327-328:31 – 4, 2000.

[4] M. S. Alam, M. A. Youssef, and M. Nehdi. Utilizing shape memory alloys to enhance the performance and safety of civil infrastructure: a review. *Canadian Journal of Civil Engineering*, 34(9):1075–1086, 2007.

[5] P. Barooah and N. Rey. Closed-loop control of a shape memory alloy actuation system for variable area fan nozzle. In V. S. Rao, editor, *Proceedings of SPIE*, volume 4693 of *Smart Structures and Materials 2002: Modeling, Signal Processing, and Control*, pages 384–395, 2002.

[6] N. J. Bechle and S. Kyriakides. Localization in NiTi tubes under bending. *International Journal of Solids and Structures*, 2013.

[7] B. Berg. Bending of superelastic wires, Part I: Experimental aspects. *Journal of Applied Mechanics*, 62:459, 1995.

[8] B. Berg. Twist and stretch: Combined loading of pseudoelastic NiTi tubing. *Proceedings of the 2nd International Conference on SMA and Superelastic Technologies*, Jan 1997. test notes.

[9] O. Bertacchini, D. Lagoudas, F. Calkins, and J. Mabe. Thermomechanical cyclic loading and fatigue life characterization of nickel rich niti shape-memory alloy actuators. *Society of Photo-Optical Instrumentation Engineers (SPIE) Conference Series*, 6929:27, 2008.

[10] K. Bhattacharya. *Microstructure of Martensite: Why it forms and how it gives rise to the shape-memory effect*. Oxford Series on Materials Modelling. Oxford University Press, NY, first edition, 2003.

[11] U. Blum, G. Voshage, J. Lammer, F. Beyersdorf, D. TÃllner, G. Kretschmer, G. Spillner, P. Polterauer, G. Nagel, T. HÃlzenbein, S. Thurnher, and M. Langer. Endoluminal stent–grafts for infrarenal abdominal aortic aneurysms. *New England Journal of Medicine*, 336(1):13–20, 1997.

[12] B. Bundara, M. Tokuda, B. Kuselj, B. Ule, and J. Tuma. Superelastic tension and bending characteristics of shape memory alloys. *Metals and Materials International*, 6:293–299, 2000. 10.1007/BF03028074.

[13] H. S. Carslaw and J. C. Jaeger. *Conduction of Heat in Solids*. Oxford University Press, London, UK, 2nd edition, 1959.

[14] B.-C. Chang, J. A. Shaw, and M. A. Iadicola. Thermodynamics of shape memory alloy wire: Modeling, experiments, and application. *Continuum Mechanics and Thermodynamics*, 18(1-2):83–118, 2006.

[15] E. Choi, D. Lee, and N. Choei. Shape memory alloy bending bars as seismic restrainers for bridges in seismic areas. *Int. J. Steel Struct*, 9(4):261–273, 2009.

[16] C. B. Churchill. *Experimental Techniques for Characterizing the Thermo-Electro-Mechanical Shakedown Response of SMA Wires and Tubes*. PhD dissertation, The University of Michigan, Department of Aerospace Engineering, Dec. 2010.

[17] C. B. Churchill and J. A. Shaw. Shakedown response of conditioned shape memory alloy wire. In *Behavior and Mechanics of Multifunctional and Composite Materials, Proceedings of the SPIE 15th Annual International Symposium on Smart Structures and Materials*, volume 6929, page 6929F, 2008.

[18] C. B. Churchill and J. A. Shaw. Thermo-electro-mechanical shakedown response of conditioned shape memory alloy wires. In *Proceedings of the ASME 2009 Conference on Smart Materials, Adaptive Structures and Intelligent Systems (SMASIS 2009)*, volume 1, pages 137–148. ASME, Sep. 2009.

[19] C. B. Churchill and J. A. Shaw. Thermo-mechanical modeling of a shape memory alloy heat engine. In *Proceedings of the ASME 2011 Conference on Smart Materials, Adaptive Structures and Intelligent Systems (SMASIS 2011)*, volume 1, pages 641–650, Sep. 2011.

[20] C. B. Churchill, J. A. Shaw, and M. A. Iadicola. Tips and tricks for characterizing shape memory alloy wire: Part 2 – fundamental isothermal responses. *Experimental Techniques*, 33(1):51–62, Jan-Feb 2009.

[21] C. B. Churchill, J. A. Shaw, and M. A. Iadicola. Tips and tricks for characterizing shape memory alloy wire: Part 3 – localization and propagation phenomena. *Experimental Techniques*, 33(5):70–78, Sept/Oct 2009.

[22] C. B. Churchill, J. A. Shaw, and M. A. Iadicola. Tips and tricks for characterizing shape memory alloy wire: Part 4 – thermo-mechanical coupling. *Experimental Techniques*, 34(2):63–80, Mar/Apr 2010.

[23] D. S. S. Corp. *ABAQUS Manual*. Dassault Systèmes Simulia Corp., 6.14 edition, 2015.

[24] Correlated Solutions. *Vic-Snap Manual*. Correlated Solutions, Inc., Columbia, SC, 2009.

[25] Correlated Solutions. *Vic-3D Manual*. Correlated Solutions, Inc., Columbia, SC, 2010.

[26] Correlated Solutions. *Vic-3D Testing Guide*. Correlated Solutions, Inc., Columbia, SC, 2010.

[27] G. Costello. *Theory of Wire Rope*. Springer, New York, NY, 2nd edition, 1998.

[28] R. DesRoches and M. Delemont. Seismic retrofit of simply supported bridges using shape memory alloys. *Engineering Structures*, 2002.

[29] R. DesRoches and J. McCormick. Properties of large diameter shape memory alloys under cyclical loading. *Proceedings of SPIE - The International Society for Optical Engineering*, 5057:187 – 196, 2003.

[30] J. C. Dixon. *The Shock Absorber Handbook*. John Wiley & Sons, 1999.

[31] M. Dolce and D. Cardone. Mechanical behaviour of shape memory alloys for seismic applications 1. martensite and austenite NiTi bars subjected to torsion. *International Journal of Mechanical Sciences*, 43(11):2631 – 2656, 2001.

[32] M. Dolce and D. Cardone. Mechanical behaviour of shape memory alloys for seismic applications 2. austenite NiTi wires subjected to tension. *International Journal of Mechanical Sciences*, 43(11):2657 – 2677, 2001.

[33] T. W. Duerig, K. N. Melton, D. Stöckel, and C. M. Wayman, editors. *Engineering Aspects of Shape Memory Alloys*. Butterworth-Heinemann, Boston, MA, 1990.

[34] Duerig, T. W. and Pelton, A. and Stöckel, D. An overview of nitinol Medical applications. *Materials Science and Engineering A*, 273-275:149–160, 1999.

[35] S. Edo. Shape deterioration and reversible shape-memory effect in Ni-Ti alloys. *Journal of Materials Science Letters*, 24:3991–3993, 1989.

[36] G. Eggeler, E. Hornbogen, A. Yawny, A. Heckmann, and M. Wagner. Structural and functional fatigue of niti shape memory alloys. *Mat Sci Eng A-Struct*, 378(1-2):24–33, Jan 2004.

[37] J. L. Ericksen. *Introduction to the Thermodynamics of Solids*. Chapman and Hall, New York, NY, 1991.

[38] X.-Q. Feng and Q. Sun. Shakedown analysis of shape memory alloy structures. *International Journal of Plasticity*, 23(2):183–206, 2 2007.

[39] Fluent Computational Fluid Dynamics. ANSYS Academic Research, release 14.0, ANSYS Inc., 2016.

[40] C. P. Frick, A. M. Ortega, J. Tyber, A. E. M. Maksound, H. J. Maier, Y. Liu, and K. Gall. Thermal processing of polycrystalline NiTi shape memory alloys. *Materials Science and Engineering: A*, 405(1-2):34–49, 2005.

[41] H. Funakubo. *Shape Memory Alloys*. Gordon and Breach Science Publishers, New York, NY, 1987.

[42] C. Grabe and O. Bruhns. Path dependence and multiaxial behavior of a polycrystalline NiTi alloy within the pseudoelastic and pseudoplastic temperature regimes. *International Journal of Plasticity*, 25:513–545, 2009.

[43] J. F. Hallai and S. Kyriakides. Underlying material response for Lüders-like instabilities. *International Journal of Plasticity*, 47:1, 2013.

[44] D. Hartl and D. Lagoudas. Aerospace applications of shape memory alloys. *Proceedings of the Institution of Mechanical Engineers, Part G: Journal of Aerospace Engineering*, 221(4):535–552, 01 2007.

[45] D. A. Hebda and S. R. White. Effect of training conditions and extended thermal cycling on nitinol two-way shape memory behavior. *Smart Mater Struct*, 4:298–304, Oct 1995.

[46] L. Heller, P. Šittner, J. Pilch, and M. Landa. Factors controlling superelastic damping capacity of SMAs. *Journal of materials engineering and performance*, 18(5):603–611, 2009.

[47] J. V. Humbeeck. Non-medical applications of shape memory alloys. *Materials Science and Engineering A*, 273-275:134–148, 1999.

[48] M. A. Iadicola and J. A. Shaw. An experimental setup for measuring unstable thermo–mechanical behavior of shape memory alloy wire. *Journal of Intelligent Material Systems and Structures*, 13(2):157–166, 2002.

[49] M. A. Iadicola and J. A. Shaw. Rate and thermal sensitivities of unstable transformation behavior in a shape memory alloy. *International Journal of Plasticity*, 20:577–605, 2004.

[50] M. A. Iadicola and J. A. Shaw. An experimental method to measure initiation events during unstable stress–induced martensitic transformation in a shape memory alloy wire. *Smart Materials and Structures*, 16:S155–S169, 2007.

[51] T. F. Irvine and P. E. Liley. *Steam and gas tables with computer equations*. Academic press New York, 1984.

[52] L. Janke, C. Czaderski, M. Motavalli, and J. Ruth. Applications of shape memory alloys in civil engineering structures - overview, limits and new ideas. *Materials and Structures*, 2005.

[53] D. Jiang, N. J. Bechle, C. M. Landis, and S. Kyriakides. Buckling and recovery of niti tubes under axial compression. *International Journal of Solids and Structures*, 80:52–63, 2016.

[54] A. Johnson and J. Kramer. State-of-the-art of shape memory actuators. In *Proc. 6th Int. Conf. on New Actuators (Bremen, Germany, June 1998)*, 1998.

[55] G. B. Kauffman and I. Mayo. The story of Nitinol: The serendipitous discovery of the memory metal and its applications. *The Chemical Educator*, 2(2):1–21, June 1997.

[56] A. C. Keefe, G. P. McKnight, G. A. Herrera, P. A. Bedegi, C. B. Churchill, A. L. Browne, and J. Brown. Development of a Shape Memory Alloy Heat Engine Through Experiment and Modeling. In *Proceedings of the ASME 2011 Conference on Smart Materials, Adaptive Structures and Intelligent Systems (SMASIS 2011)*, volume 5212, pages 669–674, 2011.

[57] B. Kockar, I. Karaman, J. I. Kim, Y. J. Chumlyakov, J. Sharp, and C. J. M. Yu. Thermomechanical cyclic response of an ultrafine-grained NiTi shape memory alloy. *Acta Materialia*, 56(14):3630–3646, Jan 2008.

[58] Z. Kopel. Forced-air heater control system and method, Oct. 10 2006. US Patent 7,119,308.

[59] H. Kramers. Heat transfer from spheres to flowing media. *Physica*, 12(2):61–80, June 1946.

[60] D. Lagoudas and Z. Bo. Thermomechanical modeling of polycrystalline smas under cyclic loading, part ii: material characterization and experimental results for a stable transformation cycle. *International Journal of Engineering Science*, 37(9):1141–1173, 1999.

[61] D. Lagoudas, D. Miller, L. Rong, and P. Kumar. Thermomechanical fatigue of shape memory alloys. *Smart Materials and Structures*, 18:1–12, Jan 2009.

[62] Matlab R2013a. *Matlab Documentation*. MathWorks, Natick, MA, 2013.

[63] J. McCormick, J. Tyber, R. DesRoches, K. Gall, and H. J. Maier. Structural engineering with NiTi. II: Mechanical behavior and scaling. *J Eng Mech-Asce*, 133(9):1019–1029, Jan 2007.

[64] H. A. McKenna, J. W. S. Hearle, and N. O'Hear. *Handbook of Fibre Rope Technology*. CRC Press LLC, 2004.

[65] A. Ortega, J. Tyber, C. Frick, K. Gall, and H. Maier. Cast NiTi shape-memory alloys. *Adv. Eng. Mater. (Germany)*, 7(6):492 – 507, June 2005.

[66] K. Otsuka and X. Ren. Physical metallurgy of Ti-Ni-based shape memory alloys. *Progress in Materials Science*, 50:511–678, 2005.

[67] K. Otsuka and C. M. Wayman. *Shape Memory Materials*. Cambridge University Press, Cambridge, UK, 1998.

[68] A. M. Pankonien, C. T. Faria, and D. J. Inman. Synergistic smart morphing aileron: Experimental quasi-static performance characterization. *Journal of Intelligent Material Systems and Structures*, 26(10):1179–1190, 2015.

[69] H. M. Paranjape, S. Manchiraju, and P. M. Anderson. A phase field - finite element approach to model the interaction between phase transformations and plasticity in shape memory alloys. *International Journal of Plasticity*, 2015.

[70] A. Pelton, G. Huangb, P. Moinec, and R. Sinclair. Effects of thermal cycling on microstructure and properties in nitinol. *Materials Science and Engineering A*, 2012.

[71] F.-J. Pérez-Reche, L. Truskinovsky, and G. Zanzotto. Training-induced criticality in martensites. *Phys. Rev. Lett.*, 99(7):075501, Aug 2007.

[72] B. Reedlunn. *Thermomechanical Behavior of Shape Memory Alloy Cables and Tubes*. PhD dissertation, The University of Michigan, Department of Mechanical Engineering, Dec. 2011.

[73] B. Reedlunn, C. B. Churchill, E. Nelson, S. Daly, and J. A. Shaw. Tension, compression, and bending of superelastic shape memory alloy tubes. *Journal of the Mechanics and Physics of Solids*, 63:506–537, 2014.

[74] B. Reedlunn, S. Daly, L. G. J. Hector, P. Zavattieri, and J. A. Shaw. Tips and tricks for characterizing shape memory alloy wire: Part 5 – full-field strain measurement by digital image correlation. *Experimental Techniques*, 37(3):62–78, 2013.

[75] B. Reedlunn, S. Daly, and J. A. Shaw. Superelastic shape memory alloy cables: Part I – isothermal tension experiments. *International Journal of Solids and Structures*, 50:3009–3026, 2013. (2013 IJSS best paper award).

[76] B. Reedlunn, S. Daly, and J. A. Shaw. Superelastic shape memory alloy cables: Part II – isothermal subcomponent responses. *International Journal of Solids and Structures*, 50:3027–3044, 2013.

[77] J. Rejzner, C. Lexcellent, and B. Raniecki. Pseudoelastic behaviour of shape memory alloy beams under pure bending: experiments and modelling. *International journal of mechanical sciences*, 44(4):665–686, 2002.

[78] E. Reshotko and I. E. Beckwith. Compressible laminar boundary layer over a yawed infinite cylinder with heat transfer and arbitrary prandtl number. *NACA TN 3986*, 1957.

[79] N. M. Rey, G. Tillman, R. M. Miller, T. Wynosky, M. J. Larkin, J. D. Flamm, and L. S. Bangert. Shape memory alloy actuation for a variable area fan nozzle. In A.-M. R. McGowan, editor, *Society of Photo-Optical Instrumentation Engineers (SPIE) Conference Series*, volume 4332, pages 371–382, June 2001.

[80] S. Saadat, J. Salichs, M. Noori, Z. Hou, H. Davoodi, I. Bar-on, Y. Suzuki, and A. Masuda. An overview of vibration and seismic applications of NiTi shape memory alloy. *Smart Mater. Struct. (UK)*, 11(2):218 – 29, 2002/04/.

[81] V. A. Sandborn. *Resistance Temperature Transducers*. Metrology Press, Fort Collins, Colorado, 1972.

[82] J. A. Shaw. Simulations of localized thermo–mechanical behavior in a NiTi shape memory alloy. *International Journal of Plasticity*, 16(5):541–562, 2000.

[83] J. A. Shaw, C. B. Churchill, and M. A. Iadicola. Tips and tricks for characterizing shape memory alloy wire: Part 1 – differential scanning calorimetry & basic phenomena. *Experimental Techniques*, pages 55–62, Sep-Oct 2008.

[84] J. A. Shaw and S. Kyriakides. Thermomechanical aspects of NiTi. *Journal of the Mechanics and Physics of Solids*, 43(8):1243–1281, 1995.

[85] J. A. Shaw and S. Kyriakides. Initiation and propagation of localized deformation in elasto–plastic strips under uniaxial tension. *International Journal of Plasticity*, 13(10):837–871, 1998.

[86] G. Song, N. Ma, and H.-N. Li. Applications of shape memory alloys in civil structures. *Engineering Structures*, 28(9):1266–1274, 2006.

[87] G. Song, Y. L. Mo, K. Otero, and H. Gu. Health monitoring and rehabilatation of a concrete structure using intelligent materials. *Smart Materials and Structures*, 15:309–314, 2006.

[88] P. Stainback and K. Nagabushana. Review of hot-wire anemometry techniques and the range of their applicability for various flows. *Journal of Fluids Engineering*, 1993.

[89] H. Sun, A. Pathak, J. Luntz, D. Brei, P. W. Alexander, and N. L. Johnson. Stabilizing shape memory alloy actuator performance through cyclic shakedown: an empirical study. In L. P. Davis, B. K. Henderson, and M. B. McMickell, editors, *In: Proceedings of SPIE, Industrial and Commercial Applications of Smart Structures Technologies 2008*, volume 6930, page 69300Q. SPIE, 2008.

[90] Q. P. Sun and Z.-Q. Li. Phase transformation in superelastic NiTi polycrystalline micro-tubes under tension and torsion–from localization to homogeneous deformation. *International Journal of Solids and Structures*, 39(13-14):3797–3809, 2002.

[91] V. Torra, A. Isalgue, G. Carreras, F. Lovey, H. Soul, P. Terriault, and B. Zapico. The SMA properties in civil engineering applications. The SMARTeR project: Use of SMA in damping of stayed cables for bridges. In *ESOMAT 2009-8th European Symposium on Martensitic Transformations*, pages 7016–7016, 2009.

[92] J. Van Humbeeck. Damping capacity of thermoelastic martensite in shape memory alloys. *J. Alloys Compd. (Switzerland)*, 355:58 – 64, June 2003.

[93] Y. Wang, Z. Yue, and J. Wang. Experimental and numerical study of the superelastic behaviour on NiTi thin-walled tube under biaxial loading. *Computational Materials Science*, 40(2):246–254, 2007.

[94] R. Watkins. *Thermomechanical Characterization and Modeling of Superelastic Shape Memory Alloy Beams and Frames*. PhD thesis, University of Michigan, 2015.

[95] R. Watkins, B. Reedlunn, S. Daly, and J. A. Shaw. Uniaxial, pure bending and buckling experiments on superelastic NiTi rods and tubes. *International Journal of Solids and Structures*, (submitted), 2017.

[96] X. C. Wu, D. S. Grummon, and T. J. Pence. Modeling phase fraction shakedown during thermomechanical cycling of shape memory materials. *Materials Science and Engineering A – Structural Materials Properties, Microstructure and Processing*, 275:245–250, Dec 15 1999.

[97] X. Zhang, P. Feng, Y. He, T. Yu, and Q. Sun. Experimental study on rate dependence of macroscopic domain and stress hysteresis in niti shape memory alloy strips. *International Journal of Mechanical Sciences*, 52(12):1660–1670, 2010.

[98] A. Zukauskas. *Heat Transfer from Tubes in Crossflow*, volume 18 of *Advances in Heat Transfer*, pages 87–160. Elsevier Science, 1987.

[99] A. Zukauskas and J. Ziugzda. *Heat transfer of a cylinder in crossflow*. Hemisphere Publishing,New York, NY, 1985.